

KAUNAS UNIVERSITY OF TECHNOLOGY

MANTAS MARČINSKAS

[2-(9*H*-CARBAZOL-9-YL)ETHYL]PHOSPHONIC ACID SELF-ASSEMBLED MONOLAYER ALTERNATIVES FOR APPLICATION IN OPTOELECTRONICS

Doctoral dissertation
Natural Sciences, Chemistry (N 003)

2025, Kaunas

The dissertation has been prepared at the Department of Organic Chemistry of the Faculty of Chemical Technology of Kaunas University of Technology in 2020–2024.

Research supervisor:

Prof. Dr. Tadas MALINAUSKAS (Kaunas University of Technology, Natural Sciences, Chemistry, N 003).

Edited by: English language editor Dr. Armandas Rumšas (Publishing House *Technologija*), Lithuanian language editor Aurelijā Gražina Rukšaitė (Publishing House *Technologija*).

Dissertation Defence Board of the Chemistry Science Field:

Prof. Dr. Saulius GRIGALEVIČIUS (Kaunas University of Technology, Natural Sciences, Chemistry, N 003) – **chairperson**;

Assoc. Prof. Dr. Birutė GRYBAITĖ (Kaunas University of Technology, Natural Sciences, Chemistry, N 003);

Dr. Karolis KAZLAUSKAS (Vilnius University, Natural Sciences, Physics, N 002);

Dr. Karolis NORVAIŠA (Université Libre de Bruxelles, Belgium, Natural Sciences, Chemistry, N 003);

Prof. Dr. Edvinas ORENTAS (Vilnius University, Natural Sciences, Chemistry, N 003).

The dissertation defence will be held on 25 February 2025, at 11 a.m. in a public meeting of the Dissertation Defence Board of the Chemistry science field at the Rectorate Hall of Kaunas University of Technology.

Address: K. Donelaičio 73-402, LT-44249, Kaunas, Lithuania.

Phone: (+370) 608 28 527; e-mail doktorantura@ktu.lt

The dissertation was sent out on 24 January 2025.

The dissertation is available on <http://ktu.edu> and at the library of Kaunas University of Technology (Gedimino 50, LT-44239, Kaunas, Lithuania).

© M. Marčinskas, 2025

KAUNO TECHNOLOGIJOS UNIVERSITETAS

MANTAS MARČINSKAS

SAVITVARKI MONOSLUOKSNĮ
FORMUOJANČIOS [2-(9H-KARBAZOL-9-
IL)ETIL]FOSFONRŪGŠTIES ALTERNATYVOS
IR JŲ TAIKYMAS OPTOELEKTRONIKOJE

Daktaro disertacija
Gamtos mokslai, chemija (N 003)

2025, Kaunas

Disertacija rengta 2020–2024 metais Kauno technologijos universiteto Cheminės technologijos fakultete Organinės chemijos katedroje.

Mokslinis vadovas:

prof. dr. Tadas MALINAUSKAS (Kauno technologijos universitetas, gamtos mokslai, chemija, N003).

Redagavo: anglų kalbos redaktorius dr. Armandas Rumšas (leidykla „Technologija“), lietuvių kalbos redaktorė Aurelija Gražina Rukšaitė (leidykla „Technologija“).

Chemijos mokslo krypties disertacijos gynimo taryba:

prof. dr. Saulius GRIGALEVIČIUS (Kauno technologijos universitetas, gamtos mokslai, chemija, N 003) – **pirmininkas/(-ė)**;

doc. dr. Birutė GRYBAITĖ (Kauno technologijos universitetas, gamtos mokslai, chemija, N 003);

dr. Karolis KAZLAUSKAS (Vilniaus universitetas, gamtos mokslai, fizika, N 002);

dr. Karolis NORVAIŠA (Briuselio laisvasis universitetas, Belgija, gamtos mokslai, chemija, N 003);

prof. dr. Edvinas ORENTAS (Vilniaus universitetas, gamtos mokslai, chemija, N 003).

Disertacija bus ginama viešame Chemijos mokslo krypties disertacijos gynimo tarybos posėdyje 2025 m. vasario 25 d. 11 val. Kauno technologijos universiteto Rektorato salėje.

Adresas: K. Donelaičio g. 73-402, LT-44249, Kaunas, Lietuva.

Tel: (+370) 608 28 527; el. paštas doktorantura@ktu.lt

Disertacija išsiusta 2025 m. sausio 24 d.

Su disertacija galima susipažinti interneto svetainėje <http://ktu.edu> ir Kauno technologijos universiteto bibliotekoje (Gedimino g. 50, LT-44239 Kaunas, Lietuva).

© M. Marčinskas, 2025

CONTENTS

LIST OF TABLES.....	8
LIST OF FIGURES.....	9
LIST OF ABBREVIATIONS AND DEFINITIONS	14
INTRODUCTION.....	16
1. LITERATURE REVIEW	20
1.1. Self-Assembled Monolayer	20
1.2. Phosphonic Acid Synthesis and Reactions.....	24
1.3. SAM Application in Perovskite Solar Cells.....	28
1.3.1. Perovskite	28
1.3.2. Perovskite solar cell architectures.....	30
1.3.3. Phosphonic acid SAM HTMs application in p-i-n PSCs	33
1.4. SAM Application in Bulk-Heterojunction Organic Solar Cells	41
1.4.1. Organic solar cells	41
1.4.2. Charge transporting materials in organic solar cells	45
1.5. Conclusions of the Chapter.....	49
2. RESULTS AND DISCUSSION	50
2.1. Halogenated Carbazole-Based Hole Transporting SAM Materials	50
2.1.1. Synthesis of halogenated carbazole-based materials containing the phosphonic acid functional group.....	50
2.1.2. Photoelectrical properties	53
2.1.3. Performance in bulk heterojunction organic solar cells	54
2.1.4. Performance in organic light emitting diodes	58
2.1.5. Chapter summary.....	62
2.2. SAM Materials Containing Phosphonic Acid Functional Groups and Non-Carbazole Central Fragments	62
2.2.1. Synthesis of non-carbazole materials containing the phosphonic acid functional group	63
2.2.2. Photoelectrical properties	65
2.2.3. Performance in bulk heterojunction organic solar cells	68

2.2.4. Performance of perovskite solar cells	69
2.2.5. Chapter summary.....	75
2.3. SAM Materials Containing Phosphonic Acid and Other Functional Groups	75
2.3.1. Synthesis of compounds containing different functional groups and the phosphonic acid group.....	76
2.3.2. Photoelectrical properties	80
2.3.3. Performance in bulk heterojunction organic solar cells	81
2.3.4. Performance in perovskite solar cells	82
2.3.5. Application in gas sensors based on ZnO tetrapods	87
2.3.6. Chapter summary.....	91
2.4. SAM Materials Containing Phosphonic Acid Functional Groups and Ammonium Functional Groups	91
2.4.1. Synthesis of compounds containing ammonium groups and phosphonic acid	91
2.4.2. Photoelectrical properties	97
2.4.3. Ionic SAM performance in NBG Pb-Sn perovskite solar cells	98
2.4.4. Chapter summary.....	100
3. METHODS AND MATERIALS	102
3.1. General Methods	102
3.2. Detailed Synthesis Procedures and Materials	110
4. CONCLUSIONS	158
5. SANTRAUKA	160
5.1. Halogeninti karbazolo centrinių fragmentų turintys skyles pernešantys SAM sudarantys junginiai.....	163
5.1.1. Halogenintų karbazolo darinių, turinčių fosfonrūgšties funkcinę grupę, sintezė.....	164
5.1.2. Junginių panaudojimas tūrio heterosandūros organiniuose saulės elementuose.....	165
5.1.3. Junginių panaudojimas organiniuose šviesos dioduose.....	167
5.1.4. Skyriaus išvados	169
5.2. Nekarbazoliniai SAM sudarantys junginiai, turintys fosfonrūgšties funkcinės grupes	170

5.2.1. Nekarbazolinių junginių, turinčių fosfonrūgšties funkcinės grupes, sintezė.....	170
5.2.2. Junginių panaudojimas perovskitiniose saulės elementuose	171
5.2.3. Skyriaus apibendrinimas.....	174
5.3. SAM sudarantys junginiai su fosfonrūgšties bei kitomis funkcinėmis grupėmis.....	174
5.3.1 Fosfonrūgšties ir kitas funkcinės grupes turinčių molekulių sintezė	174
5.3.2. Junginių panaudojimas organiniuose saulės elementuose	178
5.3.3. Junginių panaudojimas perovskitiniose saulės elementuose	179
5.3.4. Junginių panaudojimas ZnO tetrapodų dujujutikliuose	185
5.3.5. Skyriaus apibendrinimas.....	188
5.4. SAM sudarantys junginiai su fosfonrūgšties bei amonio funkcinėmis grupėmis.....	189
5.4.1. Junginių su amonio ir fosfonrūgšties grupėmis sintezė	189
5.4.2. Junginių panaudojimas NBG perovskitiniose saulės elementuose	191
5.4.3. Skyriaus apibendrinimas.....	192
REFERENCES.....	195
CURRICULUM VITAE.....	211
ACKNOWLEDGEMENTS	213
ANNEXES	214

LIST OF TABLES

Table 2.1. Measured ionization potential and work function values of the synthesized halogenated SAM derivatives	53
Table 2.2. Summary of the key operating parameters of OPVs based on PM6:PM7-Si:BTP-eC9 BHJs with different HTMs measured under illumination of AM 1.5G (100 mW/cm ²).....	55
Table 2.3. Summary of the key operating parameters of OPVs based on PM6:BTP-eC9 BHJs with different HTMs measured under illumination of AM 1.5G (100 mW/cm ²)	56
Table 2.4. Summary of the key operating parameters of OPVs based on PM6:BTP-eC9 BHJs with different HTMs measured under illumination of AM 1.5G (100 mW/cm ²)	56
Table 2.5. Summary of the key operating parameters of OPVs based on PM1:BTP-eC9 BHJs with different HTMs measured under illumination of AM 1.5G (100 mW/cm ²)	57
Table 2.6. Summary of the key operating parameters of OPVs based on PM6:PM7-Si:BTP-eC9 BHJ with BV dopant based on compound 8 or PEDOT:PSS measured under illumination of AM 1.5G (100 mW/cm ²).....	57
Table 2.7. Performance parameters of OLEDs based on CBP:Ir(ppy) ₂ acac with different hole-injection layers.....	61
Table 2.8. Measured ionization potential values of synthesized non-carbazole HTMs	66
Table 2.9. Summary of the key operating parameters of OPVs based on PM6:BTP-eC9 BHJ based on compound 58 or 61 measured under illumination of AM 1.5G (100 mW/cm ²).....	68
Table 2.10. Summary of the key operating parameters of OPVs based on PM6:BTP-eC9 BHJ based on compound 84 measured under illumination of AM 1.5G (100 mW/cm ²)	81
5.1 lentelė. OPV naudojant PM6:PM7-Si:BTP-eC9 BHJ su skirtiniais HTMs fotovoltinių charakteristikų apibendrinimas esant AM 1.5G (100 mW/cm ²) apšvietai	166
5.2 lentelė. OPV naudojant PM6:PM7-Si:BTP-eC9 BHJ, BV legirantą bei junginį 8 ir PEDOT:PSS fotovoltinių charakteristikų apibendrinimas esant AM 1.5G (100 mW/cm ²) apšvietai	166
5.3 lentelė. CBP:Ir(ppy) ₂ acac pagrindu sukonstruotų OLED su skirtinė medžiagų skylių injekcijos sluoksniu charakteristikos	169
5.4 lentelė. PM6:BTP-eC9 BHJ pagrindu sukonstruotų OPV su junginiu 84 fotovoltinių charakteristikų apibendrinimas esant AM 1.5G (100 mW/cm ²) apšvietai	179

LIST OF FIGURES

Figure 1.1. Structure of self-assembled monolayer [20]	20
Figure 1.2. (a) Schematic of the thiol and phosphonic acid-based SAMs deposited on ZnO; (b) the ratio of carbon to either phosphorus or sulfur in the SAMs on ZnO at different temperatures [22]	21
Figure 1.3. Crystal lattice structure of perovskite [49].....	29
Figure 1.4. One-step and two-step spin-coating procedures for perovskite ($\text{CH}_3\text{NH}_3\text{PbI}_3$) layer formation [61].....	29
Figure 1.5. Perovskite-based DSSC architecture [79].....	31
Figure 1.6. Mesoscopic architecture PSC [79]	31
Figure 1.7. Mesoscopic architecture PSC [84]	32
Figure 1.8. (a) J-V characteristics of the best-performing PSCs with 10% V1036 90% C4 SAM and PTAA HTMs; (b) Shelf lifetime of representative PTAA (cell 1 max. PCE=18.5%) and 10% V1036 90% C4 SAM (cell 1 max. PCE=17.8%) based devices [4]	34
Figure 1.9. (a) Schematic of the device structure studied, where the zoom-in illustrates how SAM molecules attach to the ITO surface, enabling hole-selective contact with the perovskite above; (b) Box plot of power conversion efficiency (PCE) values for V1036 (41 pixels), PTAA (53 pixels), MeO-2PACz (47 pixels) and 2PACz (46 pixels) solar cells [5]	35
Figure 1.10. SEM images of ‘triple cation’ perovskite layers fabricated on PTAA and MeO-2PACz surfaces with illustration of buried interface differences [112]....	36
Figure 1.11. (a) Schematic structure of PSC and (b) Bias-induced PSCs with HTL as PTAA or MeO-2PACz; photovoltaic characteristics of fresh and biased devices: (c) V_{oc} , (d) J_{sc} , (e) FF, and (f) efficiency [112].....	37
Figure 1.12. (a) Schematic structure of PSC containing double-sided 2D/3D perovskites; (b) Photovoltaic characteristics of PSCs with and without 2D/3D perovskite interfaces; (c) Stability of encapsulated PSCs with and without 2D/3D perovskite interfaces under 1-sun illumination at 85 °C and open-circuit conditions [118].....	38
Figure 1.13. (a) Schematic structure of perovskite/silicon tandem solar cell containing Me-4PACz SAM; (b) Chemical structure of Me-4PACz; (c) Photovoltaic characteristics of the device related to maximum power P_{max} scan [119]	39
Figure 1.14. Examples of non-carbazole SAM materials [120-123].....	40
Figure 1.15. OPV operational mechanism [131].....	41
Figure 1.16. Different device structures of OPVs: (a) Single layer; (b) Bilayer; (c) Bulk heterojunction [131].....	42
Figure 1.17. Chemical structures of PC ₆₁ BM and PC ₇₁ BM	43
Figure 1.18. Examples of non-fullerene molecules of the A-D-A structure [131]...44	44
Figure 1.19. Examples of donor molecules [131]	44

Figure 1.20. Examples of donor molecules.....	45
Figure 1.21. Examples of ETMs used in OPVs	46
Figure 1.22. Chemical structure of the PEDOT:PSS.....	46
Figure 1.23. (a) Chemical structure of the 2PACz; (b) Schematic structure of BHJ organic solar cell; (c) Evolution of normalized PCEs of BHJ OPVs based on 2PACz and PEDOT:PSS [136]	47
Figure 1.24. (a) <i>J-V</i> curves of BHJ OPVs when using Br-2PACz, MeO-2PACz, and PEDOT:PSS. The inset shows the schematic of the employed cell architecture; (b) Box plot of V_{oc} , J_{sc} , FF, and PCE for OPV cells based on Br-2PACz and PEDOT:PSS [180].....	48
Figure 2.1. (a) Schematic architecture of the BHJ organic solar cell; (b) Chemical structures of BHJ materials	54
Figure 2.2. (a) <i>J-V</i> curves of PM6:PM7-Si:BTP-eC9 BHJ with BV dopant solar cells; (b) Change of PCE of OPVs over time	58
Figure 2.3. (a) Schematic OLED device architecture; (b) Structures of materials used to construct OLED devices	59
Figure 2.4. (a) STM topographic images of bare and SAM treated ITO samples; (b) SAMs molecular islands size distribution, obtained from statistical analysis on ITO/SAM STM images	60
Figure 2.5. (a) Electroluminescence spectra and chromaticity diagram (inset) of green phosphorescent OLEDs; (b) Device EQE statistics	61
Figure 2.6 Photoemission in air spectra of SAM derivatives 58 and 61	66
Figure 2.7 Work functions' values of compounds 55 , 64 and 70 compared to the reference SAM materials 2PACz and Me-4PACz.....	67
Figure 2.8. (a) Schematic architecture of BHJ organic solar cell; (b) <i>J-V</i> curves of the best cells in the batch using SAMs 58 and 61	68
Figure 2.9. Analysis of SAMs 58 and 61 photovoltaic characteristics in p-i-n perovskite solar cells (two batches were evaluated): (a) V_{oc} statistical results; (b) J_{sc} statistical results; (c) Fill factor statistical results; (d) Efficiency statistical results .	69
Figure 2.10. <i>J-V</i> curves of the best cells in the batch using 2PACz, 4PACz, and SAM derivatives 58 and 61	70
Figure 2.11. PL spectra of perovskite deposited on quartz and different ITO/SAM substrates.....	71
Figure 2.12. QFLS values of the perovskite film on quartz substrate and different SAMs on ITO.....	72
Figure 2.13. Transient surface photovoltage curves taken with samples of perovskite on bare quartz, ITO, and ITO/SAM.....	73
Figure 2.14. Photovoltaic characteristics of p-i-n architecture perovskite solar cells of ITO/SAM/Pero/C ₆₀ /SnO ₂ /Ag architecture comparing different HTMs used as SAMs: (a) V_{oc} statistical results; (b) J_{sc} statistical results; (c) Fill factor statistical results; (d) Efficiency statistical results	74

Figure 2.15. Photoemission in air spectra of SAM derivatives 73, 77, 84 and 89 ...	80
Figure 2.16. (a) Schematic architecture of the BHJ organic solar cell; (b) <i>J-V</i> curve of the best cell in the batch using carbazole 84	81
Figure 2.17. Chemical structures of the materials used for the formation of monolayers: (a) Me-4PACz and (b) 6dPA. Close-up optical images of the representative PSCs with (c) Me-4PACz and (d) Me4-PACz+6dPA selective contact layer. Highlighted in red are the active cell areas not covered by perovskite film. Scale bar = 5 mm. (e, f) Optical images of the contact angle measurements were made by using triple-cation perovskite precursor solution on top of ITO/ monolayer substrates.....	82
Figure 2.18. Statistical distribution of the PCE (reverse scan – darker color, forward scan – lighter color) for a device with pure Me-4PACz and mixed monolayer with two different perovskite compositions (shunted devices were excluded from this analysis)	83
Figure 2.19. Reverse scan of the best pixel for the devices, fabricated by using carbazole 73+6dPA monolayer	84
Figure 2.20. Photovoltaic characteristics of p-i-n architecture perovskite solar cells, utilizing different perovskites and comparing different HTMs used as SAMs: (a) V_{OC} statistical results; (b) J_{SC} statistical results; (c) Fill factor statistical results; (d) Efficiency statistical results	85
Figure 2.21. Stability experiment of PSCs based on triple halide perovskite and Me-4PACz or compound 84 as HTM.....	86
Figure 2.22. J-V curves and photovoltaic characteristics of the best cells in the batch when using Me-4PACz, and SAM derivatives 77, 84 and 89	87
Figure 2.23. Contact angle measurements of water on non-modified and modified ZnO-T surfaces.....	88
Figure 2.24. Schematic of ZnO tetrapods (ZnO-Ts) with a self-assembled monolayer of carbazole derivative: a) chemoresistive sensor schematics; b) Carbazole-based SAM structure.	89
Figure 2.25. Characterization of ZnO-T and ZnO-T with SAM sensors: a) Response to VOCs and gases at 10ppm; b) Response and recovery at different NO_2 concentrations	89
Figure 2.26. ZnO-T sensor response at RT. ZnO-T with SAM under different UV conditions: UV illumination (UV ON), dark (UV OFF) and UV modulation with 10 s period and 50 % duty cycle.....	90
Figure 2.27. Photoemission in air spectra of SAM derivatives 93, 94, 99 and 100 . Figure 2.28. Photoemission in air spectra of SAM derivatives 108, 111, 118 and 119	97
Figure 2.29. (a) Sn-Pb based PSC architecture; (b) Chemical structures of the materials used for the formation of the monolayers.....	99

Figure 2.30. Photovoltaic characteristics of NBG p-i-n architecture perovskite solar cells comparing different HTMs used as SAMs: (a) V_{OC} statistical results; (b) J_{SC} statistical results; (c) Fill factor statistical results; (d) Efficiency statistical results 100

5.1 pav. (a) BHJ organinio saulės elemento architektūros schema;	(b) medžiagą, naudojamą BHJ formuoti, cheminės struktūros.....	165
5.2 pav. (a) saulės elementų su PM6:PM7-Si:BTP-eC9 BHJ ir BV legirantu J-V kreivės; (b) OPV PCE pokytis per tam tikrą laikotarpį.....	167	
5.3 pav. (a) Schematiška OLED įrenginio architektūra; (b) medžiagą, naudotą OLED konstruoti, struktūrinės formulės	168	
5.4 pav. (a) Žaliai fosforescuojančių OLED elektroliuminescencijos spektrai ir spalvų diagrama (intarpas); (b) įrenginių EQE statistikos	168	
5.5 pav. Efektyviausių įrenginių naudojant 2PACz, 4PACz, 58 ir 61 J-V kreivės	171	
5.6 pav. Perovskito ant kvarco, ITO ir ITO/SAM trSPV kreivės.....	172	
5.7 pav. ITO/SAM/Pero/C ₆₀ /SnO ₂ /Ag architektūros, p-i-n konfigūracijos perovskitinių saulės elementų fotovoltinės charakteristikos, lyginant skirtingus HTM, naudotus kaip SAM: (a) V_{OC} statistiniai rezultatai; (b) J_{SC} statistiniai rezultatai; (c) užpildymo koeficiente statistiniai rezultatai; (d) efektyvumo statistiniai rezultatai.....	173	
5.8 pav. (a) BHJ organinio saulės elemento schematiška architektūra; (b) geriausio įrenginio naudojant karbazolą 84 J-V kreivė	179	
5.9 pav. Junginių, naudotų monosluoksnui formuoti, cheminės struktūros: (a) Me-4PACz ir (b) 6dPA. Reprezentacinės PSCs su (c) Me-4PACz ir (d) Me4-PACz+6dPA nuotraukos. Raudona spalva pažymėtos vietas, nepadengtos perovskitu. Mastelis = 5 mm. (e, f) Vilgymo kampo matavimų nuotraukos, lašinant trijų katijonų perovskito komponentų tirpalą ant ITO/monosluoksnio substratų.	180	
5.10 pav. Prietaisų PCE statistinis pasiskirstymas (neveikiantys įrenginiai nebuvo iutraukti) naudojant skirtingus perovskitus bei Me-4PACz ir Me-4PACz + 6dPA (skenavimas atgal – tamsesnė spalva, skenavimas pirmyn – šviesesnė spalva).....	181	
5.11 pav. Geriausias efektyvumas buvo prietaiso, sukonstruoto naudojant karbazolą 73 + 6dPA, skenavimo atgal J-V kreivė.....	182	
5.12 pav. P-i-n architektūros perovskitinių saulės elementų fotovoltinės charakteristikos, naudojant skirtingus perovskitus ir lyginant skirtingus SAM sudarančius HTMs: (a) V_{OC} statistiniai rezultatai; (b) J_{SC} statistiniai rezultatai; (c) užpildymo faktoriaus statistiniai rezultatai; (d) efektyvumo statistiniai rezultatai .	183	
5.13 pav. PSCs naudojant Me-4PACz and SAM sudarančius junginius 77 , 84 ir 84 J-V kreivės bei fotovoltinės charakteristikos.....	185	
5.14 pav. Modifikuotų ZnO-Ts karbazolo 77 monosluoksniu schemas: a) jutiklio schema; b) karbazolo 77 cheminė struktūra.....	186	
5.15 pav. ZnO-T ir modifikuotų ZnO-T jutiklių charakterizavimas: a) atsakas į lakiuosius junginius ir dujas, kai koncentracija yra 10 ppm; b) atsakas ir atsistatymas esant skirtingai NO ₂ koncentracijai	187	

5.16 pav. ZnO-T jutiklio atsakas esant kambario temperatūrai. Naudoti modifikuoti ZnO-T su su 77 esant skirtingoms UV sąlygomis: esant UV apšvietimui (UV On), tamsoje (UV Off) ir moduliuojant UV (10 s periodas)	188
5.17 pav. (a) Sn-Pb PSC architektūra; (b) junginių, naudotų monosluoksniniui formuoti, cheminės struktūros	191
5.18 pav. NBG p-i-n architektūros perovskitinių saulės elementų fotovoltaikinės charakteristikos, lyginant skirtingus HTM, naudojamus kaip SAM: (a) Voc statistiniai rezultatai; (b) J_{SC} statistiniai rezultatai; (c) užpildymo koeficiente statistiniai rezultatai; (d) efektyvumo statistiniai rezultatai	192

LIST OF ABBREVIATIONS AND DEFINITIONS

¹³ C NMR	carbon (¹³ C) nuclear magnetic resonance;
¹ H NMR	proton nuclear magnetic resonance;
2PACz	[2-(9H-carbazol-9-yl)ethyl]phosphonic acid;
ACN	acetonitrile;
Ar	argon;
BCP	bathocuproine;
BHJ	bulk-heterojunction;
Boc ₂ O	di- <i>tert</i> -butyl dicarbonate;
Br-2PACz	[2-(3,6-dibromo-9H-carbazol-9-yl)ethyl]phosphonic acid;
CBP	4,4'-bis(<i>N</i> -carbazolyl)-1,1'-biphenyl;
Cz	carbazole;
DMA	dimethylacetamide;
DMF	dimethylformamide;
DMSO	dimethyl sulfoxide;
DSSC	dye-sensitized solar cell;
ETM	electron transporting material;
FA	fullerene acceptor;
FF	fill factor;
FTO	fluorine doped tin oxide;
HIL	hole injection layer;
HOMO	highest occupied molecular orbital;
Ht	heterocycle;
HTL	hole transporting layer;
HTM	hole transporting material;
Imb	iminodibenzyl;
Ind	indole;
I _p	ionization potential;
iPrOH	isopropylalcohol;
Ir(ppy) ₂ (acac)	bis[2-(2-pyridinyl- <i>N</i>)phenyl-C](acetylacetato)iridium(III);
Isb	iminostilbene;
ITO	indium tin oxide;
J _{sc}	short-circuit current density;
M.p.	melting point;
Me-4PACz	[4-(3,6-dimethyl-9H-carbazol-9-yl)butyl]phosphonic acid;
MeO-2PACz	[2-(3,6-dimethoxy-9H-carbazol-9-yl)ethyl]phosphonic acid;
MeOH	methanol;
NBG	narrow band-gap;
NBS	<i>N</i> -bromosuccinimide;
NFA	non-fullerene acceptor;

OLED	organic light emitting diode;
OPV	organic photovoltaic;
OSC	organic semiconductor;
PCE	power conversion efficiency;
Pd(PPh_3) ₄	tetrakis(triphenylphosphine)palladium(0);
PEDOT:PSS	poly(3,4-ethylenedioxythiophene)-poly(styrenesulfonate);
PESA	photoelectron spectroscopy in air;
Ph	phenyl;
PL	photoluminescence;
PSC	perovskite solar cell;
PTAA	poly[bis(4-phenyl)(2,4,6-trimethylphenyl)amine];
Ptz	phenothiazine;
PV	photovoltaic;
QFLS	Quasi-Fermi-level splitting;
RT	room temperature;
SAM	self-assembled monolayer;
TBAB	tetrabutylammonium bromide;
TCO	transparent conductive oxide;
TEA	triethylamine;
THF	tetrahydrofuran;
TLC	thin-layer chromatography;
TMS	trimethylsilane;
TPBi	2,2',2''-(1,3,5-benzenetriyl)-tris(1-phenyl-1- <i>H</i> -benzimidazole);
V_{OC}	open-circuit voltage;
WF	work function;
ZnO-T	zinc oxide tetrapods.

INTRODUCTION

As we live in a modern world which is inseparable from electronics and smart technologies, in order to maintain and improve the pace of their development, new materials will always be needed. As a consequence, the importance and research interest in *organic semiconductors* (OSCs) has also been significantly growing. OSCs can offer advantageous and attractive properties such as flexibility, light weight, and ease of processing. The choice of starting materials is very large, the selection of molecular fragments for the structural variations is also rich, which, overall, helps to obtain organic compounds with the desired electrical properties. At this moment, OSCs are often referred to as a ‘hot spot’ in the multidisciplinary fields such as chemistry, physics, materials science, medicine, and biology, starting from fundamental studies, followed by practical applications, and ending with commercial products. The versatility of synthetic organic chemistry allows to obtain the desired materials which are needed to be used in electronics such as light-emitting diodes, solar cells, transistors, or sensors, which can be flexible, printable, and scalable [1,2].

One of the best examples of the importance of OSCs is optoelectronic devices, such as *organic light-emitting diodes* (OLEDs) or *organic/hybrid photovoltaics* (PVs). Apart from inorganic electrodes, a lot of materials in OLEDs and PVs are organic semiconductors, including polymers and small molecules. They are being used as *hole transporting materials* (HTMs), *electron transporting materials* (ETMs), emitters or hosts (for OLEDs), or the photo active layer consisting of electron donors and electron acceptors in organic PVs [3].

One of the most recent approaches in the development of hole transporting OSCs was the introduction of self-assembled monolayer (SAM) carbazole-based HTMs containing a phosphonic acid anchoring group. Phosphonic acid moiety allows molecules to bind onto the metal oxide surface, such as ITO or FTO, which are often used as electrodes in solar cells and OLEDs, thus forming a one-molecule-thick layer. The monolayer can be formed from dilute solutions, with the self-assembly process enabling conformal substrate coverage. It also allows for minimal parasitic absorption, its deposition procedure is suitable for larger-scale production, even if the surface is textured, with a minimal material consumption [4]. The application of SAM materials enabled a faster progress of the p-i-n architecture perovskite solar cells (PSCs). The previously standard HTM polymer PTAA (18.9% of PCE) was outperformed by carbazole SAM semiconductors (20.8% of PCE) [2-(9H-carbazol-9-yl)ethyl]phosphonic acid (2PACz) [5] and (20.2% of PCE) [2-(3,6-Dimethoxy-9H-carbazol-9-yl)ethyl]phosphonic acid (MeO-2PACz). MeO-2PACz was further investigated in single-crystal PSCs where an enhanced operational device stability and a PCE of 23.1% was demonstrated [6]. The 2PACz family of materials was further investigated in other photovoltaic systems, which all resulted in the top-tier performance of the devices. As an example, [4-(3,6-Dimethyl-9H-carbazol-9-yl)butyl]phosphonic acid (Me-4PACz) was applied both in monolithic CIGSe/perovskite tandems and in perovskite/silicon tandems, resulting in a certified record PCEs of 24.2% and 29.15% respectively [7,8]. However, a wider use of Me-

4PACz is hindered by a rather high surface hydrophobicity, and, consequently, by poor coverage by the perovskite precursor solution. In this thesis, new materials based on SAM concept have been designed, synthesized, and tested in a variety of optoelectronic devices to solve the currently incurred SAM problems, and to further develop these extremely promising research areas.

The **aim of this work** is the synthesis and investigation of optoelectronic properties of the alternatives to 2PACz capable of transporting positive charge and forming self-assembled monolayers, as well as expanding the scope of SAM applicability.

The objectives proposed to achieve the above-stated aim are as follows:

1. To synthesize halogenated carbazole-based derivatives containing phosphonic acid groups and investigate the influence of different halogen substituents on the performance of bulk-heterojunction organic solar cells and organic light-emitting diodes.
2. To synthesize non-carbazole-based derivatives containing phosphonic acid groups and compare them with carbazole analogues by investigating the compatibility and performance of different chromophores in terms of performance of perovskite solar cells.
3. To propose an approach to solve Me-4PACz monolayer wettability issues.
4. To synthesize carbazole, phenothiazine and indole-based materials containing both a phosphonic acid group and additional functional groups, which would be able to interact with perovskite; to investigate the passivation effect in perovskite solar cells.

Scientific novelty

For a relatively long time, 2,2',7,7'-tetrakis (*N,N*-dimethoxyphenylamine)-9,9'-spirobifluorene (spiro-MeOTAD) was being considered as the etalon hole transporting material for the construction of perovskite solar cells. However, it was highly unsuitable for commercial production prospects due to its expensive synthesis and relatively low conductivity, requiring doping to increase it. Its processing versatility is also limited, as it could only be used in a regular (n-i-p) PSC architecture whose operational stability and upscaling were limited by the presence of dopants. As an alternative, inverted (p-i-n) PSCs can be constructed, allowing fabrication at moderate temperatures, longer operating lifetimes, and a good compatibility with flexible substrates. However, due to less attention being paid to this field, the performance and development speed of p-i-n type perovskite solar cells lagged behind the regular n-i-p PSCs. Scarce selection of suitable HTMs also contributed to slower development, as the hole transporting layer of small-molecule HTMs is often damaged by the polar solvents used in perovskite precursor solutions. Therefore, polymeric PTAA poly-[bis(4-phenyl)(2,4,6-trimethylphenyl)amine] (PTAA) was one of the best choices for constructing PSCs with the p-i-n architecture. However, due to the poor wettability of PTAA, special surface treatments were required to overcome this problem and achieve

high efficiency [9,10]. Combined with a high cost of approximately 2500€ per gram, PTAA was a choice that was far from ideal for HTM.

A significant breakthrough in the development of p-i-n architecture PSCs was achieved with the introduction of carbazole-based OSCs capable of forming a self-assembled monolayer (SAM), of which, 2PACz and its family of materials (e.g., MeO-2PACz or Me-4PACz) were able not only to simplify the device construction procedure, but also to outperform polymeric HTMs. Not long after, SAM derivatives started to attract more and more attention as the number of synthesized materials and the range of possible applications has been increasing. In this dissertation, a series of SAM HTMs have been designed, synthesized, and tested in various optoelectronic devices to further expand this research field.

Two main strategies have been used to obtain new SAM molecules containing phosphonic acid groups. The first strategy involved the incorporation of different functional groups into the carbazole, phenothiazine or indole central core. By synthesizing materials with halogen substituents, higher ionization potential values were obtained, thereby making halogenated SAM materials suitable for the construction of efficient BHJ OPV devices. Not only different halogen substituents, but also the number and different positions of the substituents were included in the comparison. Among them, carbazole containing chlorine atoms as functional groups showed the best performance in BHJ OPVs, and, combined with the doping strategy, led to a record-breaking efficiency of 18.9% for SAM-based OPVs. In addition, the potential of halogenated SAM derivatives as an interlayer for hole injection in OLEDs has been demonstrated. Among the tested materials, iodine atoms-substituted carbazole emerged as the most suitable molecule, with superior performance if compared to the traditional PEDOT:PSS. The strategy of different substituents was further extended by incorporating *tert*-butyl, methoxy, thiophene or ammonium groups. The synthesized materials were successfully applied in OPVs and PSCs, in particular, in the presence of thiophene and ammonium additional interactions with other device components were induced, and this resulted in favorable photovoltaic properties.

Since most of the currently investigated SAMs are based on carbazole, the second group of synthesized materials included different central fragments for comparison with the currently known molecules, and, for better understanding of which chromophore is most favorable for the application in optoelectronics. The obtained results revealed that, among the tested materials, the diphenylamine core emerged as a promising material for further synthesis optimization and investigation in PSCs since its SAM derivative demonstrated the best charge extraction capabilities and good device reproducibility.

Finally, two new approaches of SAM material application and SAM wettability improvement have been presented. The synthesized carbazole SAM derivative was used to modify zinc oxide tetrapods (ZnO-T) to construct gas sensors capable of operating at room temperature. After functionalization the selectivity to NO₂ was improved nearly tenfold, compared to the bare ZnO-T device, which was further enhanced by employing UV modulation. Furthermore, a simple way to overcome

SAM wettability problems was introduced by the use of 1,6-hexylenediphosphonic acid as a second component in the SAM material solution for monolayer formation. As a result, the wetting properties have been significantly improved without any negative effect on the performance of the PSCs under consideration.

The main statements of the doctoral dissertation are as follows:

1. Among all synthesized SAM materials, halogen-substituted derivatives are the best and most promising candidates for application in bulk heterojunction organic solar cells and organic light-emitting diodes.
2. Thiophene moieties and ammonium halides offer a great potential as functional groups for perovskite passivation and application in PSCs.
3. Diphenylamine chromophore is a promising candidate for the synthesis of SAM materials containing the phosphonic acid group, as well as for further investigation in PSCs.
4. The application range of SAM materials containing the phosphonic acid group keeps growing; it is possible to modify nanostructured ZnO tetrapods and use them to construct gas sensors.

1. LITERATURE REVIEW

1.1. Self-Assembled Monolayer

Self-assembly is a well-known spontaneous process where intra- or intermolecular interactions are taking place and ordered aggregates are created through the organization of molecular building blocks. This process usually requires no human intervention, and, in most cases, noncovalent interactions are involved, such as hydrogen bonding and van der Waals forces. Molecular self-assembly examples are the formation of molecular crystals, colloids, lipid bilayers, phase-separated polymers, or self-assembled monolayers [11]. Among them, the application of *self-assembled monolayers* (SAMs) has gained increasing attention in the various research fields of electronics, including thin film transistors, sensors, patterning, or next-generation organic optoelectronics, such as *organic light emitting diodes* (OLEDs) or *organic photovoltaics* (OPVs) [12-15].

SAMs are ordered and highly oriented two-dimensional molecular assemblies that are formed spontaneously on the surface of various substrates [16]. SAMs are also one of the self-assembly exceptions, where strong interactions take place. Usually, SAMs are composed of three main parts, which are shown in Figure 1.1. The head group is responsible for binding to the respective substrate, and the process is mediated by a specific functional group which has a strong affinity for a particular surface. Therefore, SAMs can form strong chemical bonds at the molecule-substrate interface, resulting in a stable and durable monolayer. The backbone, which connects the head and the end groups, is required for the ordering of the molecules, and it is usually made of an aliphatic chain consisting of carbon atoms. The end group defines the purpose of the formed monolayer, as it can determine the surface energy, topography, and functionality of SAM in general [17-19].

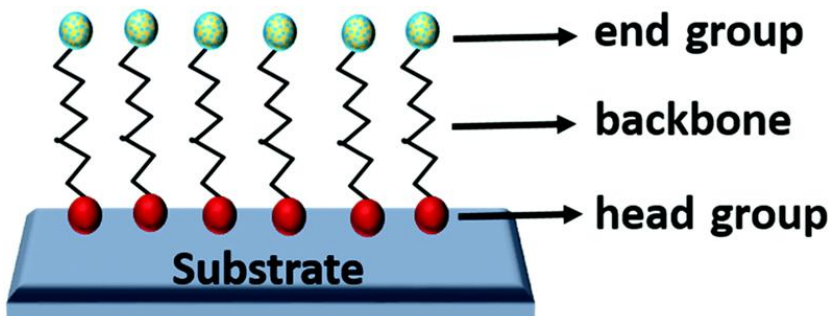


Figure 1.1. Structure of self-assembled monolayer [20]

The head group also defines the class of SAM materials. The four main classes of SAMs that have been used for various device applications are as follows: thiols, silanes, carboxylates, and phosphonic acids, which can be deposited on a variety of different surfaces including gold, hydroxylated silicon oxide, or metal oxide. Thiols are one of the most in-depth explored SAM materials, with a well-known monolayer formation mechanism, and reactions taking place at the gold surface. The formed bond

strength properties of Au-S are also well-defined [16,21]. Thiols can interact with metal oxides, such as ITO or FTO, which are important contact materials for applications in next-generation organic electronics, including *perovskite solar cells* (PSCs), *organic photovoltaics* (OPVs) and *organic light emitting diodes* (OLEDs). However, for this purpose, they can be considered as an inferior linker group compared to phosphonic acid, as the adsorption process on substrate is slower, and the resistance to high temperatures is much worse. Differences in high temperature tolerance were investigated by comparing 1-hexanethiol and 1-hexanephosphonic acid SAMs deposited on the ZnO surface (Figure 1.2a). Studies revealed that 1-hexanethiol is sensitive enough to start degrading at temperatures lower than 100 °C, by C-S bond scission (Figure 1.2b). In contrast, a phosphonic acid-containing analogue demonstrated significantly superior thermal stability, as the stoichiometry of its C/P atoms was preserved up to 350 °C [22].

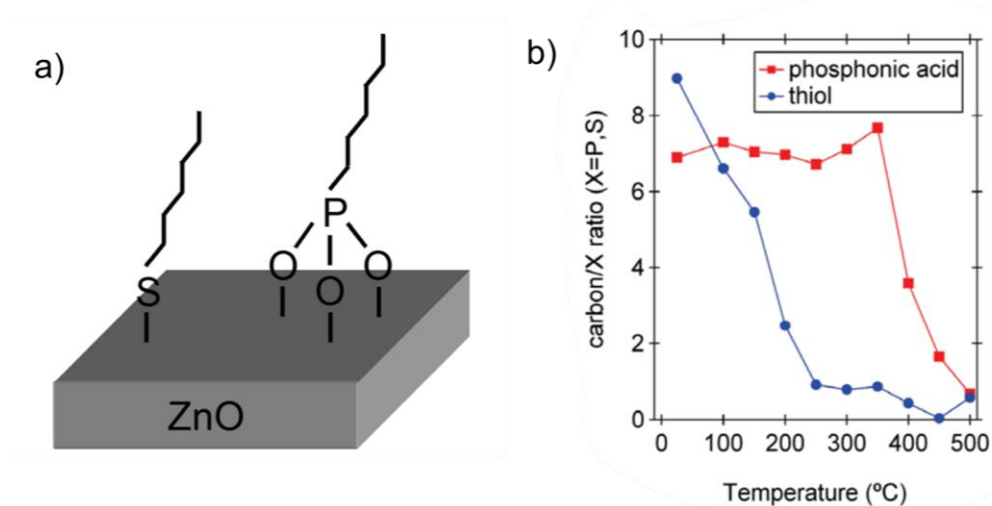
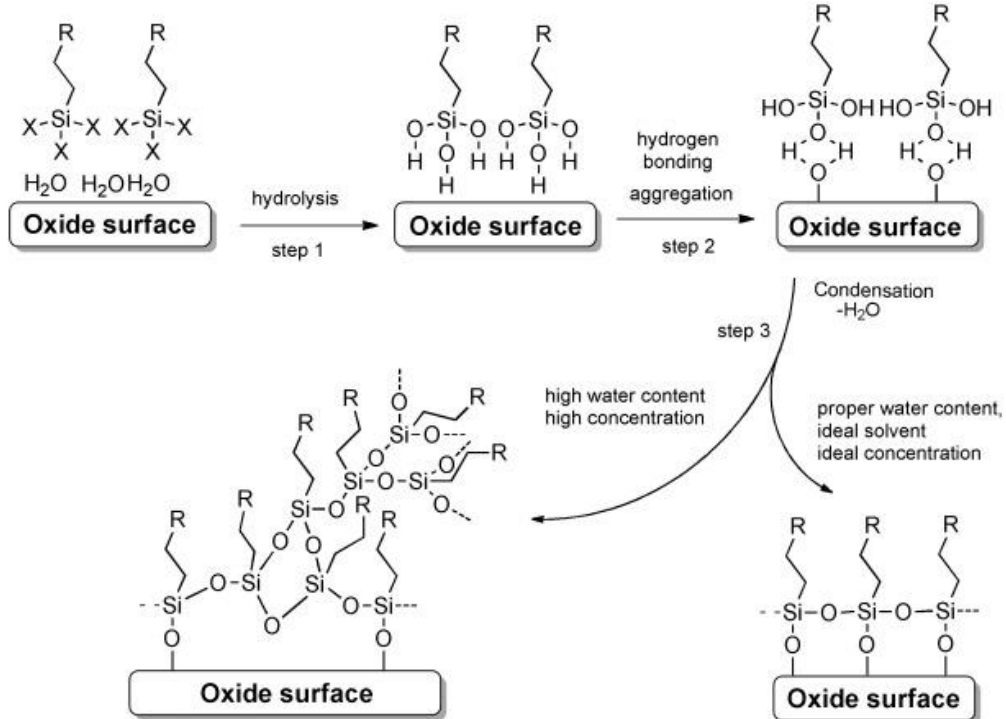


Figure 1.2. (a) Schematic of the thiol and phosphonic acid-based SAMs deposited on ZnO; (b) the ratio of carbon to either phosphorus or sulfur in the SAMs on ZnO at different temperatures [22]

Organosilanes, such as alkylsilanes, or simply just silanes are represented by the general formula of $R'Si(OR)_n$, where R is considered as a leaving group (e.g., chlorine, hydrogen atoms or alkoxy moieties). Silanes are commonly used materials for monolayer formation on surface of various oxides, the general SAM deposition procedure on SiO_2 is shown in Scheme 1.1. SAM is formed by a condensation reaction with hydroxyl groups which are present on oxide substrates. To increase the amount of -OH groups, the substrate is usually treated beforehand with ‘piranha solution’ or oxygen plasma. The corresponding hydroxysilanes are then formed by the hydrolysis reaction of the starting organosilanes, in the presence of water molecules, either adsorbed on the polar oxide surface or present as moisture in the solvent being used. Next, molecules attach on the oxide surface by hydrogen bonding and become

significantly less mobile due to the aggregation driven by attractive forces. Lastly, during condensation, Si-O-Si bonds are formed, both with the surface -OH groups and with the neighboring silanol groups, resulting in a cross-linked network [20,23,24].

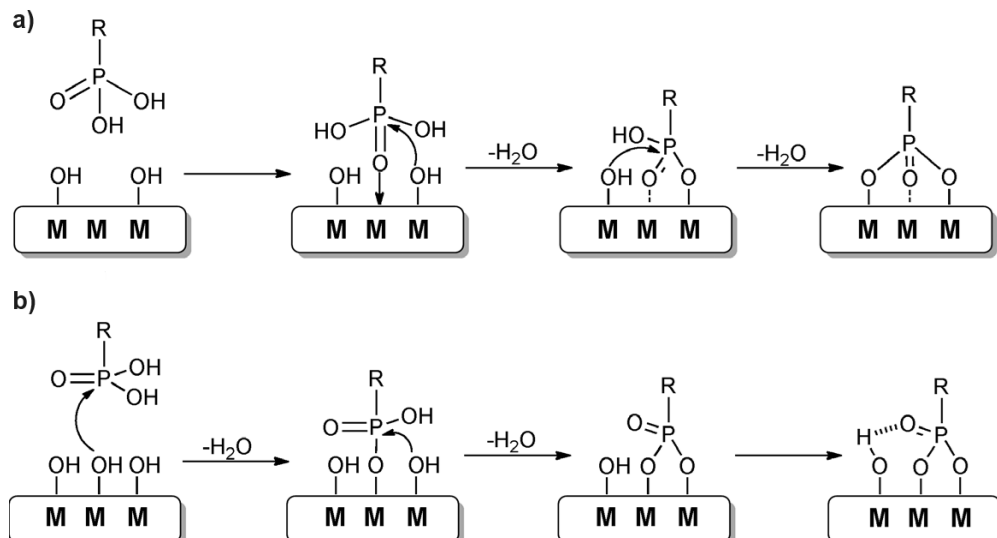


Scheme 1.1. Three-step mechanism for monolayer formation by silanes on SiO_2 substrate [24]

Although SAMs formed from silanes are mechanically robust with thermal stability typically exceeding 250 °C [25], there are some drawbacks to consider in terms of reproducibility. The first hydrolysis reaction is one of the most critical steps which affects the final quality and morphology of the formed monolayer. If hydrolysis is not finished, incomplete SAM may be formed. On the contrary, if hydrolysis is excessive, polysiloxanes will be formed on the surface. Additionally, if the surface features an insufficient amount of adsorbed H_2O molecules and the solvent in use is anhydrous, it will react with silanes poorly [26]. The materials themselves can be difficult to synthesize and isolate, they are sensitive to moisture and can relatively easily self-condensate or decompose during storage. These shortcomings may lead to a difficulty in experimental applications [15].

Phosphonate-derived acid and esters are one of the best alternatives to overcome the limitations of silanes and thiols as they can also be attached to a wide range of oxides. Compared to silane analogues, phosphonate derivatives are far less susceptible to self-condensation reactions, that occur only under high-temperature dehydrating conditions. This makes phosphonate derivatives easy to handle and store at ambient

conditions [24]. The mechanism of monolayer formation is strongly influenced by the reaction conditions (e.g., temperature, concentration, or solvent) and the type of oxide. On Lewis acidic metal oxides (Scheme 1.2a), the phosphoryl oxygen atom ($P=O$) first coordinates with the Lewis acidic site, thus making the P atom more electrophilic. Subsequently, heterocondensation with the adjacent surface hydroxy groups is induced, and strong covalent $P-O-M$ anchoring is formed. Phosphonic acids can bind to surfaces of low Lewis acidity (Scheme 1.2b), where the coordination of the phosphoryl oxygen is minimal, and the heterocondensation reaction is promoted mainly by the initial hydrogen bonding [27,28].



Scheme 1.2. Mechanism of phosphonic acid attachment: (a) to Lewis acid metal oxides; (b) to poorly Lewis acid metal oxides [15]

The presence of three oxygen atoms on the phosphonic acid structure allows for monodentate, bidentate, and tridentate binding modes in combination with possible electrostatic and hydrogen-bonding interactions. Additionally, all three oxygen atoms can bind to the same metal site (chelation) or bind to different metal atoms on the surface. Overall, the final binding modes of the phosphonic acid depend on the nature of the oxide substrate as well as on the reaction conditions applied, such as thermal annealing [29].

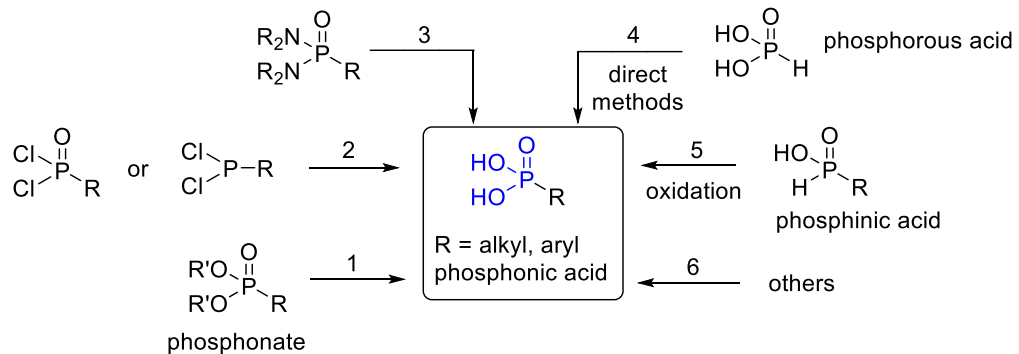
Carboxylate-based SAM materials can also be used to modify metal oxides, as carboxylic acids were the first choice for coating TiO_2 nanoparticles in dye-sensitized solar cell research [30]. One of the most common ways to prepare SAM from carboxylates is similar to phosphonic acids, where solution processing is employed with subsequent thermal annealing at $100\text{ }^{\circ}\text{C}$. This process is relatively inexpensive and easily applicable, yet it is slow and usually non-polar solvents (e.g., THF) are used. In addition, the main disadvantage is that the bond between carboxylic acids and

the metal oxide surface is typically weaker and less hydrolytically stable compared to silanes or phosphonic acids [31].

To summarize, phosphonic acids possess favorable binding properties for metal oxide functionalization compared to organosilanes or carboxylic acids. Phosphonate SAMs exhibit higher a degree of order and are more durable. The formed monolayer is usually more homogeneous, and it adheres strongly to the substrate. Their high moisture resistance and ability to be formed under ambient conditions, together with their great versatility, make these SAMs attractive candidates for various applications in modern optoelectronics, where conductive metal oxides are used [32,33].

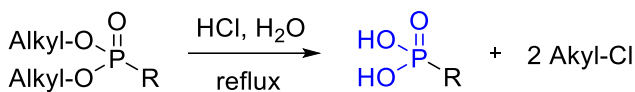
1.2. Phosphonic Acid Synthesis and Reactions

Phosphonic acids can be synthesized in numerous different ways, as shown in Scheme 1.3. The most common method to obtain phosphonic acid derivatives is to use phosphonates as a starting material for the hydrolysis reaction (Section 1). Other materials such as dichlorophosphines and dichlorophosphine oxides (Section 2) and phosphonodiamides (Section 3) can also be hydrolyzed to phosphonic acids. The direct method of P-C bond creation using phosphorous acid (Section 4) or the oxidation of phosphinic acid (Section 5) can be used to form phosphonic acids as well. There are also some more ‘exotic methods to prepare phosphonic acids, such as reaction of carboxylic acids by using white phosphorous or benzaldehyde reaction with red phosphorus in the presence of HI [34-36].



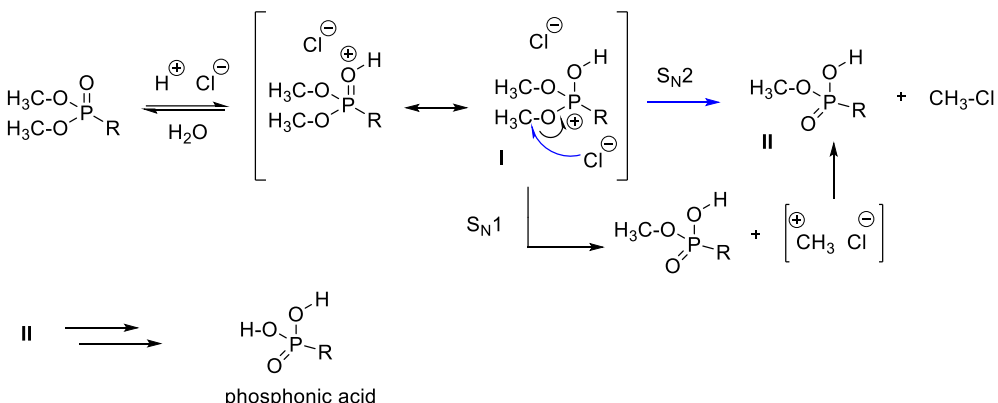
Scheme 1.3. Possible synthetic routes to prepare phosphonic acids [34]

The most popular and feasible methods to transform phosphonates to phosphonic acids is hydrolysis under acidic conditions (Scheme 1.4). It is common to reflux phosphonates in concentrated hydrochloric acid (35–37% in water), but hydrobromic acid can also be employed. By applying this method, the product formed typically does not require additional purification, as excess of HCl and water can be readily removed by distillation. If purification is required, it can be performed by recrystallization in polar solvents [37,38].



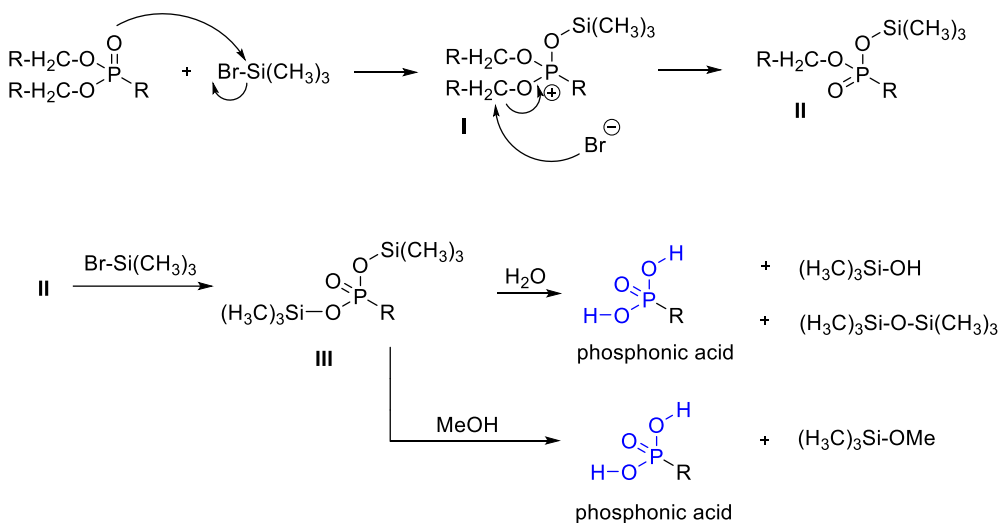
Scheme 1.4. Hydrolysis of dialkyl phosphonate to phosphonic acid under acidic conditions [34]

The possible mechanism of phosphonate by hydrolysis using hydrochloric acid is outlined in Scheme 1.5. It suggests that, initially, the phosphonate oxygen atom that is double bonded to the phosphorus atom is being protonated, forming intermediate I, that could exist as two mesomeric forms. Two competitive mechanisms can then occur. Intermediate I can lose a carbocation according to the S_N1 mechanism, while the second way could be nucleophilic substitution (S_N2) involving chloride ions as nucleophilic species to produce the intermediate II. Afterwards, the repetition of this mechanism yields phosphonic acid [34].



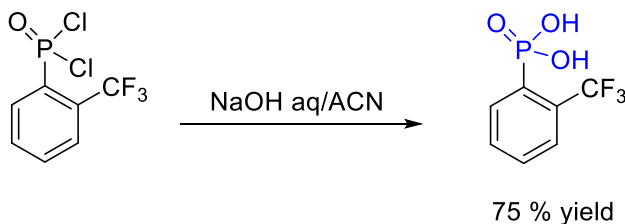
Scheme 1.5. Suggested hydrolysis mechanism of dialkyl phosphonate using hydrochloric acid [34]

Acidic hydrolysis of phosphonates requires harsh conditions (usually strong acid at reflux); therefore, its application can be limited if the molecules possess sensitive fragments or functional groups. A milder reaction alternative was presented by the McKenna group in 1977. Bromotrimethylsilane was introduced as a hydrolysis agent, which allowed efficient transesterification of dialkyl phosphonate to bis(trimethylsilyl) phosphonate. The mechanism presented in (Scheme 1.6) suggests that, in the first step, oxophilic substitution on the bromotrimethylsilane silicon atom occurs, whereas bromide acts as a leaving group to produce intermediate I, followed by dealkylation, which results in intermediate II. Then, the mechanism is repeated, and disilylated intermediate III is obtained. Finally, phosphonic acid is obtained from silylated phosphonates quantitatively by adding water (hydrolysis) or methanol (methanolysis). The latter method is often a better choice, as the side product methoxytrimethylsilane is more volatile than those obtained when using water (trimethylsilanol and hexamethyldisiloxane) [34].



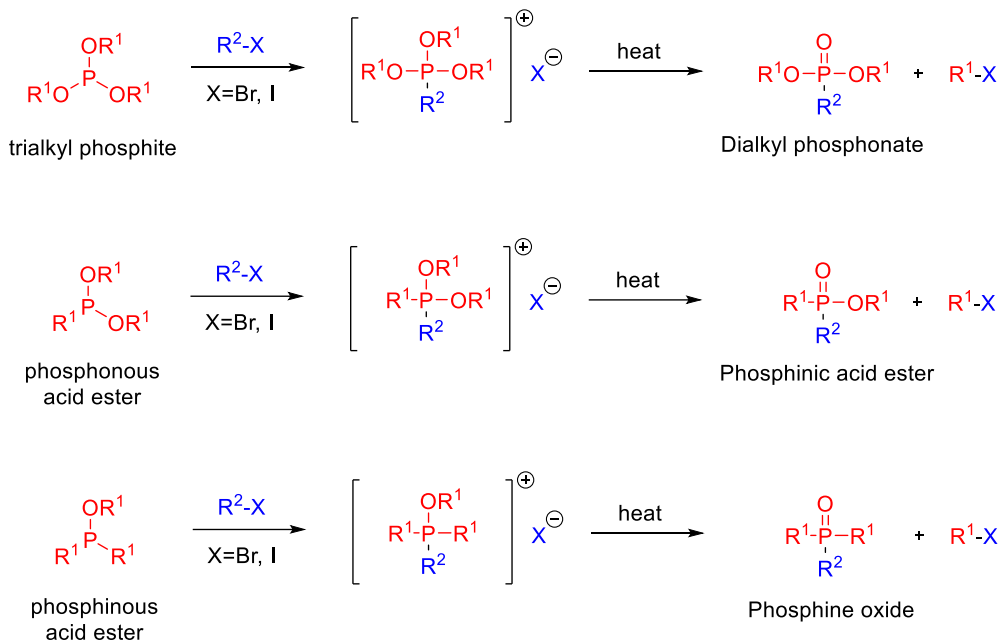
Scheme 1.6. Suggested mechanism for the preparation of phosphonic acid from dialkyl phosphonate by using bromotrimethylsilane [34]

In some reports, bases have been also employed instead of acids to hydrolyze phosphonates; however, when using this method, usually, only one alkoxy group is hydrolyzed, and the products are obtained in the form of organophosphorus monoacids [39]. For the complete alkaline hydrolysis, phosphinates as the starting materials are a better choice. An example of *o*-trifluoromethylbenzenephosphonic acid synthesis using NaOH in acetonitrile is given in Scheme 1.7. The same molecule can be obtained in acidic conditions (10% HCl) with a similar yield (75–85%); however, the reaction time in this case is extended [40].



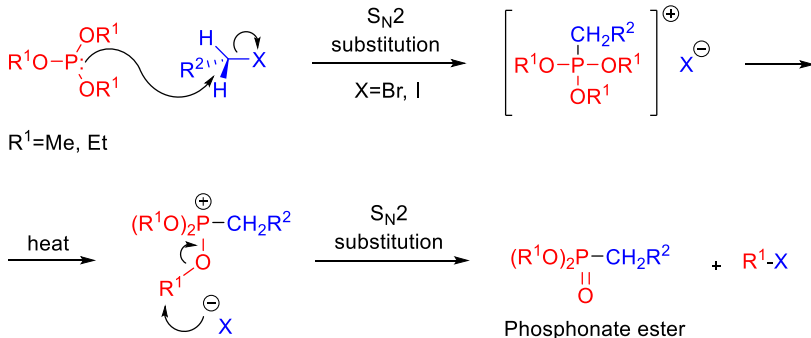
Scheme 1.7. Hydrolysis of CF_3 substituted phenyldichlorophosphine [40]

The most common way to obtain phosphonates which could be used for the hydrolysis, as described above, is by employing the Michaelis-Arbuzov reaction. During this reaction, various phosphorus esters react with alkyl halides, forming pentavalent phosphorus derivatives and other alkyl halides (Scheme 1.8). Trialkyl phosphites, phosphonous acid esters or phosphinous acid esters can be used, which results in dialkyl phosphonates, phosphinic acid esters or phosphine oxides, respectively [41–42].



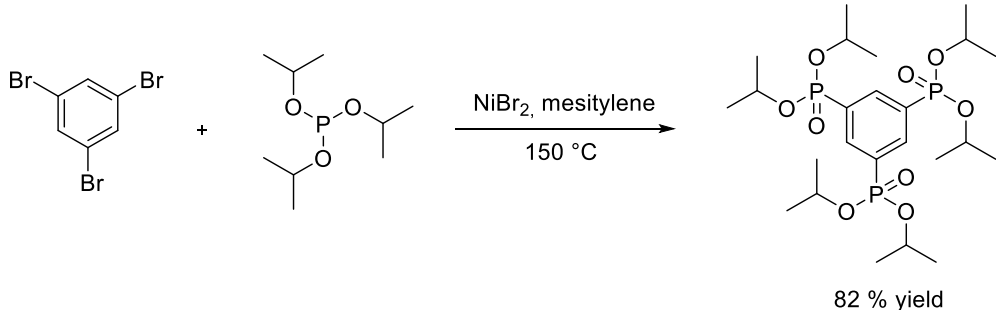
Scheme 1.8. Examples of Michaelis-Arbuzov reaction [42]

The Michaelis-Arbuzov reaction mechanism (Scheme 1.9) involves a nucleophilic attack by the phosphorus lone pair of electrons to the alkyl halide (S_N2 mechanism), producing a highly unstable quasiphosphonium intermediate which is subjected to internal rearrangement upon heating. Afterwards, another S_N2 substitution takes place where alkyl phosphonate ester is subsequently cleaved, resulting in the reaction product. During this reaction, new alkyl halide side products are always formed which can act as a reactant by reacting with the phosphite and competing with the starting alkyl halides. If trimethyl or triethyl phosphite is used, this problem usually does not occur as the generated byproducts possess low boiling temperatures and are removed from the mixture during the reaction [43-45].



Scheme 1.9. Michaelis-Arbuzov reaction mechanism [43]

Although usually alkyl halides are used in the Michaelis-Arbuzov reaction, with the addition of metal catalysts (palladium, nickel or copper catalysts) aryl halides can also react with phosphites. As an example, 1,3,5-tribromobenzene reacted with triisopropyl phosphite in mesitylene in the presence of nickel(II) bromide to give a fully phosphorylated product in a good yield of 82% [43,46].



Scheme 1.10. Example of nickel-catalyzed phosphorylation reaction [46]

To sum up, in order to obtain phosphonic acid derivatives, various synthesis methods were introduced, investigated and developed. Among them, the most common strategy is the hydrolysis of the respective phosphonates, although dichlorophosphines, dichlorophosphine oxides and phosphonodiamides can be used as well. Hydrolysis is usually performed by refluxing in hydrochloric or hydrobromic acid. However, the reaction conditions are harsh; therefore, McKenna introduced an alternative method where bromotrimethylsilane is involved. The Michaelis-Arbuzov reaction is commonly used for phosphonate synthesis. Respective phosphonates can be obtained during the reaction between alkyl halides and alkyl phosphites. In the presence of nickel catalysts, a phosphorylation reaction can be also performed by using aromatic halides.

1.3. SAM Application in Perovskite Solar Cells

1.3.1. Perovskite

Materials with a specific crystal lattice structure, whose structure is expressed by the general formula ABX_3 , in which A and B are cations, and X is an anion, are known as *perovskites*. In this structure (Figure 1.3), the larger A cations are arranged in an ideal cubic space (12-fold cubohedral coordination), where an octahedron of X anions is contained. The smaller B cations are stabilized inside octahedron by 6-fold coordination [47,48].

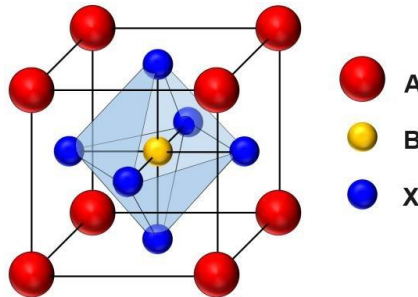


Figure 1.3. Crystal lattice structure of perovskite [49]

After the discovery of the mineral CaTiO_3 , which was the very first one characterized by a perovskite structure, the characteristic crystal lattice has also been found in other metal oxides, such as BaTiO_3 , PbTiO_3 , SrTiO_3 or BiFeO_3 , whose structure can be expressed as ABO_3 . Most of these oxides exhibited ferroelectric, piezoelectric, dielectric and pyroelectric properties and have been used in relevant applications. However, compounds of the ABO_3 structure are not good semiconductors, and their applicability in photovoltaic applications is difficult. Upon replacing oxygen atoms with halides ($\text{X}=\text{Cl}^-$, Br^- , I^-), it has been observed that such materials exhibit desirable semiconductor properties to be used in optoelectronics [49-51].

Perovskite halides containing monovalent Cs, methylammonium or formamidine cations (component *A*) and divalent metals, such as Ge, Pb or Sn (component *B*), have recently been introduced as a promising class of semiconductors for the application in photovoltaics [52,53]. The synthesis of these materials is straightforward, and layers can be deposited on substrates by various solution- or vapor-based methods, such as spin coating, spray coating, ultrasonic sputtering, printing, chemical vapor deposition and others [54-60].

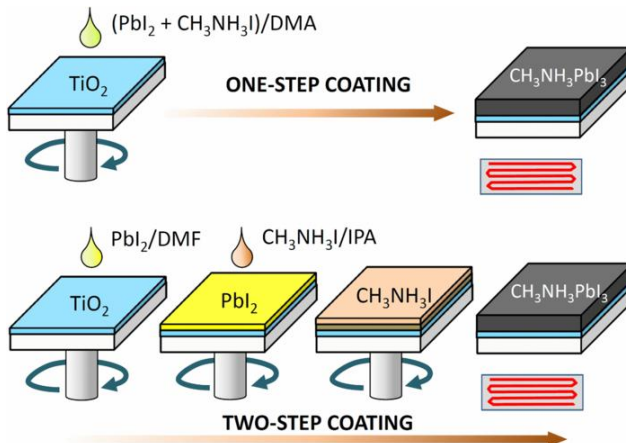


Figure 1.4. One-step and two-step spin-coating procedures for perovskite ($\text{CH}_3\text{NH}_3\text{PbI}_3$) layer formation [61]

Spin coating is one of the most common methods for perovskite absorber layer deposition. This fabrication technique is usually used for the laboratory application to produce small-area devices providing very good reproducibility and morphology control. Spin coating is divided into two main methods – one-step and two-step deposition, with a subsequent annealing regardless of the procedure (Figure 1.4). During the one-step procedure, all the precursors which are necessary to a form perovskite film (e.g., PbI_2 and methylammonium iodide) are dissolved in polar aprotic solvents (e.g., DMSO, DMF, DMA) and spin-coated onto the substrate [62,63]. Meanwhile, in the two-step deposition, films are formed by depositing precursors separately one by one, which makes the control of the process easier [64]. However, spin coating is not the best method for industrial applications, as the process speed is slow, the production of a uniform film on large areas is complicated, and the material wastage is considerable [65,66]. As an alternative, vapor deposition using vacuum can be adapted for larger-scale production, as this process delivers highly crystalline and uniform films [65,67].

Perovskites are denoted by outstanding properties which make them suitable for application in optoelectronics. They demonstrate tolerance to film defects, as well as strong and wide absorption in the visible region [68]. Also, the length of the carrier diffusion is high ($\sim 1 \mu\text{m}$) [69], their ionic structure results in a sufficiently high conductivity and electron mobility ($\sim 25 \text{ cm}^2\text{V}^{-1}\text{S}^{-1}$), and their band gap E_g is tunable and optimal for the construction of photovoltaic devices [70-74]. For all these reasons, perovskites have been widely investigated as a light-absorbing and charge-generating component for the construction of solar cells.

1.3.2. Perovskite solar cell architectures

Modified dye-sensitized solar cells (DSSCs) are considered as the pioneers of perovskite solar cells, in which the first two and most widely studied semiconducting perovskites *methylammonium lead iodide* ($\text{CH}_3\text{NH}_3\text{PbI}_3$) and *methylammonium lead bromide* ($\text{CH}_3\text{NH}_3\text{PbBr}_3$) have been applied as a light absorbing component (Figure 1.5). The *power conversion efficiency* (PCE) of such devices was not high, to be precise, 3.8% and 2.6% respectively [75-77]. Further investigation by applying spiro-OMeTAD as a solid-state hole transporting material instead of a regular liquid electrolyte resulted in an increase of PCE to 9.7 %. This also led to a significant improvement in the stability of the device, as the liquid electrolyte tended to initiate corrosion processes or encapsulation damage and simply leak out, thus making the solar cell inoperable [78].

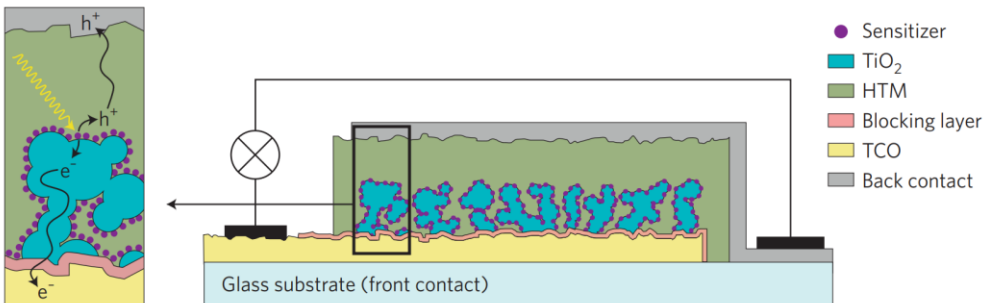


Figure 1.5. Perovskite-based DSSC architecture [79]

In the solar cell whose structure is shown above, perovskite nanoparticles absorb sunlight and photogenerate positive as well as negative charges. Mesoporous TiO_2 acts as an electron extraction and transporting unit towards the transparent and conductive oxide framework (electrode). Meanwhile, in the presence of a closed electrical circuit, the HTM layer ensures the continuous movement of electrons, by transporting positive charges (holes) towards the corresponding electrode [79].

The determination of the perovskite hole conductivity was a significant stimulus for the development of the new nanocomposite PSC structure (Figure 1.6). This allowed the thickness of the HTM layer to be reduced and for the mesoporous TiO_2 layer to be fully integrated into the perovskite layer of 200–300 nm thickness. These devices were named *mesoscopic perovskite solar cells* [80].

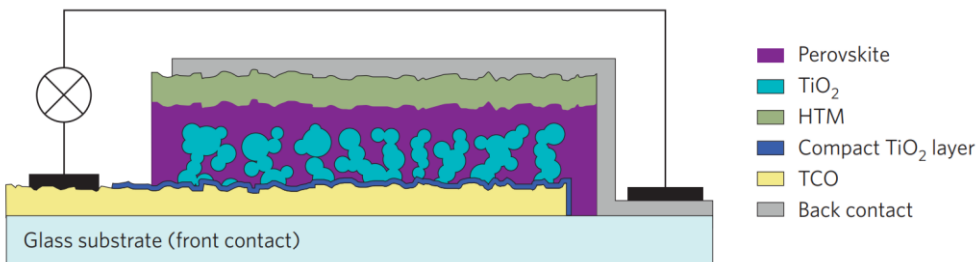


Figure 1.6. Mesoscopic architecture PSC [79]

Mesoscopic structures have become an important research object for PSCs because, as in the case of perovskite DSSCs, their fabrication was straightforward, and the starting materials were relatively inexpensive [81]. Most importantly, these solar cells outperformed their predecessors in terms of efficiency, reaching a then – high – PCE of 12%. This suggested that the transport of positive charges through the perovskite layer and their collection in the presence of the HTM layer was quite efficient. Shortly thereafter, perovskite, specifically $\text{CH}_3\text{NH}_3\text{PbI}_3$, was determined to behave as a bipolar semiconductor capable of transporting both electrons and holes. These results laid a solid foundation for the development of planar structure PSCs [82,83].

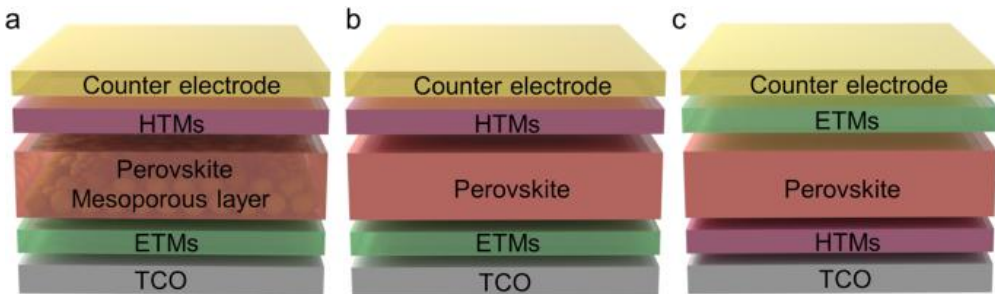


Figure 1.7. Mesoscopic architecture PSC [84]

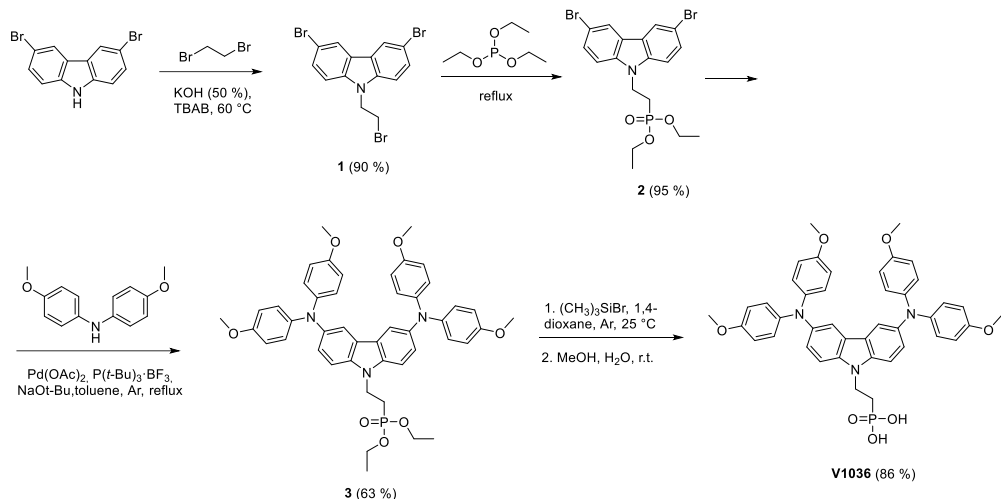
Mesoscopic PSCs (Figure 1.7a) were able to provide a stable energy conversion efficiency, which was significantly increased from the initial value. However, the fabrication of these devices suffered from high hysteresis and required the use of high temperature processes ($500\text{ }^{\circ}\text{C}$) to form the mesoporous TiO_2 electron transporting layer [85,86]. Also, this architecture is not suitable for the construction of flexible devices or tandem solar cells. The elimination of the mesoporous TiO_2 layer (Figure 1.7b), and thus high temperature processes, became an important solution to further reduce the manufacturing costs and simplify the manufacturing technology [87]. In the later stages of PSCs development, TiO_2 was replaced by SnO_2 , which offered better performance and could be prepared by using low temperature processes [88-90]. Several world records for PSC efficiency were achieved with SnO_2 -based devices of the regular (n-i-p) planar architecture. Nevertheless, they still suffered from high hysteresis, whereas the long-term stability of cells was not sufficient, as one of the limiting factors was the use of hygroscopic lithium salt-doped spiro-OMeTAD as the hole transporting material [91-95].

As an alternative, inverted (p-i-n) planar architecture PSCs (Figure 1.7c) used stable metal electrodes and electron transporting materials (PC_{61}BM or C_{60}) demonstrating a competitive efficiency along with better stability, as well as lower hysteresis compared to n-i-p devices [96-99]. This architecture is also suitable for tandem solar cells construction [8,100]. In this architecture, sunlight enters the device through the hole-transporting layer, which is the opposite to the regular architecture PSCs. Spiro-OMeTAD is not fully transparent to visible light and can be easily washed away by the perovskite precursor solution; accordingly, poly(3,4-ethylenedioxythiophene):polystyrene sulphonate (PEDOT:PSS) was one of the most widely used HTMs in p-i-n PSCs due to its better optical transmittance, conductivity and well-matched energy levels with perovskite [101-103]. However, due to its acidic nature and relatively high hygroscopicity, PEDOT:PSS could accelerate perovskite degradation, thus reducing the overall device performance and long-term stability [104,105]. Other polymers, such as poly(bis(4-phenyl) (2,4,6-trimethylphenyl) amine (PTAA) can be used instead of PEDOT:PSS, due to their high charge carrier mobility, optical transmittance, and chemical neutrality [106,107]. Nevertheless, wetting of the PTAA layer is poor, and therefore special surface treatments are required to overcome this problem and achieve high efficiency [9,10]. Combined with the burdensome cost of approximately 2500€ per gram PTAA is a choice that is far from ideal for HTMs.

On the other hand, the peculiarities of the inverted PSC structure have enabled the use of other semiconductors to form the HTM layer, such as phosphonic acid derivatives, whose application was unsuccessful or impractical for the regular n-i-p device architectures.

1.3.3. Phosphonic acid SAM HTMs application in p-i-n PSCs

The first SAM HTM containing phosphonic acid group to be successfully used in p-i-n perovskite solar cells was *V1036*, synthesized by V. Getautis research group in 2018. The material was prepared *via* a 4-step synthetic procedure (Scheme 1.11), where alkylation, phosphorylation, Buchwald-Hartwig and McKenna reactions were employed, with an overall yield of 46% [4].



Scheme 1.11. *V1036* synthesis procedure [4]

P-i-n ‘triple cation’ perovskite solar cells of ITO/HTM/Perovskite/C₆₀/BCP/Cu architecture were fabricated, and polymeric PTAA was used as a standard HTM. The best performance of *V1036* was achieved by mixing it with electrically inert filler molecule butylphosphonic acid (C4) at a ratio of 1:9 (Figure 1.8a), which resulted in a reverse scan PCE of 17.8%. It was only slightly lower compared with the standard PTAA efficiency of 19.2%. More importantly, both devices demonstrated comparable stability (Figure 1.8b), which was an important milestone for SAMs as a monolayer was demonstrated to offer stability comparable with the previous state-of-the-art materials [4].

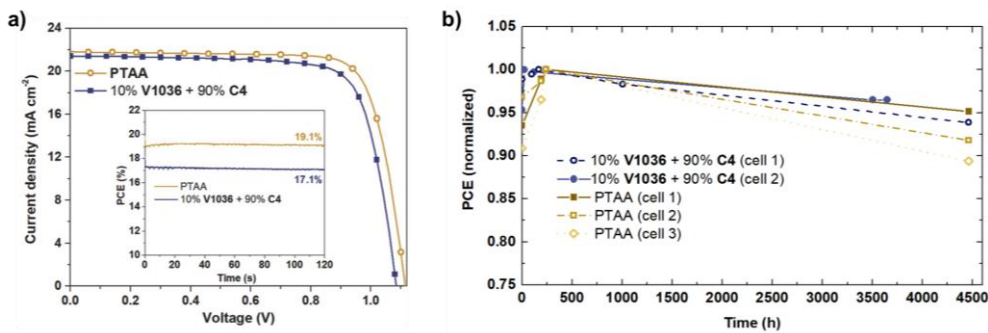
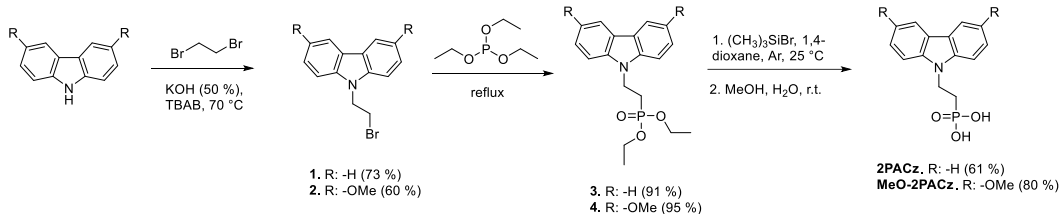


Figure 1.8. (a) J-V characteristics of the best-performing PSCs with 10% V1036 90% C4 SAM and PTAA HTMs; (b) Shelf lifetime of representative PTAA (cell 1 max. PCE=18.5%) and 10% V1036 90% C4 SAM (cell 1 max. PCE=17.8%) based devices [4]

Not long after the introduction of carbazole SAM in PSCs, simplified analogues of V1036 were designed and synthesized in order to create more energetically aligned interface to the perovskite absorber. 2PACz and MeO-2PACz were synthesized *via* a similar but shortened synthesis procedure (Scheme 1.12). Alkylation with dibromoethane of the respective carbazole derivatives was performed, followed by an introduction of phosphonic acid ester groups *via* the Arbuzov reaction to yield the intermediate materials **3** and **4**. Cleavage of the ethyl groups was performed with bromotrimethylsilane to produce the final products **5** (2PACz) and **6** (MeO-2PACz) [5].



Scheme 1.12. 2PACz and MeO-2PACz synthesis procedures [5]

2PACz and MeO-2PACz were tested in perovskite solar cells of the ITO/HTM/Perovskite/C₆₀/BCP/Cu architecture (Figure 1.9a). For the better reproducibility, ‘triple cation’ perovskite absorber Cs₅(MA₁FA₈₃)₉₅Pb(I₈₃Br₁₇)₃ (CsMAFA) was used. Polymeric PTAA, which was the best performing HTM in n-i-p PSCs to date [117-119], and the previously investigated V1036 were used for a comparison [5].

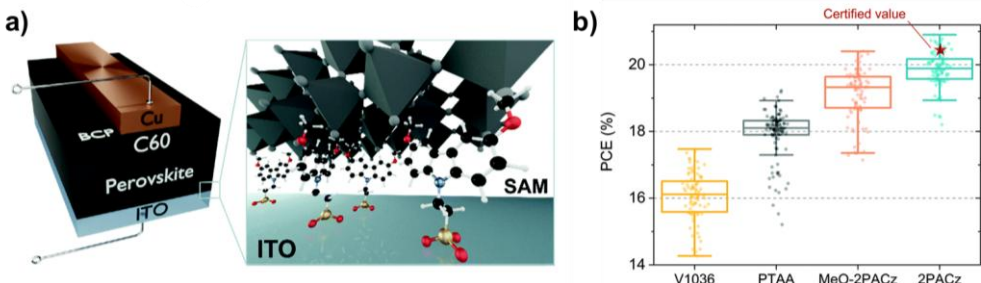


Figure 1.9. (a) Schematic of the device structure studied, where the zoom-in illustrates how SAM molecules attach to the ITO surface, enabling hole-selective contact with the perovskite above; (b) Box plot of power conversion efficiency (PCE) values for V1036 (41 pixels), PTAA (53 pixels), MeO-2PACz (47 pixels) and 2PACz (46 pixels) solar cells [5]

Both 2PACz and MeO-2PACz outperformed their predecessor V1036 and the standard PTAA (Figure 1.9b). 2PACz demonstrated the best maximum power conversion efficiency of 20.8 %, while the certified efficiency was recorded at 20.44%. In contrast, V1036 and even PTAA lagged behind, and yielded maximum PCEs of 16.9% and 18.9%, respectively. The stability during the light-soaking stress test revealed that, after 11 h of operation, 2PACz retained >97 % of its initial PCE, which remained stable after an initial drop, while the PTAA-based device degraded more and lost ~6 % of its initial PCE. This result demonstrated that carbazole-based SAMs can provide all the necessary features for efficient and stable PSCs, and highlighted the importance of the SAM technology for the future investigation of hole transporting materials [5].

Later studies revealed more beneficial factors of PTAA replacement with carbazole-based SAM. The ITO layer structure and surface are relatively rough, and their roughness remains almost unchanged after the formation of the monolayer. In contrast, polymeric films (e.g., PTAA) are thicker and tend to form much smoother layers, covering all the irregularities of the ITO surface (Figure 1.10). These differences affect the strength of perovskite adhesion to the respective substrate. As an example, single crystals of $\text{FA}_{0.6}\text{MA}_{0.4}\text{PbI}_3$ perovskite grown on MeO-2PACz demonstrated better adhesion to the substrate than those grown on PTAA [111,112].

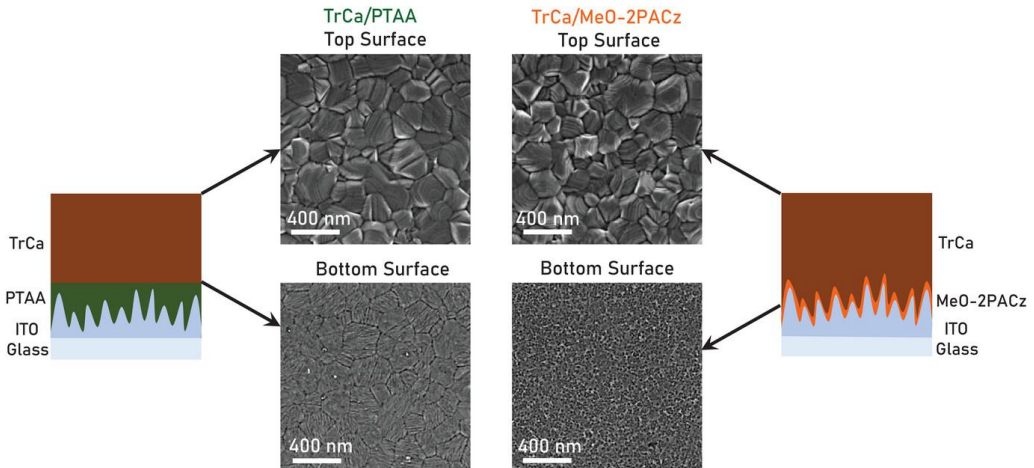


Figure 1.10. SEM images of ‘triple cation’ perovskite layers fabricated on PTAA and MeO-2PACz surfaces with illustration of buried interface differences [112]

Further studies involved the investigation of bias-induced device degradation due to ion migration in perovskite solar cells when PTAA and MeO-2PACz were employed as HTL. ‘Triple cation’ $\text{Cs}_{0.05}[(\text{FA})_{5/6}(\text{MA})_{1/6}]_{0.95}\text{Pb}(\text{I}_{0.9}\text{Br}_{0.1})_3$ PSCs of the Ag/BCP/C₆₀/Perovskite/HTL/ITO architecture (Figure 1.11a) were constructed for this experiment. Ion migration was triggered by biasing the devices under dark conditions from 0 V to a positive voltage of 5 V (Figure 1.11b). The device photovoltaic parameters (Figure 11c–f) were measured before and after biasing. The performance of fresh devices based on both PTAA and MeO-2PACz was similar, where the efficiency of multiple cells was around 20%. However, due to the significantly enhanced bias-induced ion migration, the performance of PTAA-based devices decreased more compared to SAM-based devices after the biasing. It can be related to the perovskite compositional changes occurring at the interface of perovskite and polymeric films, where an MAPbI_3 -like layer is formed. It is suggested that, due to the compositional inhomogeneity of the absorber layer, a higher degree of ion migration occurs, which, overall, results in a poorer device stability. On the contrary, the rough texture of the MeO-2PACz/ITO surface is beneficial for the ‘triple cation’ perovskite formation over polymeric films, leading to better operational stability [112].

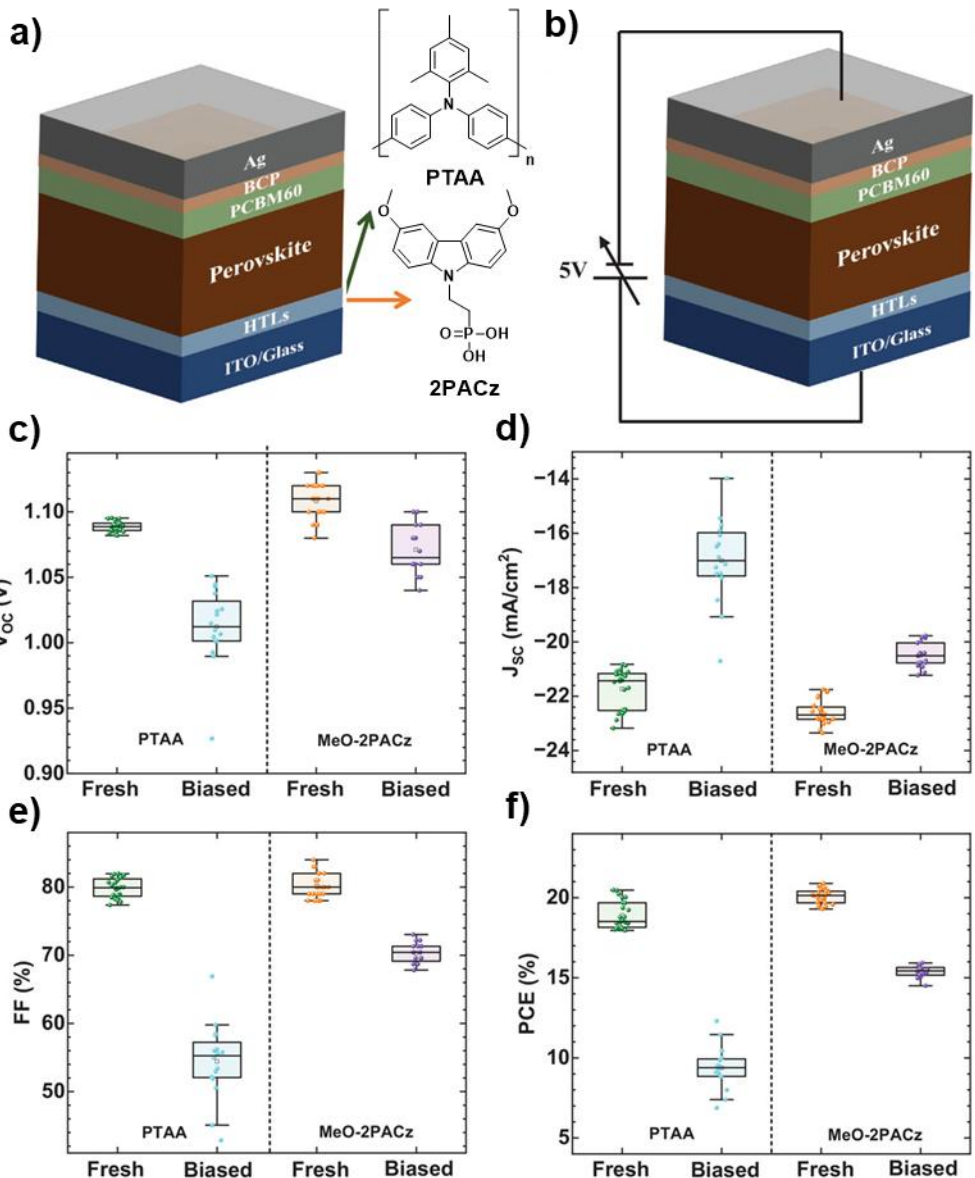


Figure 1.11. (a) Schematic structure of PSC and (b) Bias-induced PSCs with HTL as PTAA or MeO-2PACz; photovoltaic characteristics of fresh and biased devices: (c) V_{oc} , (d) J_{sc} , (e) FF, and (f) efficiency [112]

Currently, 2PACz and other carbazole family SAM derivatives are among the most widely investigated SAM materials in PSCs and perovskite/silicon or perovskite/perovskite tandems. One of the most recent advances in the performance and stability of p-i-n PSCs has been achieved by combining 2PACz SAM and perovskite interface engineering. The strategy of forming two-dimensional/three-

dimensional (2D/3D) perovskite interfaces has been employed, to resolve the issues of charge recombination, ion migration and electric-field inhomogeneities when only 3D perovskite is used [113-117]. Devices of ITO/2PACz/2D-perovskite/3D-perovskite/2D-perovskite/C₆₀/bathocuproine/Ag architecture were fabricated (Figure 1.12a), in which double-sided 2D/3D perovskite heterojunctions were formed by using 4-hydroxybenzylamine. For a comparison, devices with only the top or the bottom and no 2D/3D perovskite heterojunctions were constructed and tested as well. The latter demonstrated the worst performance, compared with 2D/3D interfaces containing devices (Figure 1.12b). The top side 2D/3D perovskite interface provides a slightly better efficiency than the bottom side interface, when only one heterojunction is present. By combining heterojunctions at both the top and the bottom sides, all the photovoltaic characteristics were improved further, yielding 25.63% (certified 25.0%) of the maximum power conversion efficiency. Additionally, the stability was also significantly improved as PSCs with double-sided 2D/3D heterojunctions retained 95% of their initial power conversion efficiency after 1,000 h of illumination at 85 °C in air (Figure 1.12c). In contrast, devices with only the top and the bottom side 2D/3D interfaces retained 86% and 76% of their initial efficiency respectively. While control devices with 3D perovskite only lost around 5% of their initial efficiency [118].

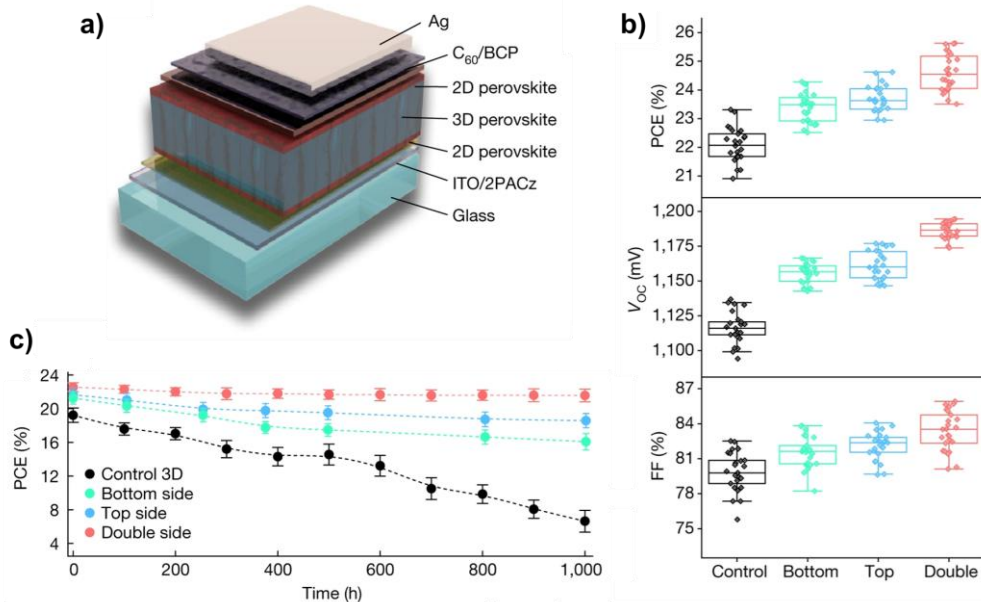


Figure 1.12. (a) Schematic structure of PSC containing double-sided 2D/3D perovskites; (b) Photovoltaic characteristics of PSCs with and without 2D/3D perovskite interfaces; (c) Stability of encapsulated PSCs with and without 2D/3D perovskite interfaces under 1-sun illumination at 85 °C and open-circuit conditions [118]

Other SAM materials of the carbazole family such as Me-4PACz have also been investigated in perovskite/silicon tandem solar cells. As an example, perovskite and crystalline silicon tandems containing Me-4PACz SAM with an area of 1 cm² and the architecture shown in Figure 1.13a were constructed. The use of Me-4PACz led to a reduction in the voltage losses, and the device showed an efficiency of 31.25% (Figure 1.13c) [119].

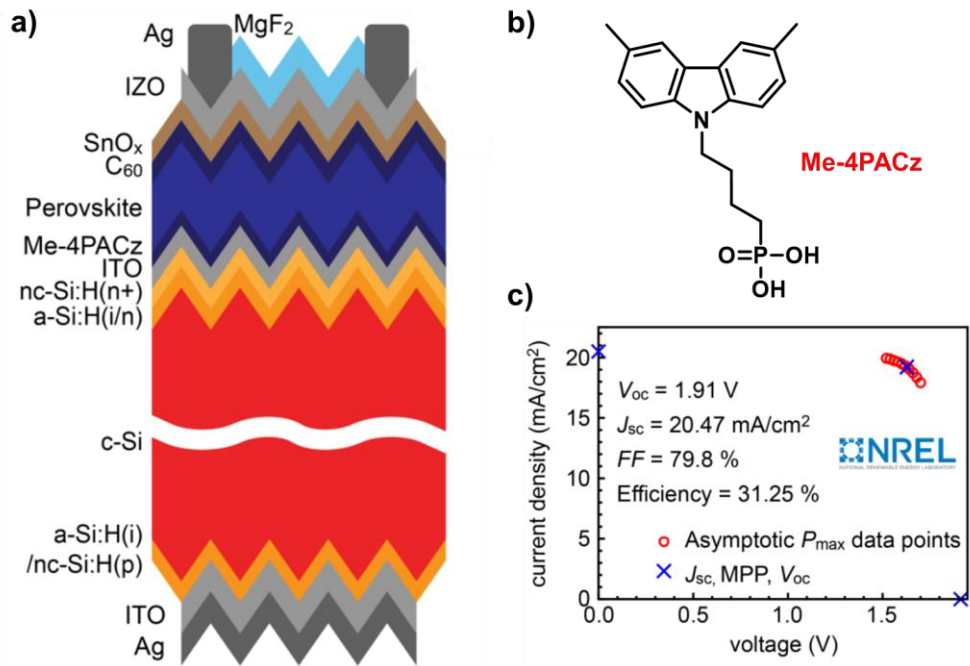


Figure 1.13. (a) Schematic structure of perovskite/silicon tandem solar cell containing Me-4PACz SAM; (b) Chemical structure of Me-4PACz; (c) Photovoltaic characteristics of the device related to maximum power P_{max} scan [119]

Due to the tremendous potential of 2PACz and other carbazole family SAM materials, new SAM derivatives containing different chromophores have been investigated in PSCs. As shown in Figure 1.14, examples of currently reported SAM HTM compounds contain phenoxazine, phenothiazine, phenoselenazine [120], triphenylamine [121,122] or triazatruxene [123] central fragments. These derivatives were tested in PSCs and demonstrated very good efficiencies (over 21%), indicating that non-carbazole SAM derivatives can also be promising candidates for application in PSCs.

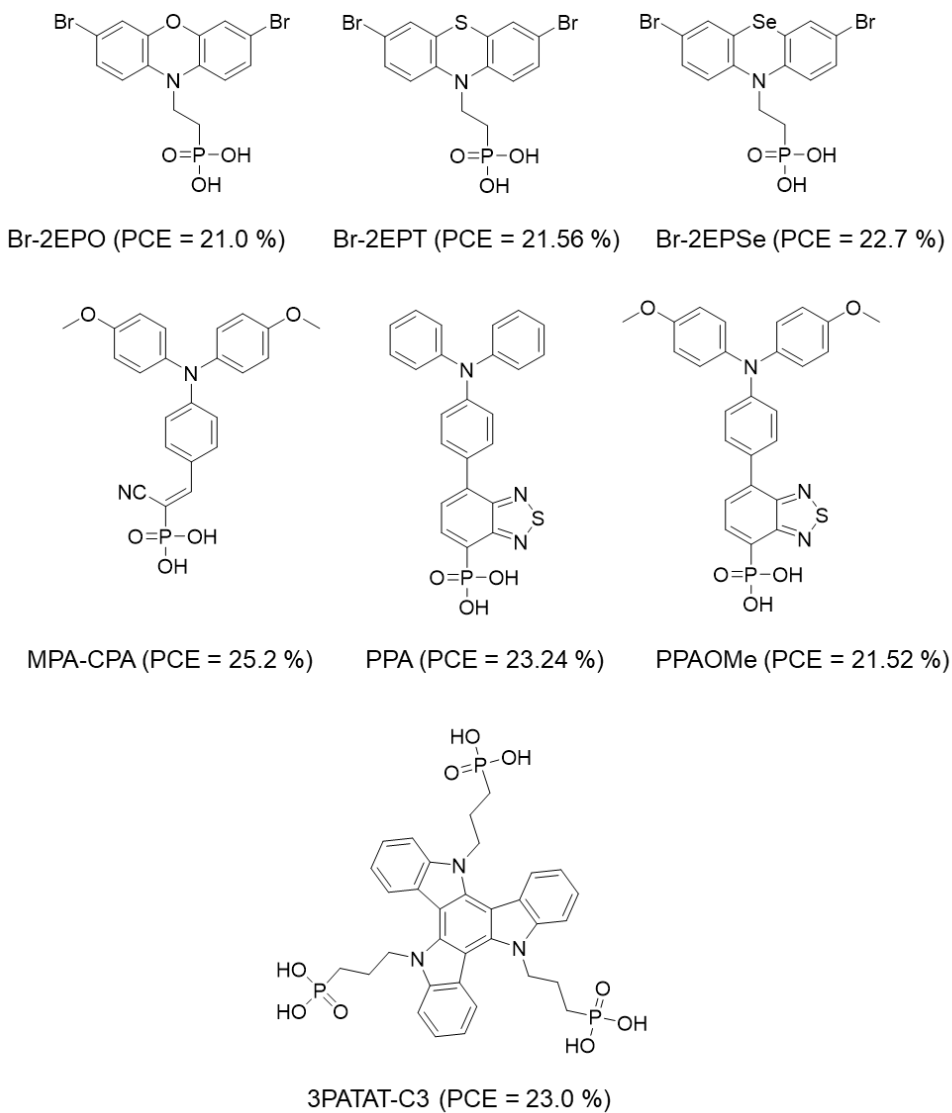


Figure 1.14. Examples of non-carbazole SAM materials [120-123]

To sum up, due to outstanding properties, such as a tunable band gap, wide absorption in the visible region or long carrier diffusion length, perovskites are considered as promising materials for new generation solar cells. A few different architectures of PSCs exist, of which, inverted architecture devices can provide better stability and lower hysteresis compared to the devices of regular architecture. The introduction of carbazole-based SAM derivatives containing a phosphonic acid group was an important advancement in the development of p-i-n PSCs. This way, commonly used polymeric HTM PTAA was outperformed by 2PACz and other SAM materials in terms of the device efficiency, and its shortcomings were also eliminated.

Currently, 2PACz and other carbazole family materials are one of the most widely investigated SAMs in inverted architecture PSCs. Consequently, due to all the benefits that SAM can provide, more and more materials with different chromophores are starting to be explored in this research field.

1.4. SAM Application in Bulk-Heterojunction Organic Solar Cells

1.4.1. Organic solar cells

Organic solar cells or organic photovoltaics (OPVs) use organic materials to convert sunlight into electricity, such as polymers or small molecule semiconductors, which can be synthesized in the laboratory and, unlike silicon, which do not need to be expensively processed [124-126]. Usually, two donor-acceptor materials are used together to form a heterojunction, where the generated charges are being separated to holes and electrons, and further transferred to the respective electrodes (Figure 1.15) [127-129]. The very first devices (first generation OPVs) consisted of a single active layer (Figure 1.16a), in which, dissociation of excitons was difficult. Combined with strong electron and hole recombination, the PCEs of these devices were poor, and they measured below 0.1% [130].

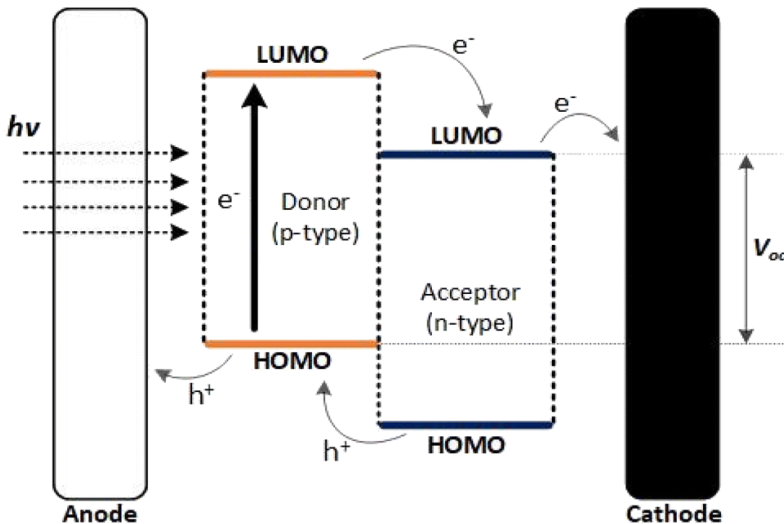


Figure 1.15. OPV operational mechanism [131]

With the introduction of the bilayer structure (Figure 1.16b), the efficiency of OPVs was only slightly improved. By stacking two active layers of copper phthalocyanine and perylene tetracarboxylic derivative, the device yielded 1% of PCE. The poor efficiency was related to the limited area of the donor-acceptor interface, which highly hindered exciton diffusion and separation [132,133].

A significant breakthrough in OPVs development was made after the introduction of the bulk heterojunction (BHJ) device structure, in which two active layers of donor and acceptor materials were blended together (Figure 1.16c). This allowed to significantly reduce the diffusion distance for exciton separation, which

resulted in an increased device efficiency [134]. Since then, the majority of works in the OPV research were focused on the BHJ architecture. Continuous development has led to an increase in device PCE to over 18%; therefore, currently, organic photovoltaics can be considered as a promising PV technology [135-137].

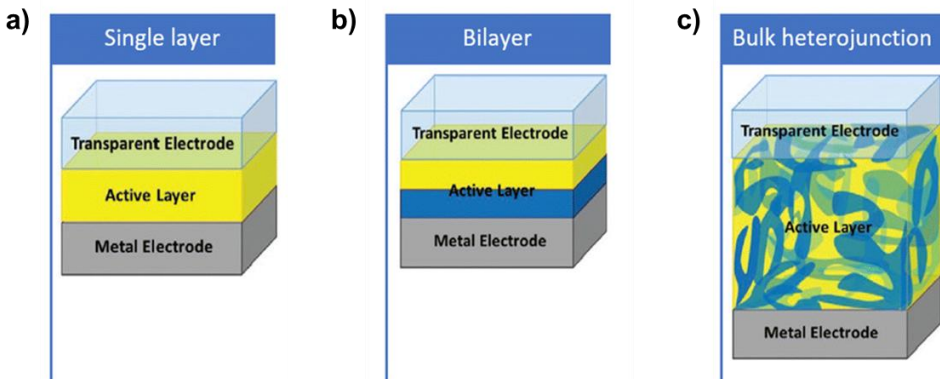


Figure 1.16. Different device structures of OPVs: (a) Single layer; (b) Bilayer; (c) Bulk heterojunction [131]

A number of different donor and acceptor materials were investigated for the construction of BHJ OPVs. Acceptor materials are generally divided into two main groups – fullerene and non-fullerene acceptors. *Fullerene acceptors* (FA) were the first ones to be introduced into the BHJ structure; however, due to their poor solubility in organic solvents, the primary selected non-modified fullerene C₆₀ demonstrated low efficiencies in BHJ OPVs [138]. The efficiency was improved to 2.5% after the introduction of soluble modified fullerene PC₆₁BM (Figure 1.17), which could blend more efficiently with the donor material and form a better donor-acceptor heterojunction [134,139]. With the adjustments in the donor material and device fabrication methods, the efficiencies of PC₆₁BM-based BHJ OPVs were continuously improved, and it did not take long for the efficiency to reach over 5% [140-142]. However, the solubility and absorption of PC₆₁BM was not ideal, and therefore its analogue with a bigger cage PC₇₁BM (Figure 1.17) was synthesized and introduced into BHJ OPVs. PC₇₁BM demonstrated an enhanced light absorption in the visible region and initially delivered a PCE value of 3.0% [143]. In later works the efficiency was increased to 4.1% [144], and again, by adjusting donor materials, it was further increased to 7.4% [145] and 10.4%, which was actually the first reported BHJ OPV over 10% of PCE [146].

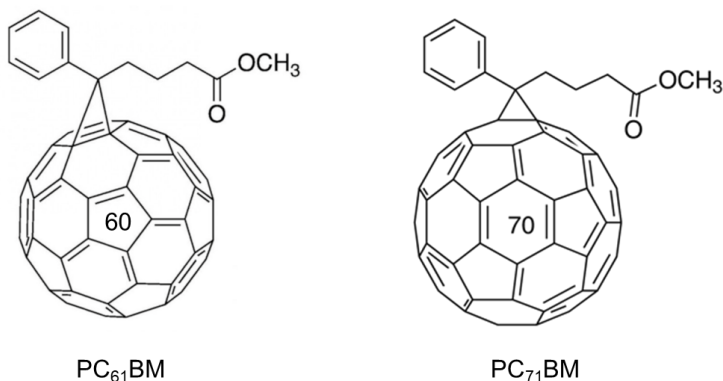


Figure 1.17. Chemical structures of PC_{61}BM and PC_{71}BM

Although numerous improvements in the OPV performance were achieved when using FA, both PC_{61}BM and PC_{71}BM were not the ideal choices to be used as acceptors due to weak absorption in the visible and near-infrared ranges, morphological instability, limited structural tunability, and a high cost [131,147,148]. Due to these reasons new *non-fullerene acceptors* (NFA) have since been investigated by synthesizing polymers and small molecules as two main NFA classes. The latter materials usually provide better performance, compared to polymeric NFAs, and they consist of two acceptor and one donor fragments (i.e., the *A-D-A* structure). Among them, ITIC, as a novel NFA electron acceptor, demonstrated intense absorption in the range of 500–800 nm and a low value of the LUMO energy, which, combined, yielded a promising PCE of 6.8% (Figure 1.18) [149]. Not long after, with several adjustments in more compatible donor materials, this efficiency when using ITIC was increased to 11.21% [150] and 12.80% [151]. Since then, a number of different NFAs have been synthesized and tested in BHJ OPVs. One of the best results have been achieved by blending NFAs with the donor PBDB-T-2 (synonym PM6) (Figure 1.17). By doing so, Y6, BTP-eC9 and L8-BO (Figure 1.18) demonstrated very good efficiencies of 17.1% [152], 17.8% [153] and 18.6% [154], respectively, and propelled BHJ OPVs into the next level.

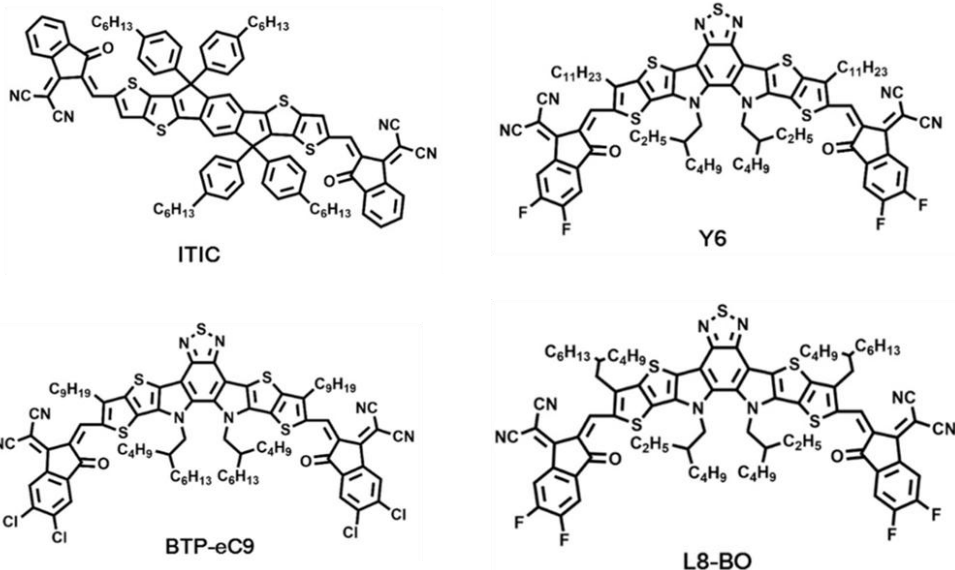


Figure 1.18. Examples of non-fullerene molecules of the A-D-A structure [131]

Donor materials play an important role in the efficiency of the BHJ OPVs, and, prior to the introduction of NFAs, these molecules were designed to match fullerenes. Initially, one of the most widely used materials was P3HT (Figure 1.19), which benefited from the high carrier mobility and good solubility, and could provide up to 6.48% of PCE [155-157]. Multiple modifications in the polymeric donor molecule structure have been made, and one of the best results was achieved by blending PffBT4T-C₉C₁₃ with the fullerene acceptor PC₇₁BM, which yielded 11.7% of PCE [156].

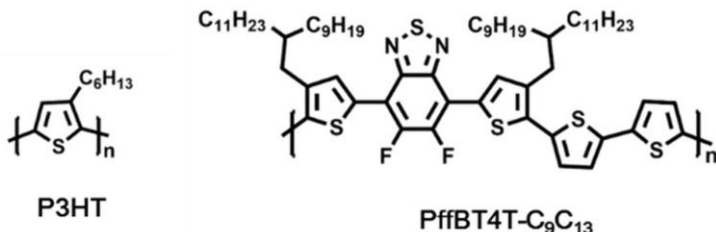


Figure 1.19. Examples of donor molecules [131]

After the introduction of NFAs and the successful replacement of fullerenes with acceptor ITIC, its blend with the new donor material PBDB-T (Figure 1.20) provided more suitable energy level alignment, showed broader absorption, and led to an efficiency of 11.21% [150]. Afterwards, numerous modifications of PDBT-T molecule have been carried out, and one of the most significant advancements was achieved by blending the fluorinated derivative PM6 (Figure 1.20) with the previously discussed

NFAs Y6 and BTP-eC9, which yielded 15.7% [158] and 17.8% of PCE, respectively [153]. Its analogue D18 was used in a device of the ITO/PEDOT:PSS/D18:N3/PDIN/Ag architecture. Due to demonstrating an efficiency of 18.22%, it was the best-performing BHJ OPV at the time [135].

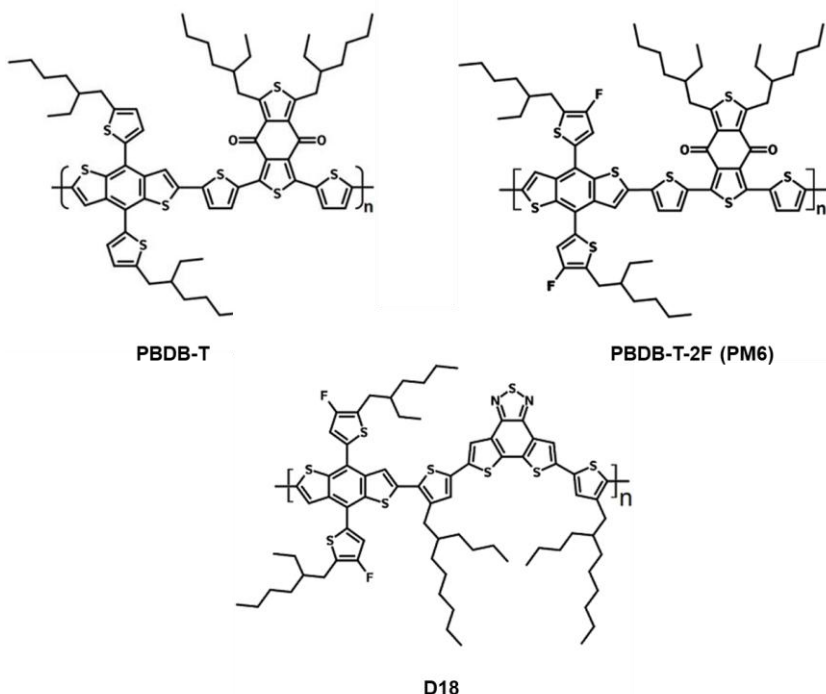


Figure 1.20. Examples of donor molecules

1.4.2. Charge transporting materials in organic solar cells

Interface layers for enhanced charge transporting can significantly improve the performance of BHJ OPVs. The efficiency record of 18.22% when using NFA D18 discussed in the previous chapter was achieved by employing both hole and electron transporting materials – PEDOT:PSS and PDIN, respectively. These interface layers can help generate a built-in electric field and a barrier-free contact between the electrode and the photoactive layer, allowing charge carriers to drift and be collected [159-161]. However, the development of these interface materials has received relatively little attention compared to the investigation of donor and acceptor materials [159,162,163]. Among the reported studies on interfacial materials, the majority of works focused on the investigation of electron transporting materials [164-166]. A number of novel ETMs were introduced (Figure 1.21), such as PFNBr [167], PNIDT-F3N [168], PDINO or PDINN [160,169], which were widely used in OVPs, and were found to provide high efficiencies.

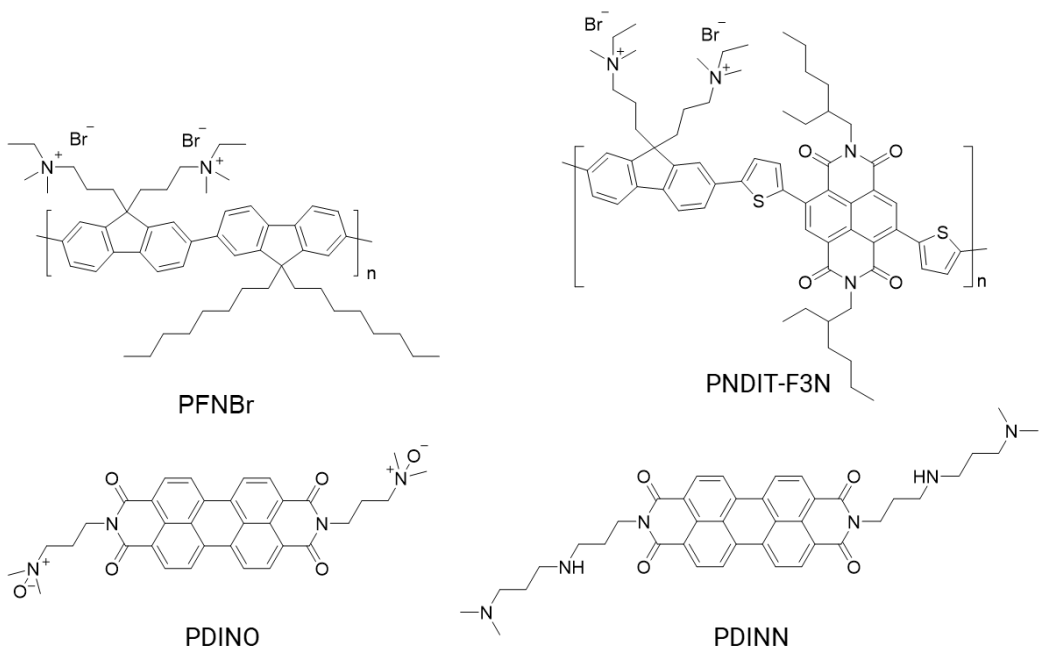


Figure 1.21. Examples of ETMs used in OPVs

The progress in the development of hole transporting materials, suitable for application in OPVs, however, has been lagging that of ETMs. Among HTMs, PEDOT:PSS (Figure 1.22) is one of the most widely studied and used materials. PEDOT:PSS can be easily processed and has good optical transparency in the visible and near-infrared ranges, thus minimizing absorption losses [170]. Also, it can provide a high value of work function, well-matched with a lot of donor materials, and a good layer coverage with tunable wettability [136,170,171,172]. Overall, PEDOT:PSS is able to provide top-tier BHJ OPVs performance, over 18% of PCE [135,173].

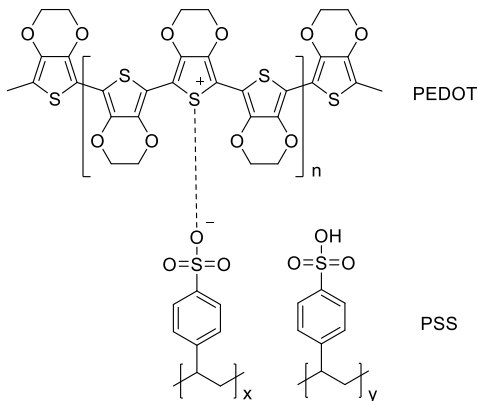


Figure 1.22. Chemical structure of the PEDOT:PSS

On the other hand, PEDOT:PSS has acidic properties that can corrode and damage an ITO anode. Combined with its ability to absorb moisture and oxygen from air, degradation of ITO can be induced at the interface with PEDOT:PSS [174-177]. Additionally, its conductivity is relatively low, and all of these drawbacks pointed towards the need for new solution-processable HTMs [159,170].

As an alternative, SAM materials were investigated instead of the regular HTMs. However, one of the earliest attempts of their application was not very successful as they were used together with the fullerene acceptor PC₆₁BM and P3HT donor at the early stage of OPV development, and the PCE values of these devices were below 4% [178,179]. In the later stages of OPV development, as new donor materials and NFAs were being introduced, new attempts were made in SAM applications. Initially, 2PACz (Figure 1.23a), which had already been reported for use in PSCs, was investigated in a device with the ITO/HTM/BHJ/PFN-Br/Ag architecture (Figure 1.23b) and compared to PEDOT:PSS. The 2PACz-based device showed slightly better photovoltaic characteristics, yielding 18.03% PCE compared to the PEDOT:PSS performance of 17.52% PCE. What is even more important, a device based on SAM demonstrated a significantly increased operational stability, compared to PEDOT:PSS. After 120 h of continuous light soaking, it retained 74% of its initial PCE (Figure 1.23c). In contrast, a device based on PEDOT:PSS lost ~80% of its initial PCE after only 50 h, thereby indicating that SAM can potentially increase the lifetime of OPVs [136].

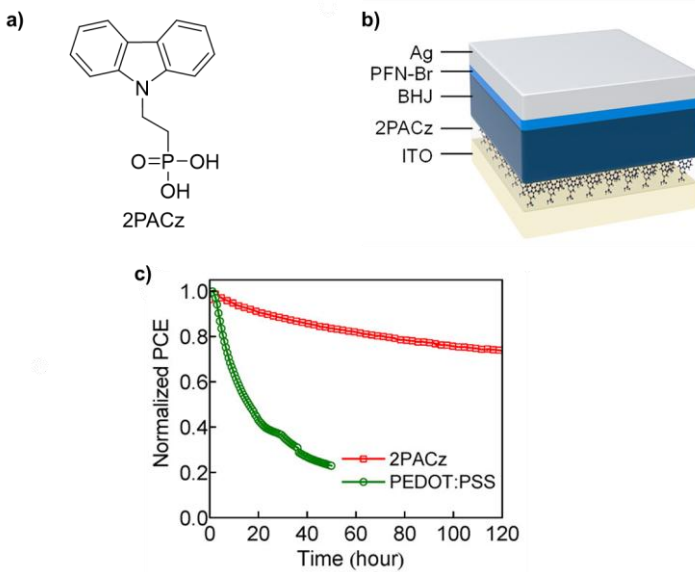
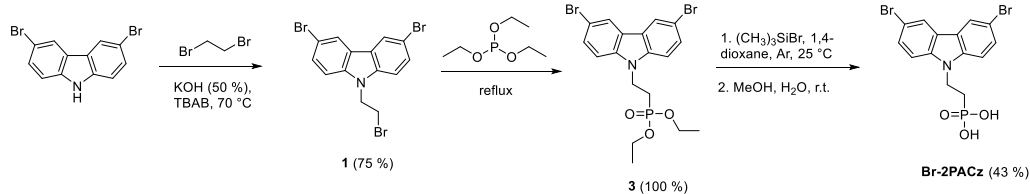


Figure 1.23. (a) Chemical structure of the 2PACz; (b) Schematic structure of BHJ organic solar cell; (c) Evolution of normalized PCEs of BHJ OPVs based on 2PACz and PEDOT:PSS [136]

In later studies, 2PACz was functionalized with bromine substituents. As shown in Scheme 1.13, Br-2PACz was synthesized by Prof. V. Getautis research group similarly to previously reported 2PACz and MeO-2PACz. Halogenated SAM material was investigated along with MeO-2PACz in the devices of the ITO/HTM/BHJ/PFN-Br/Ag architecture (Figure 1.22 inset) and compared with PEDOT:PSS.



Scheme 1.13. Br-2PACz synthesis procedure [180]

J-V curves of BHJ OPVs (Figure 1.24a) indicate that an MeO-2PACz-based device demonstrated the worst performance, yielding 14.5% of PCE and indicating that donor groups in the SAM molecule are not favorable towards best efficiency. In contrast, PEDOT:PSS provided a higher efficiency of 17.5%. Quite the opposite result was obtained with Br-2PACz; due to the acceptor halogen substituents and deeper energy levels, an improvement was observed in all the photovoltaic characteristics, compared to PEDOT:PSS (Figure 1.24b). The champion device efficiency when using Br-2PACz reached 18.4% of PCE [180].

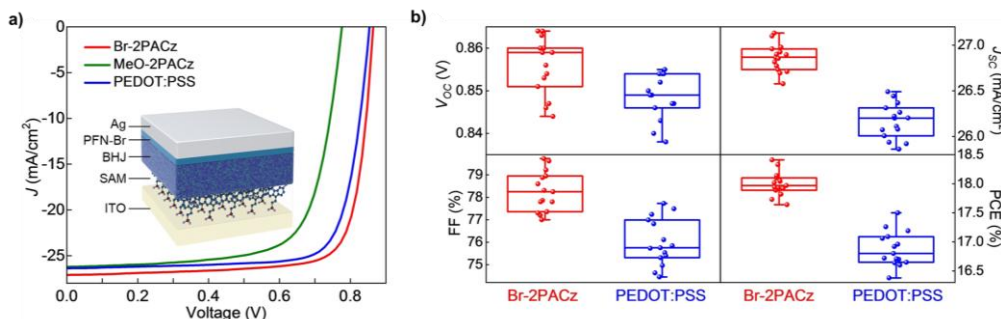


Figure 1.24. (a) *J-V* curves of BHJ OPVs when using Br-2PACz, MeO-2PACz, and PEDOT:PSS. The inset shows the schematic of the employed cell architecture; (b) Box plot of V_{OC} , J_{SC} , FF, and PCE for OPV cells based on Br-2PACz and PEDOT:PSS [180]

To summarize, organic solar cells are considered as a promising technology among the new generation photovoltaics. As a number of new donor and acceptor materials have been developed, the performance of OPVs has been significantly improved, and it has now reached over 18%. Until very recently, most of the best performing devices were constructed using PEDOT:PSS as an HTM. However, its hydrophilic and acidic nature could affect the stability of the cell. An improvement in

the device performance and operational stability has been achieved with the successful integration of SAM materials.

1.5. Conclusions of the Chapter

From the information given in this section, it is evident that a great progress has been made in the development of hole transporting materials. The synthesis of materials containing a phosphonic acid anchoring group is not complicated, with the possibility of using different synthesis methods. Usually, two synthetic steps are required. These compounds can be used to form a self-assembled monolayer on various metal oxides, and they can be integrated into various optoelectronic devices. The advantages of HTM SAM derivatives, such as 2PACz or MeO-2PACz, have been demonstrated in PSCs and OPVs over the standard polymeric HTMs, improving both the performance and stability of the devices. The most widely used SAM derivatives contain a carbazole chromophore; however, materials with different central fragments also demonstrate promising results and are worthy candidates for further investigation. Overall, the results given in this section indicate that the synthesis and study of SAM HTMs is a promising strategy for further progress in the development of optoelectronics.

2. RESULTS AND DISCUSSION

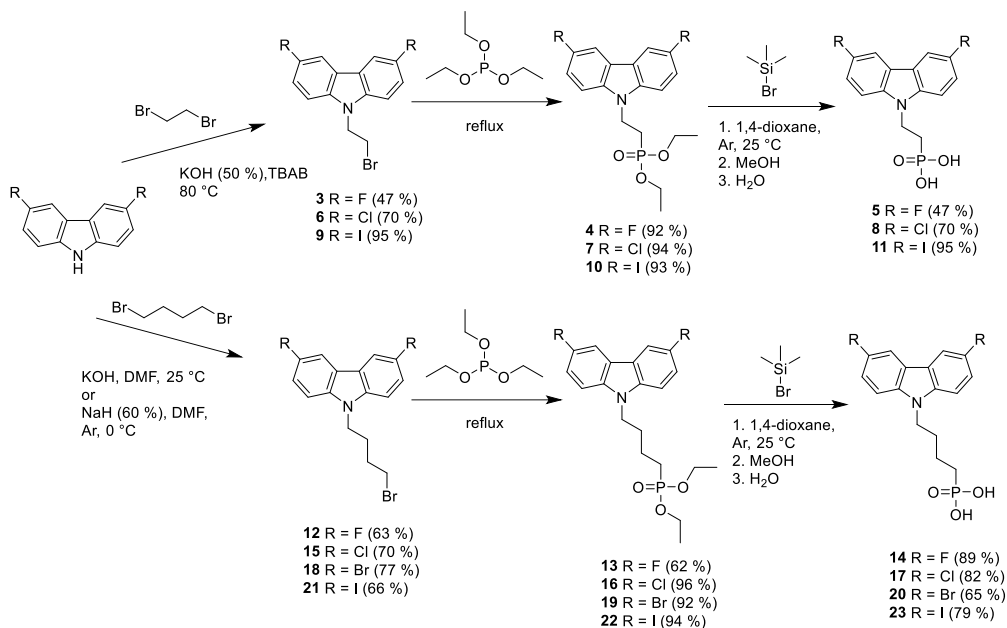
2.1. Halogenated Carbazole-Based Hole Transporting SAM Materials

Since a carbazole-based SAM derivative functionalized with bromine (Br-2PACz) found its application as a hole-extracting interlayer in organic photovoltaics (OPVs) due to a favorable HOMO energy (-6.01 eV), lower interface resistance, longer carrier lifetimes, halogenated carbazole derivatives have been gaining attention as promising SAMs for applications where a higher ionization energy is required [180].

In this chapter, a series of halogenated carbazole-based SAM molecules containing a phosphonic acid functional group are presented. Carbazole was chosen as a reliable chromophore with a previous track record of good performance in SAM materials, but, also, due to the convenient and straightforward synthesis procedures, it can be relatively easily functionalized with most halogens. Different halogen positions, the number of substituents and a different length of the aliphatic chain were investigated for the structure variation as well. The main goal was to compare all these variables so that to find the optimal structure for the most effective carbazole-based halogenated SAM derivative.

2.1.1. Synthesis of halogenated carbazole-based materials containing the phosphonic acid functional group

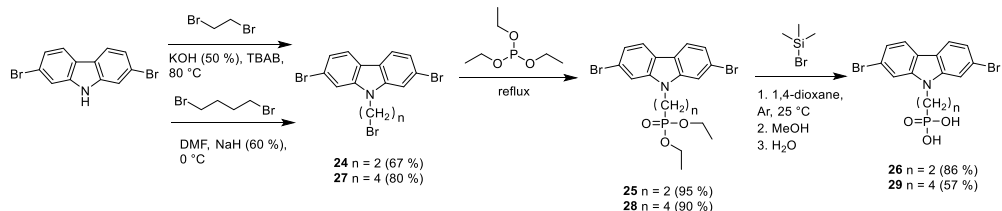
Most of the halogenated carbazoles, except for 3,6-difluoro-9*H*-carbazole, are commercially available, thus shortening and streamlining the synthesis procedure. Synthesis of 3,6-halogenated SAMs was performed in a 3-step procedure (Scheme 2.1).



Scheme 2.1. Synthesis of 3,6-halogenated carbazole derivatives containing the phosphonic acid group

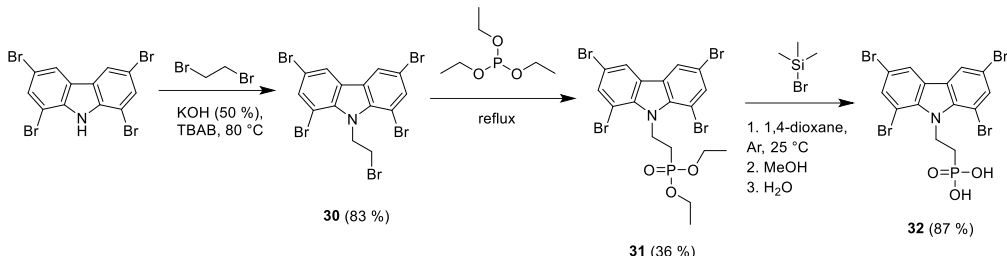
Halogenated carbazoles were alkylated by using 1,2-dibromoethane which acted both as an alkylation agent and a solvent, 50% aqueous solution of KOH and TBAB to obtain intermediates containing the bromoethyl moiety. The introduction of a longer bromobutyl aliphatic chain was done by using 1,4-dibromobutane and either powdered KOH, or NaH 60% dispersion in mineral oil. Alkylated derivatives further reacted with triethyl phosphite, thus forming intermediate phosphonic acid ethyl esters. The final products **5**, **8**, **11**, **14**, **17**, **20** and **23**, containing the phosphonic acid functional group, were obtained by the hydrolysis of phosphonates, while using bromotrimethylsilane, methanol and water.

Fluorine, as the most electronegative atom among halogens, split the aromatic proton and carbon signals of carbazole in the NMR spectra. An example of the compound **5** ^1H NMR spectra is provided in Figure A4.



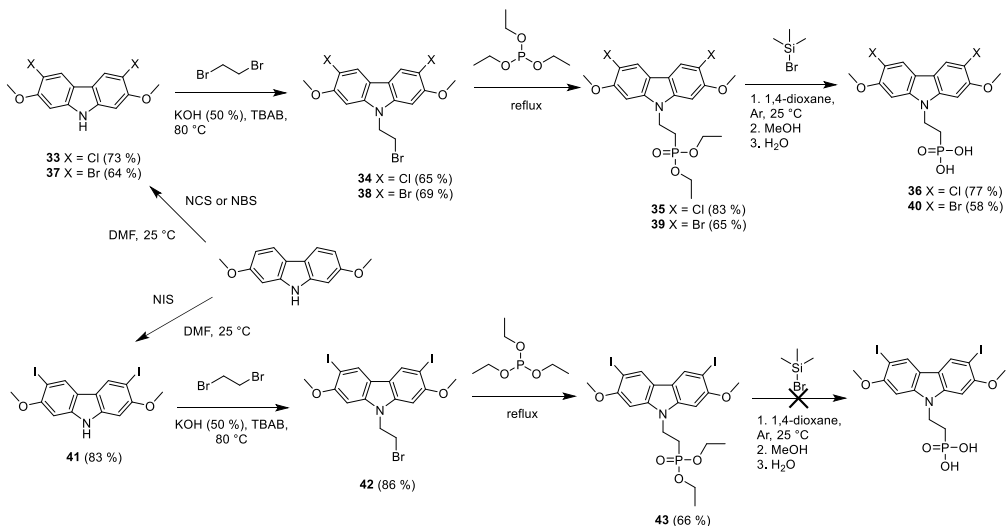
Scheme 2.2. Synthesis of 2,7-dibromocarbazole derivatives containing the phosphonic acid group

To evaluate the influence of the halogen substituent position, 2,7-dibromo-9*H*-carbazole was chosen for the synthesis of compounds **26** and **29**. Both of them were synthesized *via* a similar synthesis procedure as 3,6-halogenated carbazole analogues (Scheme 2.2)



Scheme 2.3. Synthesis of 1,3,6,8-tetrabromocarbazole **32** containing the phosphonic acid group

Furthermore, in order to evaluate the influence of bromine substituents in all the four positions of the carbazole molecules, tetrabromo-substituted carbazole derivative **32** was synthesized *via* a similar 3-step procedure (Scheme 2.3).



Scheme 2.4. Synthesis of halogen and methoxy substituted carbazole derivatives containing the phosphonic acid group

Finally, methoxy groups were introduced to induce an increased dipole moment due to the presence of both the acceptor and donor functional groups. 2,7-dimethoxy-9*H*-carbazole was halogenated by using the appropriate halogenation agent, and final materials **36** and **40**, containing chlorine and bromine substituents, respectively, were synthesized *via* a similar 3-step procedure (Scheme 2.4). Iodine containing intermediates **41**, **42** and **43** were synthesized by conducting similar halogenation, alkylation and phosphorylation reactions. However, the hydrolysis reaction of intermediate **43** was unsuccessful, which suggest side reactions between iodine and

methoxy groups in the presence of hydrolysis agent bromotrimethylsilane, since compound **11** having iodine substituents was synthesized successfully (Scheme 2.1).

The obtained compounds were used for further investigation to form a self-assembled monolayer on ITO. The procedure for the formation of the monolayer is outlined in Section 3.1.

2.1.2. Photoelectrical properties¹

The ionization potential (I_p) of the synthesized halogenated SAM materials was measured by using *photoelectron spectroscopy in air* (PESA) measurement and compared with the commonly in BHJ OPV used HTM PEDOT:PSS. Although this comparison is not entirely accurate, SAM materials are used to form a monolayer, which is often referred to as an interlayer, while, in contrast, PEDOT:PSS forms a much thicker film. It still provides useful data for the better understanding how the electrochemical properties can affect the device performance. Additionally, the work functions of modified ITO substrates were measured by using *Kelvin Probe AFM* so that to evaluate how SAMs influence the ITO surface energy.

Table 2.1. Measured ionization potential and work function values of the synthesized halogenated SAM derivatives

HTM	I_p [eV]	Work Function [eV]
ITO	-	4.70
PEDOT:PSS	5.05	4.90
Br-2PACz	6.01	5.82
5	5.92	5.68
8	6.05	5.77
11	5.92	5.73
14	5.61	5.46
17	-	-
20	5.94	5.40
23	-	-
26	5.78	4.78
29	5.96	5.52
32	5.96	5.22
36	5.81	5.60
40	5.85	5.70

The obtained results (Table 2.1) reveal that the introduction of halogen substituents resulted in deeper highest occupied molecular orbital (HOMO) energy levels, compared to 2PACz (5.6 eV) [5] and MeO-2PACz (5.30 eV) [180], which was expected, due to the electron accepting properties of the halogen substituents. Among them, chlorine containing derivative **8** demonstrated the highest HOMO energy level

¹ Photoelectrical properties were measured at King Abdullah University of Science and Technology (KAUST), Saudi Arabia, by Prof. T. D. Anthopoulos research group

value of -6.05 eV, suggesting its potential to be an effective SAM in OPVs. In contrast 2,7-dimethoxy substituted carbazole **26** stood out from the researched substances by its lowest WF (4.78 eV), thus indicating the influence of the halogen substituents' position in the carbazole core, although the analogous compound **29**, differing only by a longer length of the aliphatic chain demonstrated a much higher WF energy (5.52 eV). This difference suggests that a four carbon long aliphatic chain is sufficient to pull away the carbazole chromophore from the interface; therefore, its impact on ITO WF is altered. Furthermore, noticeable HOMO level differences (up to 1 eV) are observed between PEDOT:PSS and SAMs, but, as mentioned before, it is not very practical to compare regular HTMs with SAM materials which are used to form a monolayer instead of a regular thickness film.

2.1.3. Performance in bulk heterojunction organic solar cells²

Halogenated SAM derivatives were investigated further by using them to construct BHJ organic solar cells. The device schematic architecture is given in Figure 2.1a; in all experiments it was constant and referred to as ITO/SAM/BHJ/PNDIT-F3N/Ag, where PEDOT:PSS or Br-2PACz were used as references for SAM HTMs and poly[[2,7-bis(2-ethylhexyl)-1,2,3,6,7,8-hexahydro-1,3,6,8-tetraoxobenzo[lmn][3,8]phenanthroline-4,9-diyl]-2,5-thiophenediyl[9,9-bis[3(dimethylamino)propyl]-9H-fluorene-2,7-diyl]-2,5-thiophenediyl] (PNDIT-F3N) used as ETM. Different systems of light absorbers were tested, the names and structures of BHJ materials are given in Figure 2.1b.

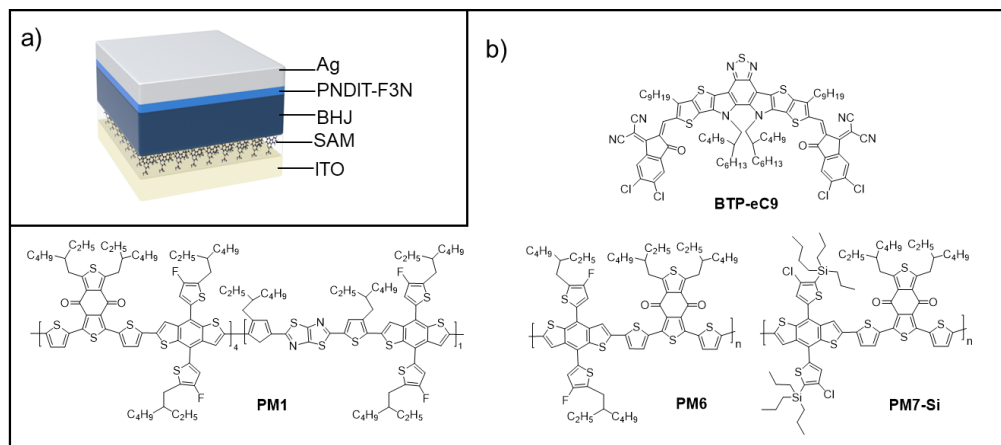


Figure 2.1. (a) Schematic architecture of the BHJ organic solar cell; (b) Chemical structures of BHJ materials

Initially, halogenated SAM derivatives **5**, **8** and **11** were tested as direct Br-2PACz analogues, differing only in terms of the type of halogen substituents, so that

² The devices were constructed, and the measurements were performed at King Abdullah University of Science and Technology (KAUST), Saudi Arabia, by Prof. T. D. Anthopoulos research group

the influence of different halogens could be evaluated. PEDOT:PSS was used as the standard HTM. The light-absorbing layer consisted of two donors and one acceptor (D1:D2:A) PM6:PM7-Si:BTP-eC9.

Table 2.2. Summary of the key operating parameters of OPVs based on PM6:PM7-Si:BTP-eC9 BHJs with different HTMs measured under illumination of AM 1.5G (100 mW/cm²).

BHJ	HTM	V _{oc} [V]	J _{sc} [mA/cm ²]	FF [%]	PCE [%]
PM6:PM7-Si:BTP-eC9	w/o	0.690	23.88	58.8	9.6 (9.2±0.3) ^a
	PEDOT:PSS	0.862	26.39	76.8	17.5 (17.1±0.2)
	Br-2PACz	0.870	26.57	77.9	18.0 (17.6±0.2)
	5	0.846	26.80	78.2	17.7 (17.3±0.2)
	8	0.863	26.96	79.4	18.5 (18.2±0.2)
	11	0.858	26.85	78.8	18.2 (17.9±0.1)

^aThe PCE_{avg} values in brackets represent averages from 15 devices.

The photovoltaic characteristics of the tested devices are shown in Table 2.2. PEDOT:PSS based devices were surpassed by all halogenated SAMs in terms of efficiency, by up to 1%, both in the maximum and average PCE values. Br-2PACz demonstrated the highest V_{oc} (0.870 V), which is often one of the most important parameters leading towards the highest performance; however, its FF (77.9%) was the lowest among all the SAM derivatives, explaining why it did not end up as a leading hole transporting material in comparison. Compound **8** with chlorine substituents stood out from the others by its highest short-circuit current (J_{sc}) of 26.96 mA/cm², a maximum PCE of 18.5% and an FF value of 79.4%. This result agrees with the previously discussed photoelectrical properties, where carbazole **8** demonstrated the highest Ip value of 6.05 eV, which is favorable for the application in BHJ OPVs. In contrast, a device without HTM demonstrated half of the efficiency (9.6%) of the device with compound **8**, thus confirming the importance of HTM in bulk heterojunction organic solar cells.

Table 2.3. Summary of the key operating parameters of OPVs based on PM6:BTP-eC9 BHJs with different HTMs measured under illumination of AM 1.5G (100 mW/cm²).

BHJ	HTM	V _{oc} [V]	J _{sc} [mA/cm ²]	FF [%]	PCE [%]
PM6:BTP-eC9	PEDOT:PSS	0.843	26.31	76.7	17.0
	14	0.843	25.59	70.1	15.1
	17	0.818	25.45	62.6	13.0
	20	0.820	25.66	67.5	14.2

The second investigated group of materials **14**, **17** and **20** contained twice as long aliphatic chains between the carbazole chromophore and the phosphonic acid group with the objective to evaluate the influence of their length on the device performance. The photovoltaic characteristics of the tested devices are shown in Table 2.3. The one donor and one acceptor (D:A) photo-active system PM6:BTP-eC9 was used. Compounds **14**, **17** and **20** substituted with fluorine, chlorine, and bromine respectively, demonstrated rather different output values in terms of PCE and other device photovoltaic characteristics. All of them were outperformed by PEDOT:PSS (17.0% PCE) by up to 4%. This result indicates the importance of the aliphatic chain length, as it also correlates with the insights on the ionization potential measurements. A four carbon long aliphatic chain is sufficient to pull away the carbazole chromophore from the interface, and therefore its impact on efficiency is also altered.

Table 2.4. Summary of the key operating parameters of OPVs based on PM6:BTP-eC9 BHJs with different HTMs measured under illumination of AM 1.5G (100 mW/cm²).

BHJ	HTM	V _{oc} [V]	J _{sc} [mA/cm ²]	FF [%]	PCE [%]
PM6:BTP-eC9	Br-2PACz	0.856	26	75.5	16.8
	26	0.83	25.546	66.7	14.1
	32	0.8466	25.323	74.9	16.1

The third group of SAM materials was investigated to evaluate the influence of the position of halogen substituents in carbazole chromophore. The photovoltaic characteristics of the tested devices are shown in Table 2.4. A one donor and one acceptor (D:A) photo-active system of PM6:BTP-eC9 was used. The synthesized compounds **26** and **32** differed from the reference material Br-2PACz in terms of the number of halogen atoms and their position; therefore, only these differences could be considered. The obtained results reveal that changing the position of the halogen atom from 3,6 carbazole positions to 2,7 positions does exert a negative impact on the performance; compound **26** underperformed by demonstrating 14.1% PCE, while Br-2PACz showed 16.8% PCE, respectively. This outcome can be related to the lower work function value (4.78 eV), resulting in a worse compatibility. In contrast, carbazole **32** containing four bromine atoms demonstrated a better efficiency of

16.1%, yet it did not outperform Br-2PACz. This can also be related to the lower WF value (5.22 eV) of **32**.

Table 2.5. Summary of the key operating parameters of OPVs based on PM1:BTP-eC9 BHJs with different HTMs measured under illumination of AM 1.5G (100 mW/cm²).

BHJ	HTM	V _{oc} [V]	J _{sc} [mA/cm ²]	FF [%]	PCE [%]
PM1:BTP-eC9	Br-2PACz	0.8290	24.353	72.3	14.6
	36	0.8262	25.275	71.9	15.0
	40	0.8253	25.603	71.9	15.2

The photovoltaic characteristics of the fourth group of materials containing both methoxy and halogen substituents **36** and **40** are shown in Table 2.5. Although the I_p values of both SAMs (5.81 eV and 5.85 eV, respectively) are lower than Br-2PACz, the increased efficiency can be related to an improved dipole moment due to the presence of both the acceptor and donor functional groups in the chromophore. The overall performance of OPVs in the different batches varies due to the different and sub optimal BHJ systems being used, as well as because of the batch-to-batch variation.

For the device optimization carbazole **8** containing chlorine substituents was chosen as the best performing halogenated SAM material. A two donors and one acceptor (D1:D2:A) photo-active system of PM6:PM7-Si:BTP-eC9 was used. Also, the n-dopant *benzyl viologen* (BV) was introduced into BHJ as an inexpensive and straightforward method to further boost the PCE of the constructed devices [181,182]. The main results are summarized in Table 2.6 and Figure 2.2a.

Table 2.6. Summary of the key operating parameters of OPVs based on PM6:PM7-Si:BTP-eC9 BHJ with BV dopant based on compound **8** or PEDOT:PSS measured under illumination of AM 1.5G (100 mW/cm²).

BHJ	HTM	V _{oc} [V]	J _{sc} [mA/cm ²]	FF [%]	PCE [%]
PM6:PM7-Si:BTP-eC9:BV	PEDOT:PSS	0.862	26.74	77.8	17.9 (17.7±0.10)
	8	0.866	27.18	80.1	18.9 (18.6±0.15) ^a

^aPCE_{avg} values in brackets represent averages from 20 devices.

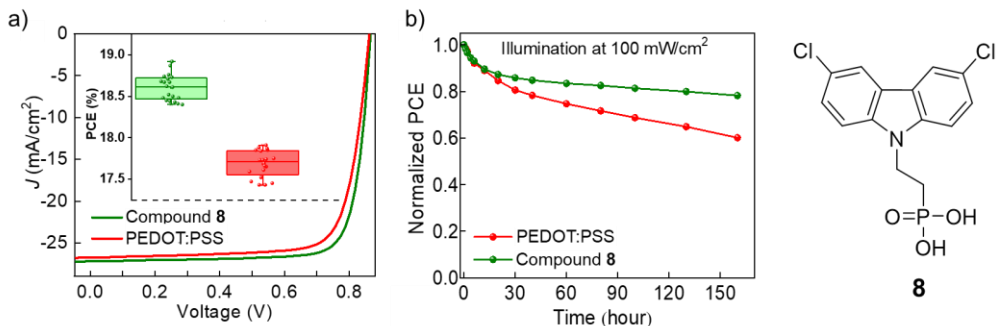


Figure 2.2. (a) J - V curves of PM6:PM7-Si:BTP-eC9 BHJ with BV dopant solar cells; (b) Change of PCE of OPVs over time

The selection of the most suitable SAM and doping strategy led to a record-breaking efficiency of 18.9% for SAM-based OPVs, and it was on par with the best-performing OPVs reported to date. A comprehensive set of characterization revealed that the enhanced performance in the OPV cells with compound **8** is associated with increased hole/carrier mobilities, a reduced interface/bulk resistance, a suppressed bimolecular/trap-assisted recombination, and a higher carrier-lifetime. Moreover, the statistical PCE values from 20 devices (see the inset in Figure 2.2a) demonstrate reproducibility and reliability of the enhancement in the cells' performance.

In addition to the improved PCE, the stability of the cells based on **8** and PEDOT:PSS has been investigated under illumination, which is of paramount importance for the commercialization of OPV devices [183]. As shown in Figure 2.2b, normalized PCE of both devices dropped by around 15% after 25 h of continuous light-soaking. However, the PCE of the cell containing SAM formed from **8** cell remains relatively steady and it only dropped around 9% from 30–160 h, whereas the PCE of the PEDOT:PSS-based device degraded by around 25%. These results indicate that chlorinated carbazole **8** could potentially help enhance the lifetime of the state-of-the-art OPVs.

2.1.4. Performance in organic light emitting diodes³

Halogenated SAM derivatives **5**, **8**, **11** were also used to fabricate green phosphorescent OLEDs. The schematic architecture of the devices is given in Figure 2.3a and referred to as ITO/HIL/CBP/CBP:Ir(ppy)₂acac/TPBi/LiF/Al, where PEDOT:PSS, MeO-2PACz, 2PACz and Br-2PACz are used as reference materials. The structures of other materials used for the OLED construction are given in Figure 2.3b.

³ The devices were constructed and the measurements were performed at King Abdullah University of Science and Technology (KAUST), Saudi Arabia, by Prof. T. D. Anthopoulos research group

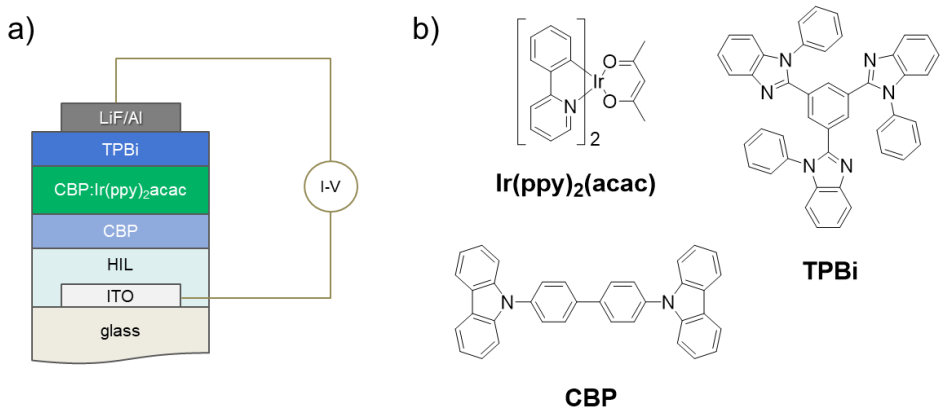


Figure 2.3. (a) Schematic OLED device architecture; (b) Structures of materials used to construct OLED devices

Before constructing full OLED devices, SAMs were deposited on ITO and directly visualized by employing *scanning tunneling microscopy* (STM). Similarly to the previous STM studies [136,184] the adsorption of the SAMs on top of the ITO substrate was successfully observed (Figure 2.4a). Interestingly, the STM analysis revealed that each SAM forms clusters/islands, and these islands vary in size (Figure 2.4b and Figure A1). The size distribution of these molecular islands suggests the presence of larger molecular islands in case of compound **11**, followed by **8** and **5** with Br-2PACz, which is an exception from this trend. It can be explained by batch-to-batch variation. Slightly smaller molecular islands are observed for 2PACz, while MeO-2PACz forms the smallest molecular islands out of all the investigated SAMs. Generally, the halogenated SAMs form more compact and uniform layers compared to 2PACz and MeO-2PACz, where the better coverage is an important parameter to achieve better device performance.

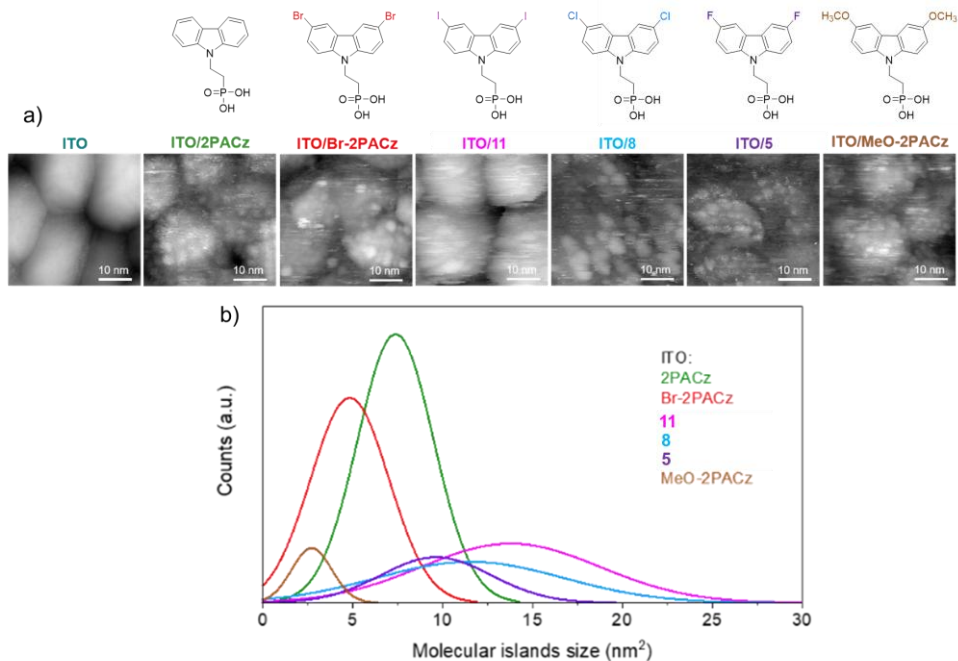


Figure 2.4. (a) STM topographic images of bare and SAM treated ITO samples; (b) SAMs molecular islands size distribution, obtained from statistical analysis on ITO/SAM STM images

All the constructed devices exhibit identical electroluminescence (EL) emission spectra, with the peak wavelength (λ_{\max}) centered at $\sim 523 \text{ nm}$ (Figure 2.5a). The green EL emission, as indicated by the *Commission Internationale de l'Eclairage* (CIE-1931) color coordinates (Figure 2.5a-inset), remains stable as the applied voltage increases (Figure A2).

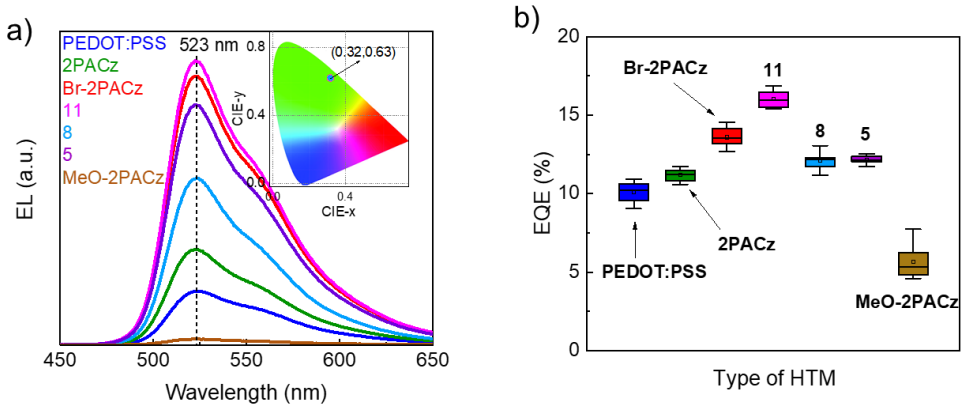


Figure 2.5. (a) Electroluminescence spectra and chromaticity diagram (inset) of green phosphorescent OLEDs; (b) Device EQE statistics

Table 2.7. Performance parameters of OLEDs based on CBP:Ir(ppy)₂acac with different hole-injection layers

HTM	V _{on} (V)	Luminance _{max} (cd m ⁻²)	EQE _{max} %	max Current efficiency (cd A ⁻¹)	max Power efficiency (lm W ⁻¹)
PEDOT:PSS	~3.3	38700	10.59	39.45	30.11
MeO-2PACz	~3.4	16180	7.73	28.78	15.25
2PACz	~2.9	49510	11.69	43.47	32.33
Br-2PACz	~2.9	55250	14.55	54.46	45.18
5	~2.9	47790	12.54	46.74	39.36
8	~2.9	44530	13.06	48.42	40.64
11	~2.9	57290	16.86	63.18	46.69

The *current-voltage-luminance* (J-V-L) characteristics and the corresponding *external quantum efficiency-voltage* (EQE-V), *current efficiency-voltage* (CE-V) and *power efficiency-voltage* (PE-V) plots for the devices employing various hole-injection layers (HILs) are summarized in Table 2.7. In control OLEDs based on PEDOT:PSS HIL, we observe a V_{on} of ~ 3.3V, reaching a maximum luminance of 38700 cd m⁻², EQE of 10.59 %, CE of 39.45 cd A⁻¹ and PE of 30.11 lm W⁻¹. Replacing PEDOT:PSS with the 2PACz reduces V_{on} to 2.9 V, resulting in a slightly improved OLED performance: the maximum luminance of 49510 cd m⁻², 11.69% EQE, the peak CE of 43.47 cd A⁻¹, and the maximum PE of 32.33 lm W⁻¹. OLEDs using halogenated SAMs exhibit the same V_{on} of ~ 2.9 V and are brighter (Table 2.7) compared to 2PACz and PEDOT:PSS based OLEDs (Figure 2.5a). This improvement can be attributed to the WF enhancement offered by the halogenated SAMs, discussed in a 2.1.2 section. However, their overall performance differs. OLEDs using Br-2PACz, **11**, **8** and **5** as

HIL achieve EQEs of 14.55%, 16.86%, 13.06% and 12.54%, respectively. The same trend is observed for the remaining performance parameters, where compound **11** stands out as the statistically best performing candidate (Figure 2.5b) by reaching the maximum brightness of 57290 cd m^{-2} , the peak CE of 63.18 cd A^{-1} and the peak PE of 46.69 lm W^{-1} . On the other hand, functionalizing ITO with MeO-2PACz increases the turn-on voltage ($V_{\text{on}} \sim 3.4 \text{ V}$), and devices are notably less efficient compared to the other SAMs and PEDOT:PSS-based OLEDs. A reduced EQE of 7.73%, CE of 28.78 cd A^{-1} and PE of 15.25 lm W^{-1} are attributed to the shallow ITO/MeO-2PACz WF.

2.1.5. Chapter summary

In summary, new halogenated carbazole-based molecules that can form a self-assembling monolayer have been synthesized and successfully utilized in BHJ OPVs and green phosphorescent OLEDs. The formation of halogenated SAMs directly onto ITO can increase its work function from 4.70 eV up to 5.77 eV, which is an important factor to the investigated systems. Compounds **5**, **8** and **11** demonstrated the highest PCE in the ternary BHJ system PM6:PM7-Si:BTP-eC9, by yielding 17.7%, 18.5% and 18.2% respectively. Furthermore, OPVs featuring SAM **8** show an enhanced stability under continuous illumination as compared to ITO/PEDOT:PSS-based cells. The introduction of the n-dopant benzyl viologen into the BHJ containing **8** further boosted the PCE of the cells to a maximum of 18.9%, which is a record-breaking value for SAM-based OPVs, and which is on par with the best-performing OPVs reported to date. The significant potential of SAM derivatives as effective materials for hole-injection in OLED applications has also been demonstrated. When using halogenated SAMs **5**, **8** and **11**, denser, more uniform, and compact layers are formed compared to 2PACz and MeO-2PACz. This resulted in OLEDs with superior performance compared to the ones using the traditional PEDOT:PSS, 2PACz or MeO-2PACz SAMs. With its combination of deep WF and good coverage, SAM **11** emerges as the most suitable molecule among the investigated materials for hole-injection in OLEDs. This approach should provide useful insights for the fabrication of efficient SAM-based LEDs and the creation of a library of SAMs that can be used for high-performing optoelectronic devices.

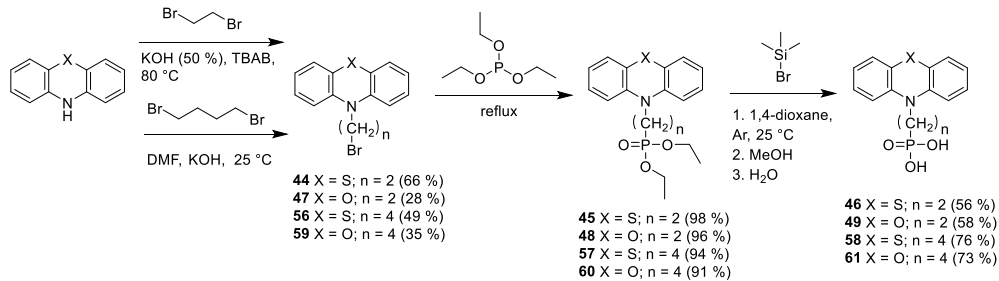
2.2. SAM Materials Containing Phosphonic Acid Functional Groups and Non-Carbazole Central Fragments

Carbazole-based SAM derivatives, such as 2PACz, MeO-2PACz or Me-4PACz, are well-known materials, currently being investigated in a wide range of optoelectronics. It is natural that more and more materials are being developed as follow ups to widen the SAM research field. This includes both carbazole and non-carbazole molecules containing the phosphonic acid functional group. Though non-carbazole analogues are not very widely explored yet, more and more molecules based on such chromophores as triphenylamine, 9,9-dimethyl-9,10-dihydroacridine, triazatruxene or phenoselenazine are emerging as promising and well performing SAMs [120,185].

In this chapter, a series of non-carbazole SAMs is presented. The chromophores that were chosen for synthesis were picked to be structurally close to well performing 2PACz, and their central cores would bear significant but not drastic chemical structure differences compared to carbazole, thus allowing us to investigate the performance of the SAMs with small changes in the structure and, hopefully, better understand the structure-performance relation.

2.2.1. Synthesis of non-carbazole materials containing the phosphonic acid functional group

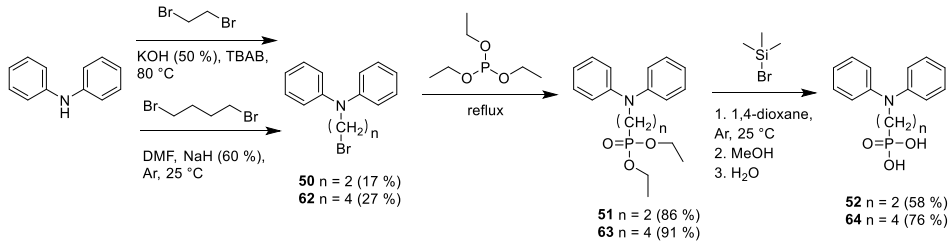
Non-carbazole SAM materials discussed in this chapter were synthesized by utilizing a 3-step synthetic procedure, similar to halogenated carbazole SAM synthesis, discussed in the previous Chapter (2.1.1.).



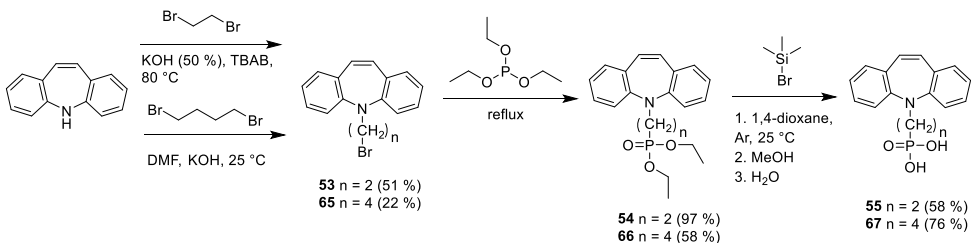
Scheme 2.5. Synthesis of phenothiazine and phenoxazine derivatives containing the phosphonic acid group

During the alkylation of phenothiazine and phenoxazine (Scheme 2.5), 2-bromoethyl or 4-bromobutyl moieties were introduced, thus obtaining alkylated derivatives **44**, **47**, **56** and **59**. By conducting the Arbuzov reaction, aliphatic bromide in the formed intermediates was substituted by phosphonic acid ethyl ester to obtain **45**, **48**, **57** and **60**. Lastly, hydrolysis was performed by utilizing bromotrimethylsilane, resulting in phenothiazine- or phenoxazine-based phosphonic acids **46**, **46**, **58** and **61**.

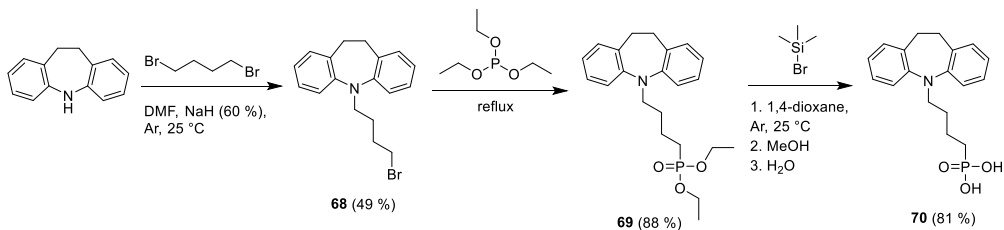
a)



b)

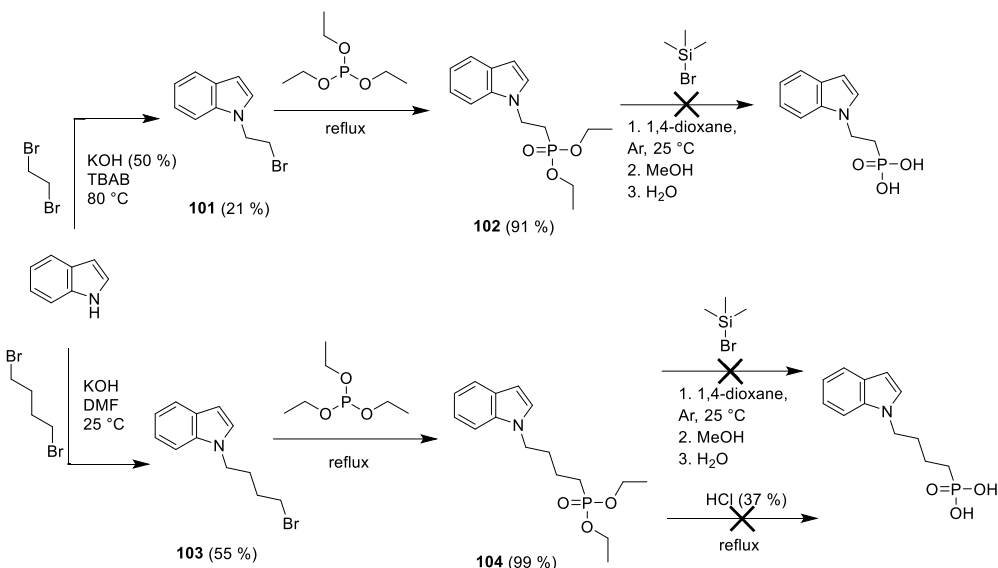


c)



Scheme 2.6. Synthesis of diphenylamine, dibenzo[b,f]azepine and 10,11-dihydro-5H-dibenzo[b,f]azepine derivatives containing the phosphonic acid group

Diphenylamine-based phosphonic acid derivatives **52**, **64** (Scheme 2.6a), 5H-dibenzo[b,f]azepine-based phosphonic acid derivatives **55** and **67** (Scheme 2.6b), and 10,11-dihydro-5H-dibenzo[b,f]azepine-based phosphonic acid derivative **70** (Scheme 2.6c) were synthesized *via* a similar 3-step procedure.



Scheme 2.7. Synthesis attempts to obtain indole derivatives containing phosphonic acid group

Attempts to synthesize indole-based derivatives containing the phosphonic acid functional group resulted in a different outcome. Indole alkylation reactions and the further transformation of alkylated intermediates **101**, **103** to the respective phosphonates **102**, **104** were successful (Scheme 2.7). However, the final hydrolysis step using bromotrimethylsilane resulted in a mixture of inseparable products which formed during side reactions due to the sufficiently reactive 3-H position of indole. Additionally, phosphonate **104** was attempted to be hydrolyzed under different conditions by using concentrated hydrochloric acid, yet, the outcome was the same, and, overall, the synthesis of non-substituted indole phosphonic acids was unsuccessful.

The obtained compounds were used for further investigation to form a self-assembled monolayer on ITO. The procedure for the formation of the monolayer is provided in Section 3.1.

2.2.2. Photoelectrical properties⁴

To evaluate the energy levels of non-carbazole SAM and compare the obtained results with the already known materials, the ionization potential (I_p) was measured in the solid-state by using the *photoelectron spectroscopy in air* (PESA) method. Examples of I_p graphs are presented in Figure 2.6.

⁴ The photoelectrical properties were measured at King Abdullah University of Science and Technology (KAUST), Saudi Arabia, by Prof. T. D. Anthopoulos research group and at the Institute of Chemical Physics, Vilnius University, by E. Kamarauskas

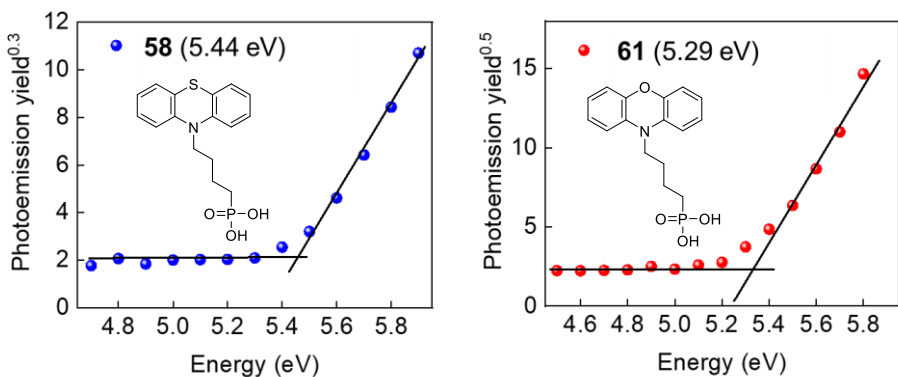
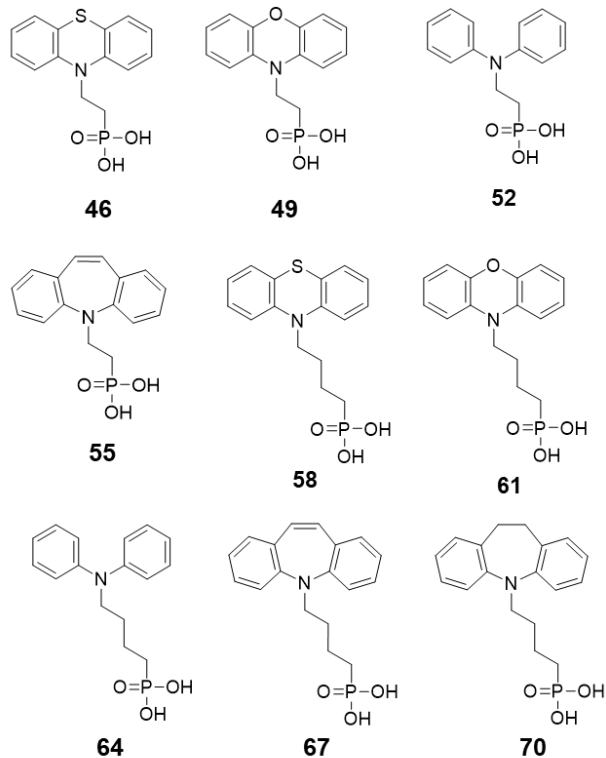


Table 2.8. Measured ionization potential values of synthesized non-carbazole HTMs

HTM	I_p [eV]
46	5.23
49	5.27
52	5.79
55	5.78
58	5.44
61	5.29
64	5.78
67	5.81
70	5.85



The I_p measurement results of all the materials discussed in this chapter are shown in Table 2.8. **46**, **49**, **58** and **61** with heteroatom-containing phenoxazine or phenothiazine chromophore demonstrated the lowest values of I_p specifically, from 5.23 to 5.44 eV, which is lower than 2PACz (5.6 eV). The remaining materials performed in a nearly opposite way, by demonstrating higher I_p values in the range of

5.78–5.85 eV. This result can be related to a different molecule conformation in space of **55** and **67**, when the central core is 5H-dibenzo[*b,f*]azepine, or a somewhat twisted out of conjugation plane aromatic systems in **52**, **64** and **70** with diphenylamine, or 10,11-dihydro-5H-dibenzo[*b,f*]azepine central cores. This information is important for the better understanding of how the energy levels can be tuned to the desired value simply by adjusting the chromophore in SAM molecules.

Compounds **55**, **64** and **70** were deposited on ITO, and the work function of the modified ITO surface was measured by using the *ultraviolet photoelectron spectroscopy* (UPS) method. SAM materials 2PACz and Me-4PACz were used as references.

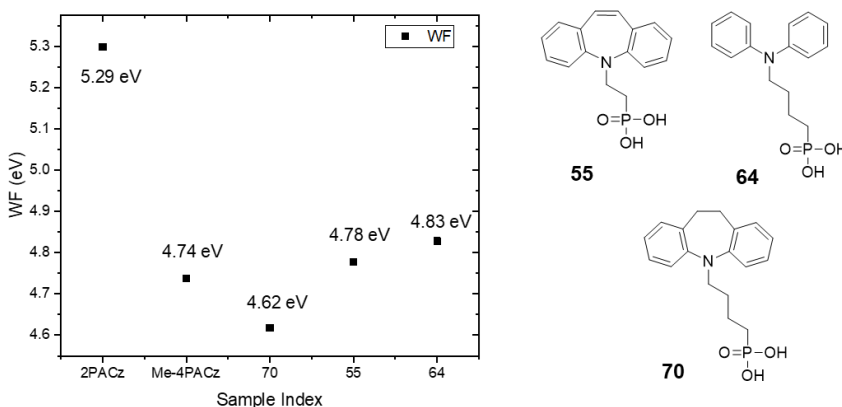


Figure 2.7 Work functions' values of compounds **55**, **64** and **70** compared to the reference SAM materials 2PACz and Me-4PACz

The obtained results reveal that the influence of compounds **55**, **64** and **70**, as well as the reference Me-4PACz on the ITO WF value is not very significant, as it changed from 4.70 eV (see Table 2.1 in Chapter 2.1.2) to 4.78 eV, 4.83 eV, 4.62 eV, and 4.74 eV, respectively (Figure 2.7). Meanwhile, the impact of the 2PACz monolayer was emphatically more noticeable, as it increased to 5.29 eV. Partly, the difference between 2PACz and Me-4PACz SAMs could be explained by the longer aliphatic chain in Me-4PACz, resulting in a more withdrawn chromophore from the ITO interface; thus, its influence on WF decreases. However, compound **55**, which also contains shorter aliphatic chain like 2PACz, did not demonstrate big changes, thereby indicating its central core similarity in terms of energetics with the ITO surface.

2.2.3. Performance in bulk heterojunction organic solar cells⁵

Phenothiazine and phenoxazine-based SAM derivatives were investigated in BHJ organic solar cells. The device schematic architecture is given in Figure 2.8a and referred to as ITO/SAM/BHJ/PNDIT-F3N/Ag, where the PM6:BTP-eC9 one donor one acceptor system was used for the absorber layer (see Figure 2.1 in Chapter 2.1.3). Materials **58** and **61**, used for an expanded investigation of SAM-based OPVs, were chosen for a substantially lower ionization potential compared to the previously tested halogenated carbazole SAMs.

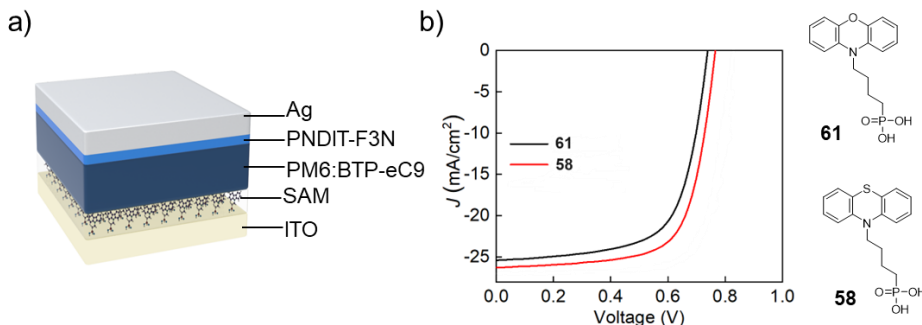


Figure 2.8. (a) Schematic architecture of BHJ organic solar cell; (b) J - V curves of the best cells in the batch using SAMs **58** and **61**

The photovoltaic characteristics and J - V curves of the tested devices are shown in Table 2.9 and Figure 2.8b respectively. Both materials lagged behind in terms of V_{OC} , the fill factor, and efficiency compared to the standard PEDOT:PSS device. **58** and **61** demonstrated a relatively good efficiency of 13.9% and 12.5% respectively, without detailed optimization. The correlation of the performance and ionization potential is also noticeable, as phenothiazine-based SAM **58** possesses higher I_p (5.44 eV) compared to **61** (5.29 eV), and its performance is better (13.9 % > 12.5 %), thus agreeing with the halogenated SAMs results, as given in the chapter 2.1.3, where the highest I_p resulted in the best performing device.

Table 2.9. Summary of the key operating parameters of OPVs based on PM6:BTP-eC9 BHJ based on compound **58** or **61** measured under illumination of AM 1.5G (100 mW/cm²).

BHJ	HTM	V_{OC} [V]	J_{sc} [mA/cm ²]	FF [%]	PCE [%]
PM6:BTP-eC9	PEDOT:PSS	0.843	26.31	76.7	17.0
	58	0.765	26.26	69.3	13.9
	61	0.739	25.38	66.4	12.5

⁵ The devices were constructed and the measurements were performed at King Abdullah University of Science and Technology (KAUST), Saudi Arabia, by Prof. T. D. Anthopoulos research group

To summarize, it is possible to construct bulk heterojunction organic solar cells operating at sufficiently good efficiencies when using non-carbazole based SAM materials possessing a lower ionization potential. For a more in-depth analysis it can be recommended to broaden this field of research by synthesizing and investigating **58** and **61** analogues containing halogen functional groups.

2.2.4. Performance of perovskite solar cells⁶

Non-carbazole SAM materials were tested in p-i-n configuration perovskite solar cells, by employing the ‘triple halide’ perovskite (1.65 eV bandgap). The main goal of this experiment was to investigate SAM derivatives containing different chromophores, to determine the optimal one, and to compare their performance with carbazole-based phosphonic acids.

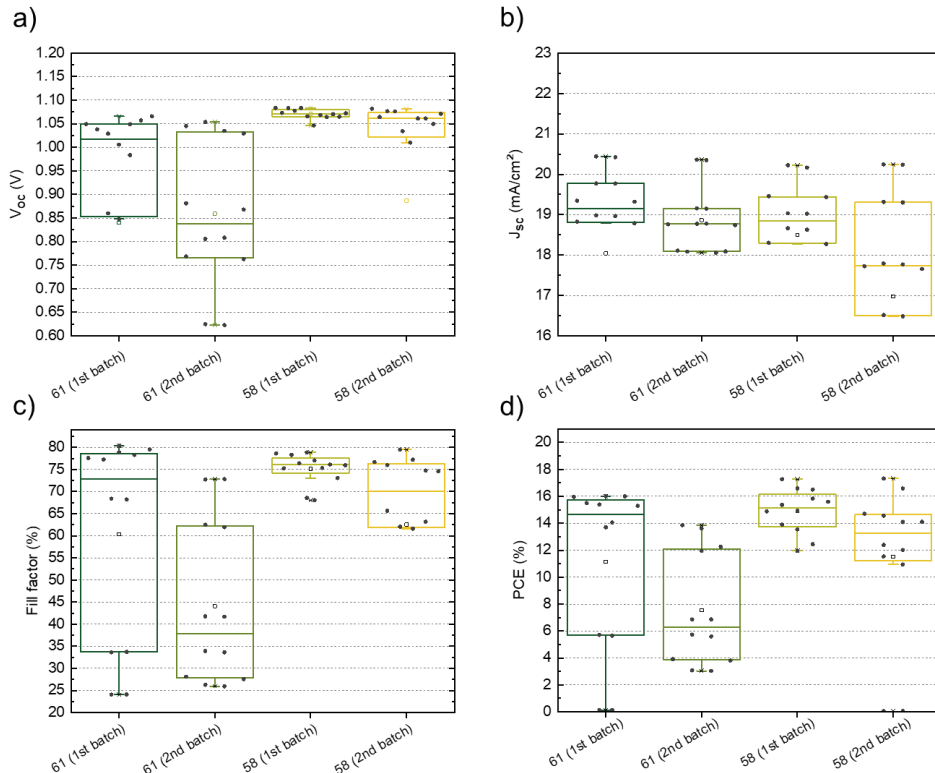


Figure 2.9. Analysis of SAMs **58** and **61** photovoltaic characteristics in p-i-n perovskite solar cells (two batches were evaluated): (a) V_{OC} statistical results; (b) J_{SC} statistical results; (c) Fill factor statistical results; (d) Efficiency statistical results

By using SAMs **58** and **61** two batches of p-i-n perovskite solar cells referred to as ITO/SAM/perovskite/LiF/C₆₀/SnO₂/Cu were constructed and investigated. The

⁶ Devices were constructed and measurements were performed at Helmholtz-Zentrum Berlin (HZB), Germany, by Prof. S. Albrecht research group

statistical photovoltaic characteristics of V_{OC} , J_{SC} , the fill factor and the efficiency values are given in Figure 2.9. The data reveal that, in most parameters, compound **58** outperformed **61**, except in the J_{SC} section (Figure 2.9b), where the values were similar or just slightly worse. Yet, what is most important here, it is the statistical distribution of the cells as compound **58** provided a much better reproducibility. A high voltage is necessary to achieve high efficiencies, while the good fill factor suggests lesser charge transport losses during the device operation. Therefore, cells based on phenothiazine **58** demonstrated a better device efficiency overall (Figure 2.9d). Meanwhile, the efficiency, the fill factor, and the V_{OC} spread are significantly bigger in case of phenoxazine **61**, demonstrating a worse reproducibility of the fabricated solar cells.

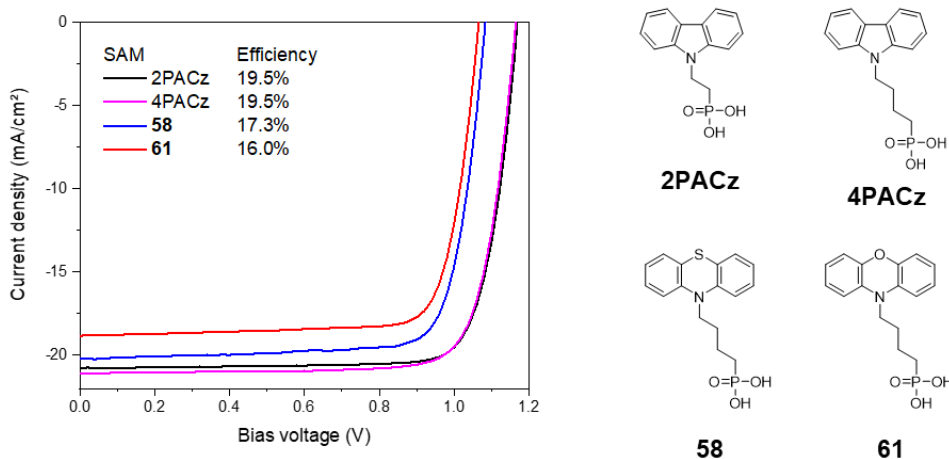


Figure 2.10. J - V curves of the best cells in the batch using 2PACz, 4PACz, and SAM derivatives **58** and **61**

Best performing cells in the batch were compared with 2PACz and 4PACz, and the latter was used as a more structurally similar derivative to **58** and **61** due to the aliphatic chain of the same length. The results revealed (Figure 2.10) that the difference in the aliphatic chain length has no impact on the device performance, where both 2PACz and 4PACz demonstrated the same efficiency of 19.5%. Both investigated derivatives **58** and **61** performed slightly worse than the reference materials (17.3% and 16.0% PCE respectively); however, the result revealed some insights about different chromophores. In this case, the efficiency gradient of 2PACz, **58** and **61** ($19.5\% > 17.3\% > 16.0\%$) can be directly related to the descending values of the ionization potential ($5.6 \text{ eV} > 5.44 \text{ eV} > 5.29 \text{ eV}$), suggesting the better compatibility with the perovskite energy levels at upper values.

Preliminary measurements of perovskite photoluminescence and perovskite *Quasi-Fermi-level splitting* (QFLS) were performed by using another group of non-carbazole HTMs **55**, **64** and **74**. This measurement is a good indicator of the overall performance in the full device. For these measurements, incomplete devices of the ITO/HTM/Perovskite architecture were constructed.

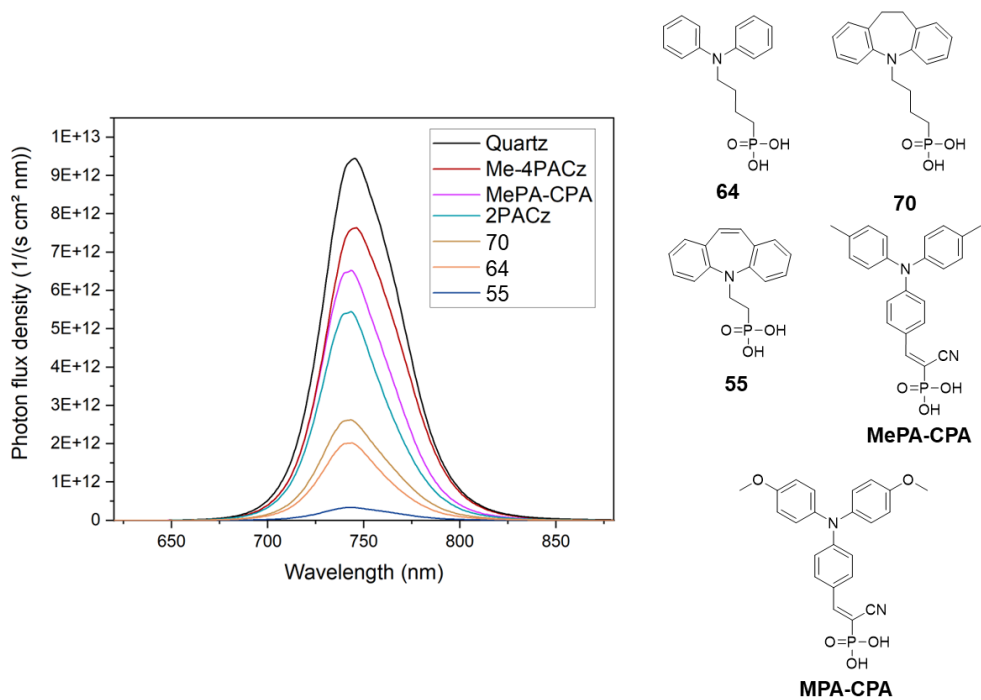


Figure 2.11. PL spectra of perovskite deposited on quartz and different ITO/SAM substrates

The device performance is highly dependent on how effectively the charge can be extracted at the perovskite/SAM interface. The hole extraction ability can be evaluated by performing perovskite steady-state *photoluminescence* (PL) measurements. The PL of perovskite deposited on quartz and different ITO/SAM substrates was measured and evaluated (Figure 2.11). HTMs Me-4PACz, MePA-CPA, 2PACz, **70** and **64** demonstrated efficient charge extraction ability in an ascending order, as perovskite on the respective modified ITO samples resulted in a gradually weaker PL level, thus indicating HTMs **70** and **64** as promising candidates for our further investigation. At the same time, strongly quenched perovskite PL on ITO/**70** and ITO/**64** substrates might also indicate the presence of defects at the interface. Compound **55**, however, led to an unusually low perovskite photoluminescence value, thereby indicating a significantly lower interface quality and *5H*-dibenzo[*b,f*]azepine as a less favorable chromophore for an efficient SAM material.

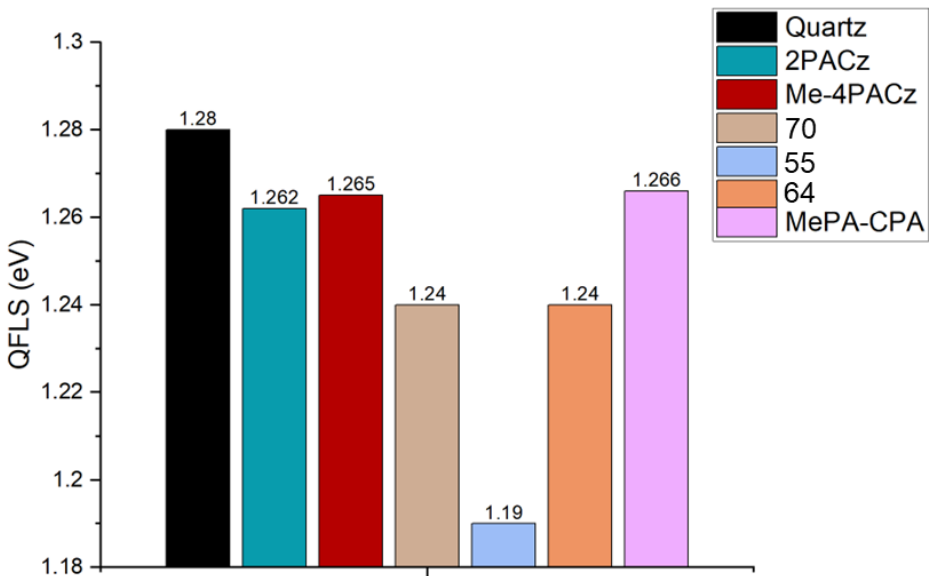


Figure 2.12. QFLS values of the perovskite film on quartz substrate and different SAMs on ITO

Quasi-Fermi-level splitting was calculated from the previous absolute PL measurements by using a calibrated 532 nm excitation laser at ~1 sun conditions. This measurement is relatively straightforward yet informative, enabling quick comparison of all the materials being tested, and predicting their performance in perovskite solar cells. The QFLS values of perovskite films deposited on reference material substrates (ITO/2PACz, ITO/Me-4PACz, ITO/MePA-CPA) were relatively similar to the one on quartz glass (1.28 eV), thus indicating a good level of passivation (Figure 2.12). The synthesized materials **70** and **64** demonstrate slightly lower QFLS values of 1.24 eV, which can be related to a slightly worse passivation, which agrees with the previous insights on perovskite photoluminescence and suggests why too strong PL quenching could be interpreted as a negative effect. The QFLS result of compound **55** also agrees with the previous PL measurements, as its worse PL intensity clearly matches with the worse QFLS value (1.19 eV).

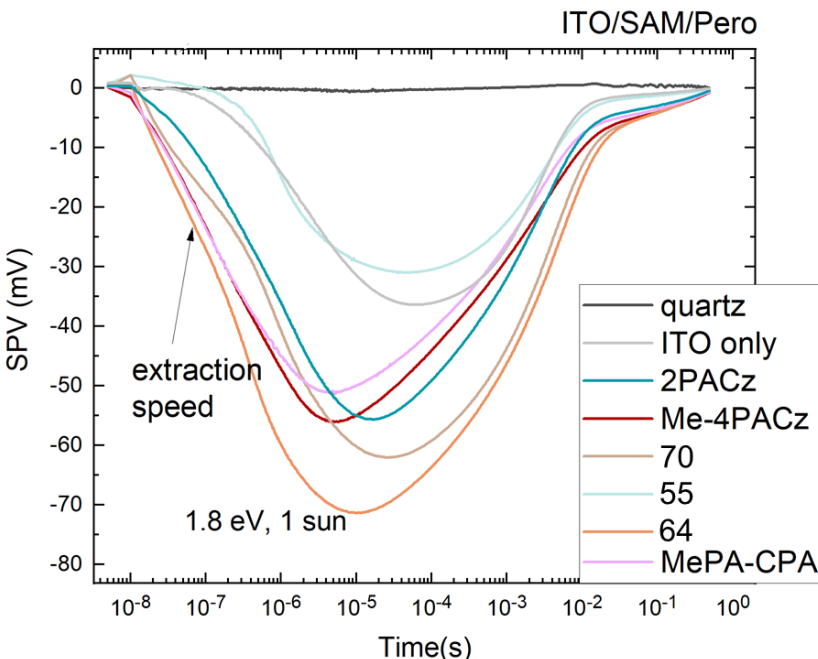


Figure 2.13. Transient surface photovoltage curves taken with samples of perovskite on bare quartz, ITO, and ITO/SAM

The charge extraction capabilities at SAM/perovskite interfaces were demonstrated by utilizing the transient surface photovoltage (trSPV) measurements with 1 sun equivalent fluence [186]. The results were compared with the quartz/perovskite sample, where charge extraction and transfer are not possible at the interface, and thus the signal is recorded as a baseline. The extraction speed was evaluated by the amplitude size and in terms of how quickly it rises. All the tested materials exhibited negative signals, thus indicating efficient hole extraction (Figure 2.13). Among them, diphenylamine-based compound **64** demonstrated the best result, surpassing all three reference materials 2PACz, Me-4PACz and MePA-CPA. 10,11-Dihydro-5H-dibenzo[*b,f*]azepine-based derivative **70** also performed exceptionally well, however, its rate of increase was relatively slower, and some positive signal at $\sim 10^{-8}$ second was noticeable, which might be a sign of electron trapping. This signal was identical for 5H-dibenzo[*b,f*]azepine derivative **55**, which demonstrated inferior hole extracting properties that were slightly worse than bare ITO.

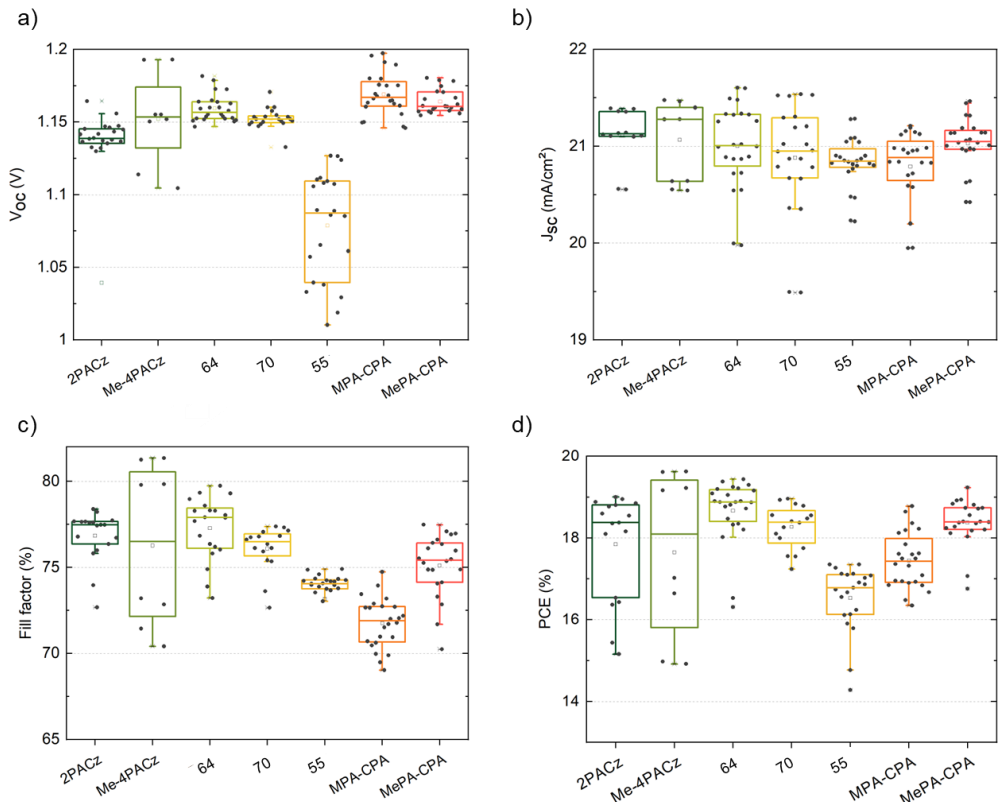


Figure 2.14. Photovoltaic characteristics of p-i-n architecture perovskite solar cells of ITO/SAM/Pero/C₆₀/SnO₂/Ag architecture comparing different HTMs used as SAMs: (a) V_{OC} statistical results; (b) J_{SC} statistical results; (c) Fill factor statistical results; (d) Efficiency statistical results

Non-carbazole SAM molecules **55**, **64** and **70** were integrated into p-i-n configuration perovskite solar cells, with the ITO/SAM/Pero/C₆₀/SnO₂/Ag architecture. An additional SAM material MPA-CPA was included into the comparison as an MePA-CPA analogue (Figure 2.11) [121]. The obtained results (Figure 2.14) reveal that all the investigated materials demonstrated solid performance, including the new materials **55**, **64** and **70**. All of them did function as effective SAM hole extracting materials. Diphenylamine **64** and 10,11-dihydro-5H-dibenzo[b,f]azepine **70** resulted in very good V_{OC} values, slightly surpassing the standard material 2PACz (Figure 2.14a). The statistical distribution of the cells, especially for **70**, is also at a good level, indicating very good reproducibility. In contrast, Me-4PACz and MPA-CPA demonstrate slightly higher maximum V_{OC} values, however, in this case, the result scattering is bigger, especially for Me-4PACz. The fill factor and PCE (Figure 2.14c and 2.14d) of compounds **64** and **70** demonstrate results comparable with 2PACz and Me-4PACz used as standards. The obtained results agree with the previously performed measurements, the QFLS values for **64** and **70** were

slightly lower than the references, yet those were compensated by better charge extraction capabilities demonstrated in trSPV measurements. The same trend can be seen for dibenzo[*b,f*]azepine **55**, which performed worse than the other materials in the batch. This lower efficiency can be directly linked to the worse results on perovskite luminescence, QFLS and trSPV measurements. Perovskite PL, QFLS and trSPV measurements are a very handy and relatively quick way to predict how new materials would perform in the solar cells without constructing the full device. Overall, the solar cell data revealed that the diphenylamine-based material **64** is the most promising for the construction of efficient and reproducible perovskite solar cells.

2.2.5. Chapter summary

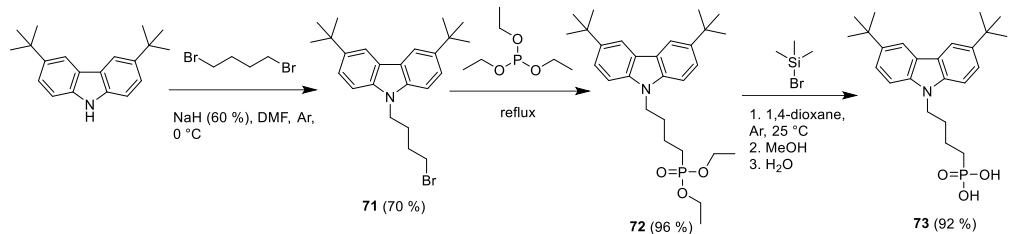
To summarize, new non-carbazole SAM molecules have been synthesized by using a variety of different chromophores, such as phenothiazine, phenoxazine, diphenylamine, 5*H*-dibenzo[*b,f*]azepine and 10,11-dihydro-5*H*-dibenzo[*b,f*]azepine. Synthesis attempts of non-substituted indole derivatives were not successful due to the reactivity at the indole 3-H position under the adopted hydrolysis reaction conditions. Compounds **58** and **61** were successfully utilized in BHJ OPVs, yielding efficiencies of 13.9% and 12.5% respectively, yet performing worse than PEDOT:PSS and halogenated SAMs (as discussed in Chapter 3.1) due to a lower ionization energy, which is not favorable if we want to achieve effective organic solar cells. Both materials were also tested in p-i-n configuration perovskite solar cells, and they demonstrated solid performance of 17.3% and 16.0% PCE, respectively. The reference 2PACz performed better (19.5%), leading to a conclusion that the efficiency of the tested materials 2PACz, **58** and **61** ($19.5\% > 17.3\% > 16.0\%$) can be directly related to descending values of their ionization potentials ($5.6 \text{ eV} > 5.44 \text{ eV} > 5.29 \text{ eV}$). Materials **55**, **64** and **70** were also investigated in p-i-n configuration perovskite solar cells ITO/SAM/Pero/C₆₀/SnO₂/Ag. Preliminary investigation indicated **64** as a most promising material, as its charge extraction speed was the best among the tested derivatives. On the other hand, **55** demonstrated the worst charge extraction capability and QFLS results among the tested materials, thus suggesting a lower performance in PSCs. These results were reflected in the device performance, where **64** demonstrated emphatically good photovoltaic characteristics as well as good reproducibility surpassing the standard material 2PACz, which indicates diphenylamine as a very promising chromophore for the synthesis of SAM molecules and integration in PSCs.

2.3. SAM Materials Containing Phosphonic Acid and Other Functional Groups

One more strategy how to broaden the range of the currently used SAM materials beyond 2PACz or Me-4PACz is to increase their functionality by incorporating additional functional groups. These groups can be used to tune the energy levels, to change the surface wetting properties, or to provide additional interaction with other device components.

2.3.1. Synthesis of compounds containing different functional groups and the phosphonic acid group

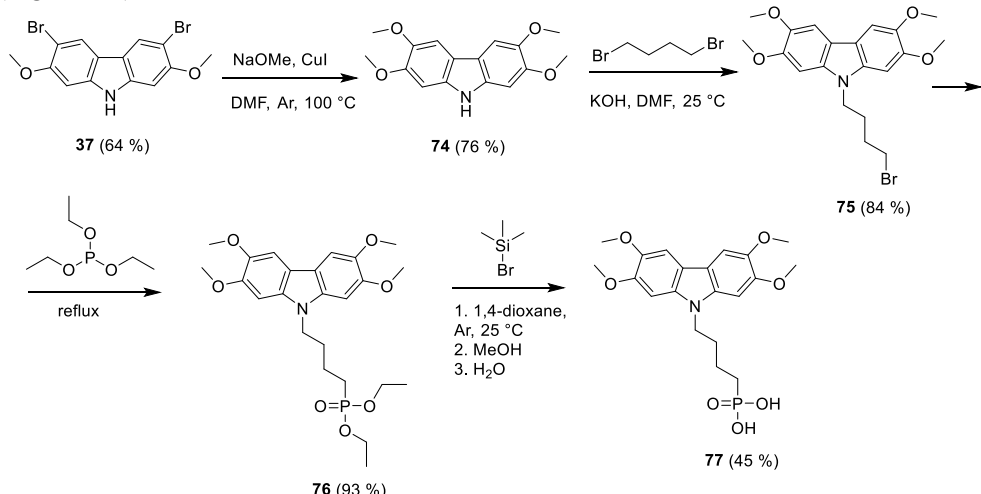
Most carbazole and phenothiazine SAMs discussed in this chapter required additional synthesis steps to isolate the desired phosphonic acid derivatives.



Scheme 2.8. Synthesis of carbazole derivative **73** containing *tert*-butyl and phosphonic acid groups

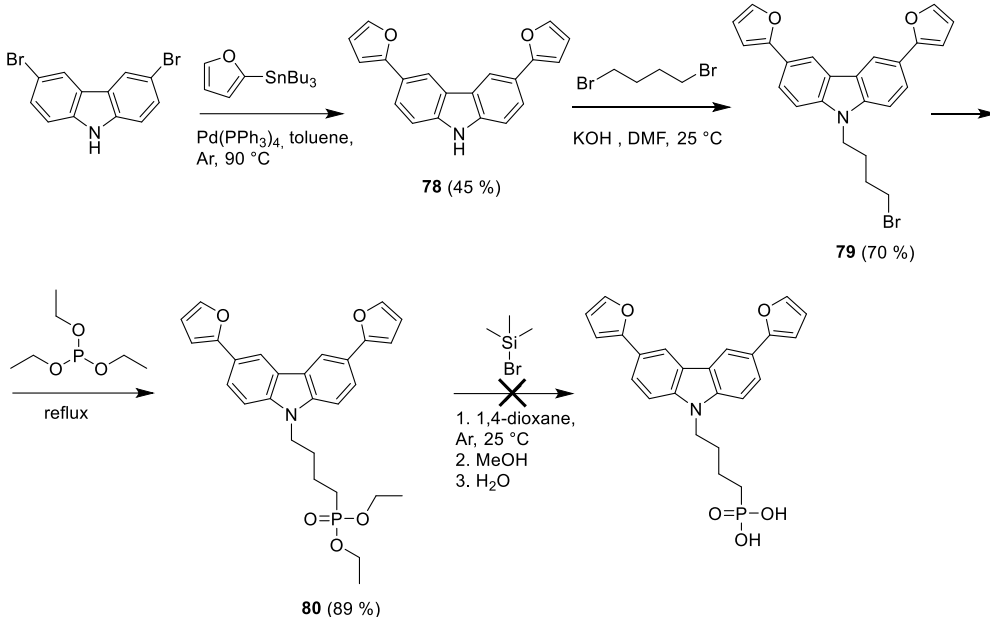
The bromobutyl moiety was introduced by the alkylation reaction using 1,4-dibromobutane and NaH 60% dispersion in mineral oil (Scheme 2.8). The formed intermediate **71** was further transformed into phosphonate **72** by using triethyl phosphite. 3,6-Di-*tert*-butylcarbazole **73** containing a phosphonic acid group was obtained *via* hydrolysis by using bromotrimethylsilane in a good yield.

Carbazole **73** excelled in terms of better solubility in organic solvents, compared to other SAM materials, and its NMR spectra were possible to be recorded using CDCl₃ as a solvent, which usually contains significantly lower amounts of water compared to DMSO-d₆. As a result, the proton signals of OH groups were visible in ¹H NMR spectra (Figure A5). For comparison purposes, NMR spectra of **73** were recorded using by DMSO-d₆, and, due to the exchange of the OH group with the water present, the proton signals of the OH group were not visible in the ¹H NMR spectra (Figure A6).



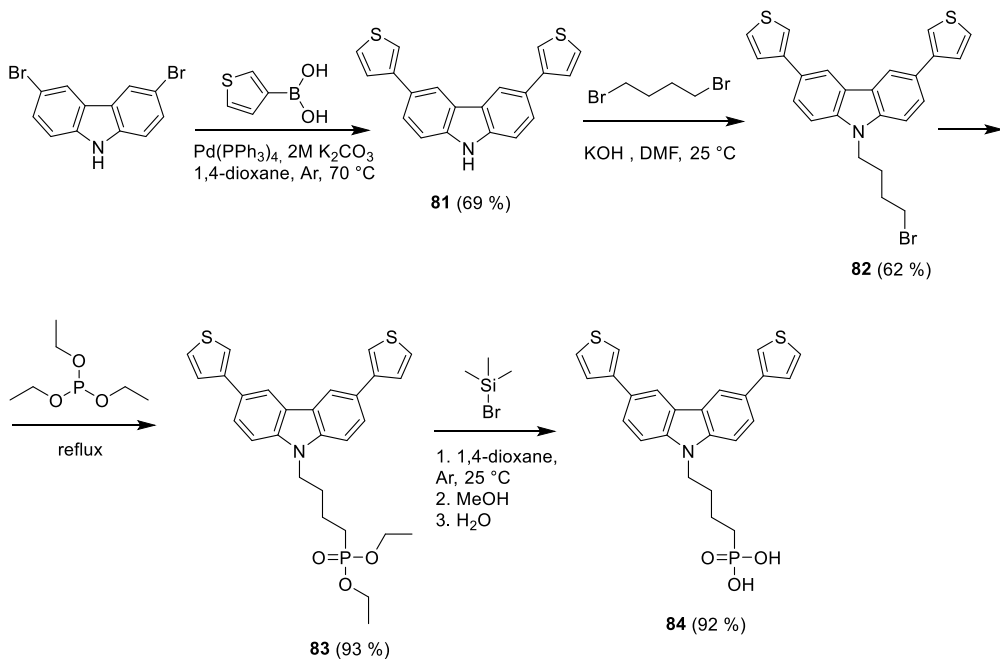
Scheme 2.9. Synthesis of carbazole **77** containing four methoxy groups and phosphonic acid

Tetra-methoxy substituted carbazole phosphonic acid was obtained *via* the intermediate carbazole **37** by using a reaction with sodium methoxide in DMF, in the presence of copper (I) iodide, resulting in 2,3,6,7-tetramethoxycarbazole **74** (Scheme 2.9). A similar 3-step alkylation/Arbuzov reaction/hydrolysis procedure was used to produce the final product **77**.



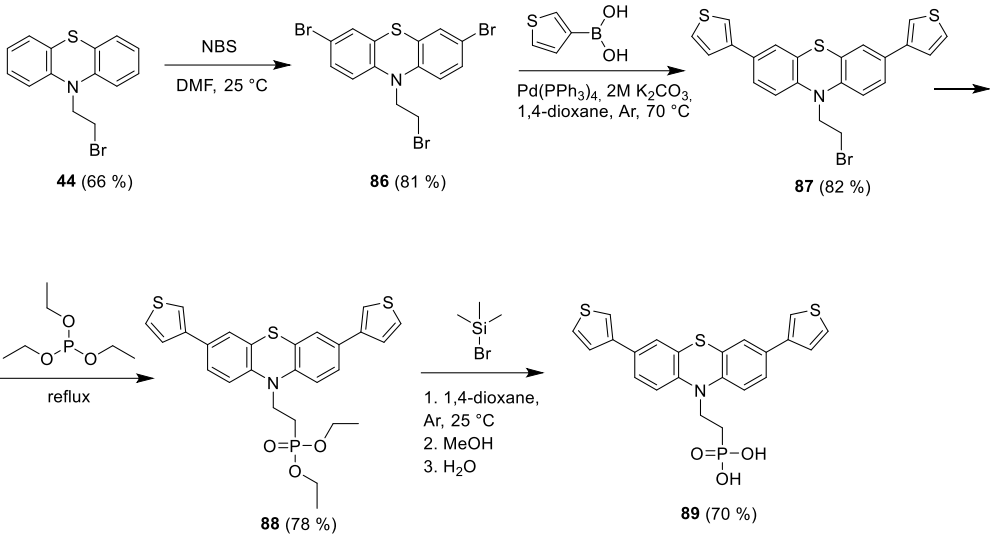
Scheme 2.10. Synthesis attempts to obtain carbazole derivative containing furan and phosphonic acid groups

The addition of furan substituents could be useful for the extension of the conjugated system of carbazole; furthermore, furane moieties could potentially interact with perovskite, similarly as thiophene-containing derivatives reported in the literature [187]. For the introduction of furan substituents (Scheme 2.10), Stille coupling was employed, by using 2-(tributylstannyl)furan and tetrakis(triphenylphosphine)palladium(0) in toluene under argon, resulting in intermediate **78**, which was further alkylated and transformed into a phosphonate derivative, thus obtaining compounds **79** and **80**, respectively. The final step of hydrolysis, however, did not go as planned, as the product was obtained as an insoluble black solid, and its structure could not be determined. This could happen due to the possible condensation of furans in the presence of hydrobromic acid which is released during the reaction as a side product [188].



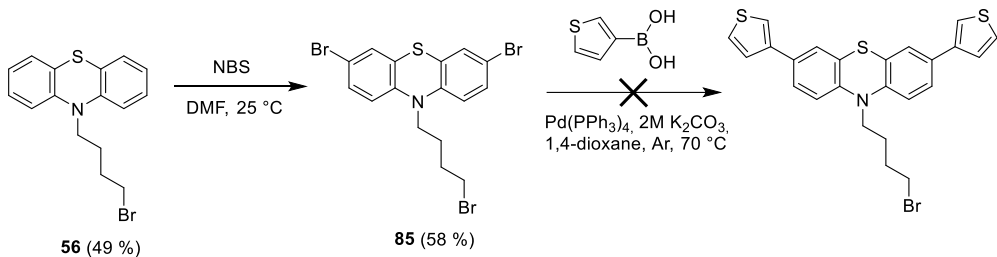
Scheme 2.11. Synthesis of carbazole derivative **84** containing thiophene and phosphonic acid groups

The similar strategy with an expanded conjugated system with additional heteroatoms able to interact with and passivate the perovskite surface was investigated further by replacing furan moieties with thiophenes. Thiophenes are known as conventional sulfur-rich functional groups providing favorable properties towards passivation interaction with perovskite [189]. A palladium-catalyzed Suzuki-Miyaura coupling reaction of 3,6-dibromocarbazole with 3-thienylboronic acid under argon in anhydrous 1,4-dioxane resulted in carbazole **81** (Scheme 2.11). The next three steps involved the previously discussed alkylation using 1,4-dibromobutane, aliphatic bromide substitution to diethyl phosphonic acid ester, and hydrolysis using bromotrimethylsilane reactions, yielding compounds **82**, **83** and the final product **84**, respectively. No deviations in the final hydrolysis step were observed, indicating that the thiophene moiety is more suitable for the synthesis of SAM materials containing the phosphonic acid group.



Scheme 2.12. Synthesis of phenothiazine derivative **89** containing thiophene and phosphonic acid groups

Phenothiazine was chosen to replace the carbazole chromophore in compound **84**, which could provide one more sulfur heteroatom in the structure [190]. Intermediate **44** was used as a starting material for the bromination reaction using NBS in dimethylformamide (Scheme 2.12). The isolated phenothiazine **86** was used for the palladium catalyzed Suzuki-Miyaura coupling reaction with 3-thienylboronic acid under argon in anhydrous 1,4-dioxane. The obtained intermediate **87** was transformed into the final product **89** containing the phosphonic acid group *via* phosphorylation and hydrolysis reactions described above.



Scheme 2.13. Synthesis attempts to obtain phenothiazine derivative containing thiophene groups

For better comparison with SAM **84**, a phenothiazine analogue was attempted to synthesize (Scheme 2.13). Starting with intermediate **56**, containing bromobutyl moiety, bromination was performed by using NBS in dimethylformamide, thus obtaining compound **85**. However, the next Suzuki-Miyaura cross-coupling reaction did not go as planned, and the desired product was not isolated.

The obtained compounds were used for further investigation to a form self-assembled monolayer on ITO. The procedure for the formation of the monolayer is provided in Section 3.1.

2.3.2. Photoelectrical properties⁷

Similarly to the previously discussed materials, the synthesized molecules containing different functional groups and a phosphonic acid group were initially investigated by measuring their ionization potential by the *photoelectron spectroscopy in air* (PESA) method.

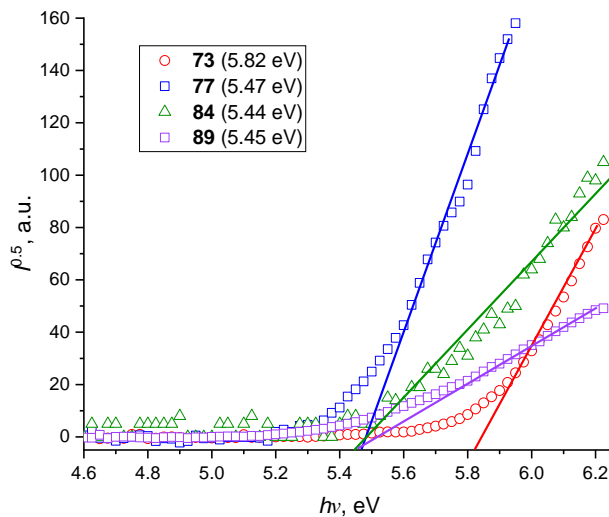


Figure 2.15. Photoemission in air spectra of SAM derivatives **73**, **77**, **84** and **89**

The measurement results are shown in Figure 2.15. Carbazole **73** demonstrated the highest I_p value (5.82 eV) among the tested materials. This was expected as compound **73** contains two *tert*-butyl groups, which minimally influence the energy levels of the molecules. It is very similar to the Me-4PACz ionization potential (5.8 eV). Other materials (i.e., **77**, **84** and **89**) possessed almost identical ionization potential values of 5.47 eV, 5.44 eV and 5.45 eV, respectively, which is significantly lower compared to carbazole **73**. All the three molecules are substituted with either electron donating methoxy or thiophene functional groups which decrease the I_p value.

⁷ The photoelectrical properties were measured at the Institute of Chemical Physics, Vilnius University, by E. Kamarauskas

2.3.3. Performance in bulk heterojunction organic solar cells⁸

Thiophene substituents containing carbazole **84** were investigated in bulk heterojunction OPVs. The schematic architecture of the device is given in Figure 2.16a and referred to as ITO/SAM/BHJ/PNDIT-F3N/Ag, where PM6:BTP-eC9 one donor one acceptor system was used for the absorber layer (see Figure 2.1 in Chapter 2.1.3).

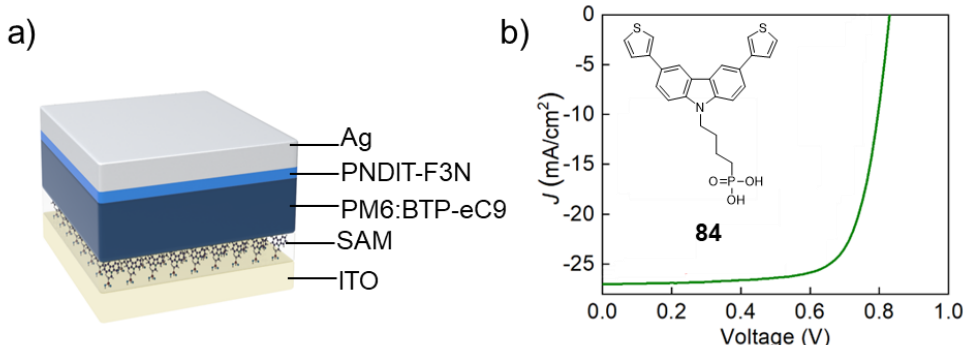


Figure 2.16. (a) Schematic architecture of the BHJ organic solar cell; (b) J - V curve of the best cell in the batch using carbazole **84**

Table 2.10. Summary of the key operating parameters of OPVs based on PM6:BTP-eC9 BHJ based on compound **84** measured under illumination of AM 1.5G (100 mW/cm²).

BHJ	HTM	V_{OC} [V]	J_{sc} [mA/cm ²]	FF [%]	PCE [%]
PM6:BTP-eC9	PEDOT:PSS	0.843	26.31	76.7	17.0
	84	0.8297	27.009	73.74	16.5

The device results reveal (Figure 2.16b and Table 2.10) that carbazole **84** demonstrates solid performance in BHJ OPVs, by reaching and efficiency of 16.5%, which is comparable to the standard PEDOT:PSS-based device PCE of 17.0%. More interestingly, compound **84** possesses a relatively low ionization potential (5.44 eV) similar to phenothiazine **58** (as discussed in Chapter 2.2.3), yet the performance is better than that of **58** (PCE=13.9%). This suggests that the energy levels are not the only important factor for the SAM hole transporting materials to be efficient in organic photovoltaics. Good performance can be related to the presence of thiophene moieties and sulfur atoms in general, as the standard HTM PEDOT:PSS also contains thiophene fragments. The absorber system in bulk-heterojunction is also sulfur-rich,

⁸ The devices were constructed and the measurements were performed at King Abdullah University of Science and Technology (KAUST), Saudi Arabia, by Prof. T. D. Anthopoulos research group

suggesting the presence of interactions between different layers, which would explain the good efficiency at a relatively low ionization potential level.

2.3.4. Performance in perovskite solar cells

Carbazole **73** containing *tert*-butyl substituents was used for a rather different investigation. Among SAM materials widely adopted by the community, Me-4PACz (Figure 2.17a) was able to provide the best enhancement to charge extraction compared to other materials, such as 2PACz and MeO-2PACz. However, its wider use is hindered by a rather high surface hydrophobicity, and, as a consequence, poor coverage by the perovskite precursor solution [191]. Ideally, the manufacturing of solar cells should be reliable and simple, yet, due to the poor wettability of ITO modified with Me-4PACz, the perovskite layer deposition is complicated, and its quality may uncontrollably vary. Therefore, it is usually hard to achieve good reproducibility from lab to lab, and even within the same lab.

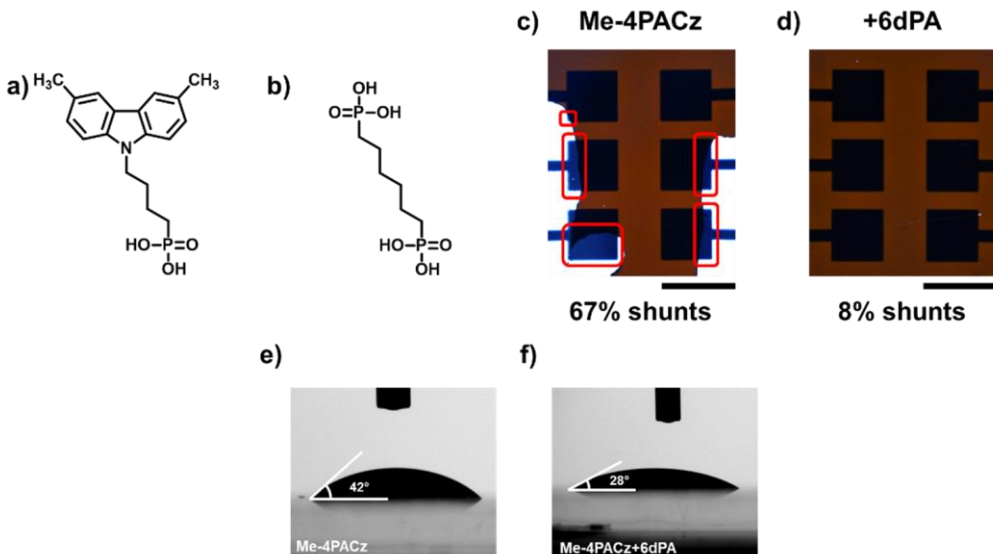


Figure 2.17. Chemical structures of the materials used for the formation of monolayers: (a) Me-4PACz and (b) 6dPA. Close-up optical images of the representative PSCs with (c) Me-4PACz and (d) Me4-PACz+6dPA selective contact layer. Highlighted in red are the active cell areas not covered by perovskite film. Scale bar = 5 mm. (e, f) Optical images of the contact angle measurements were made by using triple-cation perovskite precursor solution on top of ITO/ monolayer substrates

A simple way to overcome the Me-4PACz limitation is the addition of commercially available 1,6-hexylenediphosphonic acid (6dPA) (Figure 2.17b) as a second component to the Me-4PACz precursor solution. Devices using Me-4PACz monolayers and triple-cation perovskite were fabricated in order to evaluate the yield of the working devices. A photograph of a representative substrate is shown in Figure

2.17c. By measuring the J/V data of the Me-4PACz-based cells, it was determined that 67 % of the pixels were shunted (i.e., they had V_{OC} values significantly lower than 1 V). After the addition of 6dPA (20 mol%), this limitation was almost fully resolved, as the wetting of monolayer-covered ITO was substantially improved from 42° to 28° (see Figures 2.17e and 2.17f), leading to only 8% of shunts (Figure 2.17d).

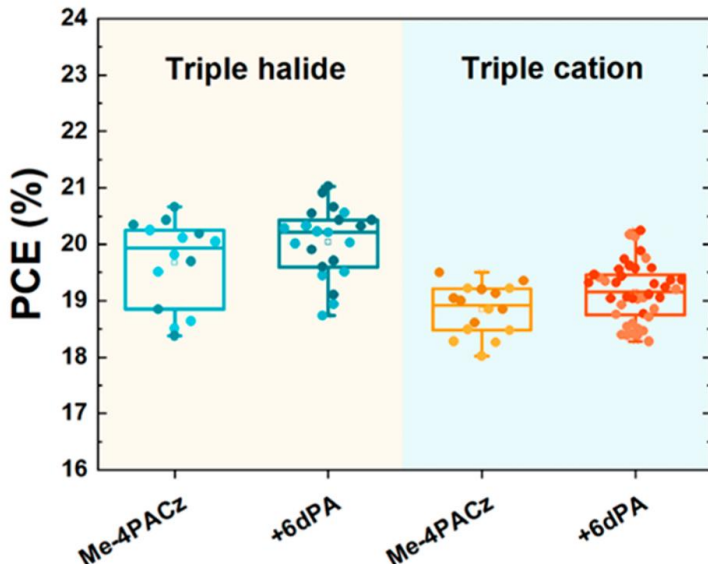


Figure 2.18. Statistical distribution of the PCE (reverse scan – darker color, forward scan – lighter color) for a device with pure Me-4PACz and mixed monolayer with two different perovskite compositions (shunted devices were excluded from this analysis)

The influence of the 6dPA additive on the performance of solar cells was checked by fabricating p-i-n perovskite solar cells with an ITO/SAM/Perovskite/LiF/C₆₀/BCP/Ag architecture⁹. Two popular perovskite compositions were used, known as ‘triple-cation’ ($FA_{0.79}MA_{0.16}Cs_{0.05}Pb(I_{0.83}Br_{0.17})_3$) [192] and ‘triple-halide’ ($FA_{0.75}Cs_{0.22}MA_{0.03}Pb(I_{0.82}Br_{0.15}Cl_{0.03})_3$) [193]. Clearly, the addition of 6dPA had no negative effect on the device performance (Figure 2.18), and both average and best pixels had slightly higher values with the mixed monolayer. The highest efficiency of 20.9% was achieved by the devices fabricated with triple-halide perovskite and a mixed Me-4PACz+6dPA monolayer.

⁹ The devices were constructed and the measurements were performed at Helmholtz-Zentrum Berlin (HZB), Germany, by Prof. S. Albrecht research group, and at the University of Colorado Boulder, Colorado, USA, by Prof. M. D. McGehee research group

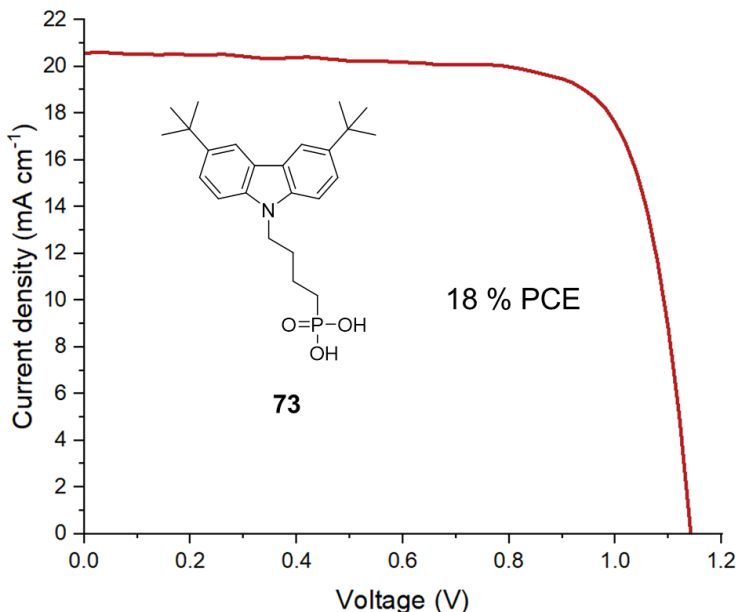


Figure 2.19. Reverse scan of the best pixel for the devices, fabricated by using carbazole **73**+6dPA monolayer

As additional proof of the significant effect of the additive on the manufacturability of PSCs, devices using the synthesized compound **73** with bulky aliphatic *tert*-butyl groups instead of methyl (Figure 2.19-inset) were investigated. Previous attempts to fabricate devices with this material were hindered by the very poor wettability of the substrate by the perovskite solution. However, by adding 6dPA, it was possible to get working devices with PCE as high as 18% (Figure 2.19). Despite the lower FF values, this example demonstrates the possibility of further expanding the structural optimization of SAM-based hole transporting materials.

Two perovskite ‘triple-cation’ ($\text{FA}_{0.79}\text{MA}_{0.16}\text{Cs}_{0.05}\text{Pb}(\text{I}_{0.83}\text{Br}_{0.17})_3$) and ‘triple-halide’ ($\text{FA}_{0.75}\text{Cs}_{0.22}\text{MA}_{0.03}\text{Pb}(\text{I}_{0.82}\text{Br}_{0.15}\text{Cl}_{0.03})_3$) compositions were also used to construct PSCs for the investigation of the carbazole-based compound **84**, containing thiophene functional groups. The new material was compared to references from the same family 2PACz and Me-4PACz with the objective to evaluate the influence of thiophenes for the passivation of the perovskite interface.

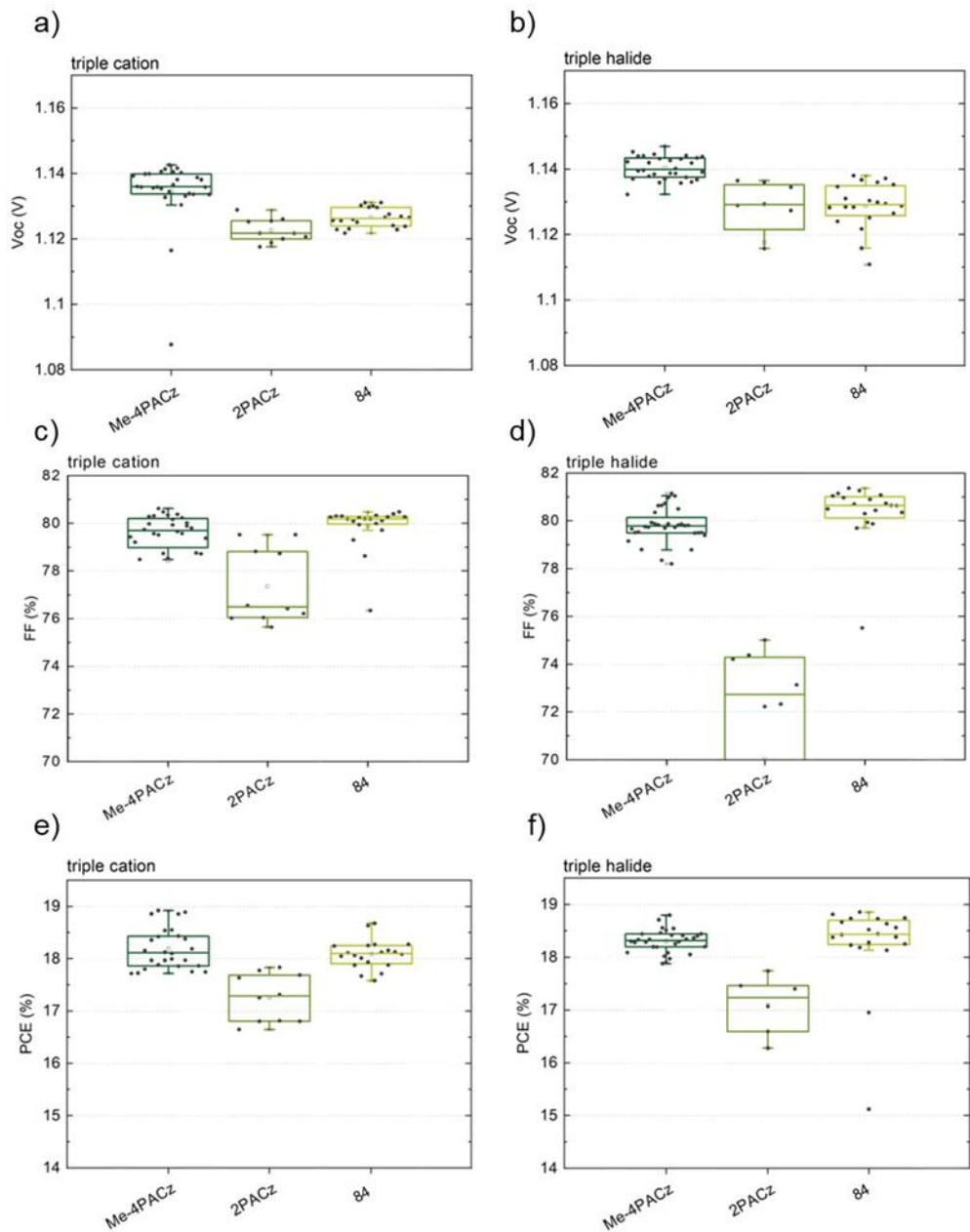


Figure 2.20. Photovoltaic characteristics of p-i-n architecture perovskite solar cells, utilizing different perovskites and comparing different HTMs used as SAMs: (a) V_{oc} statistical results; (b) J_{SC} statistical results; (c) Fill factor statistical results; (d) Efficiency statistical results

The device testing results are shown in Figure 2.20. Overall, the results revealed that 2PACz, which is considered one of the best performing SAM materials, was outperformed by both reference Me-4PACz and thiophene containing carbazole derivative **84**, especially in the ‘triple halide’ composition (Figure 2.20d and 2.20f). Compound **84** demonstrated the best FF results, combined with good reproducibility. The good fill factor was reflected in the efficiency results, where compound **84** demonstrated a similar PCE in ‘triple cation’ cells (18.27%) or slightly better PCE values in ‘triple halide’ cells (18.81%) compared to Me-4PACz PCE of 18.36% and 18.55%, respectively (Figure 2.20e, 2.20f, and Figure A3). It is of interest to note that, given the correlation between the ionization potential and PCE observed in Chapter 2.2.3, it could be expected that carbazole **84** would be less efficient due to its lowest I_p (5.44 eV) among the materials tested. However, it shows a better efficiency than 2PACz which has an I_p of 5.6 eV and similar efficiency to Me-4PACz which has an I_p of 5.8 eV [194], thereby suggesting that additional interactions, such as perovskite passivation, can indeed take place, resulting in an increased PCE. It is also worth noting that the monolayer of **84** was formed as it is, without using 6dPA, yet the wettability was sufficient for the deposition of the perovskite layer.

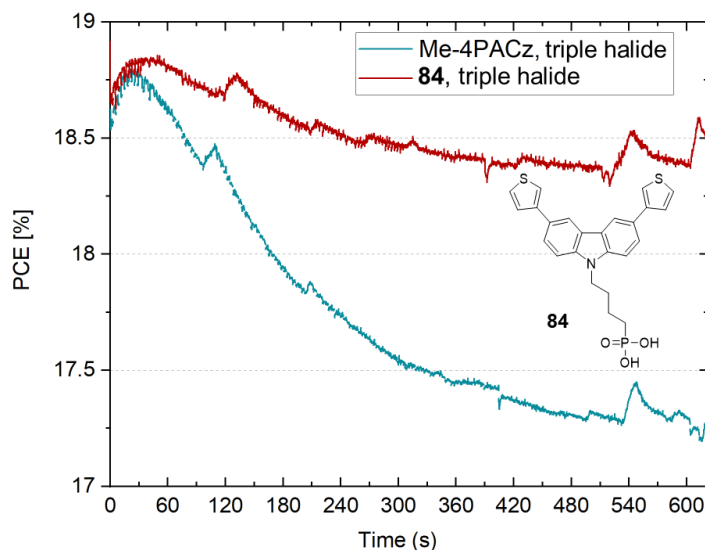


Figure 2.21. Stability experiment of PSCs based on triple halide perovskite and Me-4PACz or compound **84** as HTM

The initial investigation of the device stability by using carbazole **84** and Me-4PACz was conducted under continuous illumination (Figure 2.21). One pixel of each cell was measured, and the preliminary results give very interesting observations. After the first minute, the Me-4PACz-based cell started losing its efficiency, and 10 minutes later, it retained ~92 % of the initial PCE. Meanwhile, the SAM **84**-based cell showed better stability under illumination, its degradation was slower, and the cell retained ~98 % of the initial PCE after 10 minutes of illumination. The improved stability of the cell can be also related to the passivation effect of the SAM being used.

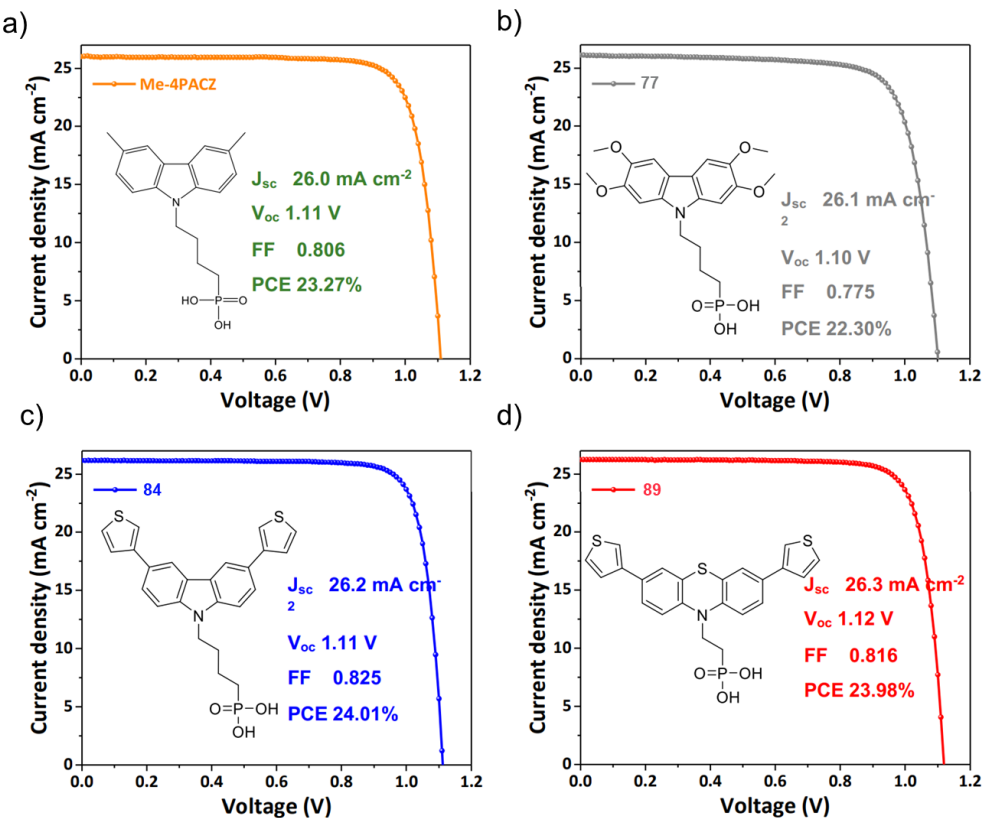


Figure 2.22. J - V curves and photovoltaic characteristics¹⁰ of the best cells in the batch when using Me-4PACz, and SAM derivatives **77**, **84** and **89**

Thiophene containing carbazole derivative **84**, along with the synthesized materials **77** and **89**, were also investigated in p-i-n perovskite solar cells. Preliminary results of the devices are given in Figure 2.22. All cells exceeded the benchmark of 22% efficiency, which indicates good quality and compatibility of the layers being used in the PSC architecture. Tetra methoxy-substituted carbazole **77** demonstrated a lower PCE value of 22.30% compared to Me-4PACz (23.27% PCE). Both **84** and **89** outperformed the standard Me-4PACz by demonstrating PCE of 24.01% and 23.98% respectively. This result could serve as one more indication of an improved interaction between thiophene containing SAMs and perovskite.

2.3.5. Application in gas sensors based on ZnO tetrapods

Carbazole **77** found its application in a relatively scarcely explored field of modified metal oxides sensors. Compared to the regular ZnO, which generally

¹⁰ The devices were constructed and the measurements were performed at École polytechnique fédérale de Lausanne (EPFL), Lausanne, Switzerland, by M. K. Nazeeruddin research group

operates at elevated temperatures, zinc oxide tetrapods (ZnO-T) demonstrate an extremely high sensitivity at ambient temperature [195] due to their large surface-to-volume ratio. High temperatures are incompatible with flexible polymer substrates and also can cause stability issues of the sensor material. Further metal oxide sensor functionalization with organic functional materials can lead to gas sensing with high responsivity, stability, selectivity, as well as fast response, while working in *room temperature* (RT) at a low cost [196]. Up to now, the majority of works have been focusing on alkyl silane SAMs [197] since these structures and their deposition methods are well established, although their influence on the surface energetics is limited due to the lack of conjugated electron acceptor or donating systems. Therefore, the potential of semiconductive compound **77** in chemoresistive sensing was investigated by using it to modify the ZnO-T surface and to construct a gas sensor device.

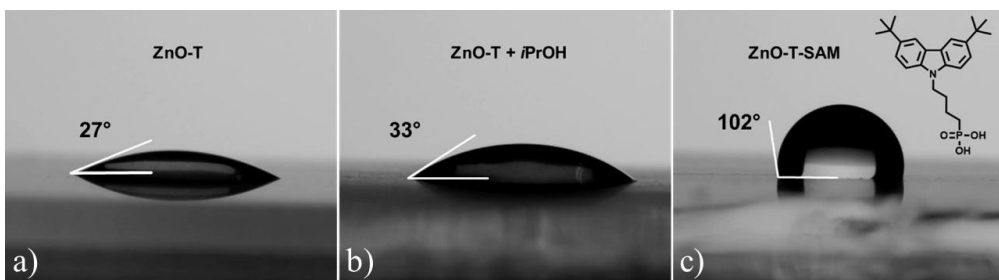


Figure 2.23. Contact angle measurements of water on non-modified and modified ZnO-T surfaces.

Contact angle measurement was performed to evaluate the attaching capability of carbazole-based SAM **77** onto the ZnO-Ts surface. ZnO-Ts were modified by using the dip-coating method and the results of the water droplet contact angle compared with the surfaces of bare ZnO-Ts, additionally, in order to determine the effect of the solvent in use, ZnO-Ts treated with *i*PrOH were also tested. The obtained results (Figure 2.23) demonstrate more than three-fold increase in the contact angle after SAM deposition (102°), compared with non-modified ZnO-T samples (27° and 33°), which indicates that the carbazole-based SAM containing phosphonic acid functional group can bind to the surface of ZnO-Ts. Furthermore, a significant difference in the contact angles, where *tert*-butyl substituents of compound **77** play a major role in the hydrophobicity increase, suggests good SAM coverage.

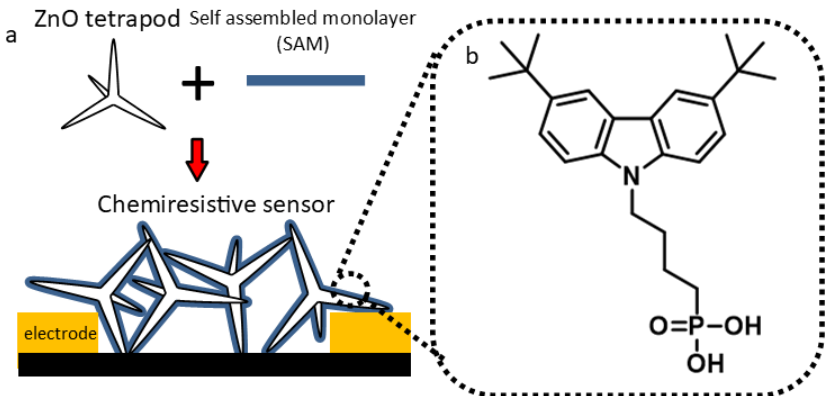


Figure 2.24. Schematic of ZnO tetrapods (ZnO-Ts) with a self-assembled monolayer of carbazole derivative: a) chemoresistive sensor schematics; b) Carbazole-based SAM structure.

The schematic of the sensor made of ZnO tetrapods with a self-assembled monolayer of **77** is presented in Figure 2.24. The electrodes are made of gold sputter-deposited on glass, forming polygons measuring 3x5mm, which are separated by gaps of 1, 3, 5, 10, and 15 micrometers. The gap of 3 μm was used in this experiment.

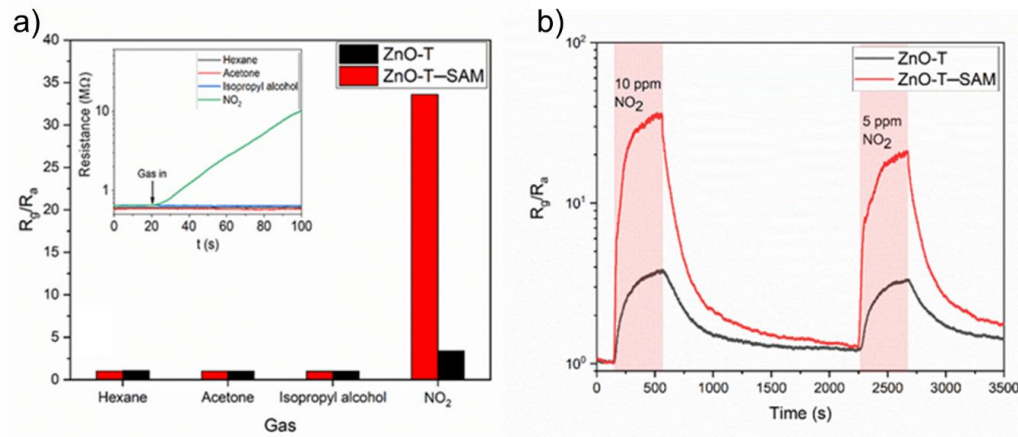


Figure 2.25. Characterization of ZnO-T and ZnO-T with SAM sensors: a) Response to VOCs and gases at 10 ppm; b) Response and recovery at different NO_2 concentrations

The characteristics of the sensors with ZnO-T and ZnO-T with SAM were assessed, involving the evaluation of their optoelectronic properties and responses to a spectrum of gases. This analysis encompassed *volatile organic compounds* (VOCs) acetone, hexane, and isopropyl alcohol, as well as oxidative gas NO_2 . Both ZnO-Ts and ZnO-T-SAM showed a minimal response to VOC, whereas the response to NO_2 at 10 ppm was an order of magnitude more intense for ZnO-T-SAM (Figure 2.25a).

The sensitivity to NO_2 was enhanced nearly tenfold by depositing compound 77 SAM onto ZnO-Ts. This improvement may be attributed to the interaction of a carbazole-based derivative with NO_2 , or to the formation of a conformal dense coating that potentially functions as a molecular sieve. While the response to NO_2 was nearly instantaneous, as depicted in Figure 2.25b, taking only a few seconds, the recovery process was sufficiently slow, requiring tens of minutes.

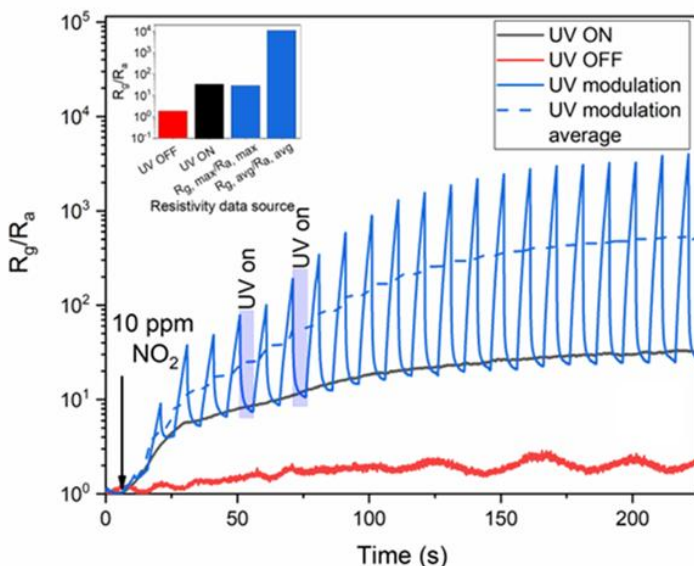


Figure 2.26. ZnO-T sensor response at RT. ZnO-T with SAM under different UV conditions: UV illumination (UV ON), dark (UV OFF) and UV modulation with 10 s period and 50 % duty cycle

In order to enhance the gas sensing response, UV modulation was employed, which involves cycling the UV irradiation on and off at one-second intervals. This dynamic process could be used to stimulate the gas adsorption and desorption processes on the surface. By allowing the system to reach new equilibrium, the measurement under UV modulation effectively improves gas sensitivity. Figure 2.26 illustrates the response of ZnO-Ts functionalized with compound 77 SAM to 10 ppm NO_2 at RT under various UV conditions. The dotted line marks the average of the UV modulated response, which is calculated by averaging the maximum values at UV off ($R_{g,\max}$) and the minimum values at UV on ($R_{g,\min}$). The lowest response of 1.9 to NO_2 occurs under dark conditions without UV illumination, which increases 17-fold when UV is turned on throughout the measurement, until reaching 33.6. This enhancement is attributed to UV activation, facilitating adsorption-desorption reactions on the surface.

2.3.6. Chapter summary

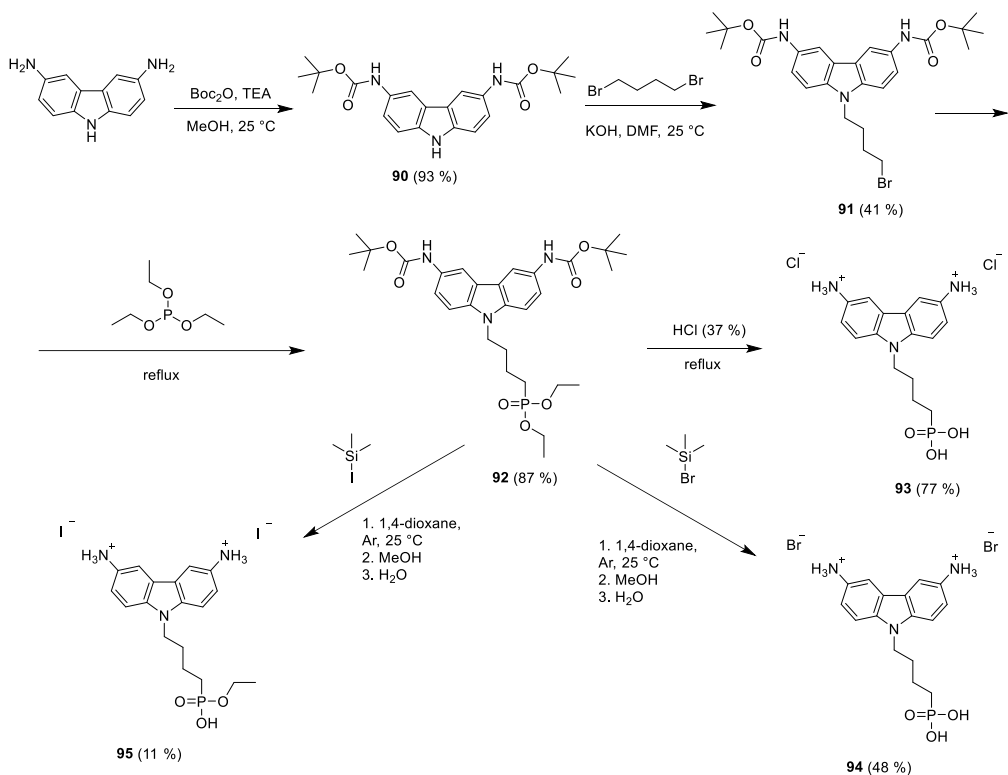
To summarize the chapter, new carbazole and thiophene-based SAM molecules containing *tert*-butyl, methoxy or thiophene functional groups have been synthesized. A synthesis attempt of a substituted furan containing phosphonic acid derivative was not successful, due to the furan ring reactivity under hydrolysis reaction conditions. A simple and easy-to-implement method to SAM-modified ITO wettability issues has been demonstrated, associated with a monolayer formed from Me-4PACz. The addition of 6dPA to the monolayer precursor solution improves the wettability of the substrate by the perovskite solution while maintaining the performance of the devices. By adding 6dPA, it was possible to get working devices by using carbazole **73** containing bulky aliphatic *tert*-butyl groups. Compounds **84** and **89** demonstrated top-tier performance in PSCs, reaching a PCE up to 24.01% and 23.98% respectively, indicating thiophenes as promising functional groups for various photovoltaic applications due to their ability to passivate the perovskite surface or interact with OPV absorbers. Carbazole SAM **73** with *tert*-butyl groups was used for the modification of ZnO tetrapods to be used in the development of efficient room-temperature gas sensors. This strategy is highly promising as the SAM functionalisation improves the selectivity towards NO₂ compared to the unmodified ZnO-T, and it can be further enhanced by using UV modulation.

2.4. SAM Materials Containing Phosphonic Acid Functional Groups and Ammonium Functional Groups

One more strategy presented in this work to increase the functionality of SAM materials containing a phosphonic acid group was to incorporate ammoniums as functional groups. Ammonium groups are known as one of the best perovskite defects passivating agents [198]. Therefore, molecules with these moieties would be able to interact both with metal oxide and perovskite layers, which could lead to an improved PSC efficiency and a long-term stability.

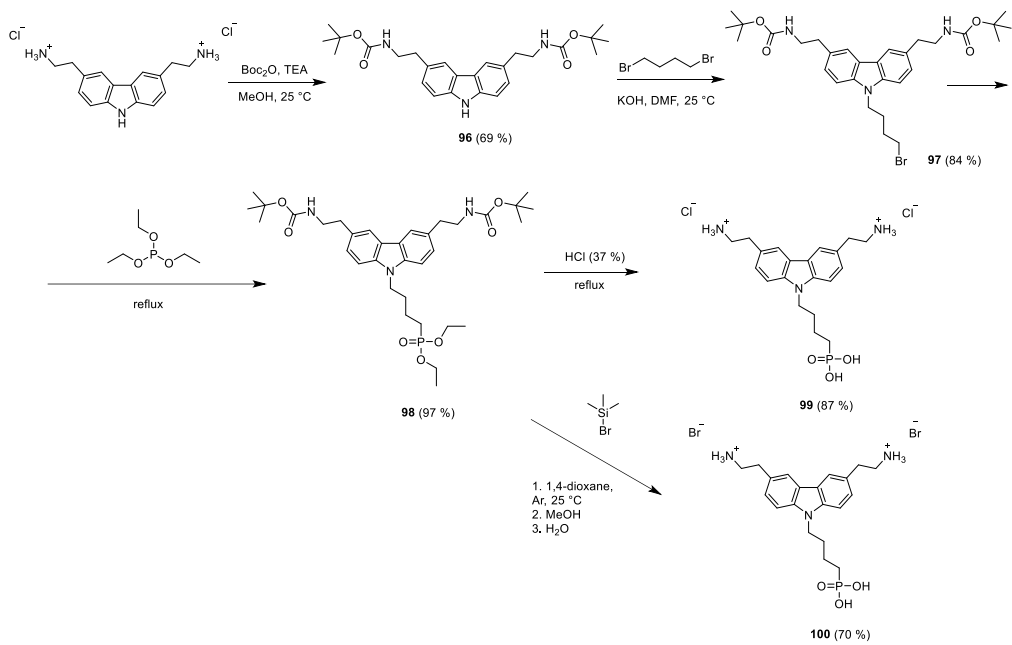
2.4.1. Synthesis of compounds containing ammonium groups and phosphonic acid

Carbazole- and indole-based SAM materials containing ammonium groups have been synthesized by first protecting amino groups of the starting materials by using *tert*-butyloxycarbonyl (Boc), and afterwards by employing a 3-step alkylation/Michaelis-Arbuzov/hydrolysis reactions sequence. Different hydrolysis reaction conditions were applied in order to obtain the final products containing different anions.



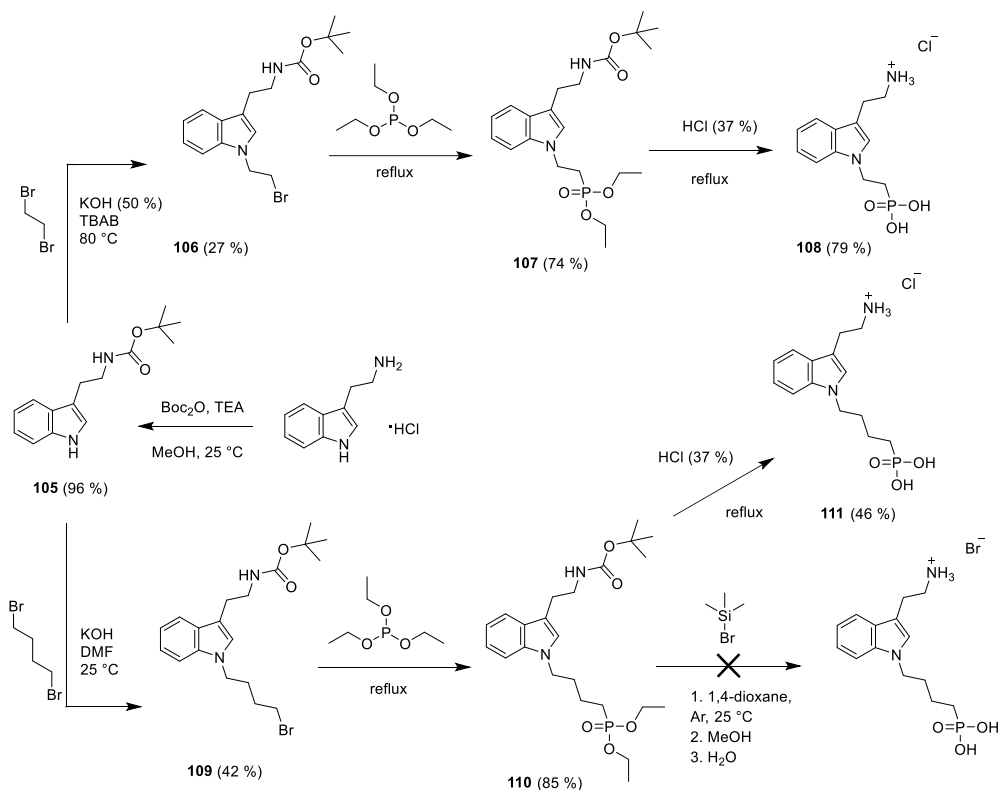
Scheme 2.14. Synthesis of carbazole derivatives containing aromatic ammonium and phosphonic acid groups

Carbazole-3,6-diamine reacted with di-*tert*-butyl dicarbonate in methanol, in the presence of triethylamine, forming the 3,6-*N*-Boc protected carbazole derivative **90** (Scheme 2.14). The further alkylation reaction using 1,4-dibromobutane and KOH in DMF was successful; however, intermediate **91** was obtained in a moderate yield (41 %), which is related to an increased chance of byproduct formation in the presence of an aromatic carbamate group. An attempt to synthesize phosphonate **92** also resulted in an unsatisfactory yield (43%); therefore, the reaction conditions were changed by reducing the Michaelis-Arbuzov reaction duration to 4 hours (instead of conducting it overnight), which resulted in the doubling of the reaction yield (87 %). For the final hydrolysis step, three different agents were used, specifically, concentrated hydrochloric acid, bromotrimethylsilane, and iodotrimethylsilane. The latter was not able to fully hydrolyze the diethyl phosphonic acid group and the isolated product **95** had one ethyl group remaining (Figure A7). Compounds **93** and **94** were synthesized successfully. They, contained ammonium groups along with chlorine and bromine anions, respectively.



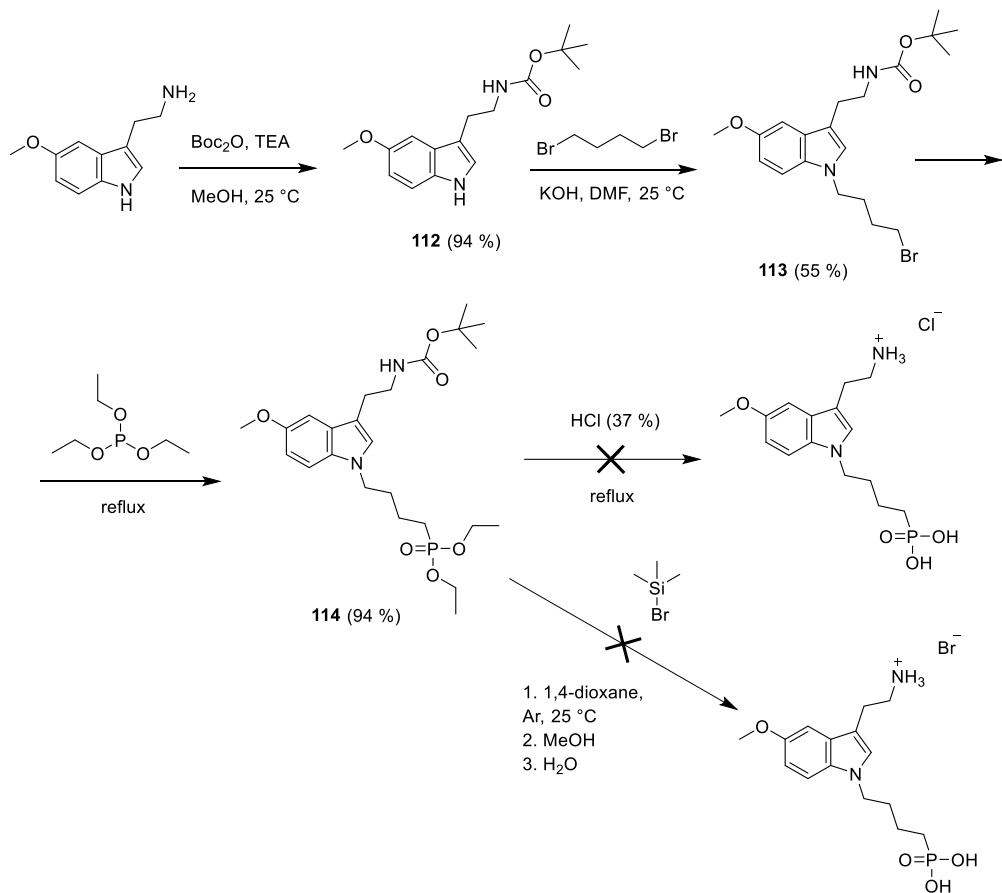
Scheme 2.15. Synthesis of carbazole derivatives containing non-aromatic ammonium and phosphonic acid groups

In order to obtain carbazole-based SAMs containing ammonium functional groups withdrawn from the central carbazole chromophore, carbazole-3,6-diethanamine dihydrochloride was used as a starting material. It was protected by using di-*tert*-butyl dicarbonate, alkylated by using 1,4-dibromobutane, phosphorylated and hydrolyzed by using either concentrated hydrochloric acid or bromotrimethylsilane, similarly to the previously synthesized materials **93** and **94**, which resulted in intermediates **96**, **97**, **98** and the final products **99**, **100** (Scheme 2.15).



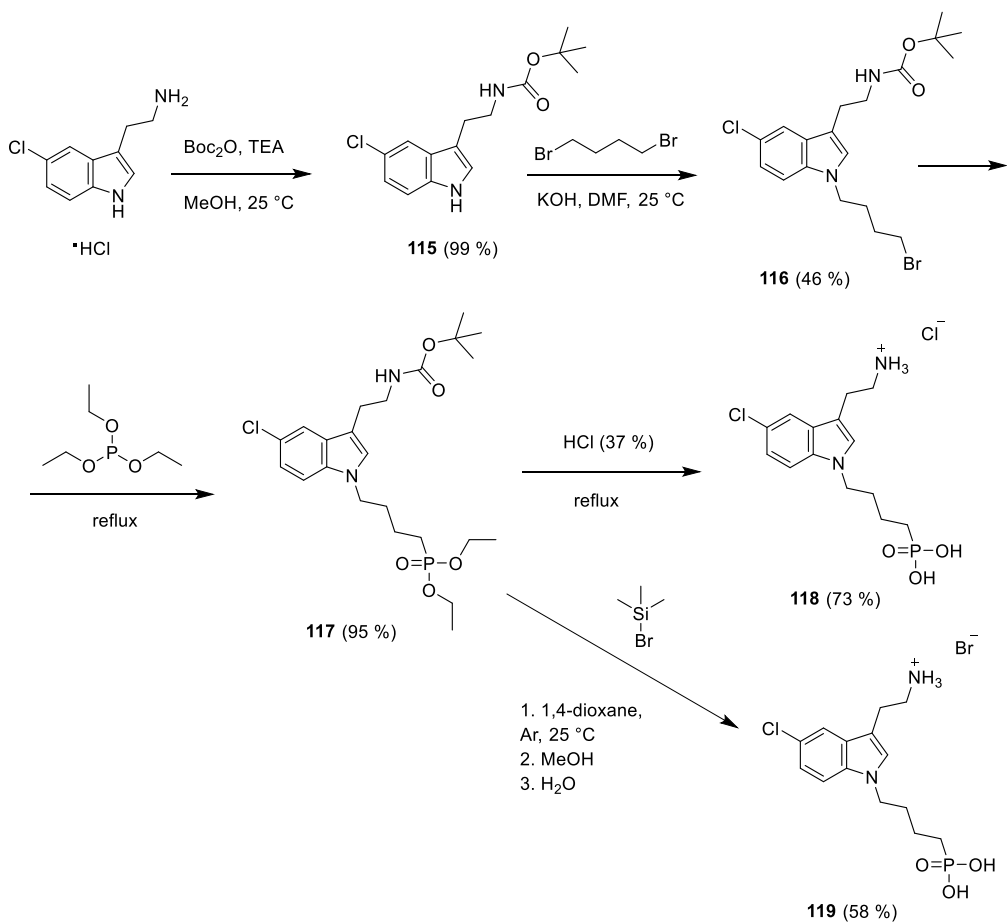
Scheme 2.16. Synthesis of indole derivatives containing non-aromatic ammonium and phosphonic acid groups

The same 4-step procedure was applied for the synthesis of functionalized indole-based SAMs, where the 3-H position would be substituted with an amino ethyl aliphatic chain (Scheme 2.16). Tryptamine hydrochloride reacted with di-*tert*-butyl dicarbonate in methanol, in the presence of triethylamine, forming *N*-Boc protected indole derivative **105**, which was further alkylated by introducing either bromoethyl or bromobutyl moieties, resulting in intermediates **106** and **109**, respectively. By reacting with triethyl phosphite phosphonates **107** and **110** were isolated. The hydrolysis reaction of both intermediates was successful, however, only when using concentrated hydrochloric acid, which resulted in products **108** and **111**. The hydrolysis of intermediate **110** using bromotrimethylsilane, in order for the final product to contain a bromine anion, was not very successful, due to the formed inseparable byproducts.



Scheme 2.17. Synthesis attempts to obtain methoxy-substituted indole derivatives containing non-aromatic ammonium and phosphonic acid groups

To expand the variety of indole-based SAMs containing a non-aromatic ammonium group, and to tune the energy levels of the molecule, 5-methoxytryptamine was chosen for the further synthesis. The starting material was protected with a Boc group, alkylated, and transformed into diethyl phosphonic acid ester, which resulted in intermediates **112**, **113** and **114**, respectively (Scheme 2.17). Phosphonate **114** was hydrolyzed by two different methods, either by using concentrated hydrochloric acid or bromotrimethylsilane. Both reactions resulted in a mixture of inseparable byproducts, and ¹H and ¹³C NMR analysis of the obtained mixture revealed that methoxygroups did not withstand the hydrolysis reaction conditions as their signals were missing from the spectra. This may explain why additional reactions could occur, with the methoxy substituent acting as a leaving group creating a reactive site. Such reactivity may be specifically related to methoxy-substituted indole derivatives as carbazole or triphenylamine SAM molecules containing methoxy groups were successfully synthesized under exactly the same conditions by using bromotrimethylsilane [8,121].



Scheme 2.18. Synthesis of chlorine-substituted indole derivatives containing non-aromatic ammonium and phosphonic acid groups

For the final group of indole derivatives, essentially, an opposite strategy was chosen, as 5-chlorotryptamine functionalized with an acceptor chloride group instead of a donor methoxy group was used a starting material. *N*-protection when using *di-tert*-butyl dicarbonate, alkylation with 1,4-dibromobutane and Arbuzov reactions were conducted to obtain intermediates **115**, **116** and **117**, respectively (Scheme 2.18). The latter was successfully hydrolyzed under two different conditions, using either hydrochloric acid or bromotrimethylsilane, resulting in products **118** containing ammonium chloride and **119** comprising ammonium bromide groups. Based on the result, the acceptor substituent in the indole chromophore allows to withstand different hydrolysis conditions.

The obtained compounds were used for the further investigation to form a self-assembled monolayer on ITO. The procedure of the formation of the monolayer is outlined in Section 3.1.

2.4.2. Photoelectrical properties

To evaluate the energy levels of SAM materials containing ammonium groups, the ionization potential (I_p) was measured in the solid-state by using the *photoelectron spectroscopy in air* (PESA) method. Examples of I_p graphs can be seen in the figures below (see Figure 2.27 and Figure 2.28).

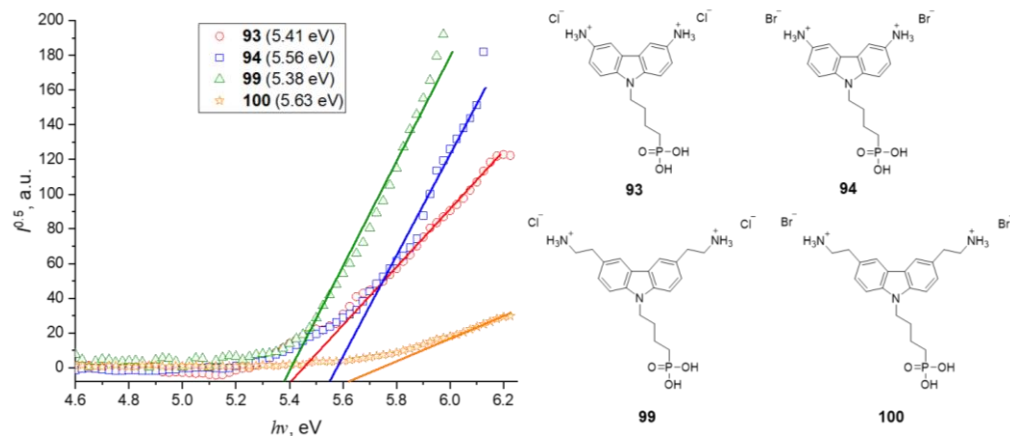


Figure 2.27. Photoemission in air spectra of SAM derivatives **93**, **94**, **99** and **100**

The obtained results reveal that carbazole derivatives **93** and **99** containing ammonium chloride groups possess very similar ionization potential values of 5.41 eV and 5.38 eV, respectively (Figure 2.27), although the ammonium group in **93** is aromatic, while **99** features an aliphatic one. The same trend applies to materials **94** and **100** containing bromide anions, which demonstrate relatively similar I_p values of 5.56 eV and 5.63 eV, respectively, and are on par with 2PACz (5.6 eV). Based on the obtained results, the type of the halogen anion exerts a bigger impact on the ionization potential compared to the distance of the ammonium group from the aromatic system of carbazole.

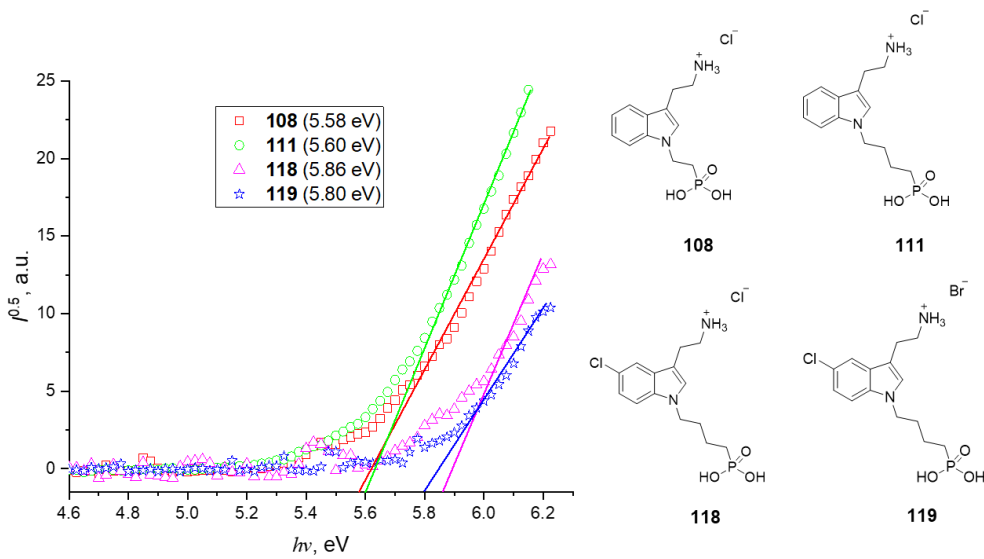


Figure 2.28. Photoemission in air spectra of SAM derivatives **108**, **111**, **118** and **119**

Indole-based materials **108** and **111** also demonstrate almost identical I_p values of 5.58 eV and 5.60 eV, which are also on par with 2PACz, thereby indicating the minimal influence of the aliphatic chain length on the energy levels. **118** and **119** demonstrated a rather different behavior compared to the carbazole analogues, as the difference in I_p was insignificant, and the bromide anion containing derivative **119** resulted in a slightly lower I_p value (5.80 eV) than its analogue **118** with a chloride anion (5.80 eV). Nevertheless, the energy levels were slightly higher in general, due to the presence of a chloride substituent, and, overall, the energy levels are very similar to those of Me-4PACz (5.80 eV).

2.4.3. Ionic SAM performance in NBG Pb-Sn perovskite solar cells¹¹

Carbazole **94** containing ammonium groups with bromide anions was tested in narrow-bandgap (NBG) perovskite solar cells. To achieve an NBG of 1.24 eV, devices of the ITO/SAM/Cs_{0.05}FA_{0.70}MA_{0.25}Sn_{0.5}Pb_{0.5}I₃/C₆₀/BCP/Ag architecture (Figure 2.29a) were constructed, in which, Pb was mixed with Sn at a 1:1 ratio. 2PACz and MeO-2PACz were used as reference SAM materials (Figure 2.29b).

¹¹ The devices were constructed and the measurements were performed at King Abdullah University of Science and Technology (KAUST), Saudi Arabia, by Prof. S. De Wolf research group

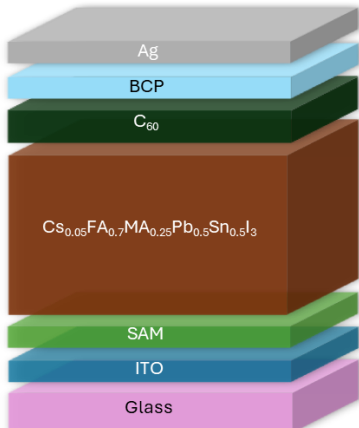
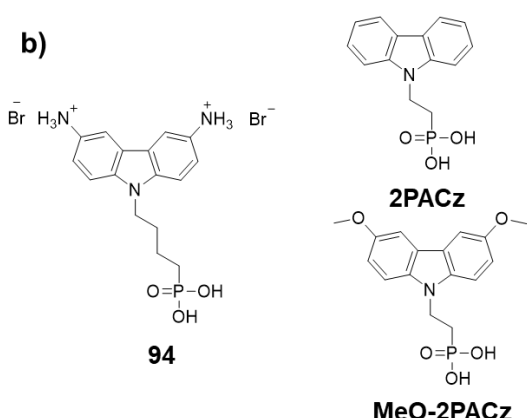
a)**b)**

Figure 2.29. (a) Sn-Pb based PSC architecture; (b) Chemical structures of the materials used for the formation of the monolayers

The statistical photovoltaic parameters of the constructed devices are shown in Figure 2.30. Devices with carbazole **94** demonstrated significantly higher V_{OC} and FF values with less deviation compared to devices with 2PACz and MeO-2PACz. The improvement in the average V_{OC} goes from 0.83 V and 0.81 V for 2PACz and MeO-2PACz, respectively, to 0.88 V for compound **94**. An increase in the FF of the cells from 76% and 73% for 2PACz and MeO-2PACz, respectively, allows reaching 82% for compound **94**. As a result, the champion device with **94** SAM exhibited a PCE of 23.0%, which is comparable to the state-of-the-art narrow bandgap Pb-Sn PSCs. This excellent performance is related to perovskite buried interface passivation via the carbazole **94** ammonium bromide moiety. This ionic moiety can easily dissociate into an ammonium cation ($-NH_3^+$) attached to the SAM surface which passivates perovskite A-site cation defects and bromide anion (Br^-) that can freely occupy iodide defects at the corners of the octahedra. Such a multifunctional passivation effect ultimately enhanced the V_{OC} of the devices by decreasing the interfacial charge trap density and reducing the non-radiative recombination losses.

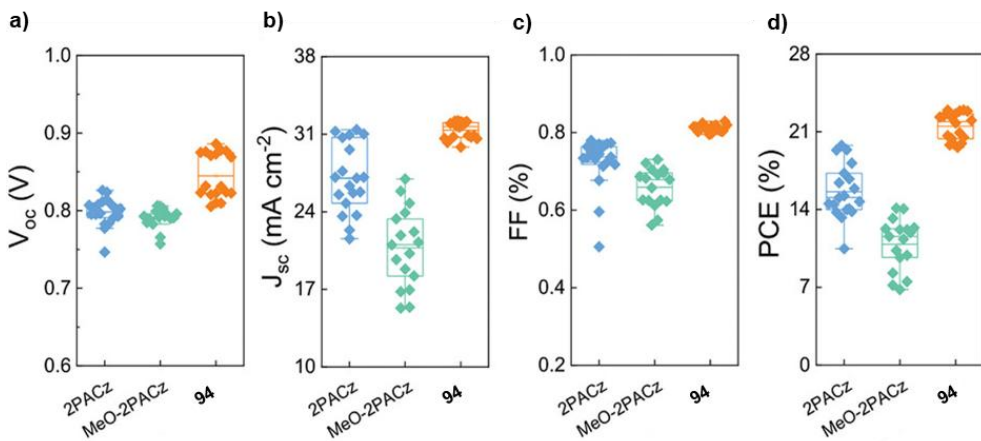


Figure 2.30. Photovoltaic characteristics of NBG p-i-n architecture perovskite solar cells comparing different HTMs used as SAMs: (a) V_{oc} statistical results; (b) J_{sc} statistical results; (c) Fill factor statistical results; (d) Efficiency statistical results

2.4.4. Chapter summary

In this chapter, a more advanced concept of SAM materials has been presented. By introducing additional ammonium functional groups, traditional materials containing phosphonic acid would be able to interact with two PSC components at the same time, namely, ITO and perovskite. To do so, carbazole-based phosphonic acids containing aromatic ammonium halides **93** and **94**, as well as aliphatic ammonium groups **99** and **100**, have been synthesized. However, the variety of ammonium halides was limited to chlorides and bromides, as the hydrolysis agent iodosotrimethylsilane was not able to fully hydrolyze diethyl phosphonate. Further synthesis involved an indole central fragment, which is commercially available with a wide variety of functional groups. The indole with an aliphatic amine substituent at the 3 Ind position was chosen to prevent side reactions from occurring during the hydrolysis step. Accordingly, indole derivatives containing phosphonic acid and an ammonium group **108** and **111**, as well as chloride-substituted indole derivatives containing phosphonic acid and an ammonium group **118** and **119** have been synthesized. Methoxy-substituted indole was not suitable for the synthesis of phosphonic acid materials, as this moiety itself reacts under hydrolysis conditions. Indole-based derivatives **118** and **119** are being investigated in organic light emitting diodes in collaboration with Prof. Thomas D. Anthopoulos research group from King Abdullah University of Science and Technology, Saudi Arabia. Carbazole **94** was tested in NBG Sn-Pb perovskite solar cells; it outperformed both standard SAM materials 2PACz and MeO-2PACz in terms of efficiency and other photovoltaic parameters, it also showed better reproducibility. Its excellent performance is related to the presence of ammonium groups which can passivate perovskite at the buried interface. All other synthesized compounds demonstrate suitable ionization potentials similar to SAM materials MeO-2PACz, 2PACz, or Me-4PACz. Combined with possible additional perovskite

passivation properties, all the materials are expected to perform well in perovskite-based optoelectronics.

3. METHODS AND MATERIALS

3.1. General Methods

The chemicals used in this research were purchased from *Sigma-Aldrich*, *TCI Europe*, and *RareChemicals*, and used as received without further purification. The solvents were purchased from *EuroChemicals* and distilled before use. The ^1H and ^{13}C NMR spectra were taken on a *Bruker Avance III* (400 MHz) spectrometer at RT. All the data are given as chemical shifts in δ (ppm). The course of the reactions was monitored by TLC on *ALUGRAM SIL G/UV254* plates and developed with UV light. Silica gel (grade 9385, 230–400 mesh, 60 Å, *Aldrich*) was used for column chromatography. Elemental analysis was performed with an *Exeter Analytical CE-440* elemental analyzer, *Model 440 C/H/N*. An electrothermal *A.KRÜSS M3000* capillary melting point apparatus was used for the determination of the melting points.

General procedure for N-alkylation when using 1,2-dibromoethane

Method I: the material to be alkylated (1 eq.) was dissolved (or suspended) in 1,2-dibromoethane (25 eq.), followed by addition of 50 % KOH aqueous solution (5 eq.) and tetrabutylammonium bromide (0.15 eq.). The reaction mixture was heated to 80 °C and stirred from 1 to 14 days. If the reaction was conducted for longer than 1 day, then, after the initial 24 hours, additional 50 % KOH solution (5 eq.) and tetrabutylammonium bromide (0.15 eq.) were added. After the termination of the reaction (TLC, the eluent shall be specified individually), the organic components were extracted with ethyl acetate, the organic layer was dried over anhydrous Na_2SO_4 and filtered, and solvent removed under reduced pressure. The crude product was purified by column chromatography (the eluent shall be specified individually).

General procedures for N-alkylation when using 1,4-dibromobutane

Method II: the material to be alkylated (1 eq.) was dissolved in anhydrous DMF under argon atmosphere, followed by the addition of 1,4-dibromobutane (1.5 eq.). The mixture was cooled down in an ice bath to 0 °C. Afterwards, NaH (60 % dispersion in mineral oil) (1.5 eq.) was added portionwise and 0 °C temperature was maintained until complete consumption of the starting material (TLC, the eluent shall be specified individually). The organic components were extracted with ethyl acetate, the organic layer was dried over anhydrous Na_2SO_4 and filtered, and the solvent was evaporated under reduced pressure. The crude product was purified by column chromatography (the eluent shall be specified individually).

Method III: the material to be alkylated (1 eq.) was dissolved in anhydrous DMF under argon atmosphere, followed by the addition of 1,4-dibromobutane (1.5 eq.) and ground KOH (1.5 eq.) The reaction mixture was stirred from 5 minutes to 24 hours at 25 °C. After the termination of the reaction (TLC, the eluent shall be specified individually), the organic components were extracted with ethyl acetate, the organic layer was dried over anhydrous Na_2SO_4 and filtered, and the solvent was evaporated

under reduced pressure. The crude product was purified by column chromatography (the eluent shall be specified individually).

General procedure for the Michaelis-Arbuzov reaction

Method IV: the alkylated derivative (1 eq.) was dissolved or suspended in triethyl phosphite (20 eq.) and the reaction was refluxed overnight. After the termination of the reaction (TLC, the eluent shall be specified individually), the solvent was removed under reduced pressure, and the crude product was purified by column chromatography (the eluent shall be specified individually).

General procedure for the diethyl phosphonate hydrolysis reaction when using hydrochloric acid

Method V: the phosphonate derivative (1 eq.) was dissolved or suspended in 37% hydrochloric acid (40 eq.) and refluxed overnight. After the termination of the reaction (TLC, the eluent shall be specified individually), the solvent was evaporated, and the product was purified (the method shall be specified individually).

General procedure for the diethyl phosphonate hydrolysis reaction when using bromotrimethylsilane

Method VI: the phosphonate derivative (1 eq.) was dissolved in anhydrous 1,4-dioxane under argon atmosphere. Afterwards, bromotrimethylsilane (10 eq.) was added dropwise, and the reaction was stirred overnight at 25 °C under argon atmosphere. After the consumption of the phosphonate starting material (TLC, the eluent shall be specified individually) methanol (10 eq.) was added, and stirring was continued for 2 hours, distilled water was added dropwise until a precipitate was formed or the solution became clear (for Boc-blocked amines containing intermediates), stirring was continued overnight, and finally the product was purified (the method shall be specified individually).

ITO/SAM Anode Fabrication

The synthesized compounds were used straight after synthesis. The SAM molecules were dissolved in absolute ethanol (*WWR Inc.*) with a concentration of 0.3 mg/ml and left to stir at room temperature for 1 hour. Before using, the SAM solution was placed into an ultrasonic bath for 15 min. *Indium tin oxide* (ITOcoated glass substrates (*Kintec Company*, 10 Ω sq.⁻¹) were cleaned by sequential ultrasonication in dilute *Extran* 300 detergent solution, deionized water, acetone and isopropyl alcohol for 10 min each. The clean substrates were then subjected to the O₂-plasma treatment step for 10 min. SAM solution (150 µl for 2.5×2.5 cm² substrate) was applied directly onto the ITO substrate for 20 s followed by a spin-coating step at 3000 rpm for 30 s. The ITO/SAM substrate was then placed onto a hotplate and annealed at 50 °C for 4 min. Next, the ITO/SAM substrate was dynamically washed 2 times with the same SAM solution (0.3 mg/ml). During the latter step, the ITO/SAM substrate was spun at 6000 rpm first while the SAM solution (150 µL for 2.5×2.5 cm² substrates) was drop-casted onto the spinning substrate. The dynamic washing step

was repeated twice. All the steps were performed in ambient air. Finally, the ITO/SAM substrates were transferred inside a dry nitrogen glove box for solar cell fabrication.

Bulk Heterojunction Organic Solar Cell Fabrication

The solar cell fabrication was performed by Prof. T. D. Anthopoulos group at King Abdullah University of Science and Technology (KAUST), Thuwal, Saudi Arabia. PNDIT-F3N, PM6, and BTP-eC9 were purchased from *Solarmer Materials Inc.* PM7-Si was synthesized as previously reported [200]. Next, a thin layer (≈ 40 nm) of PEDOT:PSS was spin-coated onto the UV-treated substrates and then dried on a hotplate at 150°C for 10 min. The samples were then transferred into a dry nitrogen glove box (< 10 ppm O₂). PM6:PM7-Si:BTP-eC9 (ratio 0.9:0.1:1.2, 17.5 mg mL⁻¹ in chloroform, plus 0.5 vol% DIO added) was then spun at 3500 rpm for 30 s to obtain an active-layer thickness around 110 nm. For the doping process, the BV in CF (0.004 wt%) was added directly into the BHJ solution, and then the blend solution was stirred over 30 minutes at 40°C . A layer of 5 nm of PNDIT-F3N (0.5 mg mL⁻¹ in methanol, and 0.5 vol% acetic acid was also added) was spun off the top of the BHJ layer. Finally, the samples were placed in a thermal evaporator, and 100 nm of silver was then thermally evaporated at 5×10^{-6} mbar through a 0.1 cm² pixel area shadow mask.

Bulk Heterojunction Organic Solar Cell Characterization

The solar cell characterization was done by Prof. T. D. Anthopoulos group at King Abdullah University of Science and Technology (KAUST), Thuwal, Saudi Arabia. The UV-vis spectra were recorded on a *Cary 5000* instrument in the single beam mode. The *J-V* measurements of solar cells were performed in an N₂ filled glove box using a *Keithley 2400* source meter and an *Oriel Sol3A Class AAA* solar simulator calibrated to 1 sun, AM1.5G, with a KG-5 silicon reference cell certified by *Newport*.

ST 1 Materials for organic light-emitting diodes (OLEDs) fabrication (KAUST)

Poly(3,4-ethylenedioxy thiophene): polystyrene sulfonate (PEDOT: PSS) was purchased from *Ossila* (AI 4083, Clevios), [2-(9H-carbazol-9-yl)ethyl]phosphonic acid (2PACz), [2-(3,6-dibromo-9H-carbazol-9-yl)ethyl]phosphonic acid (Br-2PACz), 4,4'-Bis(carbazol-9-yl)biphenyl (CBP), Bis(2-phenylpyridine)(acetylacetone)iridium(III) (Ir(ppy)₂acac), and 1,3,5-tris(1-phenyl-1*H*-benzimidazol-2-yl)benzene (TPBi) were obtained from Luminescence Technology Corp. (Lumtec). [2-(3,6-dimethoxy-9H-carbazol-9-yl)ethyl]phosphonic acid (MeO-2PACz) was purchased from *Tokyo Chemical Industry* (TCI) Co. LTD. All the above chemicals were used directly without further purification.

ST 6 Scanning tunneling microscopy (STM) (KAUST)

The STM experiments were performed in an Omicron variable-temperature scanning tunneling microscope under *ultra-high vacuum* (UHV). The samples were prepared *ex-situ* by spin-coating the different SAM molecules on top of the ITO-coated glass substrates. Then, the samples were flushed with a nitrogen flow to

remove solutions not attached to the surface. Afterwards, the samples were introduced into the UHV environment. All the samples were imaged in the constant current mode under room temperature with a tungsten tip prepared by electrochemical etching. The applied voltages on the ITO/SAM samples ranged from 1.1-1.6 V and the tunneling current ($I_{\text{tunneling}}$) was set at 100 pA.

OLED fabrication

OLED fabrication was done by Prof. T. D. Anthopoulos group at King Abdullah University of Science and Technology (KAUST), Thuwal, Saudi Arabia. *Indium tin oxide* (ITO, 20 Ω/sq, purchased from *Xinyan Technology Ltd.*) substrates were cleaned by employing the standard procedure, specifically, dilute *Extran* 300 detergent solution, deionized water, acetone, and isopropanol, respectively, in an ultrasonic bath for 10 minutes each. The cleaned substrates were treated with UV-ozone for 15 min. PEDOT:PSS was processed by spin-coating at 5000 rpm for 35 seconds, followed by thermal annealing at 150 °C for 15 minutes. The SAM solutions, 2PACz, Br-2PACz, **11**, **8**, **5**, and MeO-2PACz (0.5 mg mL⁻¹ in ethanol) were placed into an ultrasonic bath solution for 20 minutes before usage and were spin-coated atop ITO at a speed of 3000 for 30 seconds and followed by annealing at 100 °C for 10 minutes (in air). The sequence of CBP (20 nm), CBP:Ir(ppy)₂(acac) 92:8 (35 nm), TPBi (60 nm), LiF (1 nm), Al (110 nm) was thermally evaporated on top of the different HILs. Finally, after the complete deposition process, all the devices were encapsulated under a nitrogen glove box environment while using a glass cover and UV-cured resin.

OLEDs characterization

OLED characterization was done by Prof. T. D. Anthopoulos group at King Abdullah University of Science and Technology (KAUST), Thuwal, Saudi Arabia. The *current-density-voltage* (J-V-L) characteristics and *electroluminescence* (EL) spectra were obtained by using a computer-controlled programmable power source (*Keithley 2400, Tektronix*) and a luminance meter/spectrometer. For the calculation of the external quantum efficiency (EQE%), the assumption of a Lambertian emission was applied, in corroboration with the independent measurements of luminous flux with a photonic multichannel analyzer *PMA-12 (Hamamatsu)* and an integrating sphere (*Hamamatsu A10094*). All the measurements were performed in air ambience at room temperature.

Fabrication of the ‘triple cation’ ($FA_{0.79}MA_{0.16}Cs_{0.05}Pb(I_{0.83}Br_{0.17})_3$)-based perovskite solar cells (CU Boulder)

‘Triple cation’ perovskite solar cells were constructed at University of Colorado Boulder, Colorado, USA. The ITO substrates were pre-cleaned by consequentially sonicating for 15 min in *Extran* detergent, deionized water, acetone, and 2-propanol. After that, the substrates were cleaned by the UV-O₃ cleaner for 15 min. All of the subsequent steps were performed in a N₂-filled glovebox. For the deposition of the monolayer of Me-4PACz+6dPA, stock solutions of Me-4PACz (1 mg/ml) and 6dPA (0.74 mg/ml) in ethanol were mixed at 4:1 v:v ratio. Next, 120 μL of this solution was

statically (with the rest time of ~5 s) spin-coated on a pre-cleaned ITO substrate (5000 rpm, 30 s). Afterward, the ITO substrates were annealed at 100°C for 10 min and dynamically washed (5000 rpm, 30 s) with 120 µL of pure ethanol (washing can be omitted without compromising the results). For the absorber layer, perovskite precursor solution (507 mg PbI₂, 73.4 mg PbBr₂, 172 mg FAI, 22.4 mg MABr was dissolved in 0.8 ml DMF and 0.2 ml DMSO, followed by the addition of 40 µl of stock CsI solution (390 mg CsI in 1 ml DMSO), which was statically spin-coated at 5000 rpm (1.7 s ramp) for 35 s, followed by dispensing 300 µl of anisole after 10 s of the spinning program. After spin-coating, the substrates were annealed at 100°C for 1h. The device was finalized by the evaporation of LiF (1 nm), C60 (23 nm), BCP (8 nm), and Ag (100 nm).

Fabrication of the ‘triple halide’ ($FA_{0.75}Cs_{0.22}MA_{0.03}Pb(I_{0.82}Br_{0.15}Cl_{0.03})_3$)-based perovskite solar cells (HZB)

‘Triple halide’ perovskite solar cells were constructed at Helmholtz-Zentrum Berlin (HZB), Germany, by collaborating with Prof. S. Albrecht research group. The ITO substrates were subsequently cleaned in *Mucasol* solution (2% in DI-water), deionized water, acetone, and 2-propanol, each for 15 minutes in an ultrasonic bath. Afterwards, the surface was ‘activated’ for 10–15 minutes in an UV-O₃ cleaner (FHR UVOH 150 Lab), which is a crucial step before SAM deposition. The SAM solution (4:1 v:v of 1 mM/l Me-4PACz+6dPA in ethanol) was spin-coated at 3000 rpm for 10s, after which, the substrate was annealed at 100°C for 3–10 min. The cell configuration was ITO/SAM/Perovskite/LiF(1 nm)/C₆₀(20 nm)/SnO₂/Ag(100 nm), where C₆₀ and Ag were deposited by thermal evaporation, and the SnO₂ layer was deposited by atomic layer deposition in an Arradiance GEMStar reactor. Tetrakis(dimethylamino)tin(IV) (TDMAStn) was used as the Sn precursor and was held at 60 °C in a stainless-steel container. Water was used as the oxidant from a stainless-steel container without active heating, whereas the precursor delivery manifold was heated to 115 °C. For the deposition at 80 °C, the TDMAStn/purge1/H₂O/purge 2 times were 1 s/10 s/0.2 s/15 s with the corresponding nitrogen flows of 30 sccm/90 sccm/90 sccm/90 sccm. With this, 140 cycles led to 20 nm of SnO₂. All the spin-coating layer deposition steps were conducted in a nitrogen atmosphere. The ‘triple-halide’ perovskite composition was adapted due to its high V_{OC} potential and stable behavior [193]. First, 1.4 M ‘FACs’ solution (FA, Cs, PbI₂, PbBr₂; 22% Cs & 15% Br) in 3:1 DMF:DMSO was shaken at room temperature overnight. Next, it was transferred into another vial that contained MACl and PbCl₂ powders, which was shaken for 1 h at 60 °C before the perovskite layer deposition, with a nominal molar Cl percentage of 5%. Exemplary amounts of the chemicals for 1 ml of 1.4 M solution were: 500 mg PbI₂, 116 mg PbBr₂, 188 mg FAI, 80 mg CsI (weighed into one vial) + 4.7 mg MACl, 19.5 mg PbCl₂ (in another vial). The perovskite solution was spin-coated at 3500 rpm for 40 s and 250 µl anisole as the antisolvent was dripped at 28 s after the start of the spinning, followed by 20 min annealing on a hotplate at 100 °C in N₂.

Measurements of perovskite solar cells J-V characteristics

'Triple-cation' – CU

Triple-cation devices were measured by using a 0.06 cm² metal shadow mask at 1 sun intensity AM1.5 spectra solar simulator (*Newport Oriel 94043A Sol3A Class AAA*). J/V was scanned in 20 mV steps, 50 ms integration time and 50 ms delay time between each new voltage step and the start of the measurement.

'Triple-halide' – HZB

The samples contained each 6 pixels with an active area of 0.16 cm² (with an overlap of ITO and the Ag stripe), measured with an *Oriel LCS-100 ABB* solar simulator and Keithley 2400 source-measure unit. J/V was scanned in 20 mV steps, 20 ms integration time and 20 ms delay time between each new voltage step and the start of the measurement.

Fabrication of ZnO tetrapods

ZnO tetrapods (ZnO-Ts) were synthesized by using a modified combustion method previously developed [201,202]. In summary, Zn powder (Purum, Sigma-Aldrich) was introduced into a combustion chamber along with a methane atmospheric flame. The synthesized nanomaterial was collected on filters, the obtained polydispersed ZnO nanomaterial powder was then dispersed in absolute ethanol (99.5%, Emparta) and sonicated and fractioned by using a differential centrifugation procedure [203]. The ZnO nanomaterial was fractionated under 1000 for 15 minutes, and the sediments were collected, dried and used further.

Fabrication of ZnO tetrapods gas sensors

The sensors were made by spray-coating a layer of ZnO-Ts onto the deposited gold/glass electrodes by adopting the method developed previously [204]. The electrodes of 5 mm wide were formed by Au sputtering through a mask, whereas the gap between electrodes of 3 um was cut by using a focused laser. After ZnO-T deposition, the active electrode area was 5 mm x 0.003 mm.

ZnO tetrapods modification

ZnO-Ts were modified by compound **73** by using the dip-coating method. A substrate with ZnO-Ts was slowly immersed into 10 mL solution of **73** in *iPrOH* (0.2 mg/mL) and kept submerged for 3 hours at room temperature. Afterwards, the substrate was pulled out, annealed at 100 °C for 10 minutes, and washed three times by slowly immersing it into clean *iPrOH* each time.

ZnO-T gas sensors characterization

The gas sensing experimental setup was used, the sensors were fixed in the *HFS600 (LINKAM SCIENTIFIC INSTRUMENTS)* environmental control chamber connected to a *Keithley 2604B* Source meter (*Keithley Instruments*). The measurement process and data acquisition were controlled using KickStart (*Keithley Instruments*) software. Gas gas flow was controlled by using the *Bronkhorst (BRONKHORST*

HIGH-TECH B.V.) mass flow controllers. The environmental control chamber was ventilated with synthetic air (purity of 5.0). The concentrations of NO₂ (1, 5, 10 and 20 ppm) and organic compounds – hexane, acetone and 2-propanol (10 ppm) – were obtained by dosing a NO₂ mixture and organic vapors into a synthetic air stream, without humidity, at room temperature of 23 °C. The UV source (365 nm LED) was connected to *a pulse width modulation* (PWM) generator, with the current being set to 11.5 mA, which led to 300 µW/cm² UV irradiance at the surface of the sensor at 4 cm distance.

The electrical measurements were performed at 0.2 V, except for the current-voltage characterization test, where the range from -1 to +1 V was being used. Modulated UV was obtained with the period of PWM set as 10 seconds, and a duty cycle of 50%. The resistance of the sensor in air is represented by R_a , and the resistance in the target gas is represented by R_g . The gas response is defined as R_a/R_g for the reducing gas, and R_g/R_a for the oxidizing gas.

Preparation of NBG perovskite precursor solution

The preparation of the perovskite precursor was done by Prof. S. De Dewolf group at King Abdullah University of Science and Technology (KAUST), Thuwal, Saudi Arabia. The Cs_{0.05}FA_{0.70}MA_{0.25}Sn_{0.50}Pb_{0.50}I₃ perovskite precursor solution was prepared in a glovebox under N₂ atmosphere (O₂<0.1 ppm, H₂O<0.1 ppm) by mixing CsI (23.4 mg, 0.090 mmol), FAI (216.7 mg, 1.260 mmol), MAI (71.6 mg, 0.450 mmol), PbI₂ (414.9 mg, 0.900 mmol), SnI₂ (335.3 mg, 0.900 mmol), SnF₂ (14.1 mg, 0.090 mmol), GuaSCN (4.0 mg, 0.034 mmol), and 4F-PEABr (2.0 mg, 0.007 mmol) in 750 µl anhydrous DMF and 250 µl anhydrous DMSO, and shaken vigorously in dark for 2 h. The precursor solution was used immediately after filtering with 0.20 µm PTFE filter.

Fabrication of NBG perovskite thin films

The fabrication of perovskite was performed by Prof. S. De Dewolf group at King Abdullah University of Science and Technology (KAUST), Thuwal, Saudi Arabia. The substrates were cleaned sequentially with soap detergent, deionized water, acetone, and isopropyl alcohol by ultrasonication for 10 min each, dried by blowing with a nitrogen flow, and treated with UV-O₃ for 15 min before self-assembly monolayer and perovskite thin film depositions. SAM molecules were anchored onto ITO substrates from 1 mM concentration solutions in ethanol or methanol at 3000 rpm for 35 s, followed by 10 min annealing at 100 °C. Perovskite thin films were fabricated in a glovebox under N₂ atmosphere (O₂<0.1 ppm, H₂O<0.1 ppm) by spin-coating the perovskite precursor solution at 1000 rpm for 10 sec and 4000 rpm for 40 sec onto SAM-anchored ITO substrates, and quenching with antisolvent at 20 sec before the end of the second step. The substrates were immediately transferred to a hotplate and annealed at 100 °C for 10 min. Passivation by post-treatment was carried out by spin-coating a solution of 1,2-diaminoethane in chlorobenzene onto perovskite films at 4000 rpm for 35 sec, followed by annealing for 5 min at 100°C.

Fabrication of single junction NBG perovskite solar cells

Solar cell fabrication was performed by Prof. S. De Dewolff group, at King Abdullah University of Science and Technology (KAUST), Thuwal, Saudi Arabia. Pre-patterned glass/ITO substrates ($15 \Omega \text{ sq}^{-1}$) were cleaned sequentially with a detergent, deionized water, acetone, and isopropyl alcohol by ultrasonication for 10 min each and dried by blowing with a nitrogen flow. The cleaned substrates were treated with UV-O₃ for 15 min before depositing the HTL materials. The perovskite layer was fabricated onto ITO/SAM substrates while following the abovementioned procedure. The samples were moved under Ar to a vacuum deposition chamber, where 20 nm of C₆₀ (deposition rate 0.2 Å/s) and 5 nm of BCP (deposition rate 0.1 Å/s) were deposited by thermal evaporation. The top electrode was prepared by depositing 120 nm of silver (deposition rate 1 Å/s) through a shadow mask.

Contact angle measurements

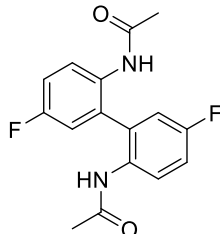
The *Ossila* optical contact angle goniometer was used for water droplet contact angle measurements of the SAM-modified ZnO-T surface. Measurement accuracy $\pm 1^\circ$, measurement range $5^\circ - 180^\circ$.

Photoelectrical measurements

The solid-state ionization potential (I_p) of the layers of the synthesized compounds was measured by adopting the electron photoemission in the air method at the Institute of Chemical Physics, Vilnius University. The samples for the ionization energy measurement were prepared by dissolving materials in THF or MeOH, and these solutions were coated on Al plates that had been pre-coated with a $\sim 0.5 \mu\text{m}$ thick methylmethacrylate and methacrylic acid copolymer adhesive layer. The thickness of the transporting material layer was $0.5-1 \mu\text{m}$. Usually, photoemission experiments are carried out in vacuum, and high vacuum is one of the main requirements for these measurements. If the vacuum is not high enough, the sample surface oxidation and the gas adsorption influence the measurement results. In this case, however, the organic materials that were being investigated were stable enough to oxygen, and the measurements could be carried out in air. The samples were illuminated with monochromatic light from a quartz monochromator with a deuterium lamp. The power of the incident light beam was $(2-5)\cdot 10^{-8} \text{ W}$. The negative voltage of -300 V was supplied to the sample substrate. The counter electrode with a $4.5 \times 15 \text{ mm}^2$ slit for illumination was placed at a distance of 8 mm from the sample surface. The counter-electrode was connected to the input of the BK2-16 type electrometer working in the open input regime for the photocurrent measurement. A $10-15 - 10-12 \text{ A}$ strong photocurrent was flowing in the circuit under illumination. Photocurrent I is strongly dependent on the incident light photon energy $h\nu$. The $I^{0.5} = f(h\nu)$ dependence chart was plotted. The linear part of this dependence was extrapolated to the $h\nu$ axis, and the I_p value was determined as the photon energy at the interception point.

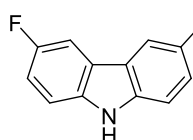
3.2. Detailed Synthesis Procedures and Materials

2,2'-Bis(acetamido)-5,5'-difluorobiphenyl (**1**)



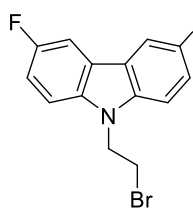
This substance was synthesized according to an earlier reported procedure [199].

3,6-Difluoro-9H-carbazole (**2**)



This substance was synthesized according to an earlier reported procedure [199].

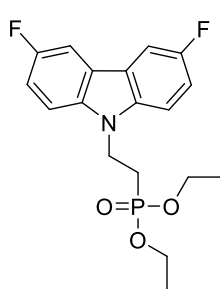
9-(2-Bromoethyl)-3,6-difluoro-9H-carbazole (**3**)



Method I. 3,6-Difluoro-9H-carbazole (**2**) (0.5 g, 2.45 mmol), 1,2-dibromoethane (5.32 ml, 61.48 mmol), 50 % KOH aqueous solution (1.4 ml, 12.29 mmol) and tetrabutylammonium bromide (0.12 g, 0.36 mmol) were used for the reaction. Reaction conducted for 48 hours. Eluent: TLC (acetone:*n*-hexane, 3:22), column (acetone:*n*-hexane, 3:22). Product obtained as brownish white crystals (0.36 g, 47% yield). M.p. 132–133.5 °C.

¹H NMR (400 MHz, CDCl₃): δ 7.70 (dd, *J* = 8.7, 2.1 Hz, 2H, 4-H, 5-H of Cz), 7.36 (dd, *J* = 8.9, 4.0 Hz, 2H, Ht), 7.26 (td, *J* = 9.1, 2.4 Hz, 2H, Ht), 4.69 (t, *J* = 7.3 Hz, 2H, NCH₂), 3.68 (t, *J* = 7.3 Hz, 2H, CH₂Br) ppm. ¹³C NMR (101 MHz, CDCl₃): δ 158.69, 156.34, 137.29, 123.26, 123.22, 123.17, 123.13, 114.65, 114.40, 109.57, 109.48, 106.69, 106.45, 45.14, 28.24 ppm. Anal. calcd. for C₁₄H₁₀BrF₂N: C 54.22, H 3.25, N 4.52; found: C 54.10, H 3.27, N 4.31.

Diethyl [2-(3,6-difluoro-9H-carbazol-9-yl)ethyl]phosphonate (**4**)

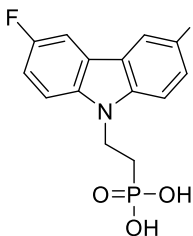


Method IV. 9-(2-Bromoethyl)-3,6-difluoro-9H-carbazole (**3**) (0.33 g, 1.06 mmol) and triethyl phosphite (3.6 ml, 21.28 mmol) were used for the reaction. Eluent: TLC (acetone:*n*-hexane, 8:17), column (acetone:*n*-hexane, 8:17). Product obtained as white crystals (0.35 g, 92% yield). M.p. 96–97.5 °C.

¹H NMR (400 MHz, CDCl₃): δ 7.67 (dd, *J* = 8.7, 2.2 Hz, 2H, 4-H, 5-H of Cz), 7.35 (dd, *J* = 8.9, 4.1 Hz, 2H, Ht), 7.23 (td, *J* = 9.0, 2.3 Hz, 2H, Ht), 4.58 (dd, *J* = 15.8, 9.8 Hz, 2H, NCH₂), 4.05 (quint, *J* = 7.2 Hz, 4H, OCH₂), 2.36 – 2.09 (m, 2H, CH₂P), 1.25

(t, $J = 7.0$ Hz, 6H, CH₃) ppm. ¹³C NMR (101 MHz, CDCl₃): δ 158.58, 156.24, 137.06, 123.21, 123.17, 123.12, 123.07, 114.56, 114.30, 109.64, 109.56, 106.61, 106.37, 62.08 (d, $^2J_{(C,P)} = 6.5$ Hz), 37.48 (d, $^2J_{(C,P)} = 0.5$ Hz), 25.41 (d, $^1J_{(C,P)} = 138.5$ Hz), 16.48 (d, $^3J_{(C,P)} = 6.0$ Hz) ppm. Anal. calcd. for C₁₈H₂₀F₂NO₃P: C 58.86, H, 5.49, N, 3.81; found: C 59.01, H 5.55, N 3.98.

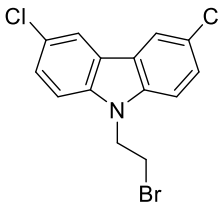
[2-(3,6-Difluoro-9H-carbazol-9-yl)ethyl]phosphonic acid (5)



Method VI. Diethyl [2-(3,6-difluoro-9H-carbazol-9-yl)ethyl]phosphonate (**4**) (0.32 g, 0.87 mmol), bromotrimethylsilane (1.4 ml, 8.7), methanol (0.4 ml, 8.7 mmol) and 10 ml of 1,4-dioxane were used. Eluent: TLC (acetone:*n*-hexane, 8:17). Product was purified by dissolving in the minimum amount of THF, precipitating into 20-fold excess of *n*-hexane, filtering, and washing with *n*-hexane to give grey crystals (0.19 g, 73% yield). M.p. 207.5–209.5 °C (melting and decomposition).

¹H NMR (400 MHz, DMSO-d₆): δ 8.02 (d, $J = 7.7$ Hz, 2H, 4-H, 5-H of Cz), 7.56 (dd, $J = 8.8, 4.1$ Hz, 2H, Ht), 7.35 (t, $J = 8.3$ Hz, 2H, Ht), 4.54 (dd, $J = 15.6, 8.0$ Hz, 2H, NCH₂), 2.08 – 1.93 (m, 2H, CH₂P) ppm. ¹³C NMR (101 MHz, DMSO-d₆): δ 157.67, 155.35, 136.89, 122.38, 122.34, 122.28, 122.24, 114.31, 114.05, 110.47, 110.38, 106.66, 106.42, 37.81, 27.30 (d, $^1J_{(C,P)} = 131.4$ Hz) ppm. Anal. calcd. for C₁₄H₁₂F₂NO₃P: C 54.03, H, 3.89, N, 4.50; found: C 54.28, H 3.97, N 4.69.

9-(2-Bromoethyl)-3,6-dichloro-9H-carbazole (6)

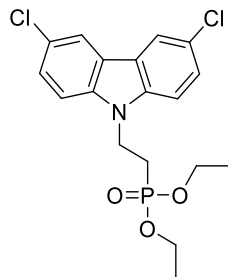


Method I. 3,6-Dichloro-9H-carbazole (0.5 g, 2.11 mmol), 1,2-dibromoethane (4.58 ml, 52.94 mmol), 50 % KOH aqueous solution (1.2 ml, 10.58 mmol) and tetrabutylammonium bromide (0.10 g, 0.32 mmol) were used for the reaction. Reaction conducted for 48 hours. Eluent: TLC (acetone:*n*-hexane, 3:22), column (acetone:*n*-hexane, 3:22). Product obtained as white crystals (0.51 g, 70% yield). M.p. 131.5–

133 °C.

¹H NMR (400 MHz, CDCl₃): δ 7.96 (d, $J = 1.2$ Hz, 2H, 4-H, 5-H of Cz), 7.44 (dd, $J = 8.7, 1.6$ Hz, 2H, Ht), 7.33 (d, $J = 8.7$ Hz, 2H, Ht), 4.64 (t, $J = 7.2$ Hz, 2H, NCH₂), 3.65 (t, $J = 7.2$ Hz, 2H, CH₂Br) ppm. ¹³C NMR (101 MHz, CDCl₃): δ 138.89, 126.85, 125.62, 123.42, 120.56, 109.91, 45.02, 28.10 ppm. Anal. calcd. for C₁₄H₁₀BrCl₂N: C 49.02, H 2.94, N 4.08; found: C 49.09, H 3.00, N 4.25.

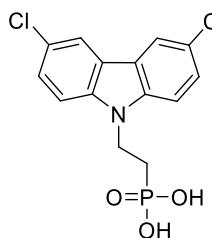
Diethyl [2-(3,6-dichloro-9H-carbazol-9-yl)ethyl]phosphonate (7)



Method IV. 9-(2-Bromoethyl)-3,6-dichloro-9H-carbazole (**6**) (0.48 g, 1.39 mmol) and triethyl phosphite (4.8 ml, 27.98 mmol) were used for the reaction. Eluent: TLC (acetone:*n*-hexane, 8:17), column (acetone:*n*-hexane, 8:17). Product obtained as white crystals (0.52 g, 94% yield). M.p. 106.5–108.5 °C.

¹H NMR (400 MHz, CDCl₃): δ 7.96 (s, 2H, 4-H, 5-H of Cz), 7.43 (d, *J* = 8.6 Hz, 2H, Ht), 7.34 (d, *J* = 8.7 Hz, 2H, Ht), 4.55 (dd, *J* = 15.2, 9.0 Hz, 2H, NCH₂), 4.08 – 3.95 (m, 4H, OCH₂), 2.33 – 2.16 (m, 2H, CH₂P), 1.24 (t, *J* = 7.0 Hz, 6H, CH₃) ppm. ¹³C NMR (101 MHz, CDCl₃): δ 138.63, 126.75, 125.33, 123.38, 120.47, 110.00, 62.12 (d, ²J_(C,P) = 5.9 Hz), 37.43, 25.40 (d, ¹J_(C,P) = 138.8 Hz), 16.27 (d, ³J_(C,P) = 6.7 Hz) ppm. Anal. calcd. for C₁₈H₂₀Cl₂NO₃P: C 54.02, H, 5.04, N, 3.50; found: C 53.93, H 5.15, N 3.68.

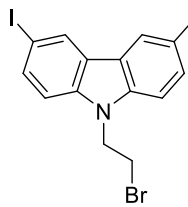
[2-(3,6-Dichloro-9H-carbazol-9-yl)ethyl]phosphonic acid (8)



Method VI. Diethyl [2-(3,6-dichloro-9H-carbazol-9-yl)ethyl]phosphonate (**7**) (0.5 g, 1.25 mmol), bromotrimethylsilane (1.6 ml, 12.49), methanol (0.5 ml, 12.49 mmol) and 15 ml of 1,4-dioxane were used. Eluent: TLC (acetone:*n*-hexane, 7:18). Product was purified by dissolving in the minimum amount of THF, precipitating into 20-fold excess of *n*-hexane, filtering, and washing with *n*-hexane to give white crystals (0.39 g, 91% yield). M.p. 220–221.5 °C (melting and decomposition).

¹H NMR (400 MHz, DMSO-d₆): δ 8.32 (s, 2H, 4-H, 5-H of Cz), 7.59 (d, *J* = 8.7 Hz, 2H, Ht), 7.51 (dd, *J* = 8.7, 1.0 Hz, 2H, Ht), 4.54 (dd, *J* = 15.8, 8.5 Hz, 2H, NCH₂), 2.13 – 1.89 (m, 2H, CH₂P) ppm. ¹³C NMR (101 MHz, DMSO-d₆): δ 138.48, 126.36, 123.74, 122.66, 120.55, 111.01, 37.81, 27.20 (d, ¹J_(C,P) = 131.5 Hz) ppm. Anal. calcd. for C₁₄H₁₂Cl₂NO₃P: C 48.86, H, 3.51, N, 4.07; found: C 48.69, H 3.40, N 3.80.

9-(2-Bromoethyl)-3,6-diiodo-9H-carbazole (9)

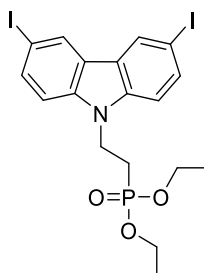


Method I. 3,6-Diiodo-9H-carbazole (1.5 g, 3.58 mmol), 1,2-dibromoethane (7.74 ml, 89.49 mmol), 50 % KOH aqueous solution (2.0 ml, 17.89 mmol) and tetrabutylammonium bromide (0.17 g, 0.53 mmol) were used for the reaction. Reaction conducted for 48 hours. Eluent: TLC (acetone:*n*-hexane, 3:22), column (acetone:*n*-hexane, 3:22). Product obtained as white crystals (1.79 g, 95% yield). M.p. 160.5–161.5 °C.

¹H NMR (400 MHz, DMSO-d₆): δ 8.61 (s, 2H, 4-H, 5-H of Cz), 7.73 (d, *J* = 8.6 Hz, 2H, Ht), 7.54 (d, *J* = 8.6 Hz, 2H, Ht), 4.82 (t, *J* = 6.1 Hz, 2H, NCH₂), 3.88 (t, *J* = 6.1 Hz, 2H, CH₂Br) ppm. ¹³C NMR (101 MHz, DMSO-d₆): δ 139.14, 134.24, 129.25,

123.59, 112.39, 82.73, 43.96, 31.23 ppm. Anal. calcd. for $C_{14}H_{10}BrI_2N$: C 31.97, H 1.92, N 2.66; found: C 32.08, H 2.02, N 2.41.

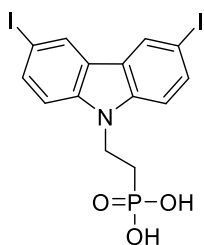
Diethyl [2-(3,6-diiodo-9H-carbazol-9-yl)ethyl]phosphonate (10)



Method IV. 9-(2-Bromoethyl)-3,6-diiodo-9H-carbazole (**9**) (1.7 g, 2.91 mmol) and triethyl phosphite (11 ml, 58.30 mmol) were used for the reaction. Eluent: TLC (acetone:*n*-hexane, 8:17), column (acetone:*n*-hexane, 8:17). Product obtained as a yellowish resin (1.74 g, 93% yield).

1H NMR (400 MHz, DMSO-d₆): δ 8.60 (s, 2H, 4-H, 5-H of Cz), 7.74 (d, J = 8.6 Hz, 2H, Ht), 7.44 (d, J = 8.6 Hz, 2H, Ht), 4.54 (dt, J = 14.3, 7.0 Hz, 2H, NCH₂), 3.85 (quint, J = 7.2 Hz, 4H, OCH₂), 2.26 (dt, J = 17.8, 6.9 Hz, 2H, CH₂P), 1.04 (t, J = 7.0 Hz, 6H, CH₃) ppm. ^{13}C NMR (101 MHz, DMSO-d₆): δ 138.73, 134.23, 129.26, 123.66, 112.09, 82.50, 61.13 (d, $^2J_{(C,P)}$ = 6.3 Hz), 36.82 (d, $^2J_{(C,P)}$ = 3.1 Hz), 24.00 (d, $^1J_{(C,P)}$ = 136.9 Hz), 15.97 (d, $^3J_{(C,P)}$ = 6.0 Hz) ppm. Anal. calcd. for $C_{18}H_{20}I_2NO_3P$: C 37.07, H, 3.46, N, 2.40; found: C 37.01, H 3.65, N 2.53.

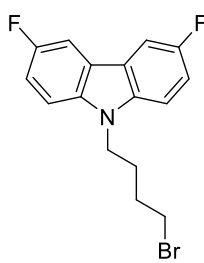
[2-(3,6-Diiodo-9H-carbazol-9-yl)ethyl]phosphonic acid (11)



Method VI. Diethyl [2-(3,6-diiodo-9H-carbazol-9-yl)ethyl]phosphonate (**10**) (1.7 g, 2.91 mmol), bromotrimethylsilane (3.8 ml, 29.15), methanol (1.2 ml, 29.15 mmol) and 30 ml of 1,4-dioxane were used. Eluent: TLC (acetone:*n*-hexane, 7:18). Product was purified by dissolving in the minimum amount of THF, precipitating into 20-fold excess of *n*-hexane, filtering, and washing with *n*-hexane to give white crystals (1.33 g, 87% yield). M.p. 209.5–211 °C (melting and decomposition).

1H NMR (400 MHz, DMSO-d₆): δ 8.61 (s, 2H, 4-H, 5-H of Cz), 7.75 (dd, J = 8.6, 1.3 Hz, 2H, Ht), 7.42 (d, J = 8.6 Hz, 2H, Ht), 4.50 (dd, J = 15.9, 8.4 Hz, 2H, NCH₂), 2.06 – 1.93 (m, 2H, CH₂P) ppm. ^{13}C NMR (101 MHz, DMSO-d₆): δ 138.66, 134.36, 129.41, 123.67, 111.79, 82.50, 37.65, 27.13 (d, $^1J_{(C,P)}$ = 131.4 Hz) ppm. Anal. calcd. for $C_{14}H_{12}I_2NO_3P$: C 31.91, H, 2.30, N, 2.66; found: C 31.79, H 2.22, N 2.76.

9-(4-Bromobutyl)-3,6-difluoro-9H-carbazole (12)

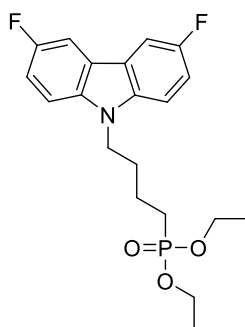


Method II. 3,6-Difluoro-9H-carbazole (**2**) (0.7 g, 3.44 mmol), 1,4-dibromobutane (0.6 ml, 5.16 mmol), NaH (0.20 g, 5.16 mmol) and 10 ml of DMF were used for the reaction. Eluent: TLC (acetone:*n*-hexane, 1:24), column (acetone:*n*-hexane, 1:24). Product obtained as a yellowish resin (0.73 g, 63 % yield).

1H NMR (400 MHz, CDCl₃): δ 7.68 (d, J = 8.7 Hz, 2H, 4-H, 5-H of Cz), 7.30 (dd, J = 8.8, 4.1 Hz, 2H, Ht), 7.22 (t, J = 8.9 Hz, 2H, Ht), 4.31 (t, J = 6.9 Hz, 2H, NCH₂), 3.38 (t, J = 6.4 Hz, 2H,

CH_2Br), 2.11 – 1.98 (m, 2H, CH_2), 1.94 – 1.84 (m, 2H, CH_2) ppm. ^{13}C NMR (101 MHz, CDCl_3): δ 158.38, 156.04, 137.59, 122.88, 122.79, 114.47, 114.21, 109.55, 109.46, 106.51, 106.28, 42.68, 33.08, 30.25, 27.73 ppm. Anal. calcd. for $\text{C}_{16}\text{H}_{14}\text{BrF}_2\text{N}$: C 56.82, H 4.17, N 4.14; found: C 56.99, H 4.02, N 4.30.

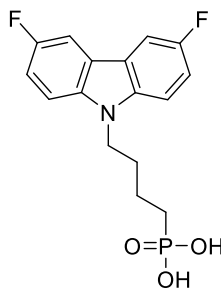
Diethyl [4-(3,6-difluoro-9H-carbazol-9-yl)butyl]phosphonate (13)



Method IV. 9-(4-Bromobutyl)-3,6-difluoro-9H-carbazole (**12**) (0.68 g, 2.01 mmol) and triethyl phosphite (7.0 ml, 40.21 mmol) were used for the reaction. Eluent: TLC (acetone:*n*-hexane, 7:18), column (acetone:*n*-hexane, 7:18). Product obtained as a yellowish resin (0.49g, 62 % yield).

^1H NMR (400 MHz, CDCl_3): δ 7.66 (d, $J = 8.7$ Hz, 2H, 4-H, 5-H of Cz), 7.28 (dd, $J = 8.8, 4.1$ Hz, 2H, Ht), 7.20 (t, $J = 8.9$ Hz, 2H, Ht), 4.26 (t, $J = 7.0$ Hz, 2H, NCH_2), 4.02 (quint, $J = 7.2$ Hz, 4H, OCH_2), 2.00 – 1.89 (m, 2H, CH_2), 1.77 – 1.60 (m, 4H, Aliph), 1.24 (t, $J = 7.1$ Hz, 6H, CH_3) ppm. ^{13}C NMR (101 MHz, CDCl_3): δ 158.33, 155.99, 137.61, 122.86, 122.82, 122.77, 122.72, 114.37, 114.12, 109.58, 109.49, 106.42, 106.19, 61.66 (d, $^2J_{(\text{C},\text{P})} = 6.6$ Hz), 43.04 (d, $^4J_{(\text{C},\text{P})} = 0.6$ Hz), 29.81 (d, $^2J_{(\text{C},\text{P})} = 15.1$ Hz), 25.52 (d, $^1J_{(\text{C},\text{P})} = 141.6$ Hz), 20.54 (d, $^3J_{(\text{C},\text{P})} = 5.0$ Hz), 16.52 (d, $^3J_{(\text{C},\text{P})} = 6.0$ Hz) ppm. Anal. calcd. for $\text{C}_{20}\text{H}_{24}\text{F}_2\text{NO}_3\text{P}$: C 60.76, H 6.12, N 3.54; found: C 60.65, H 6.27, N 3.55.

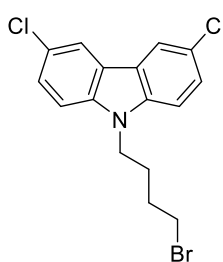
[4-(3,6-Difluoro-9H-carbazol-9-yl)butyl]phosphonic acid (14)



Method VI. Diethyl [4-(3,6-difluoro-9H-carbazol-9-yl)butyl]phosphonate (**13**) (0.43 g, 1.08 mmol), bromotrimethylsilane (1.4 ml, 10.87 mmol), methanol (0.4 ml, 10.87 mmol) and 5 ml of 1,4-dioxane were used. Eluent: TLC (acetone:*n*-hexane, 7:18). Product was purified by dissolving in the minimum amount of THF, precipitating into 20-fold excess of *n*-hexane, filtering, and washing with *n*-hexane to give greyish white crystals (0.33 g, 89%). M.p. 191–193 °C (melting and decomposition).

^1H NMR (400 MHz, DMSO-d_6): δ 8.02 (d, $J = 9.2$ Hz, 2H, 4-H, 5-H of Cz), 7.63 (dt, $J = 11.3, 5.8$ Hz, 2H, Ht), 7.31 (dd, $J = 18.1, 9.0$ Hz, 2H, Ht), 4.39 (t, $J = 6.6$ Hz, 2H, NCH_2), 1.88 – 1.75 (m, 2H, CH_2), 1.60 – 1.40 (m, 4H, Aliph) ppm. ^{13}C NMR (101 MHz, DMSO-d_6): δ 157.49, 155.17, 137.39, 122.05, 122.00, 121.95, 121.91, 114.15, 113.90, 110.77, 110.68, 106.44, 106.21, 42.38, 29.54 (d, $^2J_{(\text{C},\text{P})} = 15.1$ Hz), 27.32 (d, $^1J_{(\text{C},\text{P})} = 136.8$ Hz), 20.39 (d, $^3J_{(\text{C},\text{P})} = 4.0$ Hz) ppm. Anal. calcd. for $\text{C}_{16}\text{H}_{16}\text{F}_2\text{NO}_3\text{P}$: C 56.64, H 4.75, N 4.13; found: C 56.81, H 4.79, N 4.03.

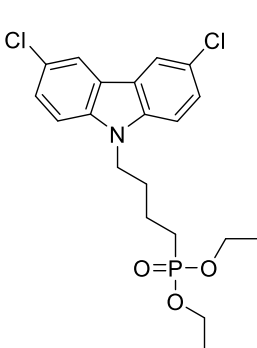
9-(4-Bromobutyl)-3,6-dichloro-9H-carbazole (15)



Method II. 3,6-Dichloro-9H-carbazole (0.7 g, 2.96 mmol), 1,4-dibromobutane (0.5 ml, 4.44 mmol), NaH (0.18 g, 4.44 mmol) and 10 ml of DMF were used. Eluent: TLC (acetone:*n*-hexane, 1:24), column (acetone:*n*-hexane, 1:24). Product obtained as white crystals (0.77 g, 70% yield). M.p. 120–122 °C.

¹H NMR (400 MHz, CDCl₃): δ 7.99 (s, 2H, 4-H, 5-H of Cz), 7.43 (d, *J* = 8.7 Hz, 2H, Ht), 7.30 (d, *J* = 8.7 Hz, 2H, Ht), 4.30 (t, *J* = 7.0 Hz, 2H, NCH₂), 3.37 (t, *J* = 6.4 Hz, 2H, CH₂Br), 2.13 – 1.94 (m, 2H, CH₂), 1.88 (dt, *J* = 13.3, 6.5 Hz, 2H, CH₂) ppm. ¹³C NMR (101 MHz, CDCl₃): δ 139.16, 126.68, 125.04, 123.19, 120.47, 109.95, 42.63, 32.99, 30.18, 27.64 ppm. Anal. calcd. for C₁₆H₁₄BrCl₂N: C 51.79, H 3.80, N 3.77; found: C 51.99, H 4.03, N 3.87.

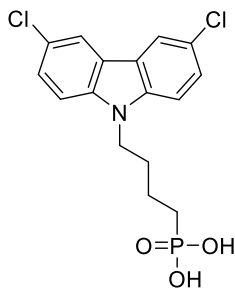
Diethyl [4-(3,6-dichloro-9H-carbazol-9-yl)butyl]phosphonate (16)



Method IV. 9-(4-Bromobutyl)-3,6-dichloro-9H-carbazole (15) (0.73 g, 1.96 mmol) and triethyl phosphite (6.7 ml, 39.3 mmol) were used for the reaction. Eluent: TLC (acetone:*n*-hexane, 7:18), column (acetone:*n*-hexane, 7:18). Product obtained as a yellowish resin (0.81g, 96 % yield).

¹H NMR (400 MHz, CDCl₃): δ 7.96 (s, 2H, 4-H, 5-H of Cz), 7.45 – 7.37 (m, 2H, Ht), 7.29 (dd, *J* = 8.4, 3.4 Hz, 2H, Ht), 4.31 – 4.19 (m, 2H, NCH₂), 4.02 (p, *J* = 7.1 Hz, 4H, OCH₂), 2.00 – 1.88 (m, 2H, CH₂), 1.78 – 1.55 (m, 4H, Aliph), 1.24 (t, *J* = 7.0 Hz, 6H, CH₃) ppm. ¹³C NMR (101 MHz, CDCl₃): δ 139.17, 126.59, 124.94, 123.13, 120.39, 109.99, 61.70 (d, ²J_(C,P) = 6.6 Hz), 42.99, 29.71 (d, ²J_(C,P) = 14.9 Hz), 25.50 (d, ¹J_(C,P) = 141.7 Hz), 20.52 (d, ³J_(C,P) = 5.0 Hz), 16.53 (d, ³J_(C,P) = 5.9 Hz) ppm. Anal. calcd. for C₂₀H₂₄Cl₂NO₃P: C 56.09, H 5.65, N 3.27; found: C 56.22, H 5.43, N 3.30.

[4-(3,6-Dichloro-9H-carbazol-9-yl)butyl]phosphonic acid (17)

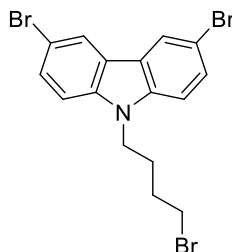


Method VI. Diethyl [4-(3,6-dichloro-9H-carbazol-9-yl)butyl]phosphonate (16) (0.75 g, 1.75 mmol), bromotrimethylsilane (2.3 ml, 17.5 mmol), methanol (0.7 ml, 17.5 mmol) and 10 ml of 1,4-dioxane were used. Eluent: TLC (acetone:*n*-hexane, 7:18). Product was purified by dissolving in the minimum amount of THF, precipitating into 20-fold excess of *n*-hexane, filtering, and washing with *n*-hexane to give grey crystals (0.54 g, 82%). M.p. 215–217 °C (melting and decomposition).

¹H NMR (400 MHz, DMSO-d₆): δ 8.32 (s, 2H, 4-H, 5-H of Cz), 7.68 (d, *J* = 8.8 Hz, 2H, Ht), 7.48 (d, *J* = 8.7 Hz, 2H, Ht), 4.39 (t, *J* = 6.9 Hz, 2H, NCH₂), 1.85 – 1.74 (m,

2H, CH₂), 1.58 – 1.44 (m, 4H, Aliph) ppm. ¹³C NMR (101 MHz, DMSO-d₆): δ 138.97, 126.26, 123.51, 122.41, 120.46, 111.34, 42.37, 29.47 (d, ²J_(C,P) = 6.7 Hz), 27.32 (d, ¹J_(C,P) = 138.7 Hz), 20.38 (d, ³J_(C,P) = 4.3 Hz) ppm. Anal. calcd. for C₁₆H₁₆Cl₂NO₃P: C 51.63, H 4.33, N 4.76; found: C 51.88, H 4.40, N 4.85.

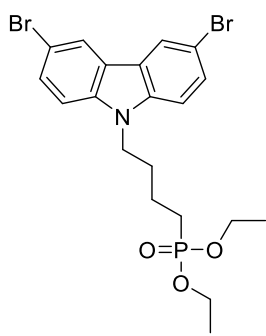
9-(4-Bromobutyl)-3,6-dibromo-9H-carbazole (**18**)



Method II. 3,6-Dibromo-9H-carbazole (1 g, 3.07 mmol), 1,4-dibromobutane (0.55 ml, 4.61 mmol), NaH (0.18 g, 4.61 mmol) and 15 ml of DMF were used for the reaction. Eluent: TLC (acetone:n-hexane, 1:24), column (acetone:n-hexane, 1:24). Product obtained as white crystals (1.09 g, 77% yield). M.p. 116.5–118 °C.

¹H NMR (400 MHz, CDCl₃): δ 8.12 (s, 2H, 4-H, 5-H of Cz), 7.55 (d, J = 8.7 Hz, 2H, Ht), 7.25 (d, J = 8.7 Hz, 2H, Ht), 4.27 (t, J = 7.0 Hz, 2H, NCH₂), 3.36 (t, J = 6.4 Hz, 2H, CH₂Br), 2.07 – 1.96 (m, 2H, CH₂), 1.91 – 1.81 (m, 2H, CH₂) ppm. ¹³C NMR (101 MHz, CDCl₃): δ 139.17, 129.19, 123.54, 123.38, 112.21, 110.27, 42.47, 32.86, 30.04, 27.47 ppm. Anal. calcd. for C₁₆H₁₄Br₃N: C 41.78, H 3.07, N 3.04; found: C 41.90, H 3.17, N 3.20.

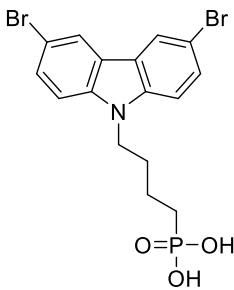
Diethyl [4-(3,6-dibromo-9H-carbazol-9-yl)butyl]phosphonate (**19**)



Method IV. 9-(6-Bromohexyl)-3,6-dibromo-9H-carbazole (**18**) (1.07 g, 2.06 mmol) and triethyl phosphite (7.1 ml, 41.37 mmol) were used for the reaction. Eluent: TLC (acetone:n-hexane, 7:18), column (acetone:n-hexane, 7:18). Product obtained as a yellowish resin (1.109 g, 92% yield).

¹H NMR (400 MHz, CDCl₃): δ 8.10 (s, 2H, 4-H, 5-H of Cz), 7.53 (d, J = 8.7 Hz, 2H, Ht), 7.24 (d, J = 8.7 Hz, 2H, Ht), 4.23 (t, J = 7.0 Hz, 2H, NCH₂), 4.01 (quint, J = 7.2 Hz, 4H, OCH₂), 2.01 – 1.86 (m, 2H, CH₂), 1.78 – 1.50 (m, 4H, Aliph), 1.24 (t, J = 7.0 Hz, 6H, CH₃) ppm. ¹³C NMR (101 MHz, CDCl₃): δ 139.29, 129.21, 123.59, 123.40, 112.22, 110.41, 61.68 (d, ²J_(C,P) = 6.6 Hz), 42.93, 29.64 (d, ²J_(C,P) = 14.9 Hz), 25.47 (d, ¹J_(C,P) = 141.8 Hz), 20.49 (d, ³J_(C,P) = 5.1 Hz), 16.52 (d, ³J_(C,P) = 6.0 Hz) ppm. Anal. calcd. for C₂₀H₂₄Br₂NO₃P: C 46.45, H, 4.68, N, 2.71; found: C 46.60, H 4.79, N 2.55.

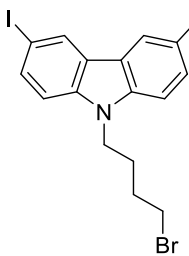
[4-(3,6-Dibromo-9H-carbazol-9-yl)butyl]phosphonic acid (20)



Method VI. Diethyl [4-(3,6-dibromo-9H-carbazol-9-yl)butyl]phosphonate (**19**) (0.5 g, 0.96 mmol), bromotrimethylsilane (1.3 ml, 9.66), methanol (0.4 ml, 9.66 mmol) and 15 ml of 1,4-dioxane were used. Eluent: TLC (acetone:*n*-hexane, 7:18). Product was purified by dissolving in the minimum amount of THF, precipitating into 20-fold excess of *n*-hexane, filtering, and washing with *n*-hexane to give white crystals (0.29 g, 65%). M.p. 203–204.5 °C (melting and decomposition).

¹H NMR (400 MHz, DMSO-d₆): δ 8.46 (s, 2H, 4-H, 5-H of Cz), 7.71 – 7.50 (m, 4H, Ht), 4.39 (t, *J* = 6.9 Hz, 2H, NCH₂), 1.90 – 1.72 (m, 2H, CH₂), 1.60 – 1.40 (m, 4H, Aliph) ppm. ¹³C NMR (101 MHz, DMSO-d₆): δ 139.05, 128.82, 123.43, 122.91, 111.76, 111.26, 42.29, 29.41 (d, ²*J*_(C,P) = 15.4 Hz), 27.29 (d, ¹*J*_(C,P) = 136.6 Hz), 20.34 (d, ³*J*_(C,P) = 4.2 Hz) ppm. Anal. calcd. for C₁₆H₁₆Br₂NO₃P: C 41.68, H, 3.50, N, 3.04; found: C 41.49, H 3.35, N 3.11.

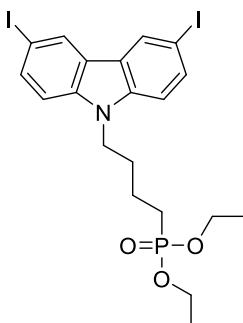
9-(4-Iodobutyl)-3,6-dibromo-9H-carbazole (21)



Method III. 3,6-Diiodo-9H-carbazole (0.7 g, 1.67 mmol), 1,4-dibromobutane (0.3 ml, 2.51 mmol), KOH (0.14 g, 2.51 mmol) and 10 ml of DMF were used for the reaction. Reaction conducted overnight. Eluent: TLC (acetone:*n*-hexane, 1:24), column (acetone:*n*-hexane, 1:24). Product obtained as white solid (0.61 g, 66% yield).

¹H NMR (400 MHz, DMSO-d₆): δ 8.61 (s, 2H, 4-H, 5-H of Cz), 7.73 (d, *J* = 8.6 Hz, 2H, Ht), 7.52 (d, *J* = 8.6 Hz, 2H, Ht), 4.41 (t, *J* = 6.4 Hz, 2H, NCH₂), 3.51 (t, *J* = 6.3 Hz, 2H, CH₂Br), 1.89 – 1.71 (m, 4H, Aliph) ppm. ¹³C NMR (101 MHz, DMSO-d₆): δ 139.10, 134.24, 129.34, 123.45, 112.03, 82.32, 41.53, 34.61, 29.68, 27.10 ppm. Anal. calcd. for C₁₆H₁₄BrI₂N: C 34.69, H 2.55, N 2.53; found: C 34.58, H 2.62, N 2.29.

Diethyl [4-(3,6-diiodo-9H-carbazol-9-yl)butyl]phosphonate (22)

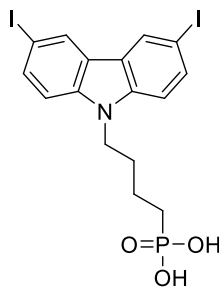


Method IV. 9-(4-Iodobutyl)-3,6-dibromo-9H-carbazole (**21**) (0.58 g, 1.05 mmol) and triethyl phosphite (3.6 ml, 20.9 mmol) were used for the reaction. Eluent: TLC (acetone:*n*-hexane, 7:18), column (acetone:*n*-hexane, 7:18). Product obtained as a yellowish resin (0.6 g, 94% yield).

¹H NMR (400 MHz, DMSO-d₆): δ 8.60 (s, 2H, 4-H, 5-H of Cz), 7.73 (d, *J* = 8.6 Hz, 2H, Ht), 7.52 (d, *J* = 8.6 Hz, 2H, Ht), 4.38 (t, *J* = 6.8 Hz, 2H, NCH₂), 3.87 (p, *J* = 7.2 Hz, 4H, OCH₂), 1.85 – 1.64 (m, 4H, Aliph), 1.50 – 1.36 (m, 2H, CH₂), 1.12 (t, *J* = 7.0 Hz, 6H, CH₃) ppm. ¹³C NMR (101 MHz, DMSO-d₆):

δ 139.14, 134.18, 129.29, 123.43, 112.12, 82.23, 60.74 (d, $^2J_{(C,P)} = 6.3$ Hz), 41.90, 29.00 (d, $^2J_{(C,P)} = 15.9$ Hz), 24.14 (d, $^1J_{(C,P)} = 138.6$ Hz), 19.60 (d, $^3J_{(C,P)} = 4.8$ Hz), 16.20 (d, $^3J_{(C,P)} = 5.7$ Hz) ppm. Anal. calcd. for $C_{20}H_{24}I_2NO_3P$: C 39.30, H, 3.96, N, 2.29; found: C 39.50, H 4.15, N 2.33.

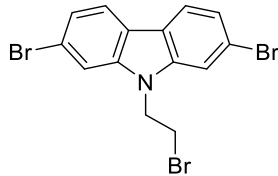
[4-(3,6-Dibromo-9*H*-carbazol-9-yl)butyl]phosphonic acid (**23**)



Method VI. Diethyl [4-(3,6-diiodo-9*H*-carbazol-9-yl)butyl]phosphonate (**22**) (0.57 g, 0.93 mmol), bromotrimethylsilane (1.2 ml, 9.32), methanol (0.4 ml, 9.32 mmol) and 15 ml of 1,4-dioxane were used. Eluent: TLC (acetone:*n*-hexane, 8:17). Product was purified by dissolving in the minimum amount of THF, precipitating into 20-fold excess of *n*-hexane, filtering, and washing with *n*-hexane to give white crystals (0.41 g, 79%). M.p. 193.5–195 °C (melting and decomposition).

1H NMR (400 MHz, DMSO-d₆): δ 8.60 (s, 2H, 4-H, 5-H of Cz), 7.72 (d, $J = 8.5$ Hz, 2H, Ht), 7.51 (d, $J = 8.6$ Hz, 2H, Ht), 4.36 (t, $J = 6.5$ Hz, 2H, NCH₂), 1.86 – 1.70 (m, 2H, CH₂), 1.58 – 1.40 (m, 4H, Aliph) ppm. ^{13}C NMR (101 MHz, DMSO-d₆): δ 139.14, 134.21, 129.29, 123.42, 112.11, 82.22, 42.17, 29.38 (d, $^2J_{(C,P)} = 15.5$ Hz), 27.28 (d, $^1J_{(C,P)} = 136.4$ Hz), 20.33 (d, $^3J_{(C,P)} = 4.2$ Hz) ppm. Anal. calcd. for $C_{16}H_{16}I_2NO_3P$: C 34.62, H, 2.91, N, 2.52; found: C 34.47, H 2.86, N 2.51.

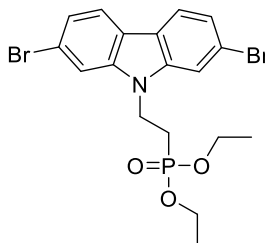
9-(2-Bromoethyl)-2,7-dibromo-9*H*-carbazole (**24**)



Method I. 2,7-Dibromo-9*H*-carbazole (0.5 g, 1.53 mmol), 1,2-dibromoethane (3.32 ml, 38.46 mmol), 50 % KOH aqueous solution (0.86 ml, 7.69 mmol) and tetrabutylammonium bromide (0.07 g, 0.23 mmol) were used for the reaction. Reaction conducted for 24 hours. Eluent: TLC (acetone:*n*-hexane, 3:22), column (acetone:*n*-hexane, 3:22). Product obtained as white crystals (0.44 g, 67% yield). M.p. 164–165 °C.

1H NMR (400 MHz, CDCl₃): δ 7.87 (d, $J = 8.3$ Hz, 2H, Ht), 7.55 (s, 2H, 1-H, 8-H of Cz), 7.37 (d, $J = 8.3$ Hz, 2H, Ht), 4.58 (t, $J = 7.2$ Hz, 2H, NCH₂), 3.65 (t, $J = 7.2$ Hz, 2H, CH₂Br) ppm. ^{13}C NMR (101 MHz, CDCl₃): δ 141.04, 123.50, 121.77, 121.68, 120.12, 112.03, 44.91, 27.82 ppm. Anal. calcd. for $C_{14}H_{10}Br_3N$: C 38.93, H 2.33, N 3.24; found: C 38.82, H 2.40, N 3.06.

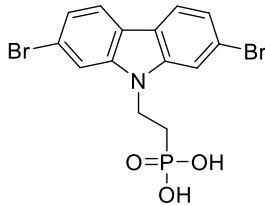
Diethyl [2-(2,7-dibromo-9H-carbazol-9-yl)ethyl]phosphonate (25)



Method IV. 9-(2-Bromoethyl)-2,7-dibromo-9H-carbazole (**24**) (0.42 g, 0.97 mmol) and triethyl phosphite (3.3 ml, 19.44 mmol) were used for the reaction. Eluent: TLC (acetone:*n*-hexane, 7:18), column (acetone:*n*-hexane, 7:18). Product obtained as white crystals (0.45 g, 95% yield). M.p. 88.5–90 °C.

¹H NMR (400 MHz, CDCl₃): δ 7.86 (d, *J* = 8.3 Hz, 2H, Ht), 7.55 (s, 2H, 2H, 1-H, 8-H of Cz), 7.35 (d, *J* = 8.3 Hz, 2H, Ht), 4.49 (dd, *J* = 15.9, 10.0 Hz, 2H, NCH₂), 4.14 – 4.02 (m, 4H, OCH₂), 2.28 – 2.19 (m, 2H, CH₂P), 1.27 (t, *J* = 7.1 Hz, 6H, CH₃) ppm. ¹³C NMR (101 MHz, CDCl₃): δ 140.67, 123.06, 121.58, 121.51, 119.91, 111.98, 62.08 (d, ²*J*_(C,P) = 6.5 Hz), 37.23 (d, ²*J*_(C,P) = 1.8 Hz), 25.28 (d, ¹*J*_(C,P) = 139.1 Hz), 16.42 (d, ³*J*_(C,P) = 6.1 Hz) ppm. Anal. calcd. for C₁₈H₂₀Br₂NO₃P: C 44.20, H 4.12, N 2.86; found: C 44.32, H 4.25, N 2.90.

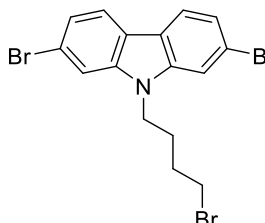
[2-(2,7-Dibromo-9H-carbazol-9-yl)ethyl]phosphonic acid (26)



Method VI. Diethyl [2-(2,7-dibromo-9H-carbazol-9-yl)ethyl]phosphonate (**25**) (0.43 g, 0.88 mmol), bromotrimethylsilane (1.1 ml, 8.79), methanol (0.4 ml, 8.79 mmol) and 15 ml of 1,4-dioxane were used. Eluent: TLC (acetone:*n*-hexane, 7:18). Product was purified by dissolving in the minimum amount of THF, precipitating into 20-fold excess of *n*-hexane, filtering, and washing with *n*-hexane to give grey crystals (0.32 g, 86% yield). M.p. 259–261 °C (melting and decomposition).

¹H NMR (400 MHz, DMSO-d₆): δ 8.12 (d, *J* = 8.3 Hz, 2H, Ht), 7.81 (s, 2H, 1-H, 8-H of Cz), 7.37 (d, *J* = 8.3 Hz, 2H, Ht), 4.52 (dd, *J* = 15.7, 8.6 Hz, 2H, NCH₂), 2.12 – 1.97 (m, 2H, CH₂P) ppm. ¹³C NMR (101 MHz, DMSO-d₆): δ 140.64, 122.38, 122.30, 120.95, 119.23, 112.30, 37.76, 27.10 (d, ¹*J*_(C,P) = 131.2 Hz) ppm. Anal. calcd. for C₁₄H₁₂Br₂NO₃P: C 38.83, H 2.79, N, 3.23; found: C 38.61, H 2.90, N 3.35.

9-(4-Bromobutyl)-2,7-dibromo-9H-carbazole (27)

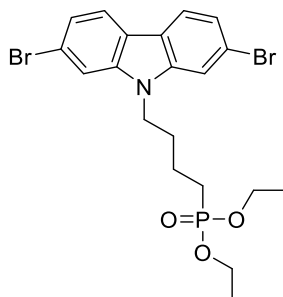


Method II. 2,7-Dibromo-9H-carbazole (0.5 g, 1.53 mmol), 1,4-dibromobutane (0.28 ml, 2.30 mmol), NaH (0.09 g, 2.30 mmol) and 10 ml of DMF were used for the reaction. Eluent: TLC (acetone:*n*-hexane, 1:24), column (acetone:*n*-hexane, 1:24). Product obtained as white crystals (0.56 g, 80% yield). M.p. 109.5–110.5 °C.

¹H NMR (400 MHz, CDCl₃): δ 7.89 (d, *J* = 8.3 Hz, 2H, Ht), 7.53 (s, 2H, 1-H, 8-H of Cz), 7.35 (d, *J* = 8.3 Hz, 2H, Ht), 4.24 (t, *J* = 7.0 Hz, 2H, NCH₂), 3.41 (t, *J* = 6.3 Hz, 2H, CH₂Br), 2.09 – 1.98 (m, 2H, CH₂), 1.97 – 1.86 (m, 2H, CH₂) ppm. ¹³C NMR (101 MHz, CDCl₃): δ 152.79, 141.35,

122.93, 121.72, 121.50, 119.97, 112.04, 42.63, 32.97, 30.17, 27.61 ppm. Anal. calcd. for C₁₆H₁₄Br₃N: C 41.78, H 3.07, N 3.04; found: C 42.01, H 3.20, N 3.17.

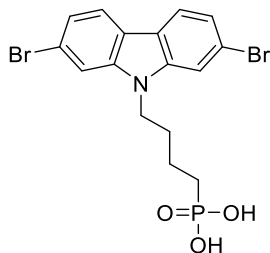
Diethyl [4-(2,7-dibromo-9H-carbazol-9-yl)butyl]phosphonate (28)



Method IV. 9-(6-Bromohexyl)-2,7-dibromo-9H-carbazole (**27**) (0.52 g, 1.13 mmol) and triethyl phosphite (3.9 ml, 22.60 mmol) were used for the reaction. Eluent: TLC (acetone:*n*-hexane, 7:18), column (acetone:*n*-hexane, 7:18). Product obtained as a lightly yellow resin (0.52 g, 90%).

¹H NMR (400 MHz, CDCl₃): δ 7.87 (d, *J* = 8.3 Hz, 2H, Ht), 7.51 (s, 2H, 1-H, 8-H of Cz), 7.33 (d, *J* = 8.3 Hz, 2H, Ht), 4.20 (t, *J* = 7.1 Hz, 2H, NCH₂), 4.13 – 3.98 (m, 4H, OCH₂), 2.03 – 1.87 (m, 2H, CH₂), 1.83 – 1.60 (m, 4H, CH₂), 1.27 (t, *J* = 7.0 Hz, 6H, CH₃) ppm. ¹³C NMR (101 MHz, CDCl₃): δ 141.35, 122.83, 121.66, 121.45, 119.89, 112.02, 61.76 (d, ²*J*_(C,P) = 6.6 Hz), 42.99, 29.62 (d, ²*J*_(C,P) = 15.1 Hz), 25.53 (d, ¹*J*_(C,P) = 141.7 Hz), 20.57 (d, ²*J*_(C,P) = 5.1 Hz), 16.58 (d, ³*J*_(C,P) = 5.9 Hz) ppm. Anal. calcd. for C₂₀H₂₄Br₂NO₃P: C 46.45, H 4.68, N, 2.71; found: C 46.58, H 4.50, N 2.84.

[4-(2,7-Dibromo-9H-carbazol-9-yl)butyl]phosphonic acid (29)

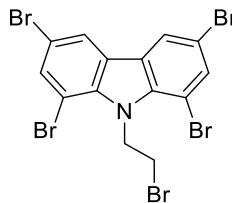


Method VI. Diethyl [4-(2,7-dibromo-9H-carbazol-9-yl)butyl]phosphonate (**28**) (0.5 g, 0.96 mmol), bromotrimethylsilane (1.3 ml, 9.66), methanol (0.4 ml, 9.66 mmol) and 15 ml of 1,4-dioxane were used. Eluent: TLC (acetone:*n*-hexane, 7:18). Product was purified by dissolving in the minimum amount of THF, precipitating into 20-fold excess of *n*-hexane, filtering, and washing with *n*-hexane to give white crystals (0.254 g, 57% yield). M.p.

189.5–190.5 °C (melting and decomposition).

¹H NMR (400 MHz, DMSO-d₆): δ 8.11 (d, *J* = 8.3 Hz, 2H, Ht), 7.94 (s, 2H, 1-H, 8-H of Cz), 7.35 (d, *J* = 8.3 Hz, 2H, Ht), 4.39 (t, *J* = 7.2 Hz, 2H, NCH₂), 1.87 – 1.70 (m, 2H, CH₂), 1.63 – 1.46 (m, 4H, CH₂) ppm. ¹³C NMR (101 MHz, DMSO-d₆): δ 141.09, 122.18, 122.14, 120.68, 119.22, 112.52, 42.26, 29.36 (d, ²*J*_(C,P) = 15.6 Hz), 27.31 (d, ¹*J*_(C,P) = 136.8 Hz), 20.24 (d, ³*J*_(C,P) = 4.5 Hz) ppm. Anal. calcd. for C₁₆H₁₆Br₂NO₃P: C 41.68, H, 3.50, N, 3.04; found: C 41.82, H 3.39, N 2.98

1,3,6,8-Tetrabromo-9-(2-bromoethyl)-9H-carbazole (30)

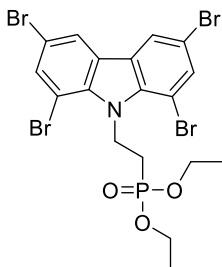


Method I. 1,3,6,8-Tetrabromo-9H-carbazole (0.6 g, 1.24 mmol), 1,2-dibromoethane (2.68 ml, 27.28 mmol), 50 % KOH aqueous solution (0.7 ml, 6.2 mmol) and tetrabutylammonium bromide (0.06 g, 0.18 mmol) were used for the reaction. Reaction conducted for 48 hours. Eluent: TLC (acetone:*n*-

hexane, 1:24), column (acetone:*n*-hexane, 1:24). Product obtained as white crystals (0.60 g, 83% yield). M.p. 188.5–190 °C.

¹H NMR (400 MHz, CDCl₃): δ 7.96 (s, 2H, 4-H, 5-H of Cz), 7.73 (s, 2H, 2-H, 7-H of Cz), 5.35 (t, *J* = 7.9 Hz, 2H, NCH₂), 3.65 (t, *J* = 8.0 Hz, 2H, CH₂Br) ppm. ¹³C NMR (101 MHz, CDCl₃): δ 136.83, 135.30, 126.42, 122.45, 113.81, 104.16, 45.32, 30.04 ppm. Anal. calcd. for C₁₄H₁₀Br₅N: C 28.51, H 1.37, N 2.38; found: C 28.74, H 1.52, N 2.47.

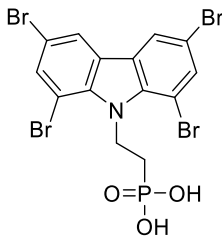
Diethyl [2-(1,3,6,8-tetrabromo-9H-carbazol-9-yl)ethyl]phosphonate (31)



Method IV. 9-(2-Bromoethyl)-1,3,6,8-tetrabromo-9H-carbazole (**30**) (0.27 g, 0.45 mmol) and triethyl phosphite (1.6 ml, 9 mmol) were used for the reaction. Eluent: TLC (acetone:*n*-hexane, 6:19), column (acetone:*n*-hexane, 6:19). Product obtained as white crystals (0.1 g, 36% yield). M.p. 211.5–213.5 °C.

¹H NMR (400 MHz, CDCl₃): δ 8.03 (s, 2H, 4-H, 5-H of Cz), 7.79 (s, 2H, 2-H, 7-H of Cz), 5.43 (dt, *J* = 8.7, 5.3 Hz, 2H, NCH₂), 4.18 – 4.06 (m, 4H, OCH₂), 2.38 – 2.20 (m, 2H, CH₂P), 1.33 (t, *J* = 7.0 Hz, 6H, CH₃) ppm. ¹³C NMR (101 MHz, CDCl₃): δ 136.91, 135.22, 126.73, 122.32, 113.65, 104.36, 61.97 (d, ²J_(C,P) = 6.4 Hz), 39.55, 28.72 (d, ¹J_(C,P) = 136.0 Hz), 16.65 (d, ³J_(C,P) = 6.2 Hz) ppm. Anal. calcd. for C₁₈H₁₈Br₄NO₃P: C 33.42, H, 2.80, N, 2.17; found: C 33.28, H 2.71, N 2.25.

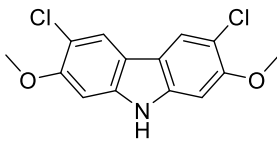
[2-(1,3,6,8-Tetrabromo-9H-carbazol-9-yl)ethyl]phosphonic acid (32)



Method VI. Diethyl [2-(1,3,6,8-tetrabromo-9H-carbazol-9-yl)ethyl]phosphonate (**31**) (0.09 g, 0.14 mmol), bromotrimethylsilane (0.2 ml, 1.39 mmol), methanol (0.05 ml, 1.39 mmol) and 6 ml of anhydrous 1,4-dioxane:DCM (1:1) were used. Eluent: TLC (acetone:*n*-hexane, 6:19). Product was purified by dissolving in the minimum amount of THF, precipitating into 20-fold excess of *n*-hexane, filtering, and washing with *n*-hexane to give white crystals (0.07 g, 87% yield). M.p. 331–332 °C (melting and decomposition).

¹H NMR (400 MHz, DMSO-d₆): δ 8.58 (s, 2H, 4-H, 5-H of Cz), 7.90 (s, 2H, 2-H, 7-H of Cz), 5.29 – 5.19 (m, 2H, NCH₂), 2.13 – 2.02 (m, 2H, CH₂P) ppm. ¹³C NMR (101 MHz, DMSO-d₆): δ 136.70, 134.30, 126.39, 123.14, 112.84, 103.89, 42.36, 30.79 (d, ¹J_(C,P) = 128.4 Hz) ppm. Anal. calcd. for C₁₄H₁₀Br₄NO₃P: C 28.46, H, 1.71, N, 2.37; found: C 28.50, H 1.79, N 2.56.

3,6-Dichloro-2,7-dimethoxy-9H-carbazole (33)

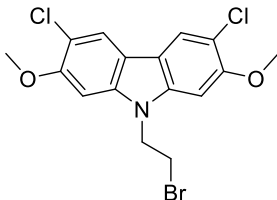


2,7-Dimethoxy-9*H*-carbazole (0.8 g, 3.52 mmol) was dissolved in 20 ml of DMF, followed by addition of (0.96 g, 7.21 mmol) *N*-chlorosuccinimide. Reaction conducted for 72 hours at 30 °C. After termination of reaction (TLC, eluent THF:*n*-hexane, 7:18), reaction mixture was poured

into excess of distilled water. Precipitated crude product was filtered off, washed with distilled water, and purified by column chromatography (eluent THF:*n*-hexane, 7:18). Product obtained as white crystals (0.76g, 73% yield). M.p. 287–288 °C (melting and decomposition).

¹H NMR (400 MHz, DMSO-d₆): δ 11.25 (s, 1H, NH), 8.13 (s, 2H, 4-H, 5-H of Cz), 7.13 (s, 2H, 1-H, 8-H of Cz), 3.92 (s, 6H, OCH₃) ppm. ¹³C NMR (101 MHz, DMSO-d₆): δ 152.60, 139.61, 120.70, 115.71, 113.31, 94.96, 56.14 ppm. Anal. calcd. for C₁₄H₁₁Cl₂NO₂: C 56.78, H, 3.74, N, 4.73; found: C 56.99, H 3.92, N 4.80.

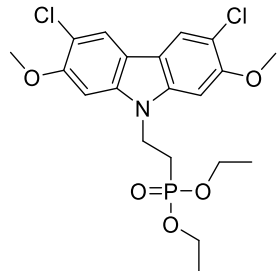
9-(2-Bromoethyl)-3,6-dichloro-2,7-dimethoxy-9H-carbazole (34)



Method I. 3,6-Dichloro-2,7-dimethoxy-9*H*-carbazole (1.15 g, 3.88 mmol), 1,2-dibromoethane (8.4 ml, 97 mmol), 50 % KOH aqueous solution (2.2 ml, 19.4 mmol) and tetrabutylammonium bromide (0.19 g, 0.58 mmol) were used for the reaction. Reaction conducted for 72 hours. Eluent: TLC (THF:*n*-hexane, 7:18), column (THF:*n*-hexane, 7:18). Product obtained as white crystals (1.01 g, 65% yield). M.p. 232.5–234 °C (melting and decomposition).

¹H NMR (400 MHz, DMSO-d₆): δ 8.16 (s, 2H, 4-H, 5-H of Cz), 7.36 (s, 2H, 1-H, 8-H of Cz), 4.85 (t, *J* = 6.2 Hz, 2H, NCH₂), 3.97 (s, 6H, OCH₃), 3.91 (t, *J* = 6.2 Hz, 2H, CH₂Br) ppm. ¹³C NMR (101 MHz, DMSO-d₆): δ 152.81, 139.85, 120.67, 115.31, 113.86, 94.43, 56.48, 43.81, 31.18 ppm. Anal. calcd. for C₁₆H₁₄BrCl₂NO₂: C 47.67, H, 3.50, N, 3.47; found: C 47.40, H 3.39, N 4.52.

Diethyl [2-(3,6-dichloro-2,7-dimethoxy-9H-carbazol-9-yl)ethyl]phosphonate (35)

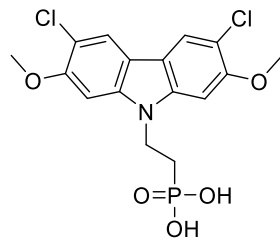


Method IV. 9-(2-Bromoethyl)-3,6-dichloro-2,7-dimethoxy-9*H*-carbazole (34) (0.97 g, 2.41 mmol) and triethyl phosphite (8.3 ml, 48.1 mmol) were used for the reaction. Eluent: TLC (acetone:*n*-hexane, 2:3), column (acetone:*n*-hexane, 2:3). Product obtained as white crystals (0.91 g, 83% yield). M.p. 189–190.5 °C.

¹H NMR (400 MHz, DMSO-d₆): δ 8.15 (s, 2H, 4-H, 5-H of Cz), 7.26 (s, 2H, 1-H, 8-H of Cz), 4.64 – 4.48 (m, 2H, NCH₂), 3.97 (s, 6H, OCH₃), 3.87 (p, *J* = 7.2 Hz, 4H, OCH₂), 2.31 (dt, *J* = 17.6, 6.7 Hz, 2H, CH₂P), 1.05 (t, *J* = 7.0 Hz, 6H, CH₂OEt) ppm. ¹³C NMR (101 MHz, DMSO-d₆): δ 152.72, 139.47, 120.68, 115.32, 113.61, 94.07, 61.09 (d, ²J_{C,P} = 6.3 Hz), 56.25,

36.74 (d, $^2J_{(C,P)} = 3.0$ Hz), 23.90 (d, $^1J_{(C,P)} = 136.7$ Hz), 15.97 (d, $^3J_{(C,P)} = 6.1$ Hz) ppm. Anal. calcd. for $C_{20}H_{24}Cl_2NO_5P$: C 52.19, H, 5.26, N, 3.04; found: C 52.01, H 5.47, N 3.00.

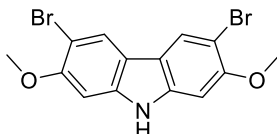
[2-(3,6-Dichloro-2,7-dimethoxy-9H-carbazol-9-yl)ethyl]phosphonic acid (36)



Method VI. Diethyl [2-(3,6-dichloro-2,7-dimethoxy-9H-carbazol-9-yl)ethyl]phosphonate (**35**) (0.88 g, 1.91 mmol), bromotrimethylsilane (2.5 ml, 19.1 mmol), methanol (0.8 ml, 19.1 mmol) and 20 ml of anhydrous 1,4-dioxane were used. Eluent: TLC (acetone:*n*-hexane, 2:3). Product was purified by dissolving in the minimum amount of THF, precipitating into 20-fold excess of *n*-hexane, filtering, and washing with *n*-hexane to give white crystals (0.59 g, 77% yield). M.p. 261.5–263.5 °C (melting and decomposition).

1H NMR (400 MHz, DMSO- d_6): δ 8.15 (s, 2H, 4-H, 5-H of Cz), 7.27 (s, 2H, 1-H, 8-H of Cz), 4.53 (dd, $J = 15.5, 8.9$ Hz, 2H, NCH_2), 3.96 (s, 6H, OCH_3), 2.14 – 1.97 (m, 2H, CH_2P) ppm. ^{13}C NMR (101 MHz, DMSO- d_6): δ 152.86, 139.45, 120.84, 115.34, 113.62, 93.80, 56.32, 37.42, 27.06 (d, $^1J_{(C,P)} = 131.9$ Hz) ppm. Anal. calcd. for $C_{16}H_{16}Cl_2NO_5P$: C 47.55, H, 3.99, N, 3.47; found: C 47.69, H 3.87, N 3.25.

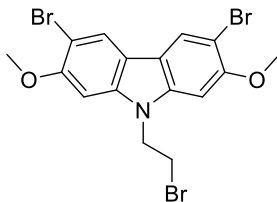
3,6-Dibromo-2,7-dimethoxy-9H-carbazole (37)



2,7-Dimethoxy-9H-carbazole (3 g, 13.2 mmol) was dissolved in 100 ml of DMF, followed by addition of *N*-chlorosuccinimide (4.81 g, 27.1 mmol). Reaction conducted for 1 hour at 25 °C. After termination of reaction (TLC, eluent THF:*n*-hexane, 7:18), reaction mixture was poured into excess of distilled water. Precipitated crude product was filtered off, washed with distilled water, and purified by column chromatography (eluent THF:*n*-hexane, 7:18). Product obtained as white crystals (3.23 g, 64% yield). M.p. 211–212 °C (melting and decomposition).

1H NMR (400 MHz, DMSO- d_6): δ 11.27 (s, 1H, NH), 8.28 (s, 2H, 4-H, 5-H of Cz), 7.11 (s, 2H, 1-H, 8-H of Cz), 3.91 (s, 6H, OCH_3) ppm. ^{13}C NMR (101 MHz, DMSO- d_6): δ 153.25, 140.19, 123.73, 116.46, 102.21, 94.90, 56.26 ppm. Anal. calcd. for $C_{14}H_{11}Br_2NO_2$: C 43.67, H, 2.88, N, 3.64; found: C 43.58, H 2.81, N 3.80.

9-(2-Bromoethyl)-3,6-dibromo-2,7-dimethoxy-9H-carbazole (38)

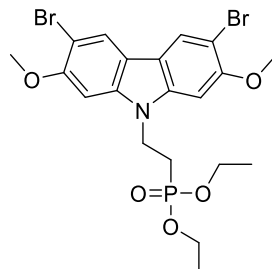


Method I. 3,6-Dibromo-2,7-dimethoxy-9H-carbazole (**37**) (1.1 g, 2.86 mmol), 1,2-dibromoethane (6.1 ml, 71.4 mmol), 50 % KOH aqueous solution (1.6 ml, 14.3 mmol) and tetrabutylammonium bromide (0.14 g, 0.43 mmol) were used for the reaction. Reaction conducted for 72 hours. Eluent: TLC (acetone:*n*-hexane, 4:21), column

(acetone:*n*-hexane, 4:21). Product obtained as white crystals (0.96 g, 69% yield). M.p. 206–208 °C (melting and decomposition).

¹H NMR (400 MHz, DMSO-d₆): δ 8.32 (s, 2H, 4-H, 5-H of Cz), 7.35 (s, 2H, 1-H, 8-H of Cz), 4.85 (t, *J* = 6.3 Hz, 2H, NCH₂), 3.96 (s, 6H, OCH₃), 3.92 (t, *J* = 6.3 Hz, 2H, CH₂Br) ppm. ¹³C NMR (101 MHz, DMSO-d₆): δ 153.47, 140.47, 123.70, 116.05, 102.77, 94.38, 56.61, 43.77, 31.17 ppm. Anal. calcd. for C₁₆H₁₄Br₃NO₂: C 39.06, H, 2.87, N, 2.85; found: C 38.92, H 2.77, N 2.99.

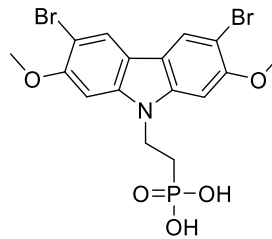
Diethyl [2-(3,6-dibromo-2,7-dimethoxy-9H-carbazol-9-yl)ethyl]phosphonate (39)



Method IV. 9-(2-Bromoethyl)-3,6-dibromo-2,7-dimethoxy-9H-carbazole (**38**) (0.92 g, 1.87 mmol) and triethyl phosphite (6.4 ml, 37.4 mmol) were used for the reaction. Eluent: TLC (acetone:*n*-hexane, 2:3), column (acetone:*n*-hexane, 2:3). Product obtained as white crystals (0.66 g, 65% yield). M.p. 207–208 °C.

¹H NMR (400 MHz, DMSO-d₆): δ 8.30 (s, 2H, 4-H, 5-H of Cz), 7.25 (s, 2H, 1-H, 8-H of Cz), 4.62 – 4.50 (m, 2H, NCH₂), 3.96 (s, 6H, OCH₃), 3.86 (p, *J* = 7.2 Hz, 4H, OCH₂), 2.31 (dt, *J* = 17.8, 6.8 Hz, 2H, CH₂P), 1.04 (t, *J* = 7.0 Hz, 6H, CH₂CH₃) ppm. ¹³C NMR (101 MHz, DMSO-d₆): δ 153.44, 140.13, 123.75, 116.11, 102.55, 94.06, 61.18 (d, ²J_(C,P) = 6.2 Hz), 56.43, 36.73 (d, ²J_(C,P) = 3.3 Hz), 23.86 (d, ¹J_(C,P) = 136.7 Hz), 16.00 (d, ³J_(C,P) = 6.1 Hz) ppm. Anal. calcd. for C₂₀H₂₄Br₂NO₅P: C 43.74, H, 4.40, N, 2.55; found: C 43.80, H 4.23, N 2.41.

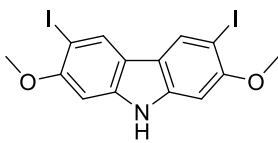
[2-(3,6-Dibromo-2,7-dimethoxy-9H-carbazol-9-yl)ethyl]phosphonic acid (40)



Method VI. Diethyl [2-(3,6-dibromo-2,7-dimethoxy-9H-carbazol-9-yl)ethyl]phosphonate (**39**) (0.63 g, 1.15 mmol), bromotrimethylsilane (1.5 ml, 11.5 mmol), methanol (0.5 ml, 11.5 mmol) and 15 ml of anhydrous 1,4-dioxane were used. Eluent: TLC (acetone:*n*-hexane, 2:3). Product was purified by dissolving in the minimum amount of THF, precipitating into 20-fold excess of *n*-hexane, filtering, and washing with *n*-hexane to give white crystals (0.33 g, 58% yield). M.p. - 204 °C (decomposition).

¹H NMR (400 MHz, DMSO-d₆): δ 8.30 (s, 2H, 4-H, 5-H of Cz), 7.25 (s, 2H, 1-H, 8-H of Cz), 4.61 – 4.43 (m, 2H, NCH₂), 3.96 (s, 6H, OCH₃), 2.04 (dd, *J* = 18.2, 9.0 Hz, 2H, CH₂P) ppm. ¹³C NMR (101 MHz, DMSO-d₆): δ 153.52, 140.06, 123.85, 116.08, 102.52, 93.74, 56.45, 37.39, 32.75, 27.02 (d, ¹J_(C,P) = 131.9 Hz) ppm. Anal. calcd. for C₁₆H₁₆Br₂NO₅P: C 38.97, H, 3.27, N, 2.84; found: C 39.01, H 3.20, N 2.77.

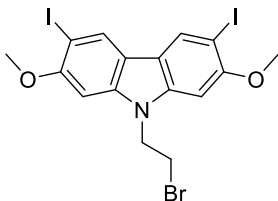
3,6-Diiodo-2,7-dimethoxy-9H-carbazole (41)



2,7-Dimethoxy-9H-carbazole (0.6 g, 2.64 mmol) was dissolved in 15 ml of DMF, followed by addition of *N*-iodosuccinimide (1.22 g, 5.41 mmol). Reaction conducted for 2 hours at 25 °C. After termination of reaction (TLC, eluent THF:*n*-hexane, 6:19), reaction mixture was poured into excess of distilled water. Precipitated crude product was filtered off, washed with distilled water, and purified by column chromatography (eluent THF:*n*-hexane, 6:19). Product obtained as white crystals (1.04 g, 83% yield). M.p. – 185 °C (decomposition).

¹H NMR (400 MHz, DMSO-d₆): δ 11.23 (s, 1H, NH), 8.44 (s, 2H, 4-H, 5-H of Cz), 7.04 (s, 2H, 1-H, 8-H of Cz), 3.88 (s, 6H, OCH₃) ppm. ¹³C NMR (101 MHz, DMSO-d₆): δ 155.16, 141.00, 129.67, 117.50, 94.04, 75.60, 56.42 ppm. Anal. calcd. for C₁₄H₁₁I₂NO₂: C 35.10, H, 2.31, N, 2.92; found: C 35.00, H 2.28, N 2.85.

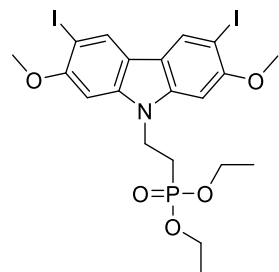
9-(2-Bromoethyl)-3,6-diiodo-2,7-dimethoxy-9H-carbazole (42)



Method I. 3,6-Diiodo-2,7-dimethoxy-9H-carbazole (41) (1 g, 2.08 mmol), 1,2-dibromoethane (4.5 ml, 52.2 mmol), 50 % KOH aqueous solution (1.2 ml, 10.4 mmol) and tetrabutylammonium bromide (0.1 g, 0.31 mmol) were used for the reaction. Reaction conducted overnight. Eluent: TLC (acetone:*n*-hexane, 4:21), column (acetone:*n*-hexane, 4:21). Product obtained as white crystals (1.05 g, 86% yield). M.p. 217–219 °C (melting and decomposition).

¹H NMR (400 MHz, DMSO-d₆): δ 8.48 (s, 2H, 4-H, 5-H of Cz), 7.27 (s, 2H, 1-H, 8-H of Cz), 4.84 (t, *J* = 6.2 Hz, 2H, NCH₂), 3.99 – 3.87 (m, 8H, CH₂Br and OCH₃ overlapped) ppm. ¹³C NMR (101 MHz, DMSO-d₆): δ 155.43, 141.35, 129.63, 117.10, 93.50, 76.29, 56.75, 43.66, 31.16 ppm. Anal. calcd. for C₁₆H₁₄BrI₂NO₂: C 32.79, H, 2.41, N, 2.39; found: C 33.01, H 2.56, N 2.47.

Diethyl [2-(3,6-diiodo-2,7-dimethoxy-9H-carbazol-9-yl)ethyl]phosphonate (43)

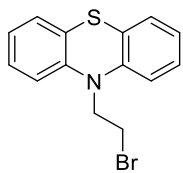


Method IV. 9-(2-Bromoethyl)-3,6-diiodo-2,7-dimethoxy-9H-carbazole (42) (1 g, 1.71 mmol) and triethyl phosphite (5.8 ml, 34.1 mmol) were used for the reaction. Eluent: TLC (acetone:*n*-hexane, 2:3), column (acetone:*n*-hexane, 2:3). Product obtained as white crystals (0.72 g, 66% yield). M.p. 218–219.5 °C.

¹H NMR (400 MHz, DMSO-d₆): δ 8.47 (s, 2H, 4-H, 5-H of Cz), 7.18 (s, 2H, 1-H, 8-H of Cz), 4.62 – 4.46 (m, 2H, NCH₂), 3.94 (s, 6H, OCH₃), 3.92 – 3.83 (m, 4H, OCH₂), 2.30 (dt, *J* = 17.7, 6.7 Hz, 2H, CH₂P), 1.05 (t, *J* = 7.0 Hz, 6H, CH₂CH₃) ppm. ¹³C NMR (101 MHz, DMSO-d₆): δ 155.37, 140.96, 129.65, 117.14, 93.16, 75.95, 61.12 (d, ²J_{C,P} = 6.3 Hz), 56.54, 36.58

(d, $^2J_{(C,P)} = 2.2$ Hz), 23.82 (d, $^1J_{(C,P)} = 135.4$ Hz), 15.98 (d, $^3J_{(C,P)} = 6.1$ Hz) ppm. Anal. calcd. for $C_{20}H_{24}I_2NO_5P$: C 37.35, H, 3.76, N, 2.18; found: C 37.54, H 3.84, N 2.11.

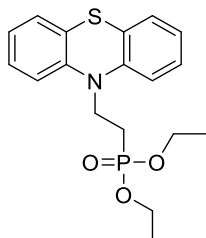
*10-(2-bromoethyl)-10*H*-phenothiazine (44)*



Method I. 10*H*-Phenothiazine (5 g, 25.1 mmol), 1,2-dibromoethane (54 ml, 627 mmol), 50 % KOH aqueous solution (14 ml, 125 mmol) and tetrabutylammonium bromide (1.21 g, 3.76 mmol) were used for the reaction. Reaction conducted for 96 hours. Eluent: TLC (acetone:*n*-hexane, 3:22), column (acetone:*n*-hexane, 3:22). Product obtained as yellow crystals (5.12 g, 66% yield). M.p. 78–80 °C.

1H NMR (400 MHz, DMSO-d₆): δ 7.24 – 7.13 (m, 4H, Ht), 7.04 (d, $J = 8.1$ Hz, 2H, Ht), 6.97 (t, $J = 7.4$ Hz, 2H, Ht), 4.30 (t, $J = 6.3$ Hz, 2H, NCH₂), 3.74 (t, $J = 6.3$ Hz, 2H, CH₂Br) ppm. ^{13}C NMR (101 MHz, DMSO-d₆): δ 143.96, 127.71, 127.26, 123.99, 122.91, 115.76, 48.36, 29.78 ppm. Anal. calcd. for $C_{14}H_{12}BrNS$: C 54.91, H, 3.95, N, 4.57; found: C 55.07, H 3.85, N 4.42.

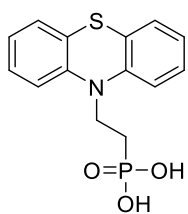
*Diethyl [2-(10*H*-phenothiazin-10-yl)ethyl]phosphonate (45)*



Method IV. 10-(2-Bromoethyl)-10*H*-phenothiazine (**44**) (1.2 g, 3.92 mmol) and triethyl phosphite (13.5 ml, 78.3 mmol) were used for the reaction. Eluent: TLC (acetone:*n*-hexane, 4:21), column (acetone:*n*-hexane, 4:21). Product obtained as a yellowish resin (1.39 g, 98% yield).

1H NMR (400 MHz, CDCl₃): δ 7.16 (m, 4H, Ht), 7.01 – 6.84 (m, 4H, Ht), 4.23 – 4.04 (m, 6H, NCH₂ and OCH₂ overlapped), 2.38 – 2.20 (m, 2H, CH₂P), 1.34 (t, $J = 7.1$ Hz, 6H, CH₃) ppm. ^{13}C NMR (101 MHz, CDCl₃): δ 144.32, 127.81, 127.71, 127.56, 123.11, 115.53, 62.03 (d, $^2J_{(C,P)} = 6.5$ Hz), 41.55 (d, $^2J_{(C,P)} = 4.8$ Hz), 24.36 (d, $^1J_{(C,P)} = 137.7$ Hz), 16.60 (d, $^3J_{(C,P)} = 6.0$ Hz) ppm. Anal. calcd. for $C_{18}H_{22}NO_3PS$: C 59.49, H, 6.10, N, 3.85; found: C 59.21, H 5.88, N 3.74.

*[2-(10*H*-phenothiazin-10-yl)ethyl]phosphonic acid (46)*

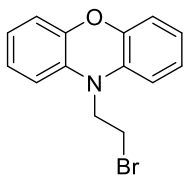


Method VI. Diethyl [2-(10*H*-phenothiazin-10-yl)ethyl]phosphonate (**45**) (0.63 g, 1.15 mmol), bromotrimethylsilane (1.5 ml, 11.5), methanol (0.5 ml, 11.5 mmol) and 15 ml of anhydrous 1,4-dioxane were used. Eluent: TLC (acetone:*n*-hexane, 2:3). Product was purified by dissolving in the minimum amount of THF, precipitating into 20-fold excess of *n*-hexane, filtering, and washing with *n*-hexane to give purple crystals (0.33 g, 62% yield). M.p. 180–181.5 °C (melting and decomposition).

1H NMR (400 MHz, DMSO-d₆): δ 7.19 (t, $J = 7.6$ Hz, 2H, Ht), 7.13 (d, $J = 7.4$ Hz, 2H, Ht), 7.01 – 6.90 (m, 4H, Ht), 4.09 – 3.93 (m, 2H, NCH₂), 2.10 – 1.93 (m, 2H, CH₂P) ppm. ^{13}C NMR (101 MHz, DMSO-d₆): δ 143.94, 127.74, 127.11, 122.91,

122.65, 115.19, 41.85, 25.91 (d, $^1J_{(C,P)} = 130.5$ Hz) ppm. Anal. calcd. for $C_{14}H_{14}NO_3PS$: C 54.72, H, 4.59, N, 4.56; found: C 54.58, H 4.40, N 4.66.

*10-(2-bromoethyl)-10*H*-phenoxazine (47)*

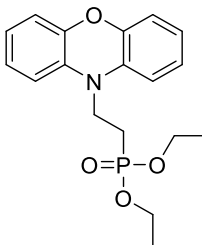


Method I. 10*H*-Phenoxazine (1 g, 5.45 mmol), 1,2-dibromoethane (11.8 ml, 136 mmol), 50 % KOH aqueous solution (3 ml, 27.3 mmol) and tetrabutylammonium bromide (0.26 g, 0.82 mmol) were used for the reaction. Reaction conducted for 72 hours. Eluent: TLC (acetone:*n*-hexane, 2:23), column (acetone:*n*-hexane, 2:23). Product obtained as brownish grey crystals (0.44 g, 28% yield).

M.p. 64–65 °C.

1H NMR (400 MHz, $CDCl_3$): δ 6.83 (t, $J = 7.6$ Hz, 2H, Ht), 6.75 – 6.63 (m, 4H, Ht), 6.51 (d, $J = 7.9$ Hz, 2H, Ht), 3.97 – 3.86 (m, 2H, NCH_2), 3.51 – 3.42 (m, 2H, CH_2P) ppm. ^{13}C NMR (101 MHz, $CDCl_3$): δ 144.86, 132.34, 123.95, 121.84, 115.96, 111.26, 46.00, 25.82 ppm. Anal. calcd. for $C_{14}H_{12}BrNO$: C 57.95, H, 4.17, N, 4.83; found: C 58.01, H 4.27, N 4.80.

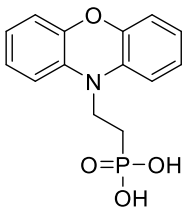
*Diethyl [2-(10*H*-phenoxazin-10-yl)ethyl]phosphonate (48)*



Method IV. 10-(2-Bromoethyl)-10*H*-phenoxazine (47) (0.4 g, 1.38 mmol) and triethyl phosphite (4.7 ml, 27.6 mmol) were used for the reaction. Eluent: TLC (acetone:*n*-hexane, 6:19), column (acetone:*n*-hexane, 6:19). Product obtained as a slightly yellow resin (0.46 g, 96% yield).

1H NMR (400 MHz, $DMSO-d_6$): δ 6.91 – 6.82 (m, 2H, Ht), 6.74 – 6.64 (m, 6H, Ht), 4.11 – 3.96 (m, 4H, OCH_2), 3.78 (dd, $J = 15.4$, 8.0 Hz, 2H, NCH_2), 2.15 – 2.01 (m, 2H, CH_2P), 1.26 (t, $J = 7.0$ Hz, 6H, CH_3) ppm. ^{13}C NMR (101 MHz, $DMSO-d_6$): δ 144.27, 132.21, 124.16, 121.23, 115.21, 111.88, 61.34 (d, $^2J_{(C,P)} = 6.3$ Hz), 37.38, 20.97 (d, $^1J_{(C,P)} = 133.8$ Hz), 16.26 (d, $^3J_{(C,P)} = 5.9$ Hz) ppm. Anal. calcd. for $C_{18}H_{22}NO_4P$: C 62.24, H, 6.38, N, 4.03; found: C 62.01, H 6.57, N 3.88.

*[2-(10*H*-phenoxazin-10-yl)ethyl]phosphonic acid (49)*

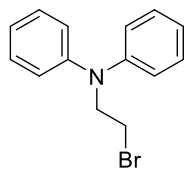


Method IV. Diethyl [2-(10*H*-phenoxazin-10-yl)ethyl]phosphonate (48) (0.41 g, 1.18 mmol), bromotrimethylsilane (2 ml, 11.8), methanol (0.5 ml, 11.8 mmol) and 7 ml of anhydrous 1,4-dioxane were used. Eluent: TLC (acetone:*n*-hexane, 8:17). Product was purified by dissolving in the minimum amount of THF, precipitating into 20-fold excess of *n*-hexane, filtering, and washing with *n*-hexane to give pale purple crystals (0.19 g, 57% yield). M.p. 205–207 °C (melting and decomposition).

1H NMR (400 MHz, $DMSO-d_6$): δ 10.23 (s, 2H, OH), 6.91 – 6.82 (m, 2H, Ht), 6.74 – 6.61 (m, 6H, Ht), 3.75 (dt, $J = 8.4$, 5.4 Hz, 2H, NCH_2), 1.97 – 1.80 (m, 2H, CH_2P) ppm. ^{13}C NMR (101 MHz, $DMSO-d_6$): δ 144.25, 132.33, 124.24, 121.16, 115.24,

111.61, 38.23, 23.12 (d, $^1J_{(C,P)} = 129.4$ Hz) ppm. Anal. calcd. for $C_{14}H_{14}NO_4P$: C 57.74, H, 4.85, N, 4.81; found: C 57.90, H 4.74, N 4.70.

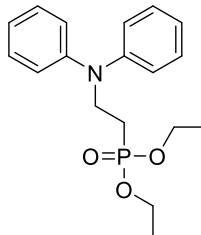
N-(2-bromoethyl)-N-phenylaniline (50)



Method I. Diphenylamine (2.5 g, 14.8 mmol), 1,2-dibromoethane (32 ml, 369 mmol), 50 % KOH aqueous solution (8.3 ml, 73.9 mmol) and tetrabutylammonium bromide (0.71 g, 2.21 mmol) were used for the reaction. Reaction conducted for 240 hours. Eluent: TLC (acetone:*n*-hexane, 1:24), column (acetone:*n*-hexane, 1:24). Product obtained as a colorless resin (0.69 g, 17% yield).

1H NMR (400 MHz, $CDCl_3$): δ 7.30 (t, $J = 7.6$ Hz, 4H, 3-H, 5-H of Ph), 7.04 – 6.98 (m, 6H, Ph), 4.11 (t, $J = 7.8$ Hz, 2H, NCH_2), 3.53 (t, $J = 7.8$ Hz, 2H, CH_2Br) ppm. ^{13}C NMR (101 MHz, $CDCl_3$): δ 146.99, 129.69, 122.26, 121.01, 53.87, 28.36 ppm. Anal. calcd. for $C_{14}H_{14}BrN$: C 60.89, H, 5.11, N, 5.07; found: C 60.90, H 5.01, N 5.00.

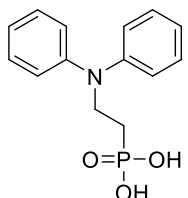
Diethyl [2-(diphenylamino)ethyl]phosphonate (51)



Method IV. *N*-(2-bromoethyl)-*N*-phenylaniline (**50**) (0.53 g, 1.92 mmol) and triethyl phosphite (6.6 ml, 38.4 mmol) were used for the reaction. Eluent: TLC (acetone:*n*-hexane, 7:18), column (acetone:*n*-hexane, 7:18). Product obtained as a slightly yellow resin (0.55 g, 86% yield).

1H NMR (400 MHz, $DMSO-d_6$): δ 7.29 (t, $J = 7.6$ Hz, 4H, 3-H, 5-H of Ph), 7.02 – 6.93 (m, 6H, Ph), 4.05 – 3.93 (m, 4H, OCH_2), 3.89 (dd, $J = 15.5, 8.0$ Hz, 2H, NCH_2), 2.13 – 2.00 (m, 2H, CH_2P), 1.20 (t, $J = 7.0$ Hz, 6H, CH_3) ppm. ^{13}C NMR (101 MHz, $DMSO-d_6$): δ 146.79, 129.46, 121.56, 120.66, 61.14 (d, $^2J_{(C,P)} = 6.2$ Hz), 45.69, 23.06 (d, $^1J_{(C,P)} = 133.2$ Hz), 16.25 (d, $^3J_{(C,P)} = 5.8$ Hz) ppm. Anal. calcd. for $C_{18}H_{24}NO_3P$: C 64.85, H, 7.26, N, 4.20; found: C 65.02, H 7.31, N 4.09.

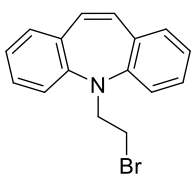
[2-(diphenylamino)ethyl]phosphonic acid (52)



Method VI. Diethyl [2-(diphenylamino)ethyl]phosphonate (**51**) (0.5 g, 1.5 mmol), bromotrimethylsilane (1.9 ml, 15 mmol), methanol (0.6 ml, 15 mmol) and 7 ml of anhydrous 1,4-dioxane were used. Eluent: TLC (acetone:*n*-hexane, 7:18). Product was purified by dissolving in the minimum amount of THF, precipitating into 20-fold excess of *n*-hexane, filtering, and washing with *n*-hexane to give bluish grey crystals (0.31 g, 58% yield). M.p. 82.5–84 °C.

1H NMR (400 MHz, $DMSO-d_6$): δ 7.28 (t, $J = 7.5$ Hz, 4H, 3-H, 5-H of Ph), 7.04 – 6.90 (m, 6H, Ph), 3.92 – 3.76 (m, 2H, NCH_2), 1.94 – 1.74 (m, 2H, CH_2P) ppm. ^{13}C NMR (101 MHz, $DMSO-d_6$): δ 146.89, 129.47, 121.39, 120.57, 46.52, 25.61 (d, $^1J_{(C,P)} = 128.5$ Hz) ppm. Anal. calcd. for $C_{14}H_{16}NO_3P$: C 60.65, H, 5.82, N, 5.05; found: C 60.41, H 5.68, N 4.99.

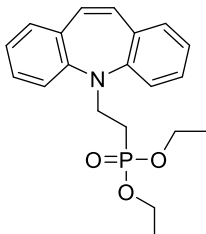
*5-(2-Bromoethyl)-5*H*-dibenzo[*b,f*]azepine (53)*



Method I. *5H-dibenzo[*b,f*]azepine* (1 g, 5.17 mmol), 1,2-dibromoethane (11.2 ml, 129 mmol), 50 % KOH aqueous solution (2.9 ml, 25.9 mmol) and tetrabutylammonium bromide (0.25 g, 0.78 mmol) were used for the reaction. Reaction conducted overnight. Eluent: TLC (acetone:*n*-hexane, 1:24), column (acetone:*n*-hexane, 1:24). Product obtained as yellow crystals (0.82 g, 51% yield). M.p. 87.5–89 °C.

¹H NMR (400 MHz, DMSO-d₆): δ 7.33 – 7.26 (m, 2H, Ht), 7.12 (t, *J* = 7.6 Hz, 4H, Ht), 7.04 (t, *J* = 7.4 Hz, 2H, Ht), 6.76 (s, 2H, 10-H, 11-H of Isb), 4.08 (t, *J* = 6.3 Hz, 2H, NCH₂), 3.46 (t, *J* = 6.3 Hz, 2H, CH₂P). ¹³C NMR (101 MHz, DMSO-d₆): δ 149.43, 133.63, 131.89, 129.19, 129.12, 123.74, 120.65, 51.86, 30.67. Anal. calcd. for C₁₆H₁₄BrN: C 64.02, H, 4.70, N, 4.67; found: C 64.23, H 4.98, N 4.85.

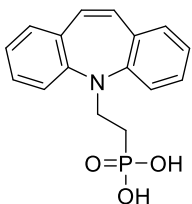
*Diethyl [2-(5*H*-dibenzo[*b,f*]azepin-5-yl)ethyl]phosphonate (54)*



Method IV. *5-(2-Bromoethyl)-5*H*-dibenzo[*b,f*]azepine* (53) (0.78 g, 2.60 mmol) and triethyl phosphite (8.9 ml, 52.0 mmol) were used for the reaction. Eluent: TLC (acetone:*n*-hexane, 7:18), column (acetone:*n*-hexane, 7:18). Product obtained as a yellow resin (0.9 g, 97% yield).

¹H NMR (400 MHz, DMSO-d₆): δ 7.31 (t, *J* = 7.6 Hz, 2H, Ht), 7.13 (d, *J* = 7.5 Hz, 2H, Ht), 7.10 – 6.99 (m, 4H, Ht), 4.02 – 3.84 (m, 6H, NCH₂ and OCH₂ overlapped), 1.95 – 1.82 (m, 2H, CH₂P), 1.19 (t, *J* = 7.0 Hz, 6H, CH₃) ppm. ¹³C NMR (101 MHz, DMSO-d₆): δ 149.63, 133.32, 131.87, 129.08, 123.56, 120.13, 61.09 (d, ²J_(C,P) = 6.2 Hz), 43.82, 24.38 (d, ¹J_(C,P) = 136.9 Hz), 16.24 (d, ³J_(C,P) = 5.8 Hz) ppm. Anal. calcd. for C₂₀H₂₄NO₃P: C 67.22, H, 6.77, N, 3.92; found: C 66.97, H 6.51, N 4.02.

*[2-(5*H*-Dibenzo[*b,f*]azepin-5-yl)ethyl]phosphonic acid (55)*

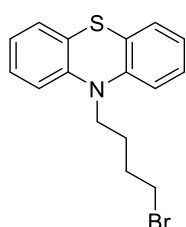


Method VI. Diethyl [2-(5*H*-dibenzo[*b,f*]azepin-5-yl)ethyl]phosphonate (54) (0.86 g, 2.41 mmol), bromotrimethylsilane (3.1 ml, 24.1 mmol), methanol (1 ml, 24.1 mmol) and 20 ml of anhydrous 1,4-dioxane were used. Eluent: TLC (acetone:*n*-hexane, 7:18). Product was purified by dissolving in the minimum amount of THF, precipitating into 20-fold excess of *n*-hexane, filtering, and washing with *n*-hexane to give yellow crystals (0.44 g, 58% yield). M.p. 165.5–167 °C (melting and decomposition).

¹H NMR (400 MHz, DMSO-d₆): δ 7.31 (t, *J* = 7.6 Hz, 2H, Ht), 7.12 (d, *J* = 7.4 Hz, 2H, Ht), 7.07 – 6.99 (m, 4H, Ht), 6.75 (s, 2H, 10-H, 11-H of Isb), 3.84 (dd, *J* = 15.1, 6.6 Hz, 2H, NCH₂), 1.78 – 1.67 (m, 2H, CH₂P) ppm. ¹³C NMR (101 MHz, DMSO-d₆): δ 149.95, 133.34, 131.96, 129.08, 129.06, 123.47, 120.21, 44.74, 27.57 (d, ¹J_(C,P)

= 132.3 Hz) ppm. Anal. calcd. for C₁₆H₁₆NO₃P: C 63.79, H, 5.35, N, 4.65; found: C 64.00, H 5.54, N 4.40.

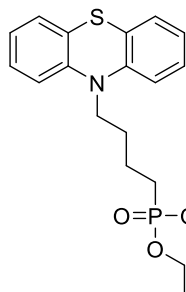
10-(4-Bromobutyl)-10H-phenothiazine (**56**)



Method III. 10H-Phenothiazine (0.5 g, 2.51 mmol), 1,4-dibromobutane (0.45 ml, 3.76 mmol), KOH (0.21 g, 3.76 mmol) and 5 ml of DMF were used for the reaction. Reaction conducted for 2 hours. Eluent: TLC (acetone:*n*-hexane, 1:24), column (acetone:*n*-hexane, 1:24). Product obtained as a yellowish resin (0.41 g, 49% yield).

¹H NMR (400 MHz, DMSO-d₆): δ 7.28 – 7.11 (m, 4H, Ht), 7.11 – 6.80 (m, 4H, Ht), 4.05 – 3.78 (m, 2H), 3.53 (t, *J* = 6.6 Hz, 2H, CH₂Br), 1.98 – 1.85 (m, 2H, CH₂), 1.85 – 1.73 (m, 2H, CH₂) ppm. ¹³C NMR (101 MHz, DMSO-d₆): δ 144.73, 127.59, 127.14, 123.82, 122.57, 115.90, 45.55, 34.76, 29.64, 24.98 ppm. Anal. calcd. for C₁₆H₁₆BrNS: C 57.49, H 4.82, N 4.19; found: C 57.61, H 4.59, N 4.02.

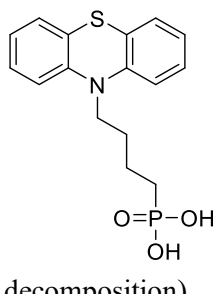
Diethyl [4-(10H-phenothiazin-10-yl)butyl]phosphonate (**57**)



Method IV. 10-(4-Bromobutyl)-10H-phenothiazine (**56**) (0.38 g, 1.13 mmol) and triethyl phosphite (3.89 ml, 22.73 mmol) were used for the reaction. Eluent: TLC (acetone:*n*-hexane, 6:19), column (acetone:*n*-hexane, 6:19). Product obtained as an orange resin (0.42 g, 94%).

¹H NMR (400 MHz, DMSO-d₆): δ 7.19 (t, *J* = 7.7 Hz, 2H, Ht), 7.14 (d, *J* = 7.5 Hz, 2H, Ht), 7.03 (d, *J* = 8.1 Hz, 2H, Ht), 6.94 (t, *J* = 7.4 Hz, 2H, Ht), 3.98 – 3.80 (m, 6H, NCH₂ and OCH₂ overlapped), 1.82 – 1.66 (m, 4H, Aliph), 1.65 – 1.49 (m, 2H, CH₂), 1.17 (t, *J* = 7.0 Hz, 6H, CH₃) ppm. ¹³C NMR (101 MHz, DMSO-d₆): δ 144.77, 127.57, 127.10, 123.70, 122.46, 115.90, 60.73 (d, ²J_(C,P) = 6.3 Hz), 45.87, 26.91 (d, ²J_(C,P) = 15.8 Hz), 24.07 (d, ¹J_(C,P) = 138.3 Hz), 19.49 (d, ³J_(C,P) = 4.8 Hz), 16.25 (d, ³J_(C,P) = 5.7 Hz) ppm. Anal. calcd. for C₂₀H₂₆NO₃PS: C 61.36, H, 6.69, N, 3.58; found: C 61.51, H 6.49, N 3.33.

[4-(10H-Phenothiazin-10-yl)butyl]phosphonic acid (**58**)

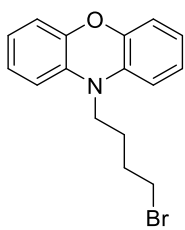


decomposition).

Method VI. Diethyl [4-(10H-phenothiazin-10-yl)butyl]phosphonate (**57**) (0.4 g, 1.02 mmol), bromotrimethylsilane (1.3 ml, 10.21 mmol), methanol (0.4 ml, 10.21 mmol) and 10 ml of 1,4-dioxane were used. Eluent: TLC (acetone:*n*-hexane, 6:19). Product was purified by dissolving in the minimum amount of THF, precipitating into 20-fold excess of *n*-hexane, filtering, and washing with *n*-hexane to give dark grey crystals (0.26 g, 76% yield). M.p. 193–195 °C (melting and

¹H NMR (400 MHz, DMSO-d₆): δ 7.19 (t, *J* = 7.7 Hz, 2H, Ht), 7.14 (d, *J* = 7.5 Hz, 2H, Ht), 7.03 (d, *J* = 8.1 Hz, 2H, Ht), 6.93 (t, *J* = 7.4 Hz, 2H, Ht), 3.86 (t, *J* = 6.6 Hz, 2H, NCH₂), 1.82 – 1.70 (m, 2H, CH₂), 1.67 – 1.44 (m, 4H, Aliph) ppm. ¹³C NMR (101 MHz, DMSO-d₆): δ 144.77, 127.61, 127.12, 123.53, 122.44, 115.80, 46.18, 27.21 (d, ²J_(C,P) = 15.3 Hz), 27.17 (d, ¹J_(C,P) = 136.6 Hz), 20.32 (d, ³J_(C,P) = 4.6 Hz) ppm. Anal. calcd. for C₁₆H₁₈NO₃PS: C 57.30, H, 5.41, N, 4.18; found: C 57.58, H 5.58, N 4.01.

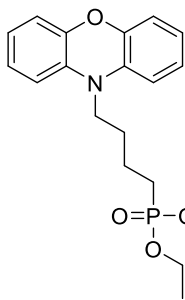
10-(4-Bromobutyl)-10*H*-phenoxazine (**59**)



Method III. 10*H*-Phenoxazine (0.5 g, 2.72 mmol), 1,4-dibromobutane (0.5 ml, 4.08 mmol), KOH (0.16 g, 4.08 mmol) and 5 ml of DMF were used for the reaction. Reaction conducted for 1 hour. Eluent: TLC (acetone:*n*-hexane, 1:24), column (acetone:*n*-hexane, 1:24). Product obtained as grey crystals (0.3 g, 35% yield). M.p. 60–61 °C.

¹H NMR (400 MHz, DMSO-d₆): δ 6.86 – 6.77 (m, 2H, Ht), 6.75 – 6.58 (m, 6H, Ht) 3.69 – 3.48 (m, 4H, NCH₂ and NCH₂Br overlapped), 2.00 – 1.86 (m, 2H, CH₂), 1.75 – 1.57 (m, 2H, CH₂) ppm. ¹³C NMR (101 MHz, DMSO-d₆): δ 144.03, 132.72, 124.06, 120.80, 115.04, 111.97, 41.92, 34.80, 29.35, 22.91 ppm. Anal. calcd. for C₁₆H₁₆BrNO: C 60.39, H 5.07, N 4.40; found: C 60.19, H 5.27, N 4.28.

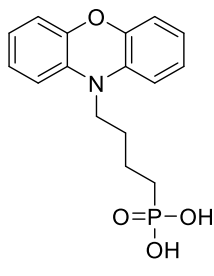
Diethyl [4-(10*H*-phenoxazin-10-yl)butyl]phosphonate (**60**)



Method IV. 10-(4-Bromobutyl)-10*H*-phenoxazine (**59**) (0.25 g, 0.78 mmol) and triethyl phosphite (2.69 ml, 15.71 mmol) were used for the reaction. Eluent: TLC (acetone:*n*-hexane, 1:4), column (acetone:*n*-hexane, 1:4). Product obtained as a yellowish resin (0.27 g, 91%).

¹H NMR (400 MHz, DMSO-d₆): δ 6.85 – 6.77 (m, 2H, Ht), 6.70 (d, *J* = 8.0 Hz, 2H, Ht), 6.68 – 6.60 (m, 4H, Ht), 4.01 – 3.90 (m, 4H, OCH₂), 3.55 (t, *J* = 6.7 Hz, 2H, NCH₂), 1.87 – 1.73 (m, 2H, CH₂), 1.69 – 1.51 (m, 4H, Aliph), 1.22 (t, *J* = 7.1 Hz, 6H, CH₃) ppm. ¹³C NMR (101 MHz, DMSO-d₆): δ 144.07, 132.83, 124.04, 120.73, 114.99, 112.07, 60.80 (d, ²J_(C,P) = 6.3 Hz), 42.38, 24.98, 24.90, 24.83, 23.53, 19.35 (d, ³J_(C,P) = 4.9 Hz), 16.30 (d, ³J_(C,P) = 5.7 Hz) ppm. Anal. calcd. for C₂₀H₂₆NO₄P: C 63.99, H, 6.98, N, 3.73; found: C 64.09, H 6.71, N 3.56.

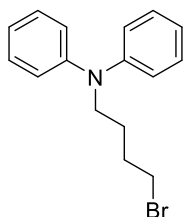
[4-(10H-Phenoxazin-10-yl)butyl]phosphonic acid (**61**)



Method VI. Diethyl [4-(10H-phenoxazin-10-yl)butyl]phosphonate (**60**) (0.24 g, 0.64 mmol), bromotrimethylsilane (0.8 ml, 6.39 mmol), methanol (0.3 ml, 6.39 mmol) and 5 ml of 1,4-dioxane were used. Eluent: TLC (acetone:*n*-hexane, 1:4). Product was purified by dissolving in the minimum amount of THF, precipitating into 20-fold excess of *n*-hexane, filtering, and washing with *n*-hexane to give dark grey crystals (0.15 g, 73% yield). M.p. 182–184 °C (melting and decomposition).

¹H NMR (400 MHz, DMSO-d₆): δ 6.86 – 6.77 (m, 2H, Ht), 6.69 (d, *J* = 8.0 Hz, 2H, Ht), 6.67 – 6.58 (m, 4H, Ht), 3.58 – 3.49 (m, 2H, NCH₂), 1.70 – 1.50 (m, 6H, Aliph) ppm. ¹³C NMR (101 MHz, DMSO-d₆): δ 144.06, 132.88, 124.10, 120.71, 114.99, 112.02, 42.66, 27.25 (d, ¹*J*_(C,P) = 136.9 Hz), 25.12 (d, ²*J*_(C,P) = 14.6 Hz), 20.08 (d, ³*J*_(C,P) = 4.4 Hz) ppm. Anal. calcd. for C₁₆H₁₈NO₄P: C 60.19, H, 5.68, N, 4.39; found: C 60.01, H 5.73, N 4.20.

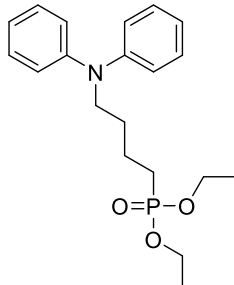
N-(4-bromobutyl)-*N*-phenylaniline (**62**)



Method II. Diphenylamine (2.5 g, 14.8 mmol), 1,4-dibromobutane (2.7 ml, 22.2 mmol), NaH (0.89 g, 22.2 mmol) and 25 ml of DMF were used for the reaction. Eluent: TLC (acetone:*n*-hexane, 1:24), column (acetone:*n*-hexane, 1:24). Product obtained as a colorless resin (1.23 g, 27% yield).

¹H NMR (400 MHz, CDCl₃): δ 7.59 (t, *J* = 7.5 Hz, 4H, 3-H, 5-H of Ph), 7.37 – 7.23 (m, 6H, Ph), 4.05 (t, *J* = 7.3 Hz, 2H, NCH₂), 3.71 (t, *J* = 6.6 Hz, 2H, CH₂Br), 2.24 (dt, *J* = 13.7, 6.7 Hz, 2H, CH₂), 2.14 (dt, *J* = 14.5, 7.3 Hz, 2H, CH₂) ppm. ¹³C NMR (101 MHz, CDCl₃): δ 147.91, 129.50, 121.66, 121.15, 51.66, 33.42, 30.47, 26.40 ppm. Anal. calcd. for C₁₆H₁₈BrN: C 63.17, H, 5.96, N, 4.60; found: C 63.40, H 5.81, N 4.37.

Diethyl [4-(diphenylamino)butyl]phosphonate (**63**)

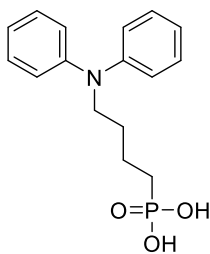


Method IV. *N*-(4-bromobutyl)-*N*-phenylaniline (**62**) (1.2 g, 3.94 mmol) and triethyl phosphite (13.5 ml, 78.9 mmol) were used for the reaction. Eluent: TLC (acetone:*n*-hexane, 7:18), column (acetone:*n*-hexane, 7:18). Product obtained as a yellowish resin (1.03 g, 91% yield).

¹H NMR (400 MHz, CDCl₃): δ 7.58 (t, *J* = 7.8 Hz, 4H, 3-H, 5-H of Ph), 7.37 – 7.25 (m, 6H, Ph), 4.44 – 4.33 (m, 4H, OCH₂), 4.07 – 3.98 (m, 2H, NCH₂), 2.15 – 1.91 (m, 6H, Aliph), 1.62 (t, *J* = 7.0 Hz, 6H, CH₃) ppm. ¹³C NMR (101 MHz, CDCl₃): δ 147.86, 129.45, 121.70, 121.13, 61.60 (d, ²*J*_(C,P) = 6.5 Hz), 52.11, 28.47 (d, ²*J*_(C,P) = 16.1 Hz), 25.68 (d, ¹*J*_(C,P) = 140.9 Hz), 20.28 (d, ³*J*_(C,P) = 5.1 Hz), 16.60 (d, ³*J*_(C,P) = 6.0

Hz) ppm. Anal. calcd. for $C_{20}H_{28}NO_3P$: C 66.47, H, 7.81, N, 3.88; found: C 66.57, H 7.81, N 3.70.

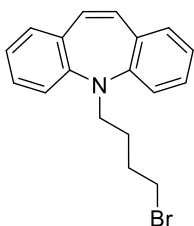
[4-(Diphenylamino)butyl]phosphonic acid (**64**)



Method VI. Diethyl [4-(diphenylamino)butyl]phosphonate (**63**) (1 g, 2.77 mmol), bromotrimethylsilane (3.6 ml, 27.7 mmol), methanol (1.1 ml, 27.7 mmol) and 15 ml of 1,4-dioxane were used. Eluent: TLC (acetone:*n*-hexane, 7:18). Product was purified by dissolving in the minimum amount of THF, precipitating into 20-fold excess of *n*-hexane, filtering, and washing with *n*-hexane to give grey crystals (0.64 g, 76% yield). M.p. 145–147 °C (melting and decomposition).

1H NMR (400 MHz, DMSO-d₆): δ 7.25 (t, J = 7.7 Hz, 4H, 3-H, 5-H of Ph), 7.01 – 6.86 (m, 6H, Ph), 3.71 – 3.62 (m, 2H, NCH₂), 1.68 – 1.58 (m, 2H, CH₂), 1.57 – 1.44 (m, 4H, Aliph) ppm. ^{13}C NMR (101 MHz, DMSO-d₆): δ 147.57, 129.31, 120.98, 120.52, 51.24, 27.97 (d, $^2J_{(C,P)}$ = 14.5 Hz), 25.94 (d, $^1J_{(C,P)}$ = 161.9 Hz), 20.36 (d, $^3J_{(C,P)}$ = 3.0 Hz) ppm. Anal. calcd. for $C_{16}H_{20}NO_3P$: C 62.94, H, 6.60, N, 4.59; found: C 63.21, H 6.84, N 4.80.

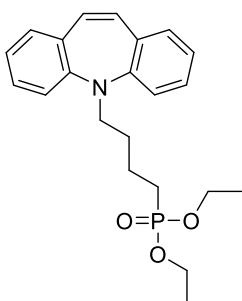
5-(4-Bromobutyl)-5*H*-dibenzo[*b,f*]azepine (**65**)



Method III. 5*H*-dibenzo[*b,f*]azepine (1 g, 5.17 mmol), 1,4-dibromobutane (0.9 ml, 7.76 mmol), KOH (0.43 g, 7.76 mmol) and 10 ml of DMF were used for the reaction. Reaction conducted overnight. Eluent: TLC (acetone:*n*-hexane, 1:24), column (acetone:*n*-hexane, 1:24). Product obtained as a dark orange resin (0.37 g, 22% yield).

1H NMR (400 MHz, DMSO-d₆): δ 7.29 (t, J = 7.6 Hz, 2H, Ht), 7.14 – 7.05 (m, 4H, Ht), 6.99 (t, J = 7.4 Hz, 2H, Ht), 6.75 (s, 2H, 10-H, 11-H of Isb), 3.71 (t, J = 6.6 Hz, 2H, NCH₂), 3.45 (t, J = 6.7 Hz, 2H, CH₂Br), 1.89 – 1.79 (m, 2H, CH₂), 1.60 – 1.51 (m, 2H, CH₂) ppm. ^{13}C NMR (101 MHz, DMSO-d₆): δ 150.45, 133.33, 131.98, 128.94, 128.93, 123.22, 120.41, 48.68, 34.96, 29.72, 25.50 ppm. Anal. calcd. for $C_{18}H_{18}BrN$: C 65.86, H, 5.53, N, 4.27; found: C 65.70, H 5.41, N 4.30.

Diethyl [4-(5*H*-dibenzo[*b,f*]azepin-5-yl)butyl]phosphonate (**66**)

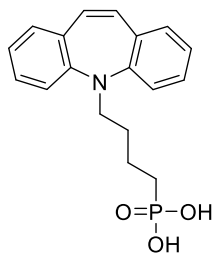


Method IV. 5-(4-Bromobutyl)-5*H*-dibenzo[*b,f*]azepine (**63**) (0.34 g, 1.04 mmol) and triethyl phosphite (3.7 ml, 20.7 mmol) were used for the reaction. Eluent: TLC (acetone:*n*-hexane, 7:18), column (acetone:*n*-hexane, 7:18). Product obtained as a yellow resin (0.23 g, 58% yield).

1H NMR (400 MHz, DMSO-d₆): δ 7.28 (t, J = 7.6 Hz, 2H, Ht), 7.13 – 7.04 (m, 4H, Ht), 6.99 (t, J = 7.4 Hz, 2H, Ht), 6.73 (s, 2H, 10-H, 11-H of Isb), 3.96 – 3.82 (m, 4H, OCH₂), 3.74 – 3.62 (m, 2H, NCH₂), 1.68 – 1.47 (m, 6H, Aliph), 1.17 (t, J =

7.0 Hz, 6H, CH₃) ppm. ¹³C NMR (101 MHz, DMSO-d₆): δ 150.57, 133.33, 131.96, 128.91, 123.14, 120.41, 60.68 (d, ²J_(C,P) = 6.3 Hz), 49.05, 27.52 (d, ²J_(C,P) = 15.9 Hz), 24.14 (d, ¹J_(C,P) = 138.2 Hz), 19.51 (d, ³J_(C,P) = 4.9 Hz), 16.26 (d, ³J_(C,P) = 5.8 Hz) ppm. Anal. calcd. for C₂₂H₂₈NO₃P: C 68.56, H, 7.32, N, 3.63; found: C 68.59, H 7.39, N 3.60.

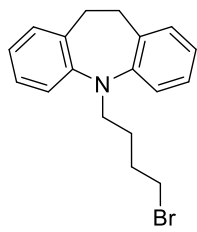
[4-(5H-Dibenzo[b,f]azepin-5-yl)butyl]phosphonic acid (67)



Method VI. Diethyl [4-(5H-dibenzo[b,f]azepin-5-yl)butyl]phosphonate (**66**) (0.2 g, 0.52 mmol), bromotrimethylsilane (0.9 ml, 5.19 mmol), methanol (0.2 ml, 5.19 mmol) and 3 ml of 1,4-dioxane were used. Eluent: TLC (acetone:n-hexane, 7:18). Product was purified by dissolving in the minimum amount of THF, precipitating into 20-fold excess of n-hexane, filtering, and washing with n-hexane to give grey crystals (0.13 g, 76% yield). M.p. 167–169 °C (melting and decomposition).

¹H NMR (400 MHz, DMSO-d₆): δ 7.28 (t, J = 7.6 Hz, 2H, Ht), 7.14 – 7.04 (m, 4H, Ht), 6.98 (t, J = 7.4 Hz, 2H, Ht), 6.73 (s, 2H, 10-H, 11-H of Isb), 3.73 – 3.60 (m, 2H, NCH₂), 1.60 – 1.37 (m, 6H, Aliph) ppm. ¹³C NMR (101 MHz, DMSO-d₆): δ 150.68, 133.33, 132.02, 128.93, 128.91, 123.13, 120.37, 49.33, 27.88, 27.27 (d, ¹J_(C,P) = 150.6 Hz), 20.26 (d, ²J_(C,P) = 4.5 Hz) ppm. Anal. calcd. for C₁₈H₂₀NO₃P: C 65.65, H, 6.12, N, 4.25; found: C 65.77, H 5.84, N 4.00.

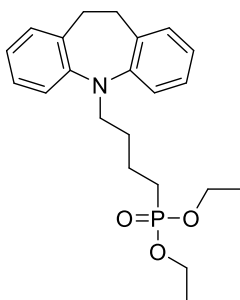
5-(4-Bromobutyl)-10,11-dihydro-5H-dibenzo[b,f]azepine (68)



Method II. 10,11-Dihydro-5H-dibenzo[b,f]azepine (1 g, 5.12 mmol), 1,4-dibromobutane (0.9 ml, 7.68 mmol), NaH (0.31 g, 7.68 mmol) and 15 ml of DMF were used for the reaction. After addition of NaH at 0 °C, reaction mixture was heated up to 80 °C and reaction conducted for 72 hours. Eluent: TLC (acetone:n-hexane, 1:24), column (acetone:n-hexane, 1:24). Product obtained as a colorless resin (0.83 g, 49% yield).

¹H NMR (400 MHz, CDCl₃): δ 7.17 – 7.07 (m, 6H, Ht), 6.94 (t, J = 7.2 Hz, 2H, Ht), 3.77 (t, J = 6.7 Hz, 2H, NCH₂), 3.35 (t, J = 6.8 Hz, 2H, CH₂Br), 3.17 (s, 4H, 10-H, 11-H of Imb), 1.95 – 1.85 (m, 2H, CH₂), 1.79 – 1.68 (m, 2H, CH₂) ppm. ¹³C NMR (101 MHz, CDCl₃): δ 148.20, 134.37, 130.04, 126.53, 122.76, 120.04, 49.70, 33.60, 32.30, 30.47, 26.46 ppm. Anal. calcd. for C₁₈H₂₀BrN: C 65.46, H, 6.10, N, 4.24; found: C 65.41, H 6.17, N 4.39.

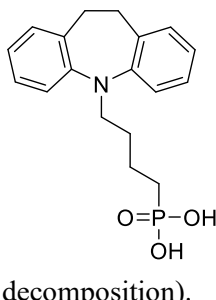
Diethyl [4-(10,11-dihydro-5H-dibenzo[b,f]azepin-5-yl)butyl]phosphonate (69)



Method IV. 5-(4-Bromobutyl)-10,11-dihydro-5*H*-dibenzo[*b,f*]azepine (**68**) (0.8 g, 2.42 mmol) and triethyl phosphite (8.3 ml, 84.4 mmol) were used for the reaction. Eluent: TLC (acetone:*n*-hexane, 7:18), column (acetone:*n*-hexane, 7:18). Product obtained as a colorless resin (0.83 g, 88% yield).

¹H NMR (400 MHz, DMSO-d₆): δ 7.14 – 7.05 (m, 6H, Ht), 6.95 – 6.86 (m, 2H, Ht), 3.90 (p, *J* = 7.2 Hz, 4H, OCH₂), 3.69 (t, *J* = 6.0 Hz, 2H, NCH₂), 3.08 (s, 4H, 10-H, 11-H of Imb), 1.68 – 1.42 (m, 6H, Aliph), 1.17 (t, *J* = 7.0 Hz, 6H, CH₃) ppm. ¹³C NMR (101 MHz, DMSO-d₆): δ 148.12, 133.55, 129.64, 126.32, 122.31, 119.87, 60.69 (d, ²*J*_(C,P) = 6.3 Hz), 49.03, 31.50, 27.87 (d, ²*J*_(C,P) = 15.9 Hz), 24.13 (d, ¹*J*_(C,P) = 138.4 Hz), 19.69 (d, ³*J*_(C,P) = 5.0 Hz), 16.24 (d, ³*J*_(C,P) = 5.8 Hz) ppm. Anal. calcd. for C₂₂H₃₀NO₃P: C 68.20, H, 7.80, N, 3.62; found: C 68.01, H 7.60, N 3.45.

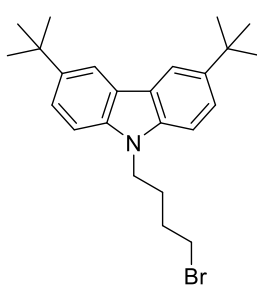
[4-(10,11-Dihydro-5H-dibenzo[b,f]azepin-5-yl)butyl]phosphonic acid (70)



Method VI. Diethyl [4-(10,11-dihydro-5*H*-dibenzo[*b,f*]azepin-5-yl)butyl]phosphonate (**69**) (0.78 g, 2.01 mmol), bromotrimethylsilane (2.6 ml, 20.1 mmol), methanol (0.8 ml, 20.1 mmol) and 20 ml of 1,4-dioxane were used. Eluent: TLC (acetone:*n*-hexane, 8:17). Product was purified by dissolving in the minimum amount of THF, precipitating into 20-fold excess of *n*-hexane, filtering, and washing with *n*-hexane to give white crystals (0.54 g, 81% yield). M.p. 176–177.5 °C (melting and decomposition).

¹H NMR (400 MHz, DMSO-d₆): δ 7.15 – 7.05 (m, 6H, Ht), 6.94 – 6.84 (m, 2H, Ht), 3.68 (t, *J* = 5.8 Hz, 2H, NCH₂), 3.08 (s, 4H, 10-H, 11-H of Imb), 1.60 – 1.35 (m, 6H) ppm. ¹³C NMR (101 MHz, DMSO-d₆): δ 148.20, 133.61, 129.67, 126.32, 122.28, 119.87, 49.15, 31.52, 28.16, 28.00, 27.80, 26.44, 20.31 (d, ³*J*_(C,P) = 4.4 Hz) ppm. Anal. calcd. for C₁₈H₂₂NO₃P: C 65.25, H, 6.69, N, 4.23; found: C 68.01, H 7.60, N 3.45.

*9-(4-Bromobutyl)-3,6-di-tert-butyl-9*H*-carbazole (71)*

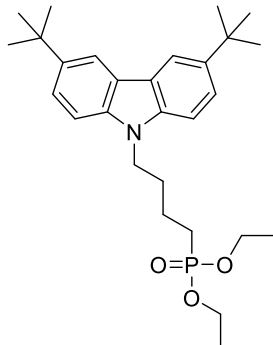


Method II. 3,6-Di-tert-butyl-9*H*-carbazole (1g, 3.57 mmol), 1,4-dibromobutane (0.64 ml, 5.36 mmol), NaH (0.21 g, 5.36 mmol) and 10 ml of DMF were used for the reaction. Eluent: TLC (acetone:*n*-hexane, 1:49), column (acetone:*n*-hexane, 1:49). Product obtained as white crystals (1.01 g, 70% yield). M.p. 125–126 °C.

¹H NMR (400 MHz, CDCl₃): δ 8.12 (s, 2H, 4-H, 5-H of Cz), 7.52 (d, *J* = 8.5 Hz, 2H, Ht), 7.31 (d, *J* = 8.6 Hz, 2H, Ht), 4.30 (t, *J* = 6.8 Hz, 2H, NCH₂), 3.39 (t, *J* = 6.4 Hz, 2H, CH₂Br),

2.11 – 2.00 (m, 2H, CH₂), 1.98 – 1.88 (m, 2H, CH₂), 1.48 (s, 18H, CH₃) ppm. ¹³C NMR (101 MHz, CDCl₃): δ 141.84, 138.98, 123.50, 122.91, 116.50, 108.04, 42.38, 34.81, 33.42, 32.20, 30.43, 27.98 ppm. Anal. calcd. for C₂₄H₃₂BrN: C 69.56, H 7.78, N 3.38; found: C 69.70, H 7.68, N 3.21.

Diethyl [4-(3,6-di-tert-butyl-9H-carbazol-9-yl)butyl]phosphonate (72)

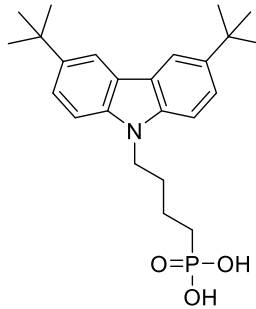


Method IV. 9-(4-Bromobutyl)-3,6-di-tert-butyl-9H-carbazole (71) (0.95 g, 2.29 mmol) and triethyl phosphite (7.86 ml, 45.84 mmol) were used for the reaction. Eluent: TLC (acetone:*n*-hexane, 4:21), column (acetone:*n*-hexane, 4:21). Product obtained as a slightly yellow resin (1.04 g, 96%).

¹H NMR (400 MHz, CDCl₃): δ 8.09 (s, 2H, 4-H, 5-H of Cz), 7.50 (d, *J* = 8.3 Hz, 2H, Ht), 7.29 (d, *J* = 8.5 Hz, 2H, Ht), 4.27 (t, *J* = 6.3 Hz, 2H, NCH₂), 4.07 – 3.96 (m, 4H, OCH₂), 2.03 – 1.90 (m, 2H, CH₂), 1.83 – 1.66 (m, 4H, Aliph), 1.45 (s, 18H, CCH₃), 1.24 (t, *J* = 6.5 Hz, 6H, CH₂CH₃) ppm. ¹³C

NMR (101 MHz, CDCl₃): δ 141.71, 138.96, 123.41, 122.83, 116.39, 108.08, 61.65 (d, ²*J*_(C,P) = 6.5 Hz), 42.66, 34.77, 32.18, 30.06 (d, ²*J*_(C,P) = 15.6 Hz), 25.59 (d, ¹*J*_(C,P) = 141.2 Hz), 20.58 (d, ³*J*_(C,P) = 5.1 Hz), 16.52 (d, ³*J*_(C,P) = 6.0 Hz) ppm. Anal. calcd. for C₂₈H₄₂NO₃P: C 71.31, H 8.98, N, 2.97; found: C 71.41, H 9.05, N 2.80.

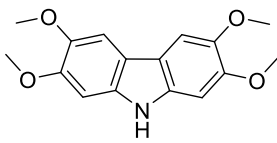
[4-(3,6-di-tert-butyl-9H-carbazol-9-yl)butyl]phosphonic acid (73)



Method VI. Diethyl [4-(3,6-di-tert-butyl-9H-carbazol-9-yl)butyl]phosphonate (72) (1 g, 2.12 mmol), bromotrimethylsilane (2.75 ml, 21.2 mmol), methanol (0.9 ml, 21.2 mmol) and 10 ml of 1,4-dioxane were used. Eluent: TLC (acetone:*n*-hexane, 4:21). Product was purified by dissolving in the minimum amount of THF, precipitating into 20-fold excess of *n*-hexane, filtering, and washing with *n*-hexane to give white crystals (0.81 g, 92% yield). M.p. 184–186 °C.

¹H NMR (400 MHz, CDCl₃): δ 9.97 – 9.00 (m, 2H, OH), 8.10 (s, 2H, 4-H, 5-H of Cz), 7.48 (d, *J* = 8.5 Hz, 2H, Ht), 7.26 (d, *J* = 8.0 Hz, 2H, Ht), 4.22 (t, *J* = 6.9 Hz, 2H, NCH₂), 2.03 – 1.91 (m, 2H, CH₂), 1.89 – 1.70 (m, 4H, CH₂), 1.44 (s, 18H, CH₃) ppm. ¹³C NMR (101 MHz, CDCl₃): δ 141.78, 138.94, 123.47, 122.89, 116.46, 108.03, 42.73, 34.78, 32.20, 29.73 (d, ³*J*_(C,P) = 14.9 Hz), 25.06 (d, ¹*J*_(C,P) = 146.6 Hz), 20.15 (d, ³*J*_(C,P) = 4.4 Hz) ppm. Anal. calcd. for C₂₄H₃₄NO₃P: C 69.38, H, 8.25, N, 3.37; found: C 69.47, H 8.39, N 3.40.

2,3,6,7-Tetramethoxy-9H-carbazole (74)

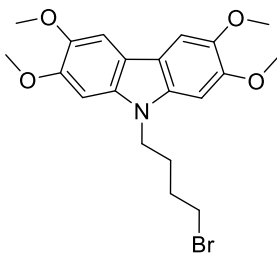


Under inert argon atmosphere sodium (2.99 g, 130 mmol) was dissolved in anhydrous MeOH (35.4 ml, 876 mmol). Afterwards 3,6-dibromo-2,7-dimethoxy-9*H*-carbazole (**37**) (2.5 g, 6.49 mmol) pre-dissolved in 20 ml of anhydrous DMF, followed by addition of CuI (5.19 g, 27.3 mmol).

Reaction conducted overnight at 100 °C. After termination of reaction (TLC, eluent acetone:*n*-hexane, 6:19), reaction mixture was cooled down, filtered through celite, washed with THF and solvent removed under reduced pressure. Organic components were further extracted with ethyl acetate, organic layer was dried over anhydrous Na₂SO₄, filtered and solvent evaporated under reduced pressure. Crude product was purified by column chromatography (TLC, eluent acetone:*n*-hexane, 6:19). Product obtained as white crystals (1.42 g, 76%). M.p. 231.5–233 °C (melting and decomposition).

¹H NMR (400 MHz, DMSO-d₆): δ 10.62 (s, 1H, NH), 7.57 (s, 2H, 4-H, 5-H of Cz), 6.97 (s, 2H, Ht, 1-H, 8-H of Cz), 3.85 – 3.79 (m, 12H, OCH₃ and OCH₃ overlapped) ppm. ¹³C NMR (101 MHz, DMSO-d₆): δ 147.81, 143.42, 134.26, 115.03, 102.81, 94.88, 56.18, 55.67 ppm. Anal. calcd. for C₁₆H₁₇NO₄: C 66.89, H 5.96, N 4.88; found: C 67.01, H 6.22, N 4.69.

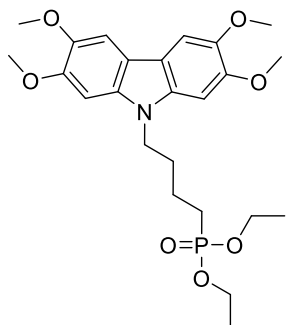
9-(4-Bromobutyl)-2,3,6,7-tetramethoxy-9H-carbazole (75)



Method III. 2,3,6,7-Tetramethoxy-9*H*-carbazole (**74**) (0.5 g, 1.74 mmol), 1,4-dibromobutane (0.3 ml, 2.61 mmol), KOH (0.15 g, 2.61 mmol) and 10 ml of DMF were used for the reaction. Reaction conducted overnight. Eluent: TLC (acetone:*n*-hexane, 7:18), column (acetone:*n*-hexane, 7:18). Product obtained as white crystals (0.62 g, 84% yield). M.p. 182–183.5 °C.

¹H NMR (400 MHz, DMSO-d₆): δ 7.61 (s, *J* = 5.3 Hz, 2H, 4-H, 5-H of Cz), 7.14 (s, 2H, 1-H, 8-H of Cz), 4.36 (t, *J* = 6.2 Hz, 2H, NCH₂), 3.87 (s, 6H, OCH₃), 3.83 (s, 6H, OCH₃), 3.57 (t, *J* = 6.2 Hz, 2H, CH₂Br), 1.91 – 1.74 (m, 4H, Aliph) ppm. ¹³C NMR (101 MHz, DMSO-d₆): δ 148.01, 143.53, 134.52, 114.42, 103.00, 93.71, 56.21, 55.97, 41.22, 34.89, 29.65, 27.16 ppm. Anal. calcd. for C₂₀H₂₄BrNO₄: C 56.88, H, 5.73, N, 3.32; found: C 58.70, H 5.79, N 3.48.

Diethyl [4-(2,3,6,7-tetramethoxy-9H-carbazol-9-yl)butyl]phosphonate (76)

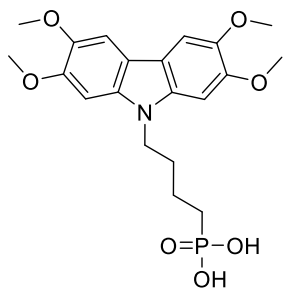


Method IV. 9-(4-Bromobutyl)-2,3,6,7-tetramethoxy-9H-carbazole (**75**) (0.55 g, 1.3 mmol) and triethyl phosphite (4.5 ml, 26 mmol) were used for the reaction. Eluent: TLC (acetone:*n*-hexane, 1:1), column (acetone:*n*-hexane, 1:1). Product obtained as a barely yellow resin (0.58 g, 93%).

¹H NMR (400 MHz, DMSO-d₆): δ 7.60 (s, 2H, 4-H, 5-H of Cz), 7.14 (s, 2H, 1-H, 8-H of Cz), 4.34 (t, *J* = 6.7 Hz, 2H, NCH₂), 3.93 – 3.84 (m, 10H, OCH₂ and OCH₃ overlapped), 3.83 (s, 6H, OCH₃), 1.88 – 1.67 (m, 4H, Aliph), 1.56 – 1.41 (m, 2H, CH₂), 1.14 (t, *J* = 7.0 Hz, 6H, CH₂CH₃) ppm. ¹³C

NMR (101 MHz, DMSO-d₆): δ 147.99, 143.50, 134.60, 114.41, 102.98, 93.83, 60.74 (d, ²J_(C,P) = 6.3 Hz), 56.23, 55.94, 41.68, 29.27 (d, ²J_(C,P) = 16.0 Hz), 24.27 (d, ¹J_(C,P) = 138.5 Hz), 19.64 (d, ³J_(C,P) = 4.7 Hz), 16.23 (d, ³J_(C,P) = 5.7 Hz) ppm. Anal. calcd. for C₂₄H₃₄NO₇P: C 60.12, H 7.15, N 2.92; found: C 60.12, H 7.06, N 2.81.

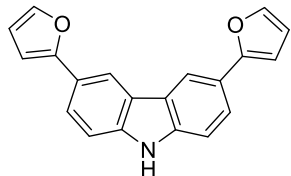
[4-(2,3,6,7-Tetramethoxy-9H-carbazol-9-yl)butyl]phosphonic acid (77)



Method VI. Diethyl [4-(2,3,6,7-tetramethoxy-9H-carbazol-9-yl)butyl]phosphonate (**76**) (0.55 g, 1.15 mmol), bromotrimethylsilane (1.5 ml, 11.5 mmol), methanol (0.5 ml, 11.5 mmol) and 15 ml of 1,4-dioxane were used. Eluent: TLC (acetone:*n*-hexane, 1:1). Product was purified by dissolving in the minimum amount of THF, precipitating into 20-fold excess of *n*-hexane, filtering, and washing with *n*-hexane to give grey crystals (0.22 g, 45% yield). M.p. 222.5–223.5 °C (melting and decomposition).

¹H NMR (400 MHz, DMSO-d₆): δ 7.60 (s, 2H, 4-H, 5-H of Cz), 7.12 (s, 2H, 1-H, 8-H of Cz), 4.31 (t, *J* = 6.4 Hz, 2H, NCH₂), 3.87 (s, 6H, OCH₃), 3.83 (s, 6H, OCH₃), 1.88 – 1.74 (m, 2H, CH₂), 1.64 – 1.46 (m, 4H, CH₂) ppm. ¹³C NMR (101 MHz, DMSO-d₆): δ 147.99, 143.48, 134.59, 114.37, 102.99, 93.78, 56.24, 55.96, 41.97, 29.58 (d, ²J_(C,P) = 15.4 Hz), 27.34 (d, ¹J_(C,P) = 136.8 Hz), 20.37 (d, ³J_(C,P) = 4.0 Hz) ppm. Anal. calcd. for C₂₀H₂₆NO₇P: C 56.74, H 6.19, N, 3.31; found: C 56.81, H 6.20, N 3.03.

3,6-Di(furan-2-yl)-9H-carbazole (78)



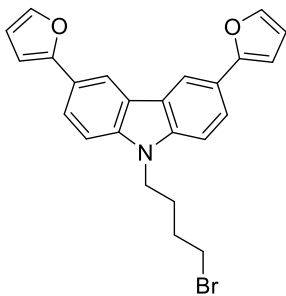
3,6-Dibromo-9H-carbazole (2 g, 6.15 mmol) was dissolved in anhydrous toluene (40 ml) under argon atmosphere, followed by addition of 2-(tributylstannyl)furan (4.8 ml, 15.4 mmol) and Pd(PPh₃)₄ (0.71 g, 0.62 mmol). Reaction conducted at 90 °C under inert argon atmosphere for 24 hours. After termination of

reaction (TLC, acetone:*n*-hexane, 4:21), reaction mixture was cooled down and filtered through celite which was washed with THF. Organic solvent was evaporated,

and the crude product was purified by column chromatography using acetone:*n*-hexane (4:21) as an eluent, resulting in white crystals (0.82 g, 45%) as a product. M.p. 166.5–168.5 °C.

¹H NMR (400 MHz, DMSO-d₆): δ 11.48 (s, 1H, NH), 8.56 (s, 2H, 4-H, 5-H of Cz), 7.83 – 7.67 (m, 4H, Ht), 7.54 (d, *J* = 8.5 Hz, 2H, Ht), 6.90 (d, *J* = 2.6 Hz, 2H, Ht), 6.65 – 6.55 (m, 2H, Ht) ppm. ¹³C NMR (101 MHz, DMSO-d₆): δ 154.43, 141.83, 139.61, 122.76, 122.16, 121.94, 115.64, 112.03, 111.56, 103.69 ppm. Anal. calcd. for C₂₀H₁₃NO₂: C 80.25, H 4.38, N 4.68; found: C 80.41, H 4.58, N 4.65.

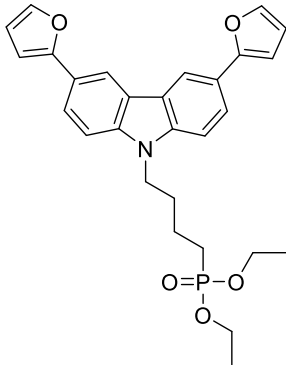
9-(4-Bromobutyl)-3,6-di(furan-2-yl)-9H-carbazole (79)



Method III. 9-(4-Bromobutyl)-3,6-di(furan-2-yl)-9H-carbazole (**78**) (0.7 g, 2.34 mmol), 1,4-dibromobutane (0.4 ml, 3.51 mmol), KOH (0.2 g, 3.51 mmol) and 15 ml of DMF were used for the reaction. Reaction conducted for 4 hours. Eluent: TLC (acetone:*n*-hexane, 4:21), column (acetone:*n*-hexane, 4:21). Product obtained as a dark yellow resin (0.71 g, 70% yield).

¹H NMR (400 MHz, DMSO-d₆): δ 8.60 (s, 2H, 4-H, 5-H of Cz), 7.83 (d, *J* = 8.6 Hz, 2H, Ht), 7.75 (s, 2H, Ht), 7.68 (d, *J* = 8.6 Hz, 2H, Ht), 6.93 (d, *J* = 2.8 Hz, 2H, Ht), 6.66 – 6.57 (m, 2H, Ht), 4.45 (t, *J* = 6.2 Hz, 2H, NCH₂), 3.54 (t, *J* = 6.2 Hz, 2H, CH₂Br), 1.97 – 1.78 (m, 4H, Aliph) ppm. ¹³C NMR (101 MHz, DMSO-d₆): δ 154.23, 141.94, 139.80, 122.44, 122.24, 122.18, 115.75, 112.05, 109.95, 103.93, 41.61, 34.63, 29.78, 27.32 ppm. Anal. calcd. for C₂₄H₂₀BrNO₂: C 66.37, H 4.64, N 3.22; found: C 66.50, H 4.71, N 3.21.

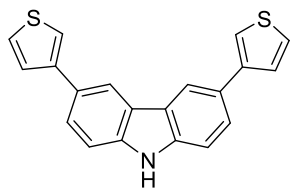
Diethyl [4-(3,6-di(furan-2-yl)-9H-carbazol-9-yl)butyl]phosphonate (80)



Method IV. 9-(4-Bromobutyl)-3,6-di(furan-2-yl)-9H-carbazole (**79**) (0.68 g, 1.57 mmol) and triethyl phosphite (5.4 ml, 31.3 mmol) were used for the reaction. Eluent: TLC (acetone:*n*-hexane, 6:19), column (acetone:*n*-hexane, 6:19). Product obtained as a dark yellow resin (0.69 g, 89%).

¹H NMR (400 MHz, DMSO-d₆): δ 8.59 (s, 2H, 4-H, 5-H of Cz), 7.83 (d, *J* = 8.6 Hz, 2H, Ht), 7.74 (s, 2H, Ht), 7.68 (d, *J* = 8.6 Hz, 2H, Ht), 6.93 (d, *J* = 2.7 Hz, 2H, Ht), 6.65 – 6.57 (s, 2H, Ht), 4.43 (t, *J* = 6.6 Hz, 2H, NCH₂), 3.89 (p, *J* = 7.2 Hz, 4H, OCH₂), 1.94 – 1.81 (m, 2H, CH₂), 1.81 – 1.67 (m, 2H, CH₂), 1.58 – 1.44 (m, 2H, CH₂), 1.13 (t, *J* = 7.0 Hz, 6H, CH₃). ¹³C NMR (101 MHz, DMSO-d₆): δ 154.25, 141.93, 139.85, 122.41, 122.17, 122.12, 115.71, 112.05, 110.04, 103.89, 60.74 (d, ²J_(C,P) = 6.3 Hz), 42.01, 29.27 (d, ²J_(C,P) = 15.9 Hz), 24.21 (d, ¹J_(C,P) = 138.6 Hz), 19.71 (d, ³J_(C,P) = 4.7 Hz), 16.21 (d, ³J_(C,P) = 5.7 Hz) ppm. Anal. calcd. for C₂₈H₃₀NO₅P: C 68.42, H 6.15, N 2.85; found: C 68.51, H 6.15, N 3.03.

3,6-Di(thiophen-3-yl)-9H-carbazole (81)



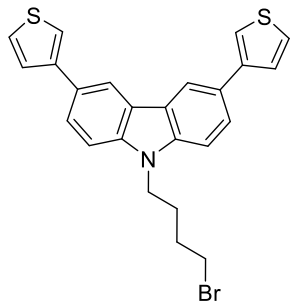
3,6-Dibromo-9H-carbazole (0.5 g, 1.53 mmol) was dissolved in anhydrous 1,4-dioxane (15 ml) under argon atmosphere, followed by the addition of 3-thienylboronic acid (0.49 g, 3.84 mmol), Pd(PPh₃)₄ (0.17 g, 0.15 mmol) and K₂CO₃ 2M aqueous solution (2.3 ml, 4.61 mmol).

Reaction conducted at 70 °C under inert argon atmosphere

for 24 hours. After termination of reaction (TLC, acetone:*n*-hexane, 4:21), reaction mixture was cooled down and filtered through celite which was washed with THF. Organic solvent was evaporated, and the crude product was purified by column chromatography using acetone:*n*-hexane (4:21) as an eluent resulting in white crystals (0.351 g, 69%) as a product. M.p. 201–202 °C.

¹H NMR (400 MHz, THF-d₈): δ 10.36 (s, 1H, NH), 8.45 (s, 2H, Ht, 4-H, 5-H of Cz), 7.71 (d, *J* = 8.4 Hz, 2H, Ht), 7.61 – 7.55 (m, 4H, Ht), 7.49 – 7.45 (m, 2H, Ht), 7.43 (d, *J* = 8.4 Hz, 2H, Ht) ppm. ¹³C NMR (101 MHz, THF-d₈): δ 144.57, 141.11, 128.42, 127.38, 126.70, 125.51, 124.93, 119.27, 118.84, 111.86 ppm. Anal. calcd. for C₂₀H₁₃NS₂: C 72.48, H 3.95, N 4.23; found: C 72.29, H 4.02, N 4.40.

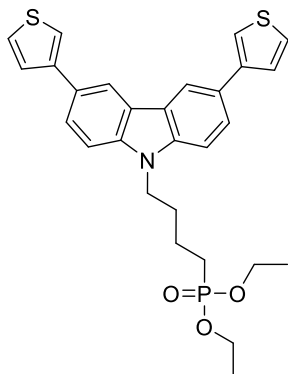
9-(4-Bromobutyl)-3,6-di(thiophen-3-yl)-9H-carbazole (82)



Method III. 3,6-Di(thiophen-3-yl)-9H-carbazole (81) (0.32 g, 0.96 mmol), 1,4-dibromobutane (0.17 ml, 1.44 mmol), KOH (0.08 g, 1.44 mmol) and 5 ml of DMF were used for the reaction. Reaction conducted for 30 minutes. Eluent: TLC (acetone:*n*-hexane, 1:4), column (acetone:*n*-hexane, 1:4). Product obtained as a colorless resin (0.28 g, 62% yield).

¹H NMR (400 MHz, DMSO-d₆): δ 8.61 (s, 2H, 4-H, 5-H of Cz), 7.84 (d, *J* = 1.1 Hz, 4H, Ht), 7.74 – 7.60 (m, 6H, Ht), 4.46 (t, *J* = 6.3 Hz, 2H, NCH₂), 3.55 (t, *J* = 6.3 Hz, 2H, CH₂Br), 1.98 – 1.79 (m, 4H, Aliph) ppm. ¹³C NMR (101 MHz, DMSO-d₆): δ 142.43, 139.68, 126.81, 126.62, 126.40, 124.54, 122.74, 118.99, 118.10, 109.75, 41.57, 34.71, 29.82, 27.34 ppm. Anal. calcd. for C₂₄H₂₀BrNS₂: C 61.80, H 4.32, N 3.00; found: C 61.99, H 4.25, N 2.87.

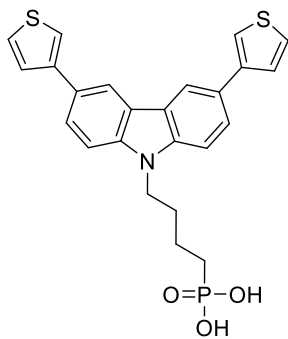
Diethyl {4-[3,6-di(thiophen-3-yl)-9H-carbazol-9-yl]butyl}phosphonate (83)



Method IV. 9-(4-Bromobutyl)-3,6-di(thiophen-3-yl)-9H-carbazole (**82**) (0.25 g, 0.53 mmol) and triethyl phosphite (1.83 ml, 10.71 mmol) were used for the reaction. Eluent: TLC (acetone:*n*-hexane, 1:1), column (acetone:*n*-hexane, 1:1). Product obtained as a yellowish resin (0.26 g, 93%).

¹H NMR (400 MHz, DMSO-d₆): δ 8.61 (s, 2H, 4-H, 5-H of Cz), 7.83 (d, *J* = 7.0 Hz, 4H, Ht), 7.73 – 7.58 (m, 6H, Ht), 4.43 (t, *J* = 6.7 Hz, 2H, NCH₂), 3.89 (p, *J* = 7.2 Hz, 4H, OCH₂), 1.94 – 1.82 (m, 2H, CH₂), 1.81 – 1.68 (m, 2H, CH₂), 1.59 – 1.44 (m, 2H, CH₂), 1.13 (t, *J* = 7.0 Hz, 6H, CH₃) ppm. ¹³C NMR (101 MHz, DMSO-d₆): δ 142.46, 139.73, 126.80, 126.56, 126.40, 124.46, 122.71, 118.95, 118.05, 109.83, 60.76 (d, ²J_(C,P) = 6.3 Hz), 41.97, 29.31 (d, ²J_(C,P) = 15.7 Hz), 24.24 (d, ¹J_(C,P) = 138.5 Hz), 19.74 (d, ³J_(C,P) = 4.8 Hz), 16.22 (d, ³J_(C,P) = 5.7 Hz) ppm. Anal. calcd. for C₂₈H₃₀NO₃PS₂: C 64.22, H 5.77, N 2.67; found: C 64.10, H 5.84, N 2.60.

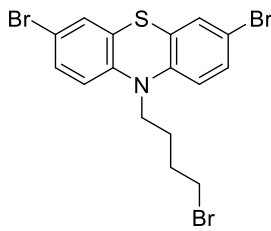
{4-[3,6-Di(thiophen-3-yl)-9H-carbazol-9-yl]butyl}phosphonic acid (84)



Method VI. Diethyl [4-(3,6-di(thiophen-3-yl)-9H-carbazol-9-yl)butyl]phosphonate (**83**) (1 g, 2.12 mmol), bromotrimethylsilane (2.75 ml, 21.2 mmol), methanol (0.9 ml, 21.2 mmol) and 20 ml of 1,4-dioxane were used. Eluent: TLC (acetone:*n*-hexane, 1:1). Product was purified by dissolving in the minimum amount of THF, precipitating into 20-fold excess of *n*-hexane, filtering, and washing with *n*-hexane to give dark grey crystals (0.81 g, 92% yield). M.p. 186.5–188 °C.

¹H NMR (400 MHz, DMSO-d₆): δ 8.61 (s, 2H, 4-H, 5-H of Cz), 7.83 (d, *J* = 7.2 Hz, 4H, Ht), 7.72 – 7.58 (m, 6H, Ht), 4.42 (t, *J* = 6.5 Hz, 2H, NCH₂), 1.95 – 1.79 (m, 2H, CH₂), 1.65 – 1.46 (m, 4H, Aliph) ppm. ¹³C NMR (101 MHz, DMSO-d₆): δ 142.48, 139.74, 126.80, 126.54, 126.42, 124.51, 122.70, 118.96, 118.07, 109.82, 42.25, 29.70 (d, ²J_(C,P) = 14.9 Hz), 27.40 (d, ¹J_(C,P) = 136.7 Hz), 20.48 (d, ³J_(C,P) = 4.3 Hz) ppm. Anal. calcd. for C₂₄H₂₂NO₃PS₂: C 61.66, H 4.74, N 3.00; found: C 61.71, H 4.90, N 3.12.

3,7-Dibromo-10-(4-bromobutyl)-10H-phenothiazine (85)

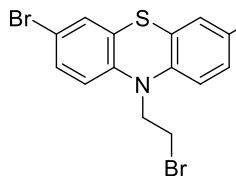


10-(4-Bromobutyl)-10H-phenothiazine (**56**) (2.7 g, 8.08 mmol) was dissolved in DMF (25 ml) and afterwards *N*-bromosuccinimide (2.95 g, 16.6 mmol) was added portionwise. Reaction conducted for 1 hour at 25 °C. After termination of reaction (TLC, eluent acetone:*n*-hexane, 1:24) organic components extracted with ethyl acetate, organic layer dried over anhydrous Na₂SO₄, filtered and

solvent evaporated under reduced pressure. The crude product was purified by column chromatography (eluent acetone:*n*-hexane, 1:24), resulting in a slightly orange resin (2.31 g, 58% yield) as a product.

¹H NMR (400 MHz, DMSO-d₆): δ 7.45 – 7.29 (m, 4H, Ht), 6.98 (d, *J* = 9.2 Hz, 2H, Ht), 3.86 (t, *J* = 6.6 Hz, 2H, NCH₂), 3.53 (t, *J* = 6.6 Hz, 2H, CH₂Br), 1.97 – 1.83 (m, 2H), 1.82 – 1.67 (m, 2H) ppm. ¹³C NMR (101 MHz, DMSO-d₆): δ 143.74, 130.37, 129.13, 125.63, 117.74, 114.15, 45.79, 34.66, 29.51, 24.76 ppm. Anal. calcd. for C₁₆H₁₄Br₃NS: C 39.05, H 2.87, N 2.85; found: C 38.81, H 3.00, N 3.01.

3,7-Dibromo-10-(2-bromoethyl)-10*H*-phenothiazine (**86**)

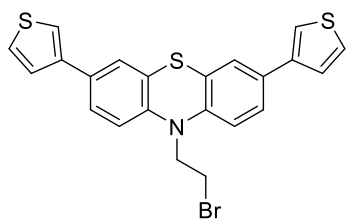


10-(2-Bromoethyl)-10*H*-phenothiazine (**44**) (2 g, 6.53 mmol) was dissolved in DMF (25 ml) and afterwards *N*-bromosuccinimide (2.38 g, 13.4 mmol) was added portionwise. Reaction conducted overnight at 25 °C. After termination of reaction (TLC, eluent acetone:*n*-hexane, 1:24) organic components extracted with ethyl acetate,

organic layer dried over anhydrous Na₂SO₄, filtered and solvent evaporated under reduced pressure. Crude product was purified by column chromatography (eluent acetone:*n*-hexane, 1:24), resulting in white crystals (2.44 g, 81% yield) as a product. M.p. 144–145 °C.

¹H NMR (400 MHz, DMSO-d₆): δ 7.39 – 7.32 (m, 4H, Ht), 6.98 (d, *J* = 8.6 Hz, 2H, Ht), 4.26 (t, *J* = 6.2 Hz, 2H, NCH₂), 3.70 (t, *J* = 6.1 Hz, 2H, CH₂Br) ppm. ¹³C NMR (101 MHz, DMSO-d₆): δ 143.05, 130.43, 129.21, 125.96, 117.70, 114.52, 48.49, 29.58 ppm. Anal. calcd. for C₁₄H₁₀Br₃NS: C 36.24, H 2.17, N 3.02; found: C 36.50, H 2.02, N 2.88.

10-(2-Bromoethyl)-3,7-di(thiophen-3-yl)-10*H*-phenothiazine (**87**)



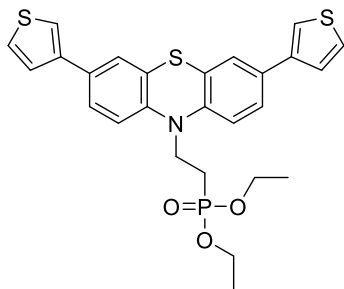
3,7-Dibromo-10-(2-bromoethyl)-10*H*-phenothiazine (**86**) (1.5 g, 3.23 mmol) was dissolved in anhydrous 1,4-dioxane (40 ml) under argon atmosphere, followed by addition of 3-thienylboronic acid (1.03 g, 8.08 mmol), Pd(PPh₃)₄ (0.37 g, 0.32 mmol) and K₂CO₃ 2M aqueous solution (5.9 ml, 9.69 mmol).

Reaction conducted at 80 °C under inert argon atmosphere for 24 hours. After termination of reaction (TLC, acetone:*n*-hexane, 2:23), reaction mixture was cooled down and filtered through celite which was washed with THF. Organic solvent was evaporated, and the crude product was purified by column chromatography using acetone:*n*-hexane (2:23) as an eluent resulting yellow crystals (1.24 g, 82%) as a product. M.p. 177.5–179 °C (melting and decomposition).

¹H NMR (400 MHz, DMSO-d₆): δ 7.82 (d, *J* = 1.1 Hz, 2H, 4-H, 6-H of Ptz), 7.62 – 7.58 (m, 2H, Ht), 7.57 – 7.48 (m, 6H, Ht), 7.10 – 7.01 (m, 2H, Ht), 4.35 (t, *J* = 6.1 Hz, 2H, NCH₂), 3.81 – 3.73 (m, 2H, CH₂Br) ppm. ¹³C NMR (101 MHz, DMSO-d₆): δ 142.55, 140.20, 130.20, 127.03, 126.00, 125.44, 124.65, 124.06, 120.12, 115.95,

48.46, 29.86 ppm. Anal. calcd. for $C_{22}H_{16}BrNS_3$: C 56.17, H 3.43, N 2.98; found: C 56.40, H 3.30, N 2.71.

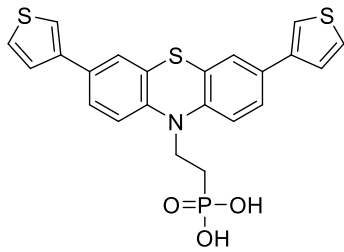
Diethyl {2-[3,7-di(thiophen-3-yl)-10H-phenothiazin-10-yl]ethyl}phosphonate (88)



Method IV. Diethyl {2-[3,7-di(thiophen-3-yl)-10H-phenothiazin-10-yl]ethyl}phosphonate (**87**) (1.2 g, 2.55 mmol) and triethyl phosphite (3 ml, 51 mmol) were used for the reaction. Eluent: TLC (acetone:*n*-hexane, 7:18), column (acetone:*n*-hexane, 7:18). Product obtained as yellow resin (1.05 g, 78 %).

¹H NMR (400 MHz, DMSO-d₆): δ 7.83 (s, 2H, 4-H, 6-H of Ptz), 7.63 – 7.52 (m, 8H, Ht), 7.05 (d, J = 8.4 Hz, 2H, Ht), 4.15 – 3.94 (m, 6H, NCH₂ and OCH₂ overlapped), 2.35 – 2.20 (m, 2H, CH₂P), 1.24 (t, J = 7.1 Hz, 6H, CH₃) ppm. ¹³C NMR (101 MHz, DMSO-d₆): δ 142.43, 140.16, 130.00, 126.99, 125.96, 125.41, 124.51, 123.37, 120.04, 115.49, 61.32 (d, $^2J_{C,P}$ = 6.2 Hz), 40.93, 23.12 (d, $^1J_{C,P}$ = 134.9 Hz), 16.28 (d, $^3J_{C,P}$ = 5.9 Hz) ppm. Anal. calcd. for $C_{26}H_{26}NO_3PS_3$: C 59.18, H 4.97, N 2.65; found: C 59.41, H 4.89, N 2.88.

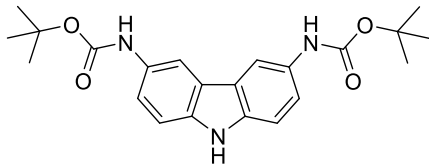
{2-[3,7-Di(thiophen-3-yl)-10H-phenothiazin-10-yl]ethyl}phosphonic acid (89)



Method VI. Diethyl {2-[3,7-di(thiophen-3-yl)-10H-phenothiazin-10-yl]ethyl}phosphonate (**88**) (1 g, 1.89 mmol), bromotrimethylsilane (2.5 ml, 18.9 mmol), methanol (0.8 ml, 18.9 mmol) and 25 ml of 1,4-dioxane were used. Eluent: TLC (acetone:*n*-hexane, 8:17). Product was purified by dissolving in the minimum amount of THF, precipitating into 20-fold excess of *n*-hexane, filtering, and washing with *n*-hexane to give brown crystals (0.62 g, 70% yield). M.p. 198–200 °C (melting and decomposition).

¹H NMR (400 MHz, DMSO-d₆): δ 7.80 (s, 2H, 4-H, 6-H of Ptz), 7.62 – 7.58 (m, 2H, Ht), 7.57 – 7.47 (m, 6H, Ht), 7.01 (d, J = 8.4 Hz, 2H, Ht), 4.13 – 3.98 (m, 2H, NCH₂), 2.16 – 2.00 (m, 2H, CH₂P) ppm. ¹³C NMR (101 MHz, DMSO-d₆): δ 142.33, 140.16, 129.89, 126.98, 125.96, 125.42, 124.45, 122.75, 119.98, 115.17, 41.98, 25.68 (d, $^1J_{C,P}$ = 130.2 Hz) ppm. Anal. calcd. for $C_{22}H_{18}NO_3PS_3$: C 56.04, H 3.85, N 2.97; found: C 56.20, H 4.01, N 2.83.

Di-tert-butyl (9H-carbazole-3,6-diy)dicarbamate (90)

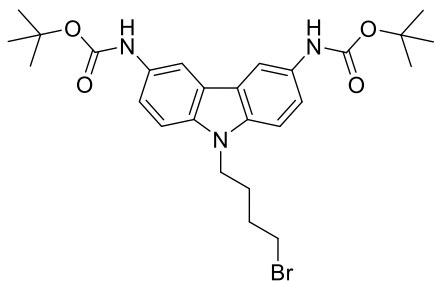


9H-carbazole-3,6-diamine (4 g, 20.3 mmol) was dissolved in MeOH (60 ml) and TEA (8.5 ml, 60.9 mmol). Afterwards, di-tert-butyl dicarbonate (9.3 ml, 40.6 mmol) was slowly added and reaction stirred for 3 h at 25 °C.

After termination of reaction (TLC, acetone:*n*-hexane, 1:4), solvents were removed under reduced pressure and organic components were extracted with ethyl acetate. Organic layer was dried over anhydrous Na₂SO₄, filtered and solvent evaporated under reduced pressure. Crude product was purified by column chromatography, using acetone:*n*-hexane (1:4) as an eluent, resulting yellow crystals (7.48 g, 93% yield) as a product. M.p. 239–241 °C (melting and decomposition).

¹H NMR (400 MHz, DMSO-d₆): δ 10.90 (s, 1H, NH), 9.23 (s, 2H, NH), 8.16 (s, 2H, 4-H, 5-H of Cz), 7.39 – 7.28 (m, 4H, Ht), 1.51 (s, 18H, CH₃) ppm. ¹³C NMR (101 MHz, DMSO-d₆): δ 153.23, 136.27, 131.06, 122.22, 118.09, 110.82, 109.28, 78.56, 28.28 ppm. Anal. calcd. for C₂₂H₂₇N₃O₄: C 66.48, H 6.85, N 10.57; found: C 66.57, H 6.99, N 10.51.

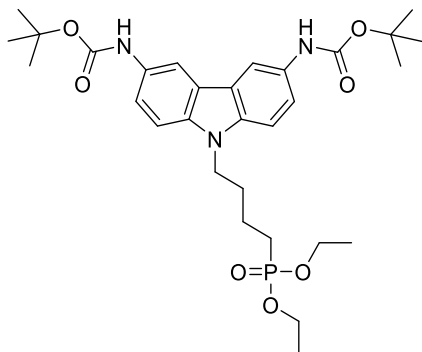
Di-tert-butyl [9-(4-bromobutyl)-9H-carbazole-3,6-diyl]dicarbamate (91)



Method III. Di-tert-butyl (9*H*-carbazole-3,6-diyl)dicarbamate (**90**) (5 g, 12.6 mmol), 1,4-dibromobutane (3 ml, 25.1 mmol), KOH (1.27 g, 25.1 mmol) and 40 ml of DMF were used for the reaction. Reaction conducted for 1 hour. Eluent: TLC (acetone:*n*-hexane, 6:19), column (acetone:*n*-hexane, 6:19). Product obtained as white crystals (2.68 g, 41% yield). M.p. 86–87.5 °C.

¹H NMR (400 MHz, DMSO-d₆): δ 9.27 (s, 2H, NH), 8.19 (s, 2H, 4-H, 5-H of Cz), 7.47 (d, *J* = 8.8 Hz, 2H, Ht), 7.40 (d, *J* = 8.6 Hz, 2H, Ht), 4.34 (t, *J* = 6.1 Hz, 2H, NCH₂), 3.52 (t, *J* = 6.3 Hz, 2H, CH₂Br), 1.97 – 1.70 (m, 4H, Aliph), 1.51 (s, 18H, CH₃) ppm. ¹³C NMR (101 MHz, DMSO-d₆): δ 153.21, 136.45, 131.32, 121.74, 118.13, 109.41, 109.20, 78.64, 41.41, 34.70, 29.82, 28.26, 27.29 ppm. Anal. calcd. for C₂₆H₃₄BrN₃O₄: C 58.65, H 6.44, N 7.89; found: C 58.50, H 6.49, N 7.99.

Di-tert-butyl {9-[4-(diethoxyphosphoryl)butyl]-9H-carbazole-3,6-diyl}dicarbamate (92)

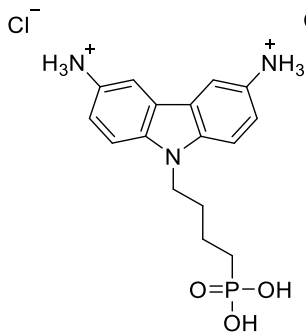


Method IV. Di-tert-butyl [9-(4-bromobutyl)-9*H*-carbazole-3,6-diyl]dicarbamate (**91**) (2.45 g, 4.68 mmol) and triethyl phosphite (16.1 ml, 93.6 mmol) were used for the reaction. Reaction conducted for 4 hours. Eluent: TLC (acetone:*n*-hexane, 2:3), column (acetone:*n*-hexane, 2:3). Product obtained as white crystals (2.37 g, 87% yield). M.p. 206.5–207.5 °C.

¹H NMR (400 MHz, DMSO-d₆): δ 9.26 (s, 2H, NH), 8.19 (s, 2H, 4-H, 5-H of Cz), 7.46 (d, *J* = 8.8 Hz, 2H, Ht), 7.40 (d, *J* = 8.7 Hz, 2H, Ht), 4.31 (t, *J* = 6.6 Hz, 2H, NCH₂), 3.88 (p, *J* = 7.2 Hz, 4H, OCH₂), 1.89 – 1.63 (m, 4H, Aliph), 1.55 – 1.41 (m, 20H), 1.13 (t, *J* =

7.0 Hz, 6H, CH_2CH_3) ppm. ^{13}C NMR (101 MHz, DMSO-d₆): δ 153.23, 136.52, 131.30, 121.74, 118.08, 109.29, 78.65, 60.78 (d, $^2J_{(\text{C},\text{P})} = 6.3$ Hz), 41.83, 29.34, 29.26 (d, $^2J_{(\text{C},\text{P})} = 15.6$ Hz), 24.22 (d, $^1J_{(\text{C},\text{P})} = 138.7$ Hz), 19.72 (d, $^3J_{(\text{C},\text{P})} = 4.8$ Hz), 16.24 (d, $^3J_{(\text{C},\text{P})} = 5.7$ Hz) ppm. Anal. calcd. for C₃₀H₄₄N₃O₇P: C 61.11, H 7.52, N 7.13; found: C 61.28, H 7.66, N 7.01.

9-(4-Phosphonobutyl)-9H-carbazole-3,6-bis(aminium) dichloride (93)

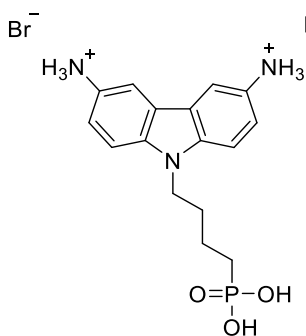


Method V. Di-*tert*-butyl {9-[4-(diethoxyphosphoryl)butyl]-9*H*-carbazole-3,6-diyi}dicarbamate (92) (0.8 g, 1.36 mmol) and hydrochloric acid (5.3 ml, 54.2 mmol) were used. Eluent: TLC (acetone:*n*-hexane, 2:3). Product was purified by dissolving in the minimum amount of MeOH, precipitating into 20-fold excess of diethyl ether, filtering and washing with diethyl ether to give brown crystals (0.42 g, 77% yield). M.p. 325–327 °C.

^1H NMR (400 MHz, DMSO-d₆): δ 9.55 (s, 6H, NH₃),

8.13 (s, 2H, 4-H, 5-H of Cz), 7.74 (d, $J = 8.6$ Hz, 2H, Ht), 7.48 (d, $J = 8.6$ Hz, 2H, Ht), 4.46 – 4.30 (m, 2H, NCH₂), 1.89 – 1.72 (m, 2H, CH₂), 1.61 – 1.40 (m, 4H, Aliph) ppm. ^{13}C NMR (101 MHz, DMSO-d₆): δ 139.33, 124.31, 121.44, 121.31, 114.51, 110.77, 42.37, 29.47 (d, $^2J_{(\text{C},\text{P})} = 15.9$ Hz), 27.26 (d, $^1J_{(\text{C},\text{P})} = 137.0$ Hz), 20.36 (d, $^3J_{(\text{C},\text{P})} = 4.4$ Hz) ppm. Anal. calcd. for C₁₆H₂₂Cl₂N₃O₃P: C 47.31, H 5.46, N 10.34; found: C 47.20, H 5.

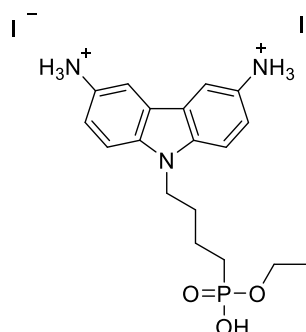
9-(4-Phosphonobutyl)-9H-carbazole-3,6-bis(aminium) dibromide (94)



Method VI. Di-*tert*-butyl {9-[4-(diethoxyphosphoryl)butyl]-9*H*-carbazole-3,6-diyi}dicarbamate (92) (0.7 g, 1.19 mmol), bromotrimethylsilane (1.5 ml, 11.9 mmol), methanol (0.5 ml, 11.9 mmol) and 30 ml of 1,4-dioxane were used. Eluent: TLC (acetone:*n*-hexane, 2:3). Solvent was evaporated under reduced pressure. Product was purified by dissolving in the minimum amount of MeOH, precipitating into 20-fold excess of diethyl ether, filtering and washing with diethyl ether to give brown crystals (0.28 g, 48% yield). M.p. 340–342 °C.

^1H NMR (400 MHz, DMSO-d₆): δ 10.11 (s, 6H, NH₃), 8.21 (s, 2H, 4-H, 5-H of Cz), 7.83 (d, $J = 8.7$ Hz, 2H, Ht), 7.52 (d, $J = 8.6$ Hz, 2H, Ht), 4.47 (t, $J = 5.9$ Hz, 2H, NCH₂), 1.93 – 1.74 (m, 2H, CH₂), 1.64 – 1.38 (m, 4H, Aliph) ppm. ^{13}C NMR (101 MHz, DMSO-d₆): δ 139.74, 123.26, 121.58, 121.44, 115.13, 111.03, 42.46, 29.47 (d, $^2J_{(\text{C},\text{P})} = 14.9$ Hz), 27.24 (d, $^1J_{(\text{C},\text{P})} = 136.5$ Hz), 20.37 (d, $^3J_{(\text{C},\text{P})} = 4.2$ Hz) ppm. Anal. calcd. for C₁₆H₂₂Br₂N₃O₃P: C 38.81, H 4.48, N 8.49; found: C 38.68, H 4.37, N 8.40.

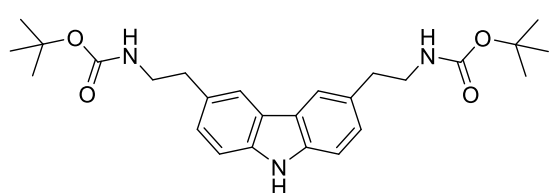
9-[4-[ethoxy(hydroxy)phosphoryl]butyl]-9H-carbazole-3,6-bis(aminium) diiodide (95)



Method VI (iodotrimethylsilane instead of bromotrimethylsilane). Di-*tert*-butyl {9-[4-(diethoxyphosphoryl)butyl]-9H-carbazole-3,6-diyil} dicarbamate (**92**) (0.5 g, 0.85 mmol), iodotrimethylsilane (1.2 ml, 8.48 mmol), methanol (0.4 ml, 8.48 mmol) and 30 ml of 1,4-dioxane were used. Eluent: TLC (acetone:*n*-hexane, 2:3). Solvent was evaporated under reduced pressure. Product was purified by dissolving in the minimum amount of MeOH, precipitating into 20-fold excess of diethyl ether, filtering and washing with diethyl ether to give black crystals (0.06 g, 11% yield). M.p. > 360 °C.

¹H NMR (400 MHz, DMSO-d₆): δ 9.99 (s, 6H, NH₃), 8.19 (s, 2H, 4-H, 5-H of Cz), 7.84 (d, *J* = 8.8 Hz, 2H, Ht), 7.50 (d, *J* = 8.7 Hz, 2H, Ht), 4.48 (t, *J* = 6.5 Hz, 2H, NCH₂), 3.38 (q, *J* = 6.9 Hz, 2H, OCH₂), 1.91 – 1.78 (m, 2H, CH₂), 1.68 – 1.44 (m, 4H, Aliph), 1.08 (t, *J* = 7.0 Hz, 3H, CH₃) ppm. ¹³C NMR (101 MHz, DMSO-d₆): δ 139.80, 123.13, 121.59, 121.45, 115.23, 111.10, 64.92, 42.47, 29.46 (d, ²*J*_(C,P) = 15.9 Hz), 27.27 (d, ¹*J*_(C,P) = 136.5 Hz), 20.35 (d, ³*J*_(C,P) = 4.6 Hz), 15.18 ppm. Anal. calcd. for C₁₈H₂₆I₂N₃O₃P: C 35.03, H 4.25, N 6.81; found: C 34.85, H 4.11, N 6.99.

Di-tert-butyl [/(9H-carbazole-3,6-diyil)bis(ethane-2,1-diyil)]dicarbamate (96)

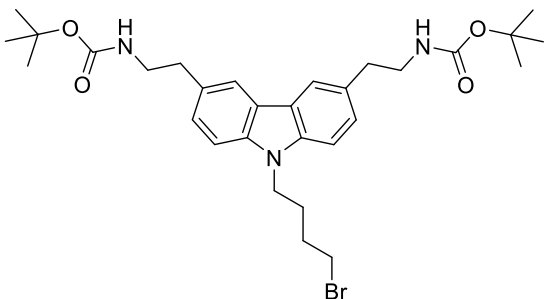


9H-Carbazole-3,6-diethanamine dihydrochloride (0.9 g, 2.76 mmol) was dissolved in MeOH (20 ml) and TEA (1.2 ml, 8.28 mmol). Afterwards, di-*tert*-butyl dicarbonate (1.4 ml, 6.07 mmol) was

slowly added and reaction stirred for 3 hours at 25 °C. After termination of reaction (TLC, acetone:*n*-hexane, 8:17), solvents were removed under reduced pressure and organic components were extracted with ethyl acetate. Organic layer was dried over anhydrous Na₂SO₄, filtered and solvent evaporated under reduced pressure. Crude product was purified by column chromatography, using acetone:*n*-hexane (8:17) as an eluent, resulting in light yellow crystals (0.86 g, 69% yield) as a product. M.p. 134–136 °C.

¹H NMR (400 MHz, DMSO-d₆): δ 11.01 (s, 1H, NH), 7.87 (s, 2H, 4-H, 5-H of Cz), 7.36 (d, *J* = 8.2 Hz, 2H, Ht), 7.19 (d, *J* = 8.2 Hz, 2H, Ht), 6.89 (s, 2H, NH), 3.26 – 3.15 (m, 4H, CH₂), 2.83 (t, *J* = 7.4 Hz, 4H, CH₂), 1.38 (s, 18H, CH₃). ¹³C NMR (101 MHz, DMSO-d₆): δ 155.56, 138.66, 129.20, 126.32, 122.40, 119.69, 110.67, 77.44, 42.31, 35.69, 28.29. Anal. calcd. for C₂₆H₃₅N₃O₄: C 68.85, H 7.78, N 9.26; found: C 68.98, H 7.78, N 9.21.

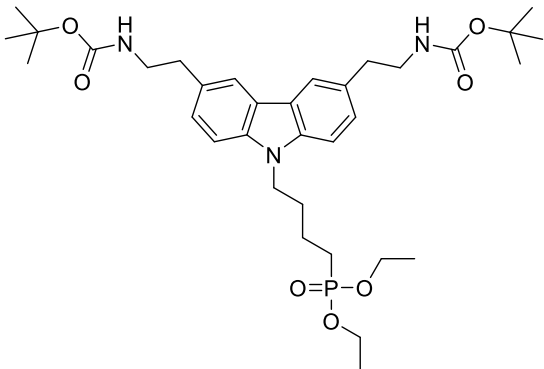
Di-tert-butyl {[9-(4-bromobutyl)-9H-carbazole-3,6-diyl]bis(ethane-2,1-diyl)}dicarbamate (97)



colorless resin (0.87 g, 84% yield).

^1H NMR (400 MHz, DMSO- d_6): δ 7.92 (s, 2H, 4-H, 5-H of Cz), 7.50 (d, $J = 8.3$ Hz, 2H, Ht), 7.26 (d, $J = 8.3$ Hz, 2H, Ht), 6.91 (s, 2H, NH), 4.37 (m, 2H, NCH_2), 3.54 (t, $J = 5.7$ Hz, 2H, CH_2Br), 3.27 – 3.15 (m, 4H, CH_2), 2.85 (t, $J = 7.3$ Hz, 4H, CH_2), 1.92 – 1.76 (m, 4H, Aliph), 1.37 (s, 18H, CH_3) ppm. ^{13}C NMR (101 MHz, DMSO- d_6): δ 155.56, 138.90, 129.52, 126.51, 122.02, 119.89, 108.98, 77.44, 42.23, 41.42, 35.57, 34.74, 29.81, 28.28, 27.30 ppm. Anal. calcd. for $\text{C}_{30}\text{H}_{42}\text{BrN}_3\text{O}_4$: C 61.22, H 7.19, N 7.14; found: C 61.27, H 7.10, N 7.03.

Di-tert-butyl {[9-[4-(diethoxyphosphoryl)butyl]-9H-carbazole-3,6-diyl]bis(ethane-2,1-diyl)}dicarbamate (98)

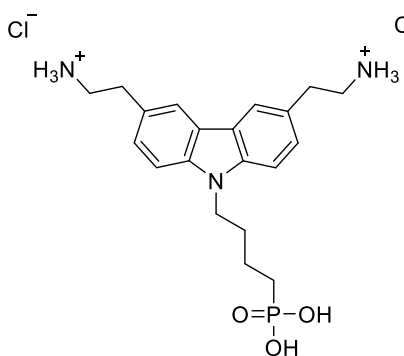


Method III. *Di-tert-butyl {[9H-carbazole-3,6-diyl]bis(ethane-2,1-diyl)}dicarbamate (96)* (0.8 g, 1.76 mmol), 1,4-dibromobutane (0.3 ml, 2.65 mmol), KOH (0.15 g, 2.65 mmol) and 10 ml of DMF were used for the reaction. Reaction conducted for 1 hour. Eluent: TLC (acetone:*n*-hexane, 1:4), column (acetone:*n*-hexane, 1:4). Product obtained as a

Method IV. *Di-tert-butyl {[9-(4-bromobutyl)-9H-carbazole-3,6-diyl]bis(ethane-2,1-diyl)}dicarbamate (97)* (0.84 g, 1.43 mmol) and triethyl phosphite (4.9 ml, 28.5 mmol) were used for the reaction. Reaction conducted for 3 hours. Eluent: TLC (acetone:*n*-hexane, 2:3), column (acetone:*n*-hexane, 2:3). Product obtained as a colorless resin (0.89 g, 97% yield).

^1H NMR (400 MHz, DMSO- d_6): δ 7.91 (s, 2H, 4-H, 5-H of Cz), 7.50 (d, $J = 8.3$ Hz, 2H, Ht), 7.25 (d, $J = 8.3$ Hz, 2H, Ht), 6.96 – 6.85 (m, 2H, NH), 4.34 (t, $J = 6.3$ Hz, 2H, NCH_2), 3.89 (p, $J = 7.1$ Hz, 4H, OCH_2), 3.28 – 3.14 (m, 4H, CH_2), 2.84 (t, $J = 7.3$ Hz, 4H, CH_2), 1.87 – 1.64 (m, 4H, Aliph), 1.58 – 1.44 (m, 2H, CH_2), 1.37 (s, 18H, CCH_3), 1.14 (t, $J = 7.1$ Hz, 6H, CH_2CH_3) ppm. ^{13}C NMR (101 MHz, DMSO- d_6): δ 155.56, 138.95, 129.45, 126.43, 122.00, 119.84, 109.07, 77.45, 60.74 (d, $^2J_{(\text{C},\text{P})} = 6.3$ Hz), 42.27, 41.81, 35.58, 29.27 (d, $^2J_{(\text{C},\text{P})} = 15.6$ Hz), 28.28, 24.25 (d, $^1J_{(\text{C},\text{P})} = 138.5$ Hz), 19.74 (d, $^3J_{(\text{C},\text{P})} = 4.7$ Hz), 16.22 (d, $^3J_{(\text{C},\text{P})} = 5.7$ Hz) ppm. Anal. calcd. for $\text{C}_{34}\text{H}_{52}\text{N}_3\text{O}_7\text{P}$: C 63.24, H 8.12, N 6.51; found: C 63.30, H 8.27, N 6.58.

2,2'-[9-(4-Phosphonobutyl)-9H-carbazole-3,6-diyl]bis(ethan-1-aminium) dichloride (99)

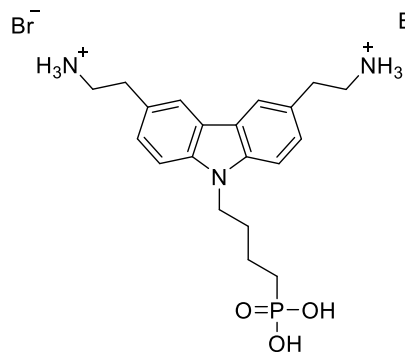


Method V. Di-*tert*-butyl (({9-[4-(diethoxyphosphoryl)butyl]-9*H*-carbazole-3,6-diyl}bis(ethane-2,1-diyl))dicarbamate (**98**) (0.4 g, 0.62 mmol) and hydrochloric acid (2.4 ml, 24.8 mmol) were used. Eluent: TLC (acetone:*n*-hexane, 1:1). Solvents was removed under reduced pressure. Product was purified by dissolving in the minimum amount of MeOH, precipitating into 20-fold excess of diethyl ether, filtering and washing with diethyl ether to give brown crystals (0.25 g,

87% yield). M.p. 227–229 °C (melting and decomposition).

¹H NMR (400 MHz, DMSO-d₆): δ 8.26 (s, 6H, NH₃), 8.02 (s, 2H, 4-H, 5-H of Cz), 7.56 (d, *J* = 8.3 Hz, 2H, Ht), 7.33 (d, *J* = 8.3 Hz, 2H, Ht), 4.41 – 4.28 (m, 2H, NCH₂), 3.16 – 2.99 (m, 8H, Aliph), 1.89 – 1.74 (m, 2H, CH₂), 1.62 – 1.42 (m, 4H, Aliph) ppm. ¹³C NMR (101 MHz, DMSO-d₆): δ 139.32, 127.50, 126.58, 122.05, 120.15, 109.53, 42.16, 40.56, 33.04, 29.66 (d, ²J_(C,P) = 15.3 Hz), 27.39 (d, ¹J_(C,P) = 136.7 Hz), 20.41 (d, ³J_(C,P) = 4.4 Hz) ppm. Anal. calcd. for C₂₀H₃₀Cl₂N₃O₃P: C 51.96, H 6.54, N 9.09; found: C 52.21, H 6.30, N 9.09.

2,2'-[9-(4-Phosphonobutyl)-9H-carbazole-3,6-diyl]bis(ethan-1-aminium) dibromide (10)



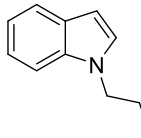
Method VI. Di-*tert*-butyl (({9-[4-(diethoxyphosphoryl)butyl]-9*H*-carbazole-3,6-diyl}bis(ethane-2,1-diyl))dicarbamate (**98**) (0.45 g, 0.69 mmol), bromotrimethylsilane (1 ml, 6.96 mmol), methanol (0.3 ml, 6.96 mmol) and 5 ml of 1,4-dioxane were used. Eluent: TLC (acetone:*n*-hexane, 1:1). Solvent was removed under reduced pressure. Product was purified by dissolving in the minimum amount of MeOH, precipitating into 20-fold excess of diethyl ether, filtering and washing with diethyl

ether to give brown crystals (0.27 g, 70% yield). M.p. 280.5–282 °C (melting and decomposition).

¹H NMR (400 MHz, DMSO-d₆): δ 8.02 (s, 2H, 4-H, 5-H of Cz), 7.95 (s, 6H, NH₃), 7.57 (d, *J* = 8.3 Hz, 2H, Ht), 7.34 (d, *J* = 8.2 Hz, 2H, Ht), 4.43 – 4.26 (m, 2H, NCH₂), 3.19 – 2.98 (m, 8H, Aliph), 1.88 – 1.74 (m, 2H, CH₂), 1.60 – 1.41 (m, 4H, Aliph) ppm. ¹³C NMR (101 MHz, DMSO-d₆): δ 139.34, 127.34, 126.59, 122.02, 120.18, 109.56, 42.15, 40.61, 33.05, 29.66 (d, ²J_(C,P) = 15.9 Hz), 27.38 (d, ¹J_(C,P) = 136.6 Hz), 20.40 (d,

$^3J_{(C,P)} = 4.1$ Hz) ppm. Anal. calcd. for C₂₀H₃₀Br₂N₃O₃P: C 43.58, H 5.49, N 7.62; found: C 43.29, H 5.42, N 7.55.

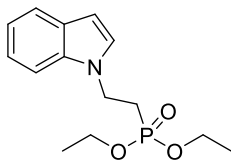
I-(2-Bromoethyl)-1H-indole (101)



Method I. 1*H*-Indole (1 g, 8.54 mmol), 1,2-dibromoethane (18.5 ml, 213 mmol), 50 % KOH aqueous solution (4.8 ml, 42.7 mmol) and tetrabutylammonium bromide (0.41 g, 1.28 mmol) were used for the reaction. The reaction conducted for 168 hours. Eluent: TLC (acetone:*n*-hexane, 1:24), column (acetone:*n*-hexane, 1:24). Product obtained as a light orange resin (0.4 g, 21% yield).

¹H NMR (400 MHz, DMSO-d₆): δ 7.54 (dd, J = 13.1, 8.1 Hz, 2H), 7.42 (d, J = 2.5 Hz, 1H, 6-H of Ind), 7.14 (t, J = 7.6 Hz, 1H, Ht, 5-H of Ind), 7.03 (t, J = 7.4 Hz, 1H, 2-H of Ind), 6.45 (d, J = 2.5 Hz, 1H, 3-H of Ind), 4.60 (t, J = 6.2 Hz, 2H, NCH₂), 3.85 (t, J = 6.2 Hz, 2H, CH₂Br) ppm. ¹³C NMR (101 MHz, DMSO-d₆): δ 135.61, 128.84, 128.17, 121.15, 120.43, 119.18, 109.79, 100.91, 46.99, 32.45 ppm. Anal. calcd. for C₁₀H₁₀BrN: C 53.60, H 4.50, N 6.25; found: C 53.74, H 4.44, N 6.21.

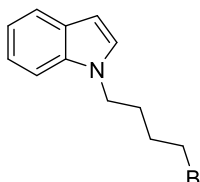
*Diethyl [2-(1*H*-indol-1-yl)ethyl]phosphonate (102)*



Method IV. 1-(2-Bromoethyl)-1*H*-indole (**101**) (0.37 g, 1.65 mmol) and triethyl phosphite (5.5 ml, 33 mmol) were used for the reaction. Eluent: TLC (acetone:*n*-hexane, 7:18), column (acetone:*n*-hexane, 7:18). Product obtained as a yellow resin (0.42 g, 91%).

¹H NMR (400 MHz, DMSO-d₆): δ 7.54 (d, J = 7.8 Hz, 1H, Ht, 4-H of Ind), 7.42 (d, J = 8.6 Hz, 2H, Ht), 7.15 (t, J = 7.6 Hz, 1H, Ht, 5-H of Ind), 7.02 (t, J = 7.4 Hz, 1H, Ht, 2-H of Ind), 6.43 (d, J = 2.2 Hz, 1H, 3-H of Ind), 4.36 (dt, J = 11.8, 7.6 Hz, 2H, NCH₂), 3.95 (p, J = 7.2 Hz, 4H, OCH₂), 2.30 (dt, J = 15.5, 7.5 Hz, 2H, CH₂P), 1.17 (t, J = 6.9 Hz, 6H, CH₃) ppm. ¹³C NMR (101 MHz, DMSO-d₆): δ 135.26, 128.49, 128.24, 121.12, 120.46, 119.07, 109.50, 100.81, 61.16 (d, $^2J_{(C,P)} = 6.2$ Hz), 25.96 (d, $^1J_{(C,P)} = 135.8$ Hz), 24.48, 16.16 (d, $^3J_{(C,P)} = 5.9$ Hz) ppm. Anal. calcd. for C₁₄H₂₀NO₃P: C 59.78, H 7.17, N 4.98; found: C 59.81, H 7.30, N 5.02.

I-(4-Bromobutyl)-1H-indole (103)

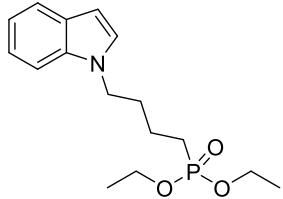


Method III. 1*H*-Indole (1 g, 0.96 mmol), 1,4-dibromobutane (1.5 ml, 12.8 mmol), KOH (0.72 g, 12.8 mmol) and 10 ml of DMF were used for the reaction. The reaction conducted for 5 minutes. Eluent: TLC (acetone:*n*-hexane, 1:24), column (acetone:*n*-hexane, 1:24). Product obtained as a yellow resin (1.19 g, 55% yield).

¹H NMR (400 MHz, DMSO-d₆): δ 7.54 (d, J = 7.8 Hz, 1H, 4-H of Ind), 7.48 (d, J = 8.2 Hz, 1H, Ht, 7-H of Ind), 7.36 (d, J = 2.7 Hz, 1H, Ht, 6-H of Ind), 7.13 (t, J = 7.6 Hz, 1H, 5-H of Ind), 7.01 (t, J = 7.4 Hz, 1H, 2-H of Ind), 6.42 (d, J = 2.6 Hz, 1H, 3-H of Ind), 4.21 (t, J = 6.8 Hz, 2H, NCH₂), 3.53 (t, J = 6.6 Hz, 2H, CH₂Br), 1.92 – 1.81

(m, 2H, CH₂), 1.80 – 1.69 (m, 2H, CH₂) ppm. ¹³C NMR (101 MHz, DMSO-d₆): δ 135.61, 128.54, 128.09, 120.97, 120.42, 118.86, 109.75, 100.50, 44.55, 34.55, 29.63, 28.52 ppm. Anal. calcd. for C₁₂H₁₄BrN: C 57.16, H 5.60, N 5.55; found: C 57.13, H 5.66, N 5.40.

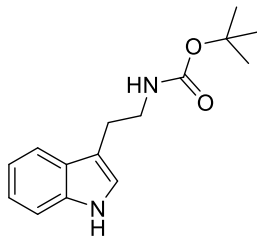
*Diethyl [4-(1*H*-indol-1-yl)butyl]phosphonate (104)*



Method IV. 1-(4-Bromobutyl)-1*H*-indole (**103**) (1.15 g, 4.65 mmol) and triethyl phosphite (15.6 ml, 91.2 mmol) were used for the reaction. Eluent: TLC (acetone:*n*-hexane, 7:18), column (acetone:*n*-hexane, 7:18). Product obtained as a yellow resin (1.39 g, 99%).

¹H NMR (400 MHz, DMSO-d₆): δ 7.53 (d, *J* = 7.8 Hz, 1H, 4-H of Ind), 7.48 (d, *J* = 8.2 Hz, 1H, 7-H of Ind), 7.35 (d, *J* = 1.5 Hz, 1H, 6-H of Ind), 7.12 (t, *J* = 7.6 Hz, 1H, Ht, 5-H of Ind), 7.00 (t, *J* = 7.4 Hz, 1H, 2-H of Ind), 6.42 (d, *J* = 0.8 Hz, 1H, 3-H of Ind), 4.18 (t, *J* = 6.8 Hz, 2H, NCH₂), 3.92 (p, *J* = 7.1 Hz, 4H, OCH₂), 1.88 – 1.67 (m, 4H, Aliph), 1.50 – 1.33 (m, 2H, CH₂), 1.17 (t, *J* = 6.9 Hz, 6H, CH₃) ppm. ¹³C NMR (101 MHz, DMSO-d₆): δ 135.62, 128.57, 128.09, 120.88, 120.38, 118.80, 109.80, 100.36, 60.75 (d, ²*J*_(C,P) = 6.3 Hz), 44.88, 30.43 (d, ²*J*_(C,P) = 16.0 Hz), 24.02 (d, ¹*J*_(C,P) = 138.5 Hz), 19.46 (d, ³*J*_(C,P) = 6.1 Hz), 16.25 (d, ³*J*_(C,P) = 5.7 Hz) ppm. Anal. calcd. for C₁₆H₂₄NO₃P: C 62.12, H 7.82, N 4.53; found: C 62.00, H 7.98, N 4.29.

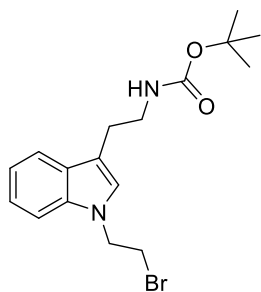
*Tert-butyl [2-(1*H*-indol-3-yl)ethyl]carbamate (105)*



Tryptamine hydrochloride (2 g, 10.2 mmol) was dissolved in MeOH (15 ml) and TEA (2.9 ml, 30.5 mmol). Afterwards, di-*tert*-butyl dicarbonate (3.5 ml, 15.3 mmol) was slowly added and reaction stirred for 3h at 25 °C. After termination of reaction (TLC, acetone:*n*-hexane, 1:4), solvents were removed under reduced pressure and organic components were extracted with ethyl acetate. The organic layer was dried over anhydrous Na₂SO₄, filtered and solvent evaporated under reduced pressure. Crude product was purified by column chromatography, using acetone:*n*-hexane (1:4) as an eluent, resulting in a colorless resin (2.54 g, 96% yield) as a product.

¹H NMR (400 MHz, DMSO-d₆): δ 10.80 (s, 1H, NH of Ind), 7.52 (d, *J* = 7.8 Hz, 1H, 4-H of Ind), 7.34 (d, *J* = 8.0 Hz, 1H, 7-H of Ind), 7.14 (s, 1H, 2-H of Ind), 7.06 (t, *J* = 7.5 Hz, 1H, 6-H of Ind), 6.98 (t, *J* = 7.4 Hz, 1H, 5-H of Ind), 6.89 (t, *J* = 5.3 Hz, 1H, Aliph NH), 3.21 (dd, *J* = 13.7, 6.7 Hz, 2H, CH₂), 2.81 (t, *J* = 7.5 Hz, 2H, CH₂), 1.39 (s, 9H, CH₃) ppm. ¹³C NMR (101 MHz, DMSO-d₆): δ 155.60, 136.23, 127.29, 122.54, 120.88, 118.26, 118.18, 111.82, 111.34, 77.43, 40.87, 28.30, 25.56 ppm. Anal. calcd. for C₁₅H₂₀N₂O₂: C 69.20, H 7.74, N 10.76; found: C 69.18, H 7.71, N 10.86.

*Tert-butyl {2-[1-(2-bromoethyl)-1*H*-indol-3-yl]ethyl}carbamate (106)*

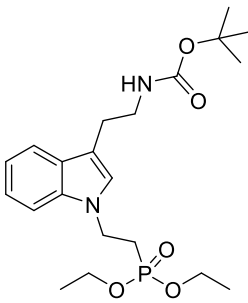


Method I. *Tert-butyl [2-(1*H*-indol-3-yl)ethyl]carbamate (105)* (2.5 g, 9.6 mmol), 1,2-dibromoethane (21 ml, 240 mmol), 50 % KOH aqueous solution (5.4 ml, 48 mmol) and tetrabutylammonium bromide (0.46 g, 1.44 mmol) were used for the reaction. Reaction conducted for 336 hours. Eluent: TLC (acetone:*n*-hexane, 1:4), column (acetone:*n*-hexane, 1:4). Product obtained as a light orange resin (0.75 g, 27% yield).

¹H NMR (400 MHz, DMSO-d₆): δ 7.54 (d, *J* = 7.8 Hz, 1H, 4-H of Ind), 7.47 (d, *J* = 8.2 Hz, 1H, 7-H of Ind), 7.23 (s, 1H, 2-H of Ind), 7.13 (t, *J* = 7.5 Hz, 1H, 7-H of Ind), 7.03 (t, *J* = 7.4 Hz, 1H, 5-H of Ind), 6.90 (t, *J* = 5.3 Hz, 1H, Aliph NH), 4.53 (t, *J* = 6.3 Hz, 2H, NCH₂), 3.81 (t, *J* = 6.3 Hz, 2H, CH₂Br), 3.25 – 3.12 (m, 2H, CH₂), 2.79 (t, *J* = 7.6 Hz, 2H, CH₂), 1.39 (s, 9H, CH₃) ppm. ¹³C NMR (101 MHz, DMSO-d₆): δ 155.57, 135.97, 127.77, 126.12, 121.26, 118.68, 118.63, 111.76, 109.72, 77.46, 46.85, 40.70, 32.40, 28.29, 25.45 ppm.

Anal. calcd. for C₁₇H₂₃BrN₂O₂: C 55.59, H 6.31, N 7.63; found: C 55.70, H 6.20, N 7.69.

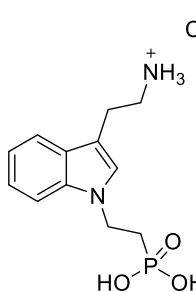
*Tert-butyl (2-{1-[2-(diethoxyphosphoryl)ethyl]-1*H*-indol-3-yl}ethyl)carbamate (107)*



Method IV. *Tert-butyl {2-[1-(2-bromoethyl)-1*H*-indol-3-yl]ethyl}carbamate (106)* (0.72 g, 1.96 mmol) and triethyl phosphite (6.7 ml, 39.2 mmol) were used for the reaction. Eluent: TLC (acetone:*n*-hexane, 2:3), column (acetone:*n*-hexane, 2:3). Product obtained as a yellow resin (0.61 g, 74%).

¹H NMR (400 MHz, DMSO-d₆): δ 7.53 (d, *J* = 7.8 Hz, 1H, 4-H of Ind), 7.37 (d, *J* = 8.2 Hz, 1H, 7-H of Ind), 7.21 (s, 1H, 2-H of Ind), 7.14 (t, *J* = 7.5 Hz, 1H, 7-H of Ind), 7.02 (t, *J* = 7.4 Hz, 1H, 6-H of Ind), 6.90 (t, *J* = 5.4 Hz, 1H, Aliph NH), 4.29 (dt, *J* = 11.5, 7.8 Hz, 2H, NCH₂), 3.95 (p, *J* = 7.1 Hz, 4H, OCH₂), 3.19 (dd, *J* = 13.8, 6.6 Hz, 2H, CH₂), 2.78 (t, *J* = 7.5 Hz, 2H, CH₂), 2.34 – 2.19 (m, 2H, CH₂P), 1.39 (s, 9H, CCH₃), 1.17 (t, *J* = 7.0 Hz, 6H, CH₂CH₃) ppm. ¹³C NMR (101 MHz, DMSO-d₆): δ 155.58, 135.58, 127.85, 125.80, 121.21, 118.66, 118.55, 111.71, 109.43, 77.46, 61.15 (d, ²J_(C,P) = 6.2 Hz), 40.71, 28.28, 26.97 (d, ¹J_(C,P) = 135.5 Hz), 25.48, 16.16 (d, ³J_(C,P) = 5.9 Hz) ppm. Anal. calcd. for C₂₁H₃₃N₂O₅P: C 59.42, H 7.84, N 6.60; found: C 59.61, H 7.94, N 6.63.

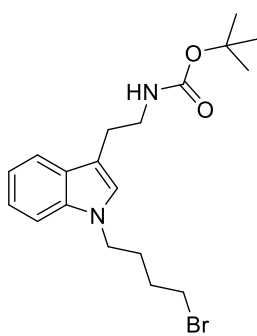
*2-[1-(2-Phosphonoethyl)-1*H*-indol-3-yl]ethan-1-aminium chloride (108)*



Method V. *Tert*-butyl (2-{1-[2-(diethoxyphosphoryl)ethyl]-1*H*-indol-3-yl}ethyl)carbamate (**107**) (0.58 g, 1.37 mmol) and hydrochloric acid (5.4 ml, 54.7 mmol) were used. Eluent: TLC (acetone:*n*-hexane, 2:3). Product was purified by dissolving in the minimum amount of MeOH, precipitating into 20-fold excess of diethyl ether, filtering and washing with diethyl ether to give greyish brown crystals (0.33 g, 79% yield). M.p. 145–147 °C (melting and decomposition).

¹H NMR (400 MHz, DMSO-d₆): δ 8.10 (s, 3H, NH₃), 7.58 (d, *J* = 7.9 Hz, 1H, 4-H of Ind), 7.39 (d, *J* = 8.2 Hz, 1H, 7-H of Ind), 7.32 (s, 1H, 2-H of Ind), 7.15 (t, *J* = 7.5 Hz, 1H, 6-H of Ind), 7.04 (t, *J* = 7.4 Hz, 1H, 5-H of Ind), 4.31 (dd, *J* = 16.0, 8.4 Hz, 2H, NCH₂), 3.02 (s, 4H), 2.11 – 1.98 (m, 2H, CH₂P) ppm. ¹³C NMR (101 MHz, DMSO-d₆): δ 135.64, 127.45, 126.84, 121.44, 118.78, 118.63, 109.61, 109.10, 40.65, 29.06 (d, ¹J_(C,P) = 131.7 Hz), 22.86 ppm. Anal. calcd. for C₁₂H₁₈ClN₂O₃P: C 47.30, H 5.95, N 9.19; found: C 47.58, H 6.13, N 9.41.

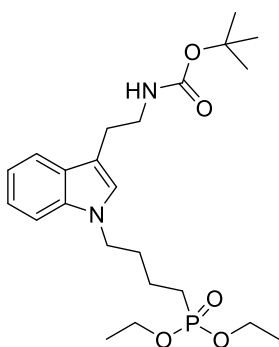
Tert-butyl {2-[1-(4-bromobutyl)-1*H*-indol-3-yl]ethyl}carbamate (**109**)



Method III. *Tert*-butyl [2-(1*H*-indol-3-yl)ethyl]carbamate (**105**) (2.5 g, 9.6 mmol), 1,4-dibromobutane (1.7 ml, 14.4 mmol), KOH (0.81 g, 14.4 mmol) and 15 ml of DMF were used for the reaction. Reaction conducted for 2 hours. Eluent: TLC (acetone:*n*-hexane, 1:4), column (acetone:*n*-hexane, 1:4). Product obtained as a colorless resin (1.58 g, 42% yield).

¹H NMR (400 MHz, DMSO-d₆): δ 7.52 (d, *J* = 7.8 Hz, 1H, 4-H of Ind), 7.43 (d, *J* = 8.2 Hz, 1H, 7-H of Ind), 7.16 (s, 1H, 2-H of Ind), 7.11 (t, *J* = 7.6 Hz, 1H, 6-H of Ind), 7.00 (t, *J* = 7.4 Hz, 1H, 5-H of Ind), 6.89 (t, *J* = 5.2 Hz, 1H, Aliph NH), 4.14 (t, *J* = 6.6 Hz, 2H, NCH₂), 3.52 (t, *J* = 6.5 Hz, 2H, CH₂Br), 3.25 – 3.13 (m, 2H, CH₂), 2.79 (t, *J* = 7.5 Hz, 2H, CH₂), 1.90 – 1.80 (m, 2H, CH₂), 1.80 – 1.70 (m, 2H, CH₂), 1.39 (s, 9H, CH₃) ppm. ¹³C NMR (101 MHz, DMSO-d₆): δ 155.57, 135.93, 127.65, 125.90, 121.03, 118.62, 118.31, 111.39, 109.64, 77.43, 44.37, 40.80, 34.60, 29.65, 28.54, 28.28, 25.44 ppm. Anal. calcd. for C₁₉H₂₇BrN₂O₂: C 57.72, H 6.88, N 7.09; found: C 57.65, H 6.91, N 7.00.

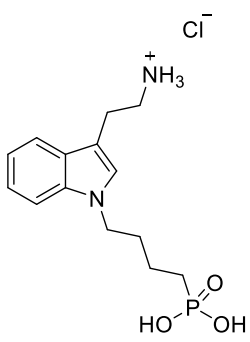
*Tert-butyl (2-{1-[4-(diethoxyphosphoryl)butyl]-1*H*-indol-3-yl}ethyl)carbamate (110)*



Method IV. *Tert-butyl {2-[1-(4-bromobutyl)-1*H*-indol-3-yl]ethyl}carbamate (109)* (1.55 g, 3.92 mmol) and triethyl phosphite (13.5 ml, 78.4 mmol) were used for the reaction. Eluent: TLC (acetone:*n*-hexane, 2:3), column (acetone:*n*-hexane, 2:3). Product obtained as a light-yellow resin (1.5 g, 85%).

¹H NMR (400 MHz, DMSO-d₆): δ 7.52 (d, *J* = 7.8 Hz, 1H, 4-H of Ind), 7.42 (d, *J* = 8.2 Hz, 1H, 7-H of Ind), 7.16 (s, 1H, 2-H of Ind), 7.11 (t, *J* = 7.6 Hz, 1H, 6-H of Ind), 7.00 (t, *J* = 7.4 Hz, 1H, 5-H of Ind), 6.91 (t, *J* = 5.3 Hz, 1H, Aliph NH), 4.11 (t, *J* = 6.8 Hz, 2H, NCH₂), 3.97 – 3.86 (m, 4H, OCH₂), 3.23 – 3.11 (m, 2H, CH₂), 2.78 (t, *J* = 7.6 Hz, 2H, CH₂), 1.87 – 1.66 (m, 4H, Aliph), 1.48 – 1.32 (m, 11H, Aliph), 1.17 (t, *J* = 7.0 Hz, 6H, CH₂CH₃) ppm. ¹³C NMR (101 MHz, DMSO-d₆): δ 155.58, 135.96, 127.63, 125.93, 120.96, 118.58, 118.26, 111.28, 109.71, 77.44, 76.12, 60.76 (d, ²J_(C,P) = 6.3 Hz), 44.67, 40.86, 31.85, 30.45 (d, ²J_(C,P) = 15.8 Hz), 28.28, 25.51, 24.03 (d, ¹J_(C,P) = 138.5 Hz), 19.49 (d, ³J_(C,P) = 4.9 Hz), 16.25 (d, ³J_(C,P) = 5.7 Hz) ppm. Anal. calcd. for C₂₃H₃₇N₂O₅P: C 61.05, H 8.24, N 6.19; found: C 60.90, H 8.10, N 6.36.

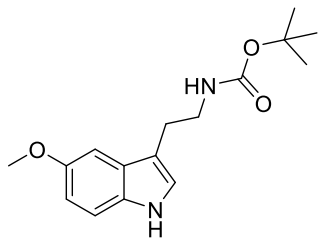
*2-[1-(4-Phosphonobutyl)-1*H*-indol-3-yl]ethan-1-aminium chloride (111)*



Method V. *Tert-butyl (2-{1-[4-(diethoxyphosphoryl)butyl]-1*H*-indol-3-yl}ethyl)carbamate (110)* (0.7 g, 1.77 mmol) and hydrochloric acid (7 ml, 70.8 mmol) were used. Eluent: TLC (acetone:*n*-hexane, 1:1). Solvent was removed under reduced pressure. Product was purified by dissolving in the minimum amount of MeOH, precipitating into 20-fold excess of diethyl ether, filtering and washing with diethyl ether to give purple crystals (0.27 g, 46% yield). M.p. 121–123 °C.

¹H NMR (400 MHz, DMSO-d₆): δ 8.17 (s, 3H, NH₃), 7.57 (d, *J* = 7.8 Hz, 1H, 4-H of Ind), 7.45 (d, *J* = 8.2 Hz, 1H, 7-H of Ind), 7.27 (s, 1H, 2-H of Ind), 7.13 (t, *J* = 7.6 Hz, 1H, 6-H of Ind), 7.02 (t, *J* = 7.4 Hz, 1H, 5-H of Ind), 4.11 (t, *J* = 6.8 Hz, 2H, NCH₂), 3.12 – 2.92 (m, 4H, Aliph), 1.81 (dt, *J* = 13.9, 6.8 Hz, 2H, CH₂), 1.58 – 1.41 (m, 4H, Aliph) ppm. ¹³C NMR (101 MHz, DMSO-d₆): δ 136.07, 127.21, 126.68, 121.27, 118.56, 118.50, 109.94, 109.02, 45.02, 30.74 (d, ²J_(C,P) = 15.4 Hz), 27.09 (d, ¹J_(C,P) = 136.1 Hz), 22.98, 20.19 (d, ³J_(C,P) = 4.4 Hz) ppm. Anal. calcd. for C₁₄H₂₂ClN₂O₃P: C 61.05, H 8.24, N 6.19; found: C 60.90, H 8.10, N 6.36.

*Tert-butyl [2-(5-methoxy-1*H*-indol-3-yl)ethyl]carbamate (112)*

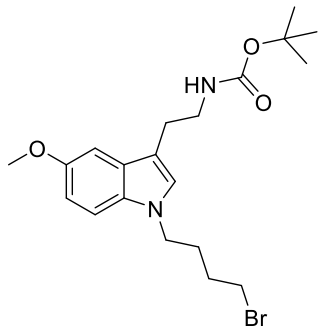


5-Methoxytryptamine (2.5 g, 13.1 mmol) was dissolved in MeOH (15 ml) and TEA (2.7 ml, 19.7 mmol). Afterwards, di-*tert*-butyl dicarbonate (3.6 ml, 15.8 mmol) was slowly added and reaction stirred for 30 minutes at 25 °C. After termination of reaction (TLC, acetone:*n*-hexane, 1:4), solvents were removed under reduced pressure and organic components were extracted with ethyl acetate. The organic layer was dried

over anhydrous Na₂SO₄, filtered and solvent evaporated under reduced pressure. Crude product was purified by column chromatography, using acetone:*n*-hexane (1:4) as an eluent, resulting in a light-yellow resin (3.62 g, 94% yield) as a product.

¹H NMR (400 MHz, DMSO-d₆): δ 10.62 (s, 1H, NH of Ind), 7.22 (d, *J* = 8.7 Hz, 1H), 7.09 (s, 1H), 7.00 (s, 1H), 6.87 (t, *J* = 4.8 Hz, 1H), 6.71 (d, *J* = 8.7 Hz, 1H), 3.76 (s, 3H, OCH₃), 3.24 – 3.12 (m, 2H), 2.76 (t, *J* = 7.4 Hz, 2H), 1.38 (s, 9H, CH₃) ppm. ¹³C NMR (101 MHz, DMSO-d₆): δ 155.58, 152.95, 131.37, 127.58, 123.22, 111.94, 111.61, 110.94, 100.25, 77.41, 55.36, 40.72, 28.30, 25.58 ppm. Anal. calcd. for C₁₆H₂₂N₂O₃: C 66.18, H 7.64, N 9.65; found: C 66.31, H 7.40, N 9.77.

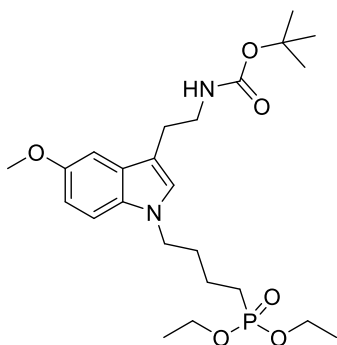
*Tert-butyl {2-[1-(4-bromobutyl)-5-methoxy-1*H*-indol-3-yl]ethyl}carbamate (113)*



Method III. *Tert-butyl [2-(5-methoxy-1*H*-indol-3-yl)ethyl]carbamate (112)* (3.5 g, 12.1 mmol), 1,4-dibromobutane (2.2 ml, 18.1 mmol), KOH (1.01 g, 18.1 mmol) and 20 ml of DMF were used for the reaction. Reaction conducted overnight. Eluent: TLC (acetone:*n*-hexane, 1:4), column (acetone:*n*-hexane, 1:4). Product obtained as a colorless resin (2.82 g, 55% yield).

¹H NMR (400 MHz, DMSO-d₆): δ 7.32 (d, *J* = 8.8 Hz), 7.12 (s, 1H), 7.02 (s, 1H), 6.87 (t, *J* = 4.8 Hz, 1H), 6.76 (d, *J* = 8.8 Hz, 1H), 4.09 (t, *J* = 6.5 Hz, 2H, NCH₂), 3.76 (s, 3H, OCH₃), 3.51 (t, *J* = 6.4 Hz, 2H, CH₂Br), 3.23 – 3.12 (m, 2H, CH₂), 2.75 (t, *J* = 7.3 Hz, 2H, CH₂), 1.88 – 1.77 (m, 2H, CH₂), 1.77 – 1.65 (m, 2H, CH₂), 1.38 (s, 9H, CH₃). ¹³C NMR (101 MHz, DMSO-d₆): δ 155.56, 153.09, 131.24, 127.95, 126.45, 110.98, 110.37, 100.68, 77.40, 55.40, 44.51, 40.67, 34.62, 29.64, 28.59, 28.28, 25.47 ppm. Anal. calcd. for C₂₀H₂₉BrN₂O₃: C 56.47, H 6.87, N 6.59; found: C 56.50, H 6.62, N 6.74.

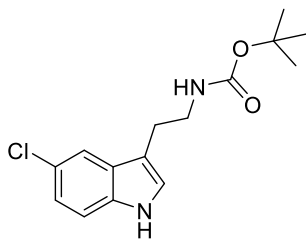
*Tert-butyl [2-{1-[4-(diethoxyphosphoryl)butyl]-5-methoxy-1*H*-indol-3-yl}ethyl]carbamate (114)*



Method IV. *Tert-butyl {2-[1-(4-bromobutyl)-5-methoxy-1*H*-indol-3-yl]ethyl}carbamate (113)* (2.75 g, 6.47 mmol) and triethyl phosphite (22.2 ml, 129 mmol) were used for the reaction. Eluent: TLC (acetone:*n*-hexane, 2:3), column (acetone:*n*-hexane, 2:3). Product obtained as a light-yellow resin (2.87 g, 94%).

¹H NMR (400 MHz, DMSO-d₆): δ 7.32 (d, *J* = 8.8 Hz, 1H), 7.11 (s, 1H), 7.01 (s, 1H), 6.89 (t, *J* = 5.0 Hz, 1H), 6.75 (d, *J* = 8.8 Hz, 1H), 4.06 (t, *J* = 6.6 Hz, 2H, NCH₂), 3.97 – 3.86 (m, 4H, OCH₂), 3.76 (s, 3H, OCH₃), 3.25 – 3.10 (m, 2H, CH₂), 2.74 (t, *J* = 7.4 Hz, 2H, CH₂), 1.84 – 1.64 (m, 4H, Aliph), 1.48 – 1.32 (m, 11H, Aliph), 1.17 (t, *J* = 7.0 Hz, 6H, CH₂CH₃) ppm. ¹³C NMR (101 MHz, DMSO-d₆): δ 155.57, 153.07, 131.28, 127.93, 126.48, 110.93, 110.87, 110.43, 100.64, 77.42, 60.76 (d, ²J_(C,P) = 6.3 Hz), 55.41, 44.83, 40.73, 30.51 (d, ²J_(C,P) = 15.9 Hz), 28.28, 25.55, 24.03 (d, ¹J_(C,P) = 138.5 Hz), 19.47 (d, ³J_(C,P) = 4.8 Hz), 16.26 (d, ³J_(C,P) = 5.7 Hz) ppm. Anal. calcd. for C₂₄H₃₉N₂O₆P: C 59.74, H 8.15, N 5.81; found: C 59.81, H 8.30, N 5.79.

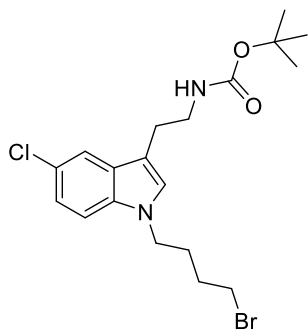
*Tert-butyl [2-(5-chloro-1*H*-indol-3-yl)ethyl]carbamate (115)*



5-Chlorotryptamine hydrochloride (2.5 g, 10.8 mmol) was dissolved in MeOH (15 ml) and TEA (3.8 ml, 27 mmol). Afterwards, di-*tert*-butyl dicarbonate (3 ml, 13 mmol) was slowly added and reaction stirred for 30 minutes at 25 °C. After termination of reaction (TLC, acetone:*n*-hexane, 1:4), solvents were removed under reduced pressure and organic components were extracted with ethyl acetate. The organic layer was dried over anhydrous Na₂SO₄, filtered and solvent evaporated under reduced pressure. Crude product was purified by column chromatography, using acetone:*n*-hexane (1:4) as an eluent, resulting in a light-yellow resin (3.16 g, 99% yield) as a product.

¹H NMR (400 MHz, DMSO-d₆): δ 11.01 (s, 1H, NH of Ind), 7.54 (s, 1H, 4-H of Ind), 7.34 (d, *J* = 8.6 Hz, 1H, 7-H of Ind), 7.22 (s, 1H, 2-H of Ind), 7.05 (d, *J* = 8.6 Hz, 1H, 6-H of Ind), 6.88 (t, *J* = 4.9 Hz, 1H, Aliph NH), 3.22 – 3.10 (m, 2H, CH₂), 2.77 (t, *J* = 7.2 Hz, 2H, CH₂), 1.37 (s, 9H, CH₃) ppm. ¹³C NMR (101 MHz, DMSO-d₆): δ 155.57, 134.66, 128.54, 124.57, 122.96, 120.77, 117.60, 112.85, 111.97, 77.43, 40.94, 28.27, 25.28 ppm. Anal. calcd. for C₁₅H₁₉ClN₂O₂: C 61.12, H 6.50, N 9.50; found: C 61.35, H 6.66, N 9.67.

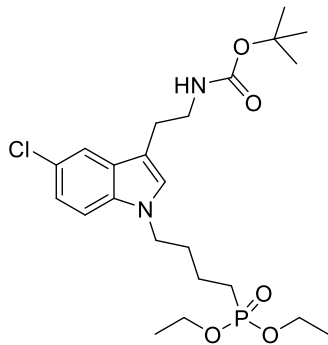
*Tert-butyl {2-[1-(4-bromobutyl)-5-chloro-1*H*-indol-3-yl]ethyl}carbamate (116)*



Method III. *Tert-butyl [2-(5-chloro-1*H*-indol-3-yl)ethyl]carbamate (115)* (3.1 g, 10.5 mmol), 1,4-dibromobutane (1.9 ml, 15.8 mmol), KOH (0.88 g, 15.8 mmol) and 20 ml of DMF were used for the reaction. Reaction conducted overnight. Eluent: TLC (acetone:*n*-hexane, 1:4), column (acetone:*n*-hexane, 1:4). Product obtained as white crystals (2.08 g, 46% yield). M.p. 92.5–93.5 °C.

¹H NMR (400 MHz, DMSO-d₆): δ 7.55 (s, 1H, 4-H of Ind), 7.48 (d, *J* = 8.7 Hz, 1H, 7-H of Ind), 7.26 (s, 1H, 2-H of Ind), 7.11 (d, *J* = 8.7 Hz, 1H, 6-H of Ind), 6.88 (t, *J* = 5.1 Hz, 1H, Aliph NH), 4.15 (t, *J* = 6.6 Hz, 2H, NCH₂), 3.52 (t, *J* = 6.4 Hz, 2H, CH₂Br), 3.20 – 3.08 (m, 2H, CH₂), 2.75 (t, *J* = 7.2 Hz, 2H, CH₂), 1.89 – 1.78 (m, 2H, CH₂), 1.78 – 1.67 (m, 2H, CH₂), 1.37 (s, 9H, CH₃) ppm. ¹³C NMR (101 MHz, DMSO-d₆): δ 155.55, 134.44, 128.82, 127.78, 123.19, 120.87, 117.94, 111.51, 111.32, 77.43, 44.57, 40.87, 34.56, 29.56, 28.52, 28.25, 25.16 ppm. Anal. calcd. for C₁₉H₂₆BrClN₂O₂: C 53.10, H 6.10, N 6.52; found: C 52.89, H 5.90, N 6.34.

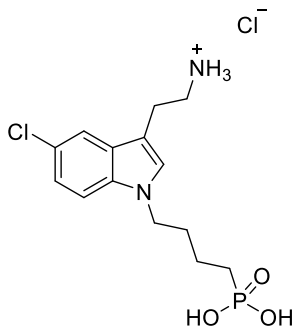
*Tert-butyl (2-{5-chloro-1-[4-(diethoxyphosphoryl)butyl]-1*H*-indol-3-yl}ethyl)carbamate (117)*



Method IV. *Tert-butyl {2-[1-(4-bromobutyl)-5-chloro-1*H*-indol-3-yl]ethyl} carbamate (116)* (2 g, 4.65 mmol) and triethyl phosphite (16 ml, 93.1 mmol) were used for the reaction. Eluent: TLC (acetone:*n*-hexane, 2:3), column (acetone:*n*-hexane, 2:3). Product obtained as a light-yellow resin (2.16 g, 95%).

¹H NMR (400 MHz, DMSO-d₆): δ 7.54 (s, 1H, 4-H of Ind), 7.47 (d, *J* = 8.7 Hz, 1H, 7-H of Ind), 7.25 (s, 1H, 2-H of Ind), 7.10 (d, *J* = 8.7 Hz, 1H, 6-H of Ind), 6.89 (t, *J* = 5.1 Hz, 1H, Aliph NH), 4.12 (t, *J* = 6.7 Hz, 2H, NCH₂), 3.97 – 3.86 (m, 4H, OCH₂), 3.19 – 3.11 (m, 2H, CH₂), 2.76 (t, *J* = 7.2 Hz, 2H, CH₂), 1.86 – 1.64 (m, 4H, Aliph), 1.47 – 1.34 (m, 11H, Aliph), 1.17 (t, *J* = 7.0 Hz, 6H, CH₂CH₃) ppm. ¹³C NMR (101 MHz, DMSO-d₆): δ 155.56, 134.47, 128.80, 127.80, 123.15, 120.81, 117.88, 111.39, 77.44, 60.77 (d, ²J_(C,P) = 6.3 Hz), 44.88, 40.93, 30.42 (d, ²J_(C,P) = 15.8 Hz), 28.25, 25.23, 24.00 (d, ¹J_(C,P) = 138.6 Hz), 19.42 (d, ³J_(C,P) = 4.9 Hz), 16.24 (d, ³J_(C,P) = 138.6 Hz) ppm. Anal. calcd. for C₂₃H₃₆ClN₂O₅P: C 56.73, H 7.45, N 5.75; found: C 56.71, H 7.28, N 5.50.

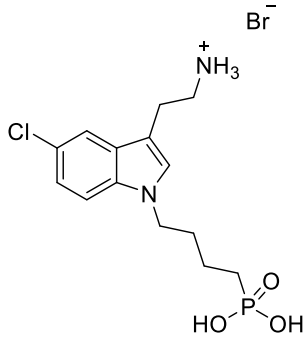
*2-[5-Chloro-1-(4-phosphonobutyl)-1*H*-indol-3-yl]ethan-1-aminium chloride (118)*



Method V. *Tert*-butyl (2-{5-chloro-1-[4-(diethoxyphosphoryl)butyl]-1*H*-indol-3-yl}ethyl)carbamate (117) (1 g, 2.05 mmol) and hydrochloric acid (8.1 ml, 82.1 mmol) were used. Eluent: TLC (acetone:*n*-hexane, 1:1). Solvent was removed under reduced pressure. Product was purified by dissolving in the minimum amount of MeOH, precipitating into 20-fold excess of diethyl ether, filtering and washing with diethyl ether to give purple crystals (0.55 g, 73% yield). M.p. 163–164.5 °C.

¹H NMR (400 MHz, DMSO-d₆): δ 8.12 (s, 3H, NH₃), 7.64 (s, 1H, 4-H of Ind), 7.49 (d, *J* = 8.5 Hz, 1H, 7-H of Ind), 7.36 (s, 1H, 2-H of Ind), 7.12 (d, *J* = 8.4 Hz, 1H, 6-H of Ind), 4.18 – 4.03 (m, 2H, NCH₂), 3.09 – 2.85 (m, 4H, Aliph), 1.87 – 1.70 (m, 2H), 1.59 – 1.37 (m, 4H) ppm. ¹³C NMR (101 MHz, DMSO-d₆): δ 134.57, 128.59, 128.31, 123.41, 121.13, 117.80, 111.62, 108.97, 45.23, 30.65 (d, ²J_(C,P) = 16.5 Hz), 27.19 (d, ¹J_(C,P) = 135.7 Hz), 22.75, 20.20 (d, ³J_(C,P) = 3.1 Hz) ppm. Anal. calcd. for C₁₄H₂₁Cl₂N₂O₃P: C 45.79, H 5.76, N 7.63; found: C 45.98, H 5.62, N 7.88.

*2-[5-Chloro-1-(4-phosphonobutyl)-1*H*-indol-3-yl]ethan-1-aminium bromide (119)*



Method VI. *Tert*-butyl (2-{5-chloro-1-[4-(diethoxyphosphoryl)butyl]-1*H*-indol-3-yl}ethyl)carbamate (117) (1 g, 2.05 mmol), bromotrimethylsilane (2.7 ml, 20.5 mmol), methanol (0.8 ml, 20.5 mmol) and 15 ml of 1,4-dioxane were used. Eluent: TLC (acetone:*n*-hexane, 1:1). Solvent was evaporated under reduced pressure. Product was purified by dissolving in the minimum amount of MeOH, precipitating into 20-fold excess of diethyl ether, filtering and washing with diethyl ether to give brown crystals (0.49 g, 58% yield). M.p. 180.5–182 °C (melting and decomposition).

¹H NMR (400 MHz, DMSO-d₆): δ 7.83 (s, 3H, NH₃), 7.65 (s, 1H, H_t, 4-H of Ind), 7.51 (d, *J* = 8.7 Hz, 1H, 7-H of Ind), 7.36 (s, 1H, 2-H of Ind), 7.13 (d, *J* = 8.7 Hz, 1H, 6-H of Ind), 4.13 (t, *J* = 6.7 Hz, 2H, NCH₂), 3.08 – 2.92 (m, 4H, Aliph), 1.87 – 1.74 (m, 2H, CH₂), 1.58 – 1.37 (m, 4H, Aliph) ppm. ¹³C NMR (101 MHz, DMSO-d₆): δ 134.61, 128.59, 128.29, 123.45, 121.16, 117.80, 111.67, 108.83, 45.23, 30.70 (d, ²J_(C,P) = 15.4 Hz), 27.09 (d, ¹J_(C,P) = 136.5 Hz), 22.80, 20.14 (d, ³J_(C,P) = 4.3 Hz) ppm. Anal. calcd. for C₁₄H₂₁BrClN₂O₃P: C 40.85, H 5.14, N 6.81; found: C 40.81, H 5.19, N 6.94.

4. CONCLUSIONS

1. Carbazole-based HTMs containing phosphonic acid functional groups have been synthesized and investigated; it has been determined that:

- The energy levels of the halogenated carbazole-based HTMs are suitable for the application in bulk-heterojunction organic photovoltaics and organic light-emitting diodes.
- The number of halogen substituents and their positions influence the OPV performance. 3,6-Substituted carbazoles **5**, **8** and **11** provided better performance than 2,7-substituted derivatives **26**, **29** and four halogens containing compound **32**.
- If comparing aliphatic chains of four and two carbon-long in the carbazole SAM structure, the latter provides better performance in terms of BHJ OPV.
- Among halogen substituents, chlorides provide the highest ionization potential value (6.05 eV), which is reflected on the best OPV efficiency (18.5%).
- The size of halogen substituents affects the ITO surface coverage. The biggest iodine substituents result in the best ITO coverage, which leads to the best OLED performance.

2. Non-carbazole derivatives containing phenothiazine, phenoxazine, diphenylamine, 5*H*-dibenzo[*b,f*]azepine or 10,11-Dihydro-5*H*-dibenzo[*b,f*]azepine chromophores and a phosphonic acid group have been synthesized and their investigation has revealed that:

- Non-substituted indole is not suitable for the synthesis of materials containing a phosphonic acid group. The 3-H position of indole reacts under hydrolysis conditions, forming inseparable side products.
- Lower I_p values of **58** and **61** (5.29 eV and 5.44 eV, respectively) are not favorable towards the best performance of BHJ OPVs, as both materials performed worse than the standard HTM PEDOT:PSS.
- Correlation between the performance in PSCs and SAM materials' ionization potential has been observed. The efficiency gradient of 2PACz and the synthesized compounds **58** and **61** ($19.5\% > 17.3\% > 16.0\%$ respectively) can be directly related to the descending values of the ionization potential ($5.6 \text{ eV} > 5.44 \text{ eV} > 5.29 \text{ eV}$ respectively), thereby suggesting the better compatibility with the perovskite at upper values.
- Diphenylamine **64** demonstrated the best charge extraction capabilities, compared to the standard SAM materials, which resulted in better performance in PSC compared with 2PACz. Diphenylamine chromophore can be indicated as a promising material for further development of efficient SAM materials.

3. SAM materials containing different functional groups have been synthesized, and their investigation has revealed that:

- Thiophenes are versatile functional groups, able to provide additional properties to SAM materials, such as interaction with different light absorbers, which exert a positive effect on the performance of both BHJ OPVs and PSCs.
- Methoxy-substituted indoles cannot be used for the phosphonate hydrolysis reactions as, in the course of these reactions, the methoxy substituent acts as a leaving group creating a reactive site.
- The incorporation of ammonium groups into SAM molecules is a promising strategy to form a monolayer on ITO, that can simultaneously passivate the perovskite at the buried interface. This strategy can highly improve the photovoltaic characteristics of PSC, as carbazole **94** containing ammonium bromides outperformed the standard 2PACz and MeO-2PACz, while also providing better reproducibility of the cells.

4. An innovative approach for solving the Me-4PACz surface wetting issues has been presented. Wettability can be significantly improved by adding 1,6-hexylenediphosphonic acid into the SAM material precursor solution, resulting in a better quality of the perovskite layer. This approach is universal and can be used with other SAM materials which tend to form monolayers with poor wetting.

5. The versatility of phosphonic acid for metal oxide modification has been presented. SAM materials containing a phosphonic acid group are able to modify nanostructured ZnO tetrapods, which were used to construct room temperature gas sensors. Their functionalization with SAM of carbazole **73** improved the selectivity to NO₂ gases. The response of the sensors can be further enhanced by employing UV modulation.

5. SANTRAUKA

Ivadas

Gyvename šiuolaikiniame pasaulyje, kuris yra neatsiejamas nuo elektronikos ir išmaniuju technologijų. Norint išlaikyti ir pagreitinti jų vystymo tempą, nuolatos reikalingos naujos medžiagos, todėl organinių puslaidininkų (OSC) svarba ir mokslinis susidomėjimas jais taip pat smarkiai auga. OSC pasižymi naudingomis savybėmis, tokiomis kaip lankstumas, lengvumas bei paprastas apdorojimas. Sintezei tinkamų pradinių medžiagų pasirinkimas yra labai didelis, molekulinių fragmentų įvairovė struktūrinėms variacijoms yra taip pat gausi, ir tai padeda gauti norimų elektrinių savybių organinius junginius. Šiuo metu OSC dažnai laikomi „karšta tema“ įvairose disciplinose, tokiose kaip chemija, fizika, medžiagų mokslas, medicina ir biologija, pradedant fundamentiniais tyrimais, o vėliau – praktiniu taikymu ir komerciniais produktais. Sintetinės organinės chemijos universalumas leidžia gauti norimas medžiagas, kurios gali būti naudojamos elektronikoje, pavyzdžiui, šviesos dioduose, saulės elementuose, tranzistoriuose ar jutikliuose, kurie gali būti įvairaus dydžio, lankstūs ar spausdinami [1,2].

Vienas iš geriausių OSC svarbos pavyzdžių yra optoelektronikos prietaisai, tokie kaip organiniai šviesos diodai (OLEDs) arba organiniai bei hibridiniai fotovoltiniai elementai (PV). Neįskaitant elektrodų, kurie paprastai yra neorganiniai, didelė dalis medžiagų skirtų OLED ir PV konstruoti yra organiniai puslaidininkai, t.y. polimerinės medžiagos bei mažamolekuliniai junginiai. Jie naudojami kaip skyles pernešančios medžiagos (HTM), elektronus pernešančios medžiagos (ETM), kaip emiteriai arba pagrindinės matricos medžiagos (OLED) ir kaip fotoaktyvusis sluoksnis, sudarytas iš elektronakceptorinių bei elektronondonorinių junginių organiniuose PV [3].

Viena iš naujausių strategijų skyles pernešantiems OSCs kurti buvo karbazolo HTMs, turinčių fosfonrūgštis „inkarinę“ grupę bei atitinkamai gebančią formuoti savitvarkę monosluoksnį (SAM) pristatymas. Fosfonrūgštis funkcinė grupė leidžia molekulėms prisijungti prie metalų oksido paviršiaus, pavyzdžiu, ITO ar FTO, kurie yra dažnai naudojami kaip elektrodai saulės elementuose ir organiniuose šviesos dioduose, suformuojant vienos molekulės storio sluoksnį. Monosluoksnį galima suformuoti iš praskiestų tirpalų, o savitvarkos procesas leidžia tolygiai padengti substratą. Monosluoksnis užtikrina minimalią parazitinę absorbciją, jo padengimo procedūra tinkama ir didesnio masto gamybai, net jei paviršius yra netolygus, o medžiagų sąnaudos yra minimalios [4]. SAM formuojančių medžiagų taikymas leido sparčiau tobulinti p-i-n architektūros perovskitinius saulės elementus (PSC).

Ankstesnio polimerinio HTM PTAA, naudoto kaip standarto, 18,9 % efektyvumas buvo pagerintas pritaikius karbazolo centrinių fragmentų turinčius savitvarkę monosluoksnį formuojančius puslaidininkinius junginius [2-(9H-karbazol-9-il)etil]fosfonrūgštis (2PACz) [5] ir [2-(3,6-dimetoksi-9H-karbazol-9-il)etil]fosfonrūgštis (MeO-2PACz), kurių efektyvumas siekė atitinkamai 20,8 % ir 20,2 %. MeO-2PACz taip pat buvo tiriamas monokristalinio PSC, kuriuose buvo pasiekta 23,1 % efektyvumas bei geresnis prietaiso veikimo stabilumas [6]. 2PACz

ir keli jo analogai buvo toliau tiriami kitose fotovoltinėse sistemose – visi jie pademonstravo aukščiausio lygio prietaisų našumus. Vienas iš pavyzdžių [4-(3,6-dimetil-9H-karbazol-9-il)butil]fosfonrūgštis (Me-4PACz) buvo panaudotas monolitiniuose CIGSe/perovskito tandemuose bei perovskito / silicio tandemuose, ir jų sertifikuoti našumai siekė atitinkamai 24,2 % ir 29,15 % [7,8], kurie tuo metu buvo rekordiniai. Tačiau platesniam Me-4PACz naudojimui trukdo gana didelis paviršiaus hidrofobišumas ir dėl to prastas perovskito prekursoriaus tirpalo padengimas. Šioje disertacijoje buvo susintetintos ir įvairiuose optoelektroniniuose prietaisuose išbandytos naujos medžiagos, pagrįstos savitvarkio monosluoksnio koncepcija, siekiant išspręsti šiuo metu egzistuojančias SAM problemas ir kartu toliau plėtoti šią itin perspektyvią mokslinių tyrimų sritį.

Šio darbo tikslas yra 2PACz alternatyvą, galinčią pernešti teigiamus krūvininkus ir sudaryti savitvarkius monosluoksnius, sintezė ir optoelektroninių savybių tyrimas bei savitvarkij monosluoksnį formuojančių junginių taikymo srities išplėtimas.

Disertacijos tikslui pasiekti išsikelti šie uždaviniai:

1. Susintetinti halogenintus karbazolo darinius, turinčius fosfonrūgšties funkcines grupes, ir ištirti skirtingų halogenidų įtaką organinių saulės elementų ir organinių šviesos diodų veikimui.
2. Susintetinti nekarbazolinius darinius, turinčius fosfonrūgšties funkcines grupes, ir palyginti juos su karbazolo analogais, tiriant skirtingų chromoforų suderinamumą ir efektyvumą perovskitinių saulės elementų veikimui.
3. Pasiūlyti metodą, kaip spręsti Me-4PACz suformuoto monosluoksnio vilgymo problemas.
4. Susintetinti karbazolo, fenotiazino ir indolo darinius, turinčius fosfonrūgšties ir kitas funkcines grupes, kurios galėtų sąveikauti su perovskitu; ištirti pasyvacijos įtaką perovskitiniuose saulės elementuose.

Mokslinis naujumas

Gana ilgą laiką 2,2',7,7'-tetrakis(*N,N*-dimetoksifenilamin)-9,9'-spirobifluorenas (spiro-OMeTAD) buvo laikomas etalonine skyles transportuojančia medžiaga perovskitiniam saulės elementams konstruoti. Tačiau dėl brangios sintezės ir santykinių mažo laidumo, kuriam padidinti reikalingi legirantai, jis nebuvo tinkamas junginys komercinės gamybos perspektyvose. Spiro-OMeTAD pritaikymas taip pat buvo ribotas, nes jis galejo būti naudojamas tik įprastinėje (n-i-p) PSC architektūroje, kurioje legiravimo medžiagos ribojo įrenginio veikimo stabilumą ir matmenų didinimą. Kaip alternatyva gali būti konstruojami invertuotos struktūros (p-i-n) perovskitiniai saulės elementai, kurie pasižymi geresniu stabilumu ir ilgaamžiškumu, juos galima konstruoti žemesnėse temperatūrose, o gamybai galima naudoti ir lanksčius substratus. Tačiau šiai sričiai dėmesio buvo skirtiama mažiau, todėl p-i-n tipo perovskitinių saulės elementų našumas ir vystymo sparta atsiliko nuo įprastos struktūros PSC. Prie lėtesnio vystymo prisidėjo ir salyginai nedidelis tinkamų HTM

pasirinkimas, nes daugumos mažamolekulinių HTM suformuotą skyles pernešančių sluoksnį pažeidžia poliniai tirpikliai, kurie yra naudojami perovskito sluoksniams lieti. Todėl polimerinis puslaidininkis poli-[bis(4-fenil)(2,4,6-trimetilfenil)aminas] (PTAA) buvo vienas geriausių konstruojant p-i-n architektūros PSC. Tačiau PTAA sluoksnis pasižymi prastu vilgymu ir, norint įveikti šią problemą bei pasiekti didelį efektyvumą, reikalingos specialios paviršiaus apdorojimo procedūros [9,10]. Kartu su didele kaina, siekiančia ~2500 eurų už gramą, PTAA nebuvo idealus kaip skyles transportuojantis junginys.

Reikšmingas proveržis kuriant p-i-n architektūros PSC buvo pasiektas pradėjus naudoti karbazolo chromoforą turinčius organinius puslaidininkius, gebančius suformuoti savitvarkę monosluoksnį (SAM), iš kurių 2PACz ir jo analogai (pvz., MeO-2PACz arba Me-4PACz) ne tik supaprastino prietaiso konstravimo procedūrą, bet ir pranoko efektyvumu polimerinius HTM. Neilgai trukus SAM sudarantys junginiai ėmė sulaukti vis daugiau dėmesio, atitinkamai didėjant sintetinamų medžiagų skaičiu ir galimų taikymo sričių spektrui. Šioje disertacijoje, siekiant toliau plėsti šią mokslinių tyrimų sritį, buvo susintetinta keletas skirtingų savitvarkų monosluoksnį formuojančių skyles pernešančių junginių, kurie buvo testuoti įvairiuose optoelektroniniuose prietaisuose.

Naujoms SAM sudarančioms molekulėms, turinčioms fosfonrūgšties grupes, gauti buvo taikomos dvi pagrindinės strategijos. Pagal pirmąją strategiją į karbazolo, fentiazino arba indolo centrinių fragmentų buvo pridedamos skirtingos funkcinės grupės. Sintetinant medžiagas su halogenų pakaitais, buvo gautos aukštesnės ionizacijos potencijalo vertės, todėl halogeninti SAM junginiai yra tinkami efektyviems BHJ OPV kurti. Palyginimo tikslais, buvo pridedami ne tik skirtingi halogenų pakaitai, bet ir jų skaičius bei parenkamos skirtingos padėtys. Iš jų geriausiu efektyvumu BHJ OPV pasižymėjo karbazolo junginys turintis chlorido funkcinius atomus, kuris kartu su legiravimo strategija leido pasiekti rekordinį 18,9 % SAM pagrindu sukonstruotų OPV efektyvumą. Taip pat buvo pademonstruotas halogenintų SAM sudarančių junginių kaip tarpsluoksnio potencialas skylių injekcijai OLED. Tarp testuotų junginių karbazolas, turintis jodido funkcinius atomus, buvo efektyviausias, payginti, su tradiciniu PEDOT:PSS bei su kitais halogenų funkcinius atomus turinčiais junginiais. Skirtingų pakaitų strategija buvo toliau plėtojama įtraukiant *tret*-butilo, metoksi-, ir amonio grupes bei tiofeno fragmentus. Susintetinti junginiai buvo sėkmingai pritaikyti OPV ir PSC, o tiofeno fragmentų bei amonio funkcinės grupės pridėjimas lėmė papildomų sąveikų su kitais prietaisų komponentais atsiradimą, ir tai turėjo įtakos pagerinant įrenginių fotovoltaikos savybes.

Kadangi dauguma šiou metu tiriamų SAM junginių yra karbazolo dariniai, į antrają susintetintų medžiagų grupę buvo įtrauktai skirtingi centriniai fragmentai, kad būtų galima atlirkti palyginimą su šiou metu esamais junginiais ir geriau suprasti, kuris chromoforas yra palankiausias naudoti optoelektronikoje. Remiantis rezultatais, iš tirtų junginių difenilamino centrinis fragmentas yra tinkamiausias kandidatas tolesniams sintezės optimizavimui ir tyrimams PSC, nes jo SAM sudarantis junginys turėjo geriausias teigiamų krūvininkų ekstrakcijos savybes bei gerą rezultatų pasikartojamumą konstruojant įrenginius.

Galiausiai buvo pristatyti du nauji SAM sudarančių medžiagų taikymo ir SAM paviršiaus vilgymo gerinimo būdai. Susintetintas karbazolo centrinių fragmentų turintis SAM sudarantis darinys buvo panaudotas modifikuojant cinko oksido tetrapodus ($ZnO-T$), dujų jutikliams, galintiems veikti kambario temperatūroje, konstruoti. Po $ZnO-T$ funkcionalizavimo jutiklių atsakas į NO_2 dujas pagerėjo beveik dešimt kartų, palyginti su nemodifikuotais $ZnO-T$, ir buvo dar labiau padidintas papildomai taikant UV moduliavimą. Taip pat buvo išbandytas paprastas būdas SAM paviršiaus vilgymo problemoms spręsti, naudojant 1,6-heksilendifosfonrūgštį kaip papildomą komponentą formuojant monosluoksnį. Taip buvo gerokai pagerintos paviršiaus vilgymo savybės, ir tai neturėjo jokio neigiamo poveikio PSC veikimui bei efektyvumui.

Pagrindiniai ginamieji disertacijos teiginiai:

1. Tarp visų susintetintų savitvarkę monosluoksnį formuojančių junginių, halogenų funkcinius atomus turintys dariniai yra efektyviausi ir perspektyviausi kandidatai taikyti tūrio heterosandūros organiniuose saulės elementuose ir organiniuose šviesos dioduose.
2. Tiofeno fragmentai ir amonio funkcinės grupės turi didelį potencialą perovskito pasyvacių bei taikyti perovskitiniuose saulės elementuose.
3. Difenilamino chromoforas yra perspektyvus centrinių fragmentas savitvarkę monosluoksnį formuojančių medžiagų, turinčių fosfonrūgšties grupes, sintezei ir tolimesniams tyrimui perovskitiniuose saulės elementuose.
4. Savitvarkę monosluoksnį formuojančių junginių, turinčių fosfonrūgšties funkcinės grupes pritaikymo spektras vis didėja; juos galima panaudoti nanostruktūriniams ZnO tetrapodams modifikuoti, tinkamiems dujų jutikliams konstruoti.

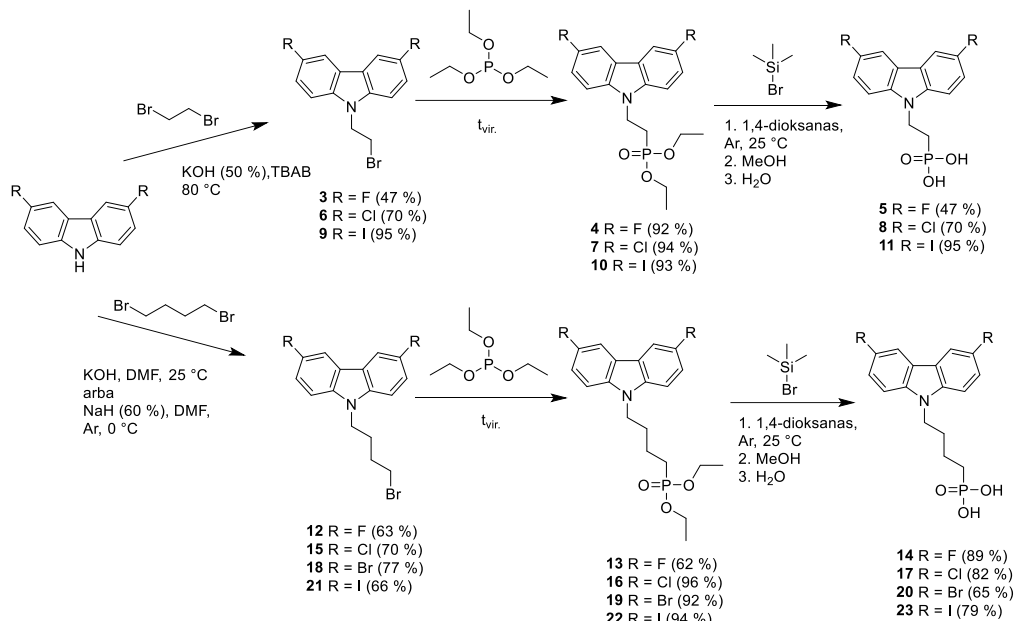
5.1. Halogeninti karbazolo centrinių fragmentų turintys skyles pernešantys SAM sudarantys junginiai

Dėl palankios HOMO energijos (-6,01 eV), mažesnės varžos sluoksnį sandūroje ir ilgesnio krūvininkų gyvavimo trukmės karbazolo centrinių fragmentų ir bromidų funkcinius atomus turintis SAM sudarantis junginys ($Br-2PACz$) buvo pritaikytas organiniuose saulės elementuose, skyles ištraukiančiam tarpsluoksniniui formuoti. Nuo tada tokio tipo halogeninti junginiai tapo perspektyviu tyrimų objektu įrenginiuose, kuriuose aukštesnė skyles pernešančių puslaideininkų jonizacijos energija yra palanki [194].

Šiame skyriuje aptariami halogeninti karbazolo centrinių fragmentų turintys SAM sudarantys junginiai. Karbazolas buvo pasirinktas kaip patikimas chromoforas, jau ir anksčiau pasižymėjęs efektyvumu formuojant monosluoksnius. Taikant patogias ir nesudėtingas sintezės procedūras, karbazolą galima funkcionalizuoti daugeliu halogenų. Keičiant struktūrą buvo tiriamos skirtinges halogenų funkcių atomų padėties, pakaityt skaičius ir skirtinges alifatinės grandinės ilgiai. Pagrindinis tikslas buvo palyginti visus šiuos kintamuosius ir rasti optimalią struktūrą efektyviausiam halogenintam karbazolo centrinių fragmentų turinčiam SAM formuojančiam junginiui.

5.1.1. Halogenintų karbazolo darinių, turinčių fosfonrūgštis funkcinę grupę, sintezė

Dauguma halogenintų karbazolų, išskyrus 3,6-difluor-9H-karbazolą, yra komerciškai prieinami, todėl sutrumpėja ir supaprastėja sintezės procedūra. 3,6-Halogenintų karbazolo SAM sudarančių junginių sintezė buvo atliekama pagal 3 žingsnių procedūrą (5.1 schema).



5.1 schema. 3,6-Halogenintų karbazolo darinių, turinčių fosfonrūgštis grupę, sintezė

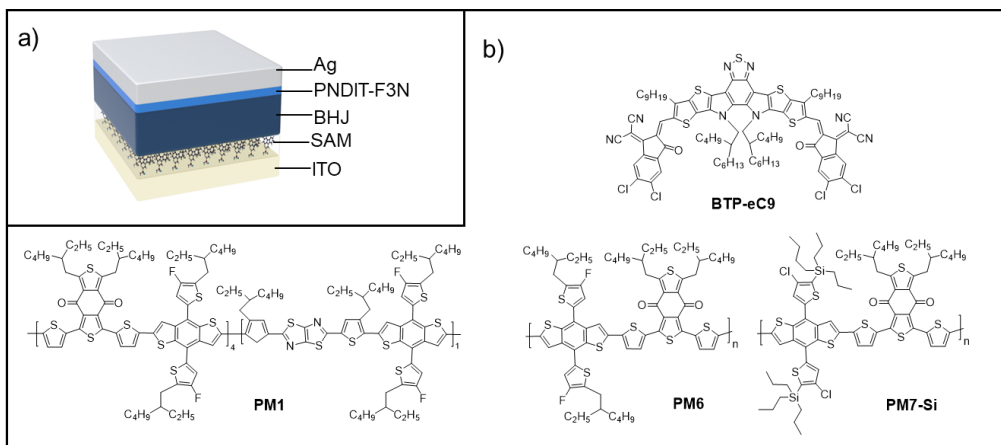
Halogeninti karbazolai buvo alkilinti naudojant 1,2-dibrometaną, kuris atliko tiek tirpiklio, tiek alkalinimo agento funkciją, 50 % vandeninį KOH tirpalą ir TBAB, taip gaunant tarpinius junginius, turinčius brometil- pakaitą. Ilgesnė brombutil- grupė buvo pridėta naudojant 1,4-dibrombutaną ir smulkintą KOH arba mineralinėje alyvoje disperguotą NaH (60 %). Alkilinti dariniai toliau reagavo su trietilfosfitu, susidarant fosfonrūgštis etilo esteriams. Tiksliniai produktai **5**, **8**, **11**, **14**, **17**, **20** ir **23**, turintys fosfonrūgštis funkcinės grupes, gauti fosfonatų hidrolizės metu, naudojant bromtrimetilsilaną, metanolį ir vandenį.

Taikant panašias sintezės procedūras, buvo susintetinti ir kiti halogeninti karbazolo dariniai, turintys pakaitus skirtingose padėtyse arba skirtingą pakaitų skaičių. Naudojant 2,7-dibromkarbazolą buvo susintetinti junginiai **26** ir **29**, 1,3,6,8-tetrabromkarbazolą – junginys **32**. 2,7-Dimetoksi-9H-karbazolas buvo halogenintas naudojant atitinkamus halogeninimo agentus, siekiant padidinti dipolio momentą dėl akceptorinių ir donorinių funkcių grupių buvimo. Tiksliniai junginiai **36** ir **40**, turintys atitinkamai chloro ir bromo atomus, buvo susintetinti taikant panašią 3 žingsnių procedūrą.

Gauti junginiai buvo naudojami tolimesniems tyrimams, formuojant savitvarkę monosluoksnį ant ITO. Monosluoksnio formavimo procedūra pateikta 3.1 skyriuje.

5.1.2. Junginių panaudojimas tūrio heterosandūros organiniuose saulės elementuose¹²

Halogeninti SAM sudarantys junginiai buvo tiriami juos panaudojant tūrio heterosandūros organiniams saulės elementams konstruoti. Įrenginio schema pateikta 5.1 pav., a, ji visuose eksperimentuose buvo pastovi ir išreikšta kaip ITO/SAM/BHJ/PNDIT-F3N/Ag, kur PEDOT:PSS arba Br-2PACz buvo naudojami kaip palyginamieji HTM, o poli[[2,7-bis(2-etylheksil)-1,2,3,3,6,7,8-heksahidro-1,3,6,8-tetraoksobenzo[lmn]]3, 8]fenantrolin-4,9-diil]-2,5-tiofenedil[9,9-bis[3(dimetilamino)propil]-9H-fluoren-2,7-diil]-2,5-tiofenedil] (PNDIT-F3N), naudojamas kaip ETM. Buvo išbandytos įvairios absorberių sistemos, junginių, naudotų BHJ formuoti, pavadinimai ir struktūros pateiktos 5.1 pav., b.



5.1 pav. (a) BHJ organinio saulės elemento architektūros schema; (b) medžiagų, naudojamų BHJ formuoti, cheminės struktūros

Tarp susintetintų junginių geriausius rezultatus pademonstravo SAM sudarantys junginiai **5**, **8** and **11**, kurie buvo tirti kaip Br-2PACz analogai, besiskiriantys tik halogenų funkciniais atomais, taip įvertinanči vien tik šių pakaitų įtaką. Šalia jų PEDOT:PSS naudotas kaip standartinis HTM. Šviesos absorberis buvo sudarytas iš dvių donorų ir vieno akceptoriaus (D1:D2:A) PM6:PM7-Si:BTP-eC9.

¹² Įrenginiai buvo sukonstruoti ir matavimai atlikti Karaliaus Abdulos mokslo ir technologijų universitete (King Abdullah University of Science and Technology (KAUST)), Saudo Arabija, prof. T. D. Anthopoulos tyrimų grupėje

5.1 lentelė. OPV naudojant PM6:PM7-Si:BTP-eC9 BHJ su skirtingais HTMs fotovoltinių charakteristikų apibendrinimas esant AM 1.5G (100 mW/cm²) apšvietai

BHJ	HTM	V_{OC} [V]	J_{sc} [mA/cm ²]	FF [%]	PCE [%]
PM6:PM7-Si:BTP-eC9	w/o	0,690	23,88	58,8	9,6 (9,2±0,3) ^a
	PEDOT:PSS	0,862	26,39	76,8	17,5 (17,1±0,2)
	Br-2PACz	0,870	26,57	77,9	18,0 (17,6±0,2)
	5	0,846	26,80	78,2	17,7 (17,3±0,2)
	8	0,863	26,96	79,4	18,5 (18,2±0,2)
	11	0,858	26,85	78,8	18,2 (17,9±0,1)

^a PCE_{avg} – atitinka 15 įrenginių vidurkines reikšmes.

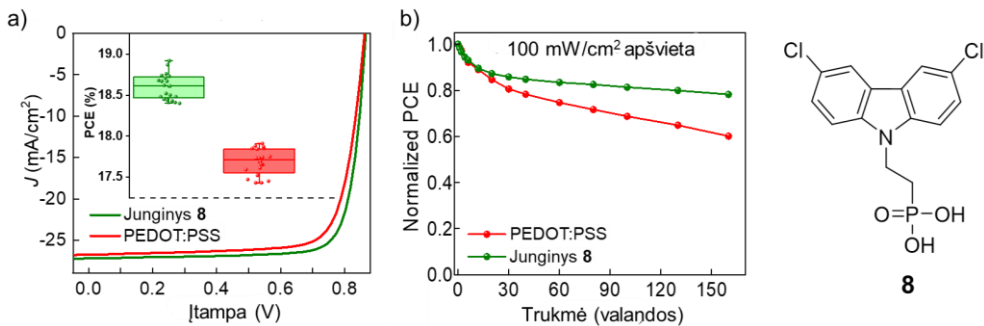
Sukonstruotų prietaisų fotovoltinės charakteristikos pateiktos 5.1 lentelėje. PEDOT:PSS nusileido efektyvumu (iki 1 %) visiems SAM sudarantiems junginiams. Tarp jų, Br-2PACz turėjo didžiausią V_{OC} (0,870 V), kuri neretai yra vienas svarbiausių parametru, lemiančių didžiausią efektyvumą, tačiau jo FF (77,9 %) buvo mažiausias, palyginti su kitais karbazolo dariniais. Geriausias rezultatas pasiektas su junginiu **8**, turinčiu chloro funkcinius atomus, kuris išsiškyrė didžiausia įrenginių trumpojo jungimo srove (26,96 mA/cm²), PCE (18,5 %) ir FF (79,4 %). Šis rezultatas sutampa ir su didžiausia šio junginio I_p verte (6,05 eV), kuri yra palanki taikyti BHJ OPV. O prietaisas be HTM pasirodė perpus mažesnio efektyvumo (9,6 %), o tai tik patvirtina HTM svarbą tūrio heterosandūros organiniuose saulės elementuose.

Įrenginiai su dviejų donorų ir vieno akceptoriaus fotoaktyvia sistema PM6:PM7-Si:BTP-eC9 bei junginiu **8** buvo optimizuoti. Efektyvumui gerinti buvo panaudotas nebrangus ir nesudėtingas metodas į BHJ sistemą pridedant n-tipo legirantą benzilo viologeną (BV) [195,196]. Eksperimento rezultatai apibendrinti 5.2 lentelėje ir 5.2 pav., a.

5.2 lentelė. OPV naudojant PM6:PM7-Si:BTP-eC9 BHJ, BV legirantą bei junginį **8** ir PEDOT:PSS fotovoltinių charakteristikų apibendrinimas esant AM 1.5G (100 mW/cm²) apšvietai

BHJ	HTM	V_{OC} [V]	J_{sc} [mA/cm ²]	FF [%]	PCE [%]
PM6:PM7-Si:BTP-eC9:BV	PEDOT:PSS	0,862	26,74	77,8	17,9 (17,7±0,10)
	8	0,866	27,18	80,1	18,9 (18,6±0,15) ^a

^a PCE_{avg} – atitinka 20 įrenginių vidurkines reikšmes.



5.2 pav. (a) saulės elementų su PM6:PM7-Si:BTP-eC9 BHJ ir BV legirantu J - V kreivės; (b) OPV PCE pokytis per tam tikrą laikotarpį

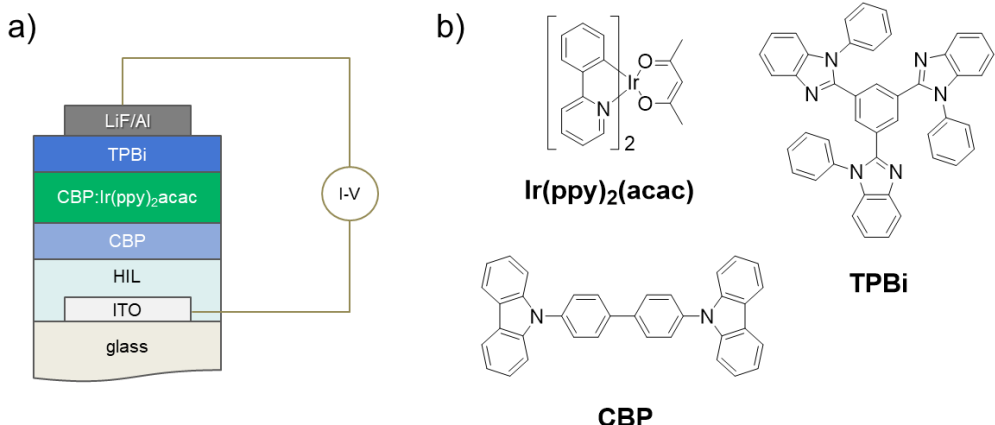
Tinkamiausio SAM sudarančio junginio parinkimas ir legiravimo strategija padėjo pasiekti rekordinį 18,9 % SAM pagrindu sukonstruotų OPV efektyvumą, kuris taip pat prilygo ir iki šiol paskelbtiems įprastos struktūros OPV efektyvumo rekordams. Išsamai fotovoltinių charakteristikų analizė atskleidė, kad geresnis OPV efektyvumas naudojant junginį **8** yra susijęs su didesniu teigiamu krūvininkų judriu, sumažėjusia varža sluoksniių sąsajoje ir ilgesne krūvininkų gyvavimo trukme. Be to, 20 prietaisų statistinės PCE vertės (5.2 pav., a, intarpas) rodo, kad rezultatai kartojausi ir yra patikimi.

Taip pat buvo ištirtas ir palygintas OPV su PEDOT:PSS ir junginiu **8** stabilumas esant apšietai, kuris yra labai svarbus parametras šių įrenginių komercIALIZAVIMUI [197]. Kaip pademonstruota 5.2 pav., b, po 25 val. nepertraukiamo apšietimo abiejų prietaisų normalizuotas PCE sumažėjo apie 15 %. Tačiau toliau įrenginio su junginiu **8** SAM PCE išlieka stabilesnis ir nuo 30 val. iki 160 val. sumažėjo tik apie 9 %, o PEDOT:PSS pagrindo įrenginys sumažėjo apie 25 %. Šie rezultatai demonstruoja, kad chloro atomus turintis karbazolas **8** potencialiai gali padidinti šiuolaikinių OPV ilgaamžiškumą.

5.1.3. Junginių panaudojimas organiniuose šviesos dioduose¹³

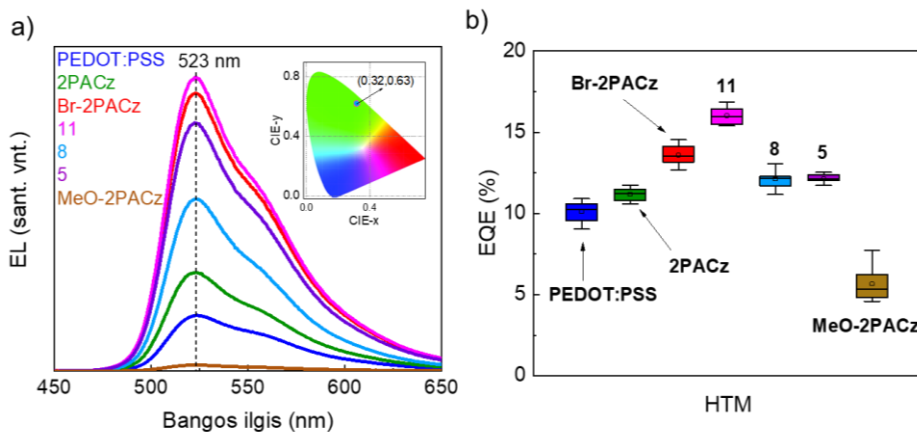
Halogeninti SAM sudarantys dariniai **5**, **8**, **11** taip pat buvo panaudoti žalia spalva fosforescuojantiems OLED konstruoti. Įrenginių schematiška architektūra, išreikšta kaip ITO/HIL/CBP/CBP:Ir(ppy)₂acac/TPBi/LiF/Al, pateikta 5.3 pav., a, o PEDOT:PSS, MeO-2PACz, 2PACz ir Br-2PACz naudoti kaip palyginamieji standartai. Kitų medžiagų, naudotų OLED konstruoti, struktūros pateiktos 5.3 pav., b.

¹³ Įrenginiai buvo sukonstruoti ir matavimai atlikti Karaliaus Abdulos mokslo ir technologijų universitete (King Abdullah University of Science and Technology (KAUST)), Saudo Arabija, prof. T. D. Anthopoulos tyrimų grupėje.



5.3 pav. (a) Schematiška OLED įrenginio architektūra; (b) medžiagų, naudotų OLED konstruoti, struktūrinės formulės

Visi sukonstruoti prietaisai pasižymėjo identiškais elektroluminescencijos (EL) emisijos spektrais, kurių didžiausias bangos ilgis (λ_{\max}) yra ~ 523 nm (5.4a pav.). Žalia EL emisija, kaip nurodyta Tarptautinės apšvietimo komisijos (CIE-1931) spalvų koordinatėse (5.4 pav., a, intarpas), išlieka stabili didinant įtampą (A2 pav.).



5.4 pav. (a) Žaliai fosforescuojančių OLED elektroluminescencijos spektrai ir spalvų diagrama (intarpas); (b) įrenginių EQE statistikos

5.3 lentelė. CBP:Ir(ppy)₂acac pagrindu sukonstruotų OLED su skirtingu medžiagų skylių injekcijos sluoksniais charakteristikos

HTM	V_{on} (V)	Šviesumas_{\max} (cd m ⁻²)	EQE_{\max} %	Maksimalus srovės efektyvumas (cd A ⁻¹)	Maksimalus energijos efektyvumas (lm W ⁻¹)
PEDOT:PSS	~3,3	38700	10,59	39,45	30,11
MeO-2PACz	~3,4	16180	7,73	28,78	15,25
2PACz	~2,9	49510	11,69	43,47	32,33
Br-2PACz	~2,9	55250	14,55	54,46	45,18
5	~2,9	47790	12,54	46,74	39,36
8	~2,9	44530	13,06	48,42	40,64
11	~2,9	57290	16,86	63,18	46,69

Irenginių, kuriuose naudojami įvairių medžiagų skylių injekcijos sluoksniai (HIL), srovės-įtampos-šviesumo ($J-V-L$) charakteristikos ir atitinkami išorinio kvantinio našumo-įtampos ($EQE-V$), srovės efektyvumo-įtampos ($CE-V$) ir galios efektyvumo-įtampos ($PE-V$) grafikai apibendrinti 5.3 lentelėje. PEDOT:PSS HIL pagrindu sukonstruotuose kontroliniuose OLED pastebima ~3,3 V V_{on} , pasiekiamas didžiausias 38700 cd m⁻² ryškumas, EQE - 10,59 %, CE – 39,45 cd A⁻¹ ir PE – 30,11 lm W⁻¹. PEDOT:PSS pakeitus 2PACz, V_{on} sumažėja iki 2,9 V, todėl šiek tiek pagerėja OLED veikimas: didžiausias šviesumas – 49510 cd m⁻², EQE – 11,69 %, CE – 43,47 cd A⁻¹ ir PE – 32,33 lm W⁻¹. OLED, kuriuose naudojami halogeninti SAM sudarančius junginiai, pasižymi tos pačios eilės V_{on} ~ 2,9 V, bet yra ryškesni, palyginti su irenginiais kuriuose naudoti 2PACz ir PEDOT:PSS (5.4 pav., a). Tačiau lyginant tarpusavyje, halogenintų darinių veikimas skiriasi. OLED, kuriuose kaip HIL naudojami Br-2PACz, **11**, **8** ir **5**, pasiekia atitinkamai 14,55 %, 16,86 %, 13,06 % ir 12,54 % EQE . Ta pati tendencija matoma ir pagal kitus parametrus, kur **11** junginys išsiskiria statistiškai geriausiais rodikliais (5.3 pav., b); jo didžiausias ryškumas siekia 57290 cd m⁻², CE – 63,18 cd A⁻¹, o PE – 46,69 lm W⁻¹.

5.1.4. Skyriaus išvados

Apibendrinant galima teigti, kad buvo susintetinti nauji halogeninti karbazolo centrinių fragmentų turintys junginiai, galintys formuoti savitvarkę monosluoksnį, kurie buvo sėkmingai pritaikyti BHJ OPVs ir žalia spalva fosforescuojančiuose OLEDs. Dėl tinkamų energetinių lygmenų junginiai **5**, **8** ir **11** turėjo didžiausius PCE OPV taikant PM6:PM7-Si:BTP-eC9 BHJ sistemą - atitinkamai 17,7 %, 18,5 % ir 18,2 %. Be to, OPV su SAM **8** pasižymėjo didesniu stabilumu esant nuolatiniam apšvietimui; palyginti su PEDOT:PSS pagrindu sukonstruotais irenginiais. I BHJ pridėjus n-tipo legirantą BV, irenginio su junginiu **8** PCE padidėjo dar labiau – iki 18,9 %, o tai yra rekordinis OPV našumas naudojant SAM sudarančius junginius, kuris prilygsta ir išprastos struktūros OPV efektyvumui. Taip pat buvo pademonstruotas SAM sudarančių junginių potencialas skylių injekcijai OLED. Naudojant halogenintus

junginius **5**, **8** ir **11** susidaro tankesni, tolygesni ir kompaktiškesni sluoksniai, palyginti su 2PACz ir MeO-2PACz. Dėl to OLED pasižymėjo geresnėmis charakteristikomis palyginti su standartu PEDOT:PSS arba 2PACz ir MeO-2PACz SAMs. Dėl gero padengimo ir tinkamų energetinių lygmenų derinio, junginys **11** pasižymėjo geriausiomis savybėmis skylių injekcijai OLED. Šis tyrimas turėtų suteikti naudingų ižvalgų konstruojant efektyvius šviesos diodus pritaikant SAMs bei kuriant tinkamų SAM sudarančių junginių, kuriuos būtų galima naudoti didelio efektyvumo optoelektroniniams prietaisams, biblioteką.

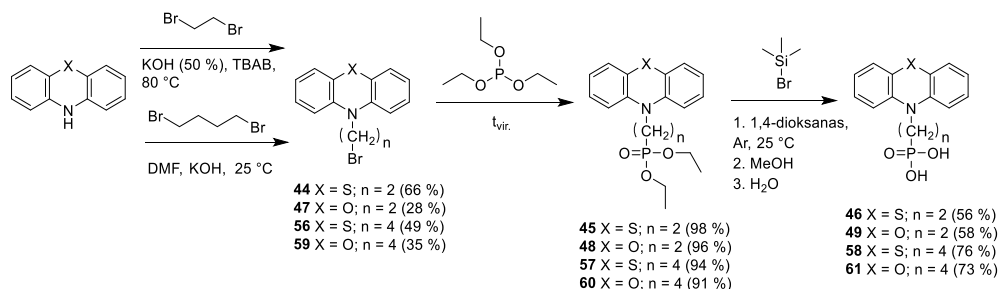
5.2. Nekarbazoliniai SAM sudarantys junginiai, turintys fosfonrūgšties funkcinės grupės

Karbazolo centrinių fragmentų turintys SAM sudarantys junginiai, tokie kaip 2PACz, MeO-2PACz ar Me-4PACz, yra gerai žinomas medžiagos, šiuo metu plačiai taikomos įvairiose optoelektronikos srityse. Siekiant dar labiau išplėsti ši SAM tyrimų lauką, yra kuriamas vis daugiau tokio tipo junginių. Tai apima tiek karbazolines 2PACz alternatyvas, tiek nekarbazolinius darinius, turinčius fosfonrūgšties funkcinės grupės. Nors nekarbazoliniai analogai dar nėra labai plačiai ištirti, vis daugiau molekulių, kurių pagrindą sudaro tokie chromoforai, kaip trifenilaminas, 9,9-dimetil-9,10-dihidroakridinas, triazatruksenas ar fenselenazinas, tampa perspektyviais ir gerai veikiančiais SAM [129,199].

Šiame skyriuje pateikiama nekarbazolinių SAM sudarančių junginių serija. Sintezei pasirinkti chromoforai, struktūriškai artimi geru efektyvumu pasižyminčiam 2PACz, tuo pat metu turintys reikšmingą, bet ne drastišką cheminės struktūros skirtumą, palyginti su karbazolu. Taip buvo tiriamas savitvarkių monosluoksniių veikimas, esant nedideliems jiems formuoti naudotų medžiagų struktūriniams pokyčiams, siekiant geriau suprasti ryšį tarp junginių struktūros ir veikimo išrenginiuose.

5.2.1. Nekarbazolinių junginių, turinčių fosfonrūgšties funkcinės grupės, sintezė

Šiame skyriuje aptariami nekarbazoliniai SAM sudarantys junginiai buvo sintetinami taikant 3 žingsnių sintezės procedūrą, panašią į ankstesniame 5.1.1 skyriuje aptartą SAM sudarančių junginių, turinčių halogeninto karbazolo chromoforą, sintezę.



5.2 schema. Fentiazino ir fenoksazino darinių, turinčių fosfonrūgšties grupės, sintezė

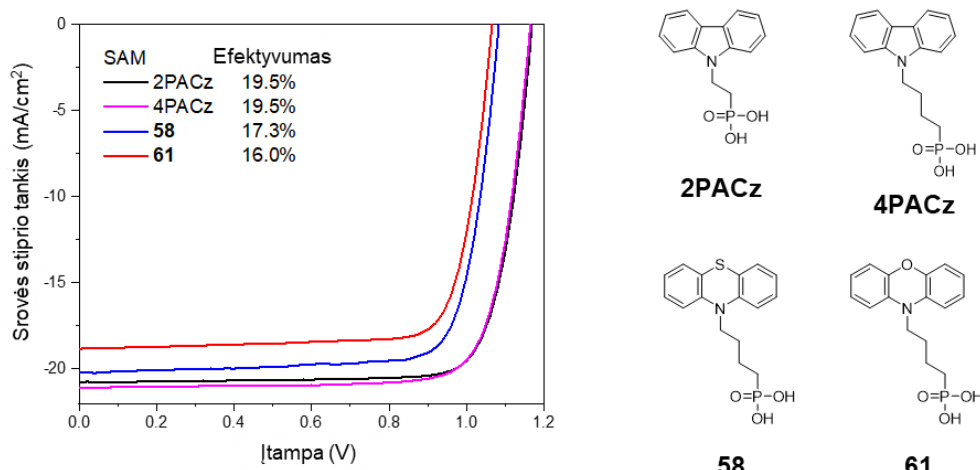
Alkilinimo reakcijos metu į fentiaziną ir fenoksaziną (5.2 schema) buvo pridėti, 2-brometil- arba 4-brombutil- fragmentai, taip gaunant alkilintus darinius **44**, **47**, **56** ir **59**. Vykdant Arbuzovo reakciją tarpinių junginių alifatinis bromidas buvo pakeistas fosfonrūgštis etilo esteriu, gaunant fosfonatus **45**, **48**, **57** ir **60**. Galiausiai jų hidrolizė buvo atlikta naudojant bromtrimetilsilaną, taip gaunant fentiazino arba fenoksazino chromoforą turinčias fosfonrūgštis **46**, **49**, **58** ir **61**.

Analogiškomis salygomis buvo susintetinti junginiai **52**, **55**, **64**, **67** ir **70**, turintys difenilamino, dibenzo[b,f]azepino ar 10,11-dihidro-5H-dibenzo[b,f]azepino chromoforus. Nesubstituotas indolo centrinis fragmentas nebuvo tinkamas fosfonrūgštims gauti dėl indolo 3-H padėties reaktingumo fosfonrūgščių esterių hidrolizės metu.

Gauti junginiai buvo naudojami tolimesniems tyrimams, formuojant savitvarkį monosluoksnį ant ITO. Monosluoksnio formavimo procedūra pateikta 3.1 skyriuje.

5.2.2. Junginių panaudojimas perovskitiniuose saulės elementuose¹⁴

Nekarbazoliniai SAM sudarantys junginiai buvo išbandyti p-i-n konfigūracijos perovskitiniuose saulės elementuose, naudojant „trijų halogenidų“ perovskitą (juostų tarpas – 1,65 eV). Pagrindinis šio eksperimento tikslas buvo ištirti SAM sudarančius darinius, turinčius skirtingus chromoforus nustatant optimalų, ir palyginti našumą su 2PACz ir kitais SAM sudarančiais junginiais.

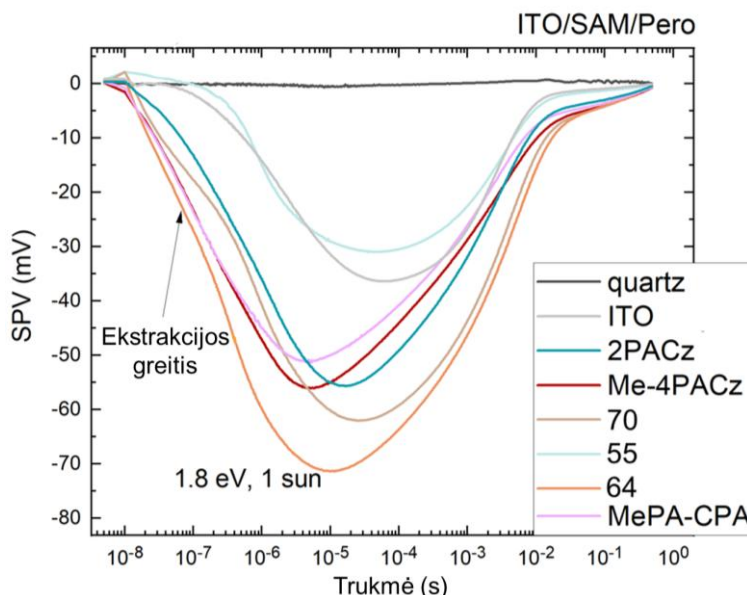


5.5 pav. Efektyviausių įrenginių naudojant 2PACz, 4PACz, **58** ir **61** J-V kreivės

Naudojant SAM sudarančius junginius **58** ir **61** buvo sukonstruoti ir ištirti p-i-n architektūros, ITO/SAM/perovskitas/LiF/C₆₀/SnO₂/Cu konstrukcijos perovskitiniai saulės elementai. Palyginimui buvo naudoti 2PACz ir 4PACz, iš kurių pastarasis buvo

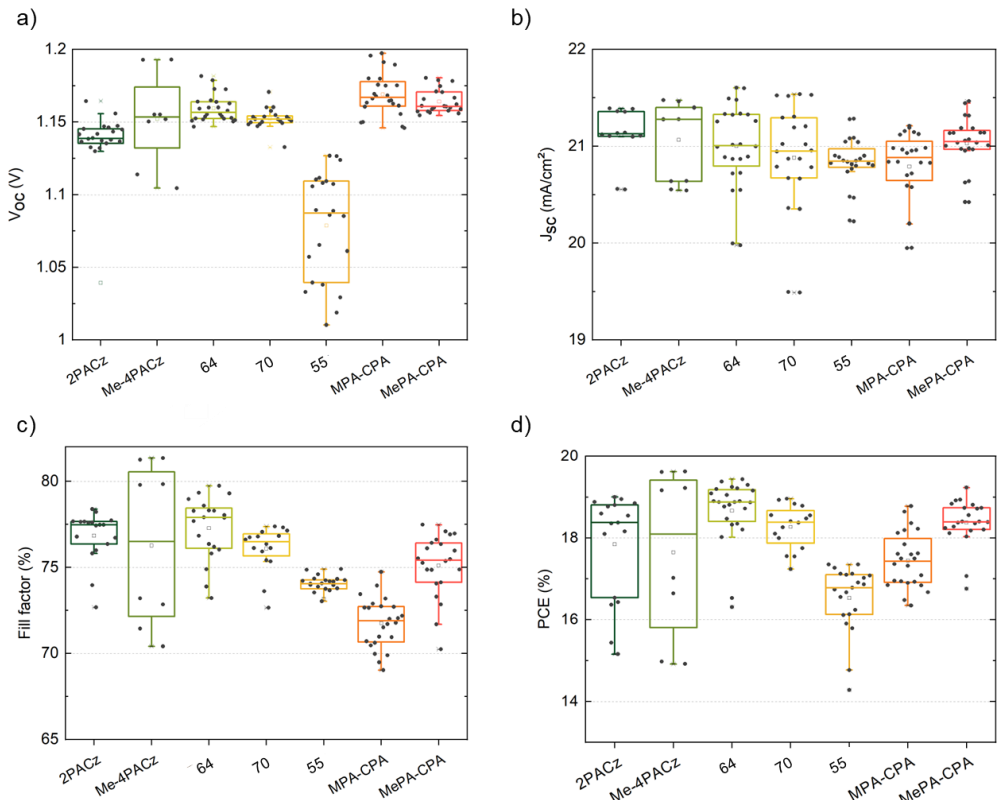
¹⁴ Įrenginiai buvo sukonstruoti ir matavimai atlikti Berlyno Helmholtz centre (Helmholtz-Zentrum Berlin (HZB)), Vokietijoje, prof. S. Albrecht tyrimų grupėje.

naudojamas kaip struktūriškai panašesnis darinys į **58** ir **61** dėl tokio paties ilgio alifatinės grandinės. Rezultatai parodė (5.5 pav.), kad alifatinės grandinės ilgio skirtumas neturi įtakos prietaiso veikimui, nes tiek 2PACz, tiek 4PACz efektyvumas buvo vienodas – 19,5 %. Junginių **58** ir **61** buvo šiek tiek mažesni efektyvumai, ir siekė atitinkamai 17,3 % ir 16,0 %, tačiau šie rezultatai pademonstravo ir tam tikrą tendenciją susijusią su skirtingais chromoforais. 2PACz, **58** ir **61** efektyvumo gradientas ($19,5\% > 17,3\% > 16,0\%$) gali būti tiesiogiai susijęs su mažėjančiomis jų jonizacijos potencialo vertėmis ($5,6\text{ eV} > 5,44\text{ eV} > 5,29\text{ eV}$), o tai rodo geresnį suderinamumą su perovskito energijos lygmenimis esant aukštesnėms vertėms.



5.6 pav. Perovskito ant kvarco, ITO ir ITO/SAM trSPV kreivės

Toliau, taikant trSPV metodą, buvo tiriamas, kaip efektyviai junginiai **55**, **64** ir **70** gali ištraukti teigiamus krūvininkus SAM ir perovskito sluoksnį sandūroje [200]. Rezultatai buvo lyginami su perovskito ant kvarco bandiniu, kadangi jų sluoksninių sandūroje krūvininkų ištraukimas ir pernešimas nėra įmanomas, todėl signalas fiksuojamas bazinės kreivės pavidalu. Ekstrakcijos greitis buvo vertinamas pagal amplitudės dydį ir tai, kaip greitai ji didėja. Visose tirtose medžiagose buvo pastebėti neigiami signalai, indikuojantys efektyvų skylių ištraukimą (5.6 pav.). Iš jų geriausias rezultatas buvo junginio **64** su difenilamino chromoforu, pranokusio visas tris etalonines medžiagas 2PACz, Me-4PACz ir MePA-CPA. 10,11-Dihidro-5H-dibenzo[b,f]azepino darinys **70** taip pat išsiskyrė geru rezultatu, tačiau amplitudės didėjimo greitis buvo lėtesnis ir pastebimas tam tikras teigiamas signalas ties $\sim 10^{-8}\text{ s}$, kuris gali būti elektrono sulaikymo požymis. Šis signalas buvo identiškas ir 5H-dibenzo[b,f]azepino dariniui **55**, kuris pasižymėjo prasčiausiomis skylių ištraukimo savybėmis.



5.7 pav. ITO/SAM/Pero/C₆₀/SnO₂/Ag architektūros, p-i-n konfigūracijos perovskitinės saulės elementų fotovoltinės charakteristikos, lyginant skirtingus HTM, naudotus kaip SAM: (a) V_{OC} statistiniai rezultatai; (b) J_{SC} statistiniai rezultatai; (c) užpildymo koeficiente statistiniai rezultatai; (d) efektyvumo statistiniai rezultatai

Junginiai **55**, **64** ir **70** buvo panaudoti konstruojant ITO/SAM/Pero/C₆₀/SnO₂/Ag architektūros, p-i-n konfigūracijos perovskitinius saulės elementus. Remiantis gautais rezultatais, visi junginiai ir jų SAM veikė efektyviai ištraukiant skyles PSCs. Difenilamino **64** ir 10,11-dihidro-5H-dibenzo[*b,f*]azepino **70** turėjo aukštesnes V_{OC} vertes palyginti su standartu 2PACz (5.7 pav., a), o jų statistinis pasiskirstymas, ypač junginio **70**, yra taip pat gero lygio ir indikuoja gerą rezultatų atkartojamumą. Šių junginių *FF* ir *PCE* vertės (5.7 pav., c, ir 5.7 pav., d) taip pat yra panašios į rezultatus, demonstruojamus standartų 2PACz ir Me-4PACz. Gauti rezultatai sutampa su anksčiau atliktais matavimais. **64** ir **70** QFLS vertės buvo šiek tiek mažesnės lyginant su etalonais, tačiau jas kompensavo geresnė krūvininkų ekstrakcija, kuri buvo įrodyta atliekant trSPV matavimus. Tokia pati tendencija pastebima ir dibenzo[*b,f*]azepino **55** atveju, kurio rezultatai palyginamojoje serijoje buvo prasčiausiai. Mažesnį efektyvumą galima tiesiogiai susieti su prastesniais perovskito luminescencijos, QFLS ir trSPV matavimų rezultatais. Šie matavimai yra patogus ir gana greitas būtas numatyti, kaip

naujos medžiagos veiktų saulės elementuose, nekonstruojant viso prietaiso. Taigi, remiantis gautais duomenimis, difenilamino chromoforą turintis junginys **64** yra perspektyvus kandidatas efektyviems perovskitiniams saulės elementams konstruoti.

5.2.3. Skyriaus apibendrinimas

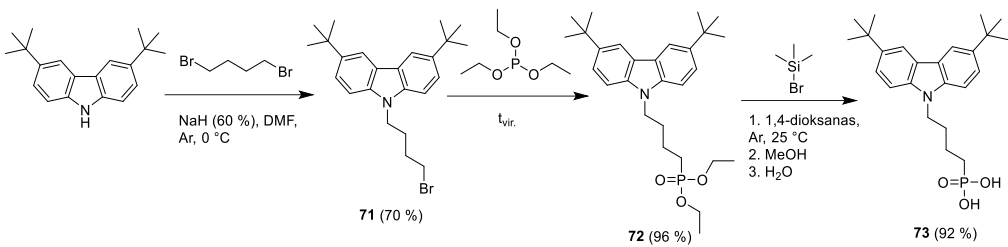
Naudojant įvairius chromoforus, tokius kaip fentiazinas, fenoksazinas, difenilaminas, *5H*-dibenzo[*b,f*]azepinas ir *10,11*-dihidro-*5H*-dibenzo[*b,f*]azepinas, buvo susintetinti nauji nekarbazoliniai SAM sudarančios junginiai. Nepakeistų indolo darinių sintezės bandymai nebuvu sėkmingi dėl indolo 3-H padėties reaktyvumo atliekant hidrolizės reakcijas. Junginiai **58** ir **61** buvo sėkmingai panaudoti BHJ OPV, o jų efektyvumas siekė atitinkamai 13,9 % ir 12,5 %. Tačiau dėl žemesnio ir mažiau palankaus jonizacijos potencialo, jų efektyvumas neprilygo PEDOT:PSS ir 1.1 skyriuje aptartiems halogenintiems karbazolo dariniams. Abu junginiai taip pat buvo išbandyti p-i-n konfigūracijos perovskitiniose saulės elementuose, kurių efektyvumas siekė atitinkamai 17,3 % ir 16,0 %. Etaloninio 2PACz PCE buvo geresnis (19,5 %), todėl galima daryti išvadą, kad tirtų 2PACz, **58** ir **61** efektyvumas ($19,5\% > 17,3\% > 16,0\%$) gali būti tiesiogiai susijęs su mažėjančiomis jų jonizacijos potencialų vertėmis ($5,6 \text{ eV} > 5,44 \text{ eV} > 5,29 \text{ eV}$). Junginiai **55**, **64** ir **70** taip pat buvo tiriami p-i-n konfigūracijos perovskitiniose saulės elementuose ir atlikus preliminarius tyrimus paažėjėjo, kad **64** yra perspektyviausia medžiaga, nes jos krūvininkų ekstrakcijos greitis buvo geriausias iš visų tirtų SAM sudarančių darinių. Šis rezultatas atsispindėjo prietaisu veikime, čia junginys **64** turėjo labai geras fotovoltaicines charakteristikas, pranokstančias standartą 2PACz bei gerą rezultatų pasikartojamumą, o tai įrodo, kad difenilaminas yra perspektyvus chromoforas SAM sudarančių junginių sintezei ir integravimui į PSCs.

5.3. SAM sudarančios junginiai su fosfonrūgšties bei kitomis funkcinėmis grupėmis

Dar viena strategija, kaip praplėsti šiuo metu naudojamų 2PACz ar Me-4PACz SAM sudarančių medžiagų įvairovę, yra padidinti jų funkcionalumą ištraukiant papildomas funkcinės grupes. Šios grupės gali būti naudojamos energetiniams lygmenims reguliuoti, suformuoto monosluoksnio paviršiaus vilgymo savybėms keisti arba papildomai sąveikai su kitais prietaiso komponentais užtikrinti.

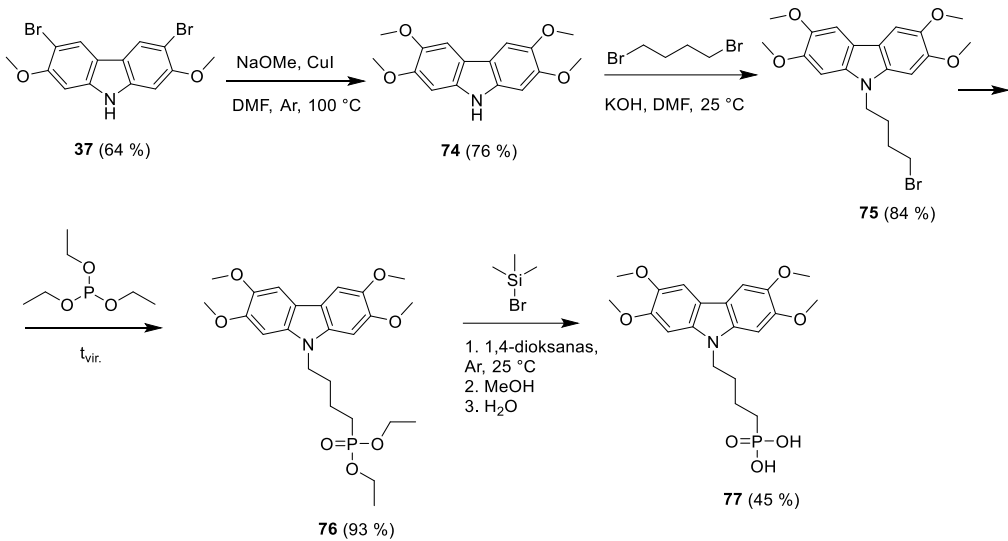
5.3.1 Fosfonrūgštis ir kitas funkcinės grupės turinčių molekulių sinteze

Daugumos karbazolo ir fentiazino SAM sudarančių junginių sintezei, aptariamai šiame skyriuje, buvo reikalingi papildomi žingsniai atliekant reakcijas, taip siekiant pridėti norimas funkcinės grupes ir gauti tikslinius produktus.



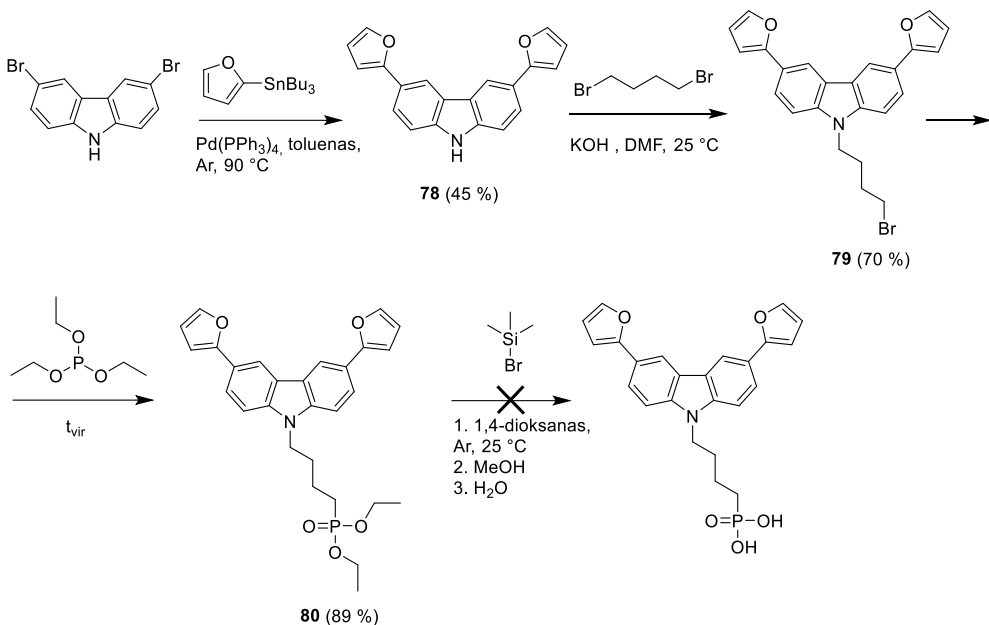
5.3 schema. Karbazolo darinio 73, turinčio *tret*-butil ir fosfonrūgštis grupes, sintezė

Brombutil fragmentas buvo pridėtas alkilinimo reakcijos metu naudojant 1,4-dibrombutaną ir NaH 60 % dispersiją mineralinėje alyvoje (5.3 schema). Išskirtas tarpinis produktas 71 toliau naudojant trietilfosfitą buvo paverstas į fosfonatą 72. 3,6-Di-*tret*-butil-karbazolas 73, turintis fosfonrūgštis grupę, buvo gautas hidrolizės reakcijos metu naudojant bromtrimetilsilaną.



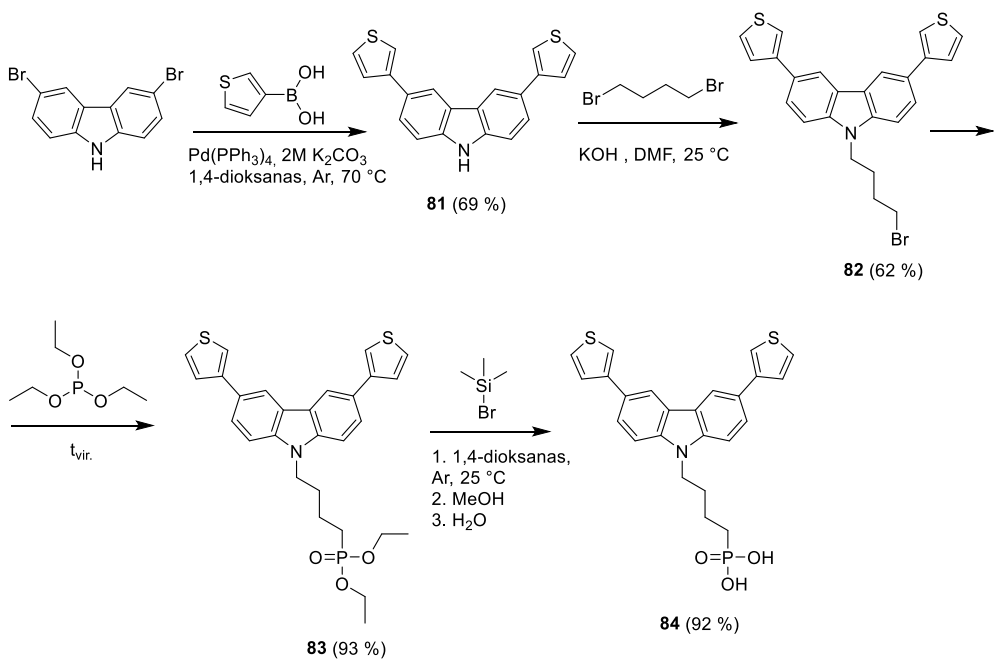
5.4 schema. Keturias metoksigrupes ir fosfonrūgštis grupę turinčio karbazolo 77 sintezė

Tetra-metoksi-pakeistas karbazolas, turintis fosfonrūgštis grupę, buvo susintetintas kaip pradinę medžiagą naudojant tarpinių junginių 37, atliekant reakciją su natrio metoksidu DMF, dalyvaujant vario (I) jodidui ir taip gaunant 2,3,6,7-tetrametoksikarbazolą 74 (5.4 schema). Toliau buvo vykdoma panaši 3 žingsnių alkilinimo / Arbuzovo reakcijos / hidrolizės procedūra galutiniam produktui 77 gauti.



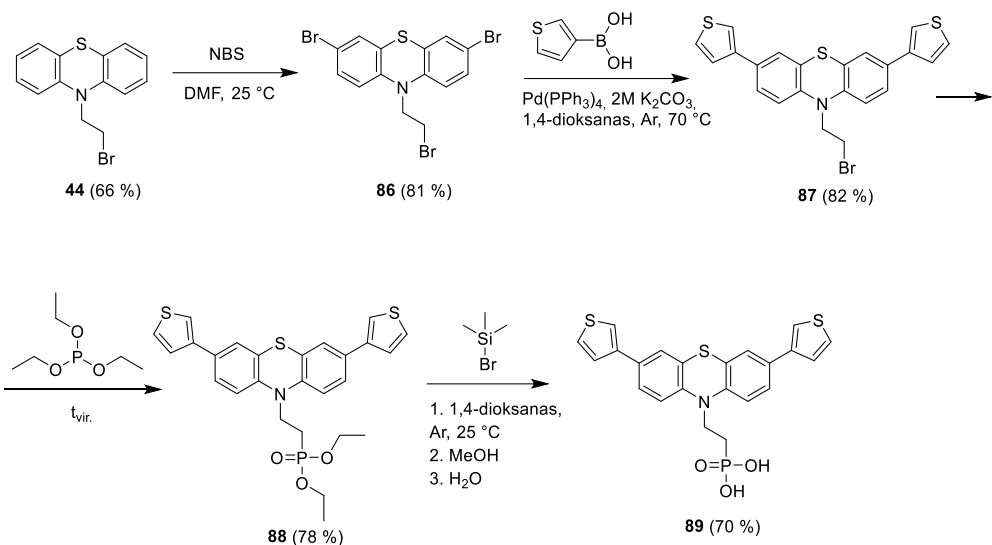
5.5 schema. Bandymai susintetinti karbazolo junginį su furano fragmentais ir fosfonrūgštis funkcinėmis grupėmis

Furano fragmentas galėtų būti naudingas siekiant praplėsti karbazolo konjuguotą sistemą, taip pat šios funkcinės grupės galėtų sąveikauti su perovskitu, panašiai kaip ir tiofenų dariniai, aprašyti literatūroje [201]. Jiems pridėti buvo pritaikyta Stille reakcija (5.5 schema), naudojant 2-(tributilalavo)furaną ir tetrakis(trifenilfosfin)paladi(0) toluene, esant argonui, taip gaunant tarpinį junginį **78**, kuris toliau buvo alkalinamas ir verčiamas fosfonatu, atitinkamai gaunant junginius **79** ir **80**. Tačiau paskutinė hidrolizės reakcija nevyko taip, kaip buvo planuota. Produktas gautas kaip netirpi juoda kieta medžiaga, todėl jo struktūros nustatyti nepavyko. Taip galėjo atsitikti dėl galimos furanų kondensacijos esant hidrobromido rūgščiai, kuri reakcijos metu išsiskiria kaip šalutinis produktas [202].



5.6 schema. Karbazolo darinio **84**, turinčio tiofeno fragmentus ir fosfonrūgšties funkcinę grupę, sintezė

Strategija, siekiant praplėsti karbazolo konjuguotą sistemą, įtraukiant papildomus heteroatomus, galinčius sąveikauti su perovskito paviršiumi ir galimai ji taip pasyvuoti, buvo tiriamas toliau, pridendant tiofenų funkcinės grupės. Tiofenai yra žinomi kaip naudingi sieros atomus turintys fragmentai, pasižymintys palankiomis savybėmis pasyvuojant perovskitą [203]. Vykdant paladžio katalizuojamą Suzuki-Miyaura kryžminio jungimo reakciją bevandeniamame 1,4-dioksane, iš 3,6-dibromkarbazolo ir 3-tienilborono rūgšties buvo gautas junginys **81** (5.6 schema). Toliau buvo vykdytos analogiškos 3 žingsnių reakcijos, atliekant alkalinimą 1,4-dibromobutanu, alifatinio bromido pakeitimą fosfonrūgšties etilo esteriu bei hidrolizę naudojant bromtrimetilsilaną. Šių reakcijų metu buvo gauti atitinkamai junginiai **82**, **83** ir galutinis produktas **84**. Atliekant hidrolizę nukrypimų nepastebėta, o tai rodo, kad tiofeno fragmentai yra tinkami kandidatai fosfonrūgšties grupę turinčių SAM sudarančių junginių sintezei.



5.7 schema. Fentiazino **89**, turinčio tiofeno fragmentus ir fosfonrūgštis funkcinę grupę, sintezė

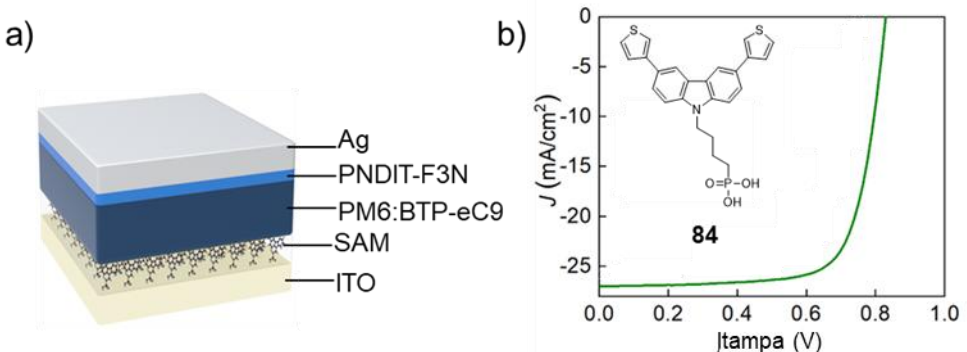
Toliau buvo sintetinamas junginio **84** analogas, pasirenkant fentiazino chromoforą vietoje karbazolo, taip į struktūrą įtraukiant dar vieną sieros heteroatomą [204]. Tarpinis produktas **44** buvo naudojamas kaip pradinė medžiaga, atliekant brominimo reakciją su NBS dimetilformamide (5.7 schema). Gautas fentiazinas **86** buvo panaudotas paladžiu katalizuojamai Suzuki-Miyaura jungimo reakcijai su 3-tienilborono rūgštimi 1,4-dioksane esant argono aplinkai. Gautas junginys **87** buvo paverstas tiksliniu produkту **89**, turinčiu fosfonrūgštis grupę, taikant anksčiau aprašytą fosfonilinimo ir hidrolizės reakcijų procedūras.

Gauti junginiai buvo naudojami tolimesniems tyrimams, formuojant savitvarkį monosluoksnį ant ITO. Monosluoksnio formavimo procedūra pateikta 3.1 skyriuje.

5.3.2. Junginių panaudojimas organiniuose saulės elementuose¹⁵

Karbazolas **84**, turintis tiofeno fragmentus, buvo testuotas tūrio heterosandūros organiniuose saulės elementuose. Konstruotų iрenginių schematiška architektūra pateikta 5.8 pav., a, ji išreiškiama kaip ITO/SAM/BHJ/PNDIT-F3N/Ag. Absorberio sluoksniniui naudota vieno donoro ir vieno akceptorius PM6:BTP-eC9 sistema (struktūros pateiktos 5.1 sk. 5.1 pav.).

¹⁵ Ірenginiai buvo sukonstruoti ir matavimai atlikti Karaliaus Abdulos mokslo ir technologijų universitete (King Abdullah University of Science and Technology (KAUST)), Saudo Arabija, prof. T. D. Anthopoulos tyrimų grupėje.



5.8 pav. (a) BHJ organinio saulės elemento schematiška architektūra; (b) geriausio įrenginio naudojant karbazolą **84** J - V kreivė

5.4 lentelė. PM6:BTP-eC9 BHJ pagrindu sukonstruotų OPV su junginiu **84** fotovoltinių charakteristikų apibendrinimas esant AM 1.5G ($100 \text{ mW}/\text{cm}^2$) apšvietai

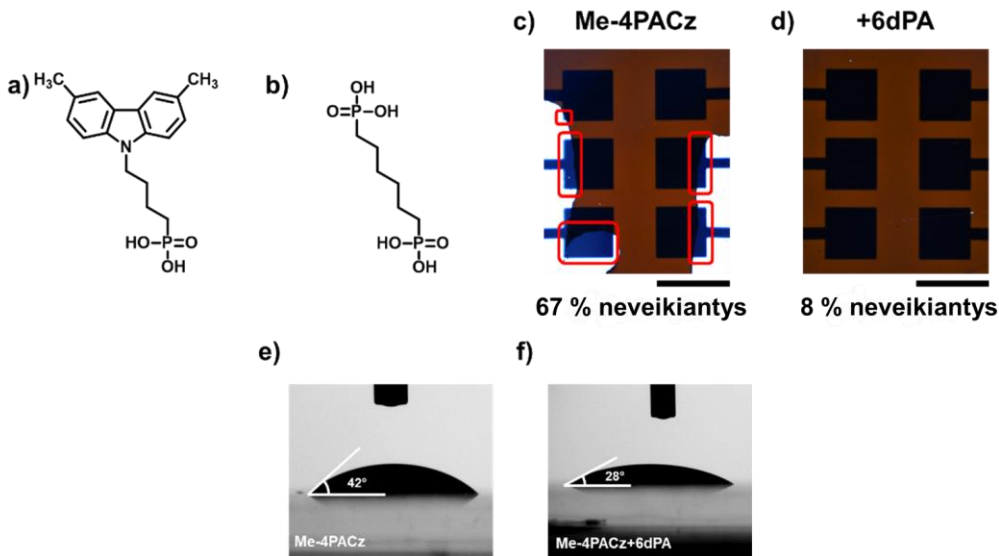
BHJ	HTM	V_{OC} [V]	J_{sc} [mA/cm^2]	FF [%]	PCE [%]
PM6:BTP-eC9	PEDOT:PSS 84	0,843 0,829	26,31 27,009	76,7 73,7	17,0 16,5

Gauti rezultatai parodė (5.8 pav., b, ir 5.4 lentelė), kad karbazolas **84** pasižymi geru našumu BHJ OPV, pasiekdamas 16,5 % efektyvumą, kuris yra labai artimas standarto PEDOT:PSS efektyvumui (17,0 %). Įdomu yra tai, kad junginys **84** turi palyginti žemą jonizacijos potencialą (5,44 eV), identišką 5.2 skyriuje aptartam fentiazinui **58**, kuris taip pat buvo testuotas BHJ OPVs, tačiau jo efektyvumas buvo prastesnis (13,9 %). Tai rodo, kad energetiniai lygmenys nėra vienintelis svarbus veiksnys, lemiantis SAM sudarančių skyles pernešančių junginių efektyvumą organiniuose fotovoltiniuose įrenginiuose. Geras veikimas gali būti susijęs su tiofeno fragmentu ir sieros atomų buvimu, nes standartiniame HTM PEDOT:PSS taip pat yra tiofeno fragmentų. BHJ absorberio sistemoje taip pat yra gausu sieros, todėl junginio **84** geras efektyvumas, net ir esant palyginti žemam jonizacijos potencialui, gali būti aiškinamas įvairiomis sąveikomis tarp skirtinį sluoksnį.

5.3.3. Junginių panaudojimas perovskitiniuose saulės elementuose

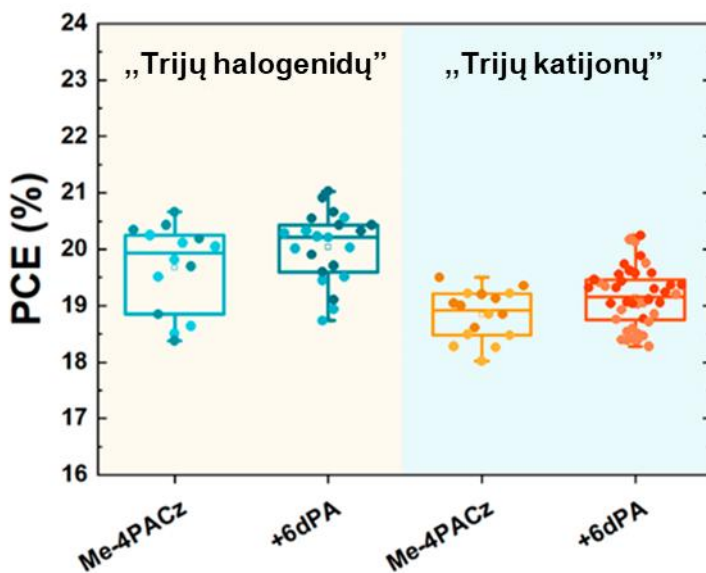
Karbazolas **73**, turintis *tret*-butilo pakaitus, buvo panaudotas kitokiam tyrimui. Struktūriškai panašus Me-4PACz (5.9 pav., a) pasižymi geresniu krūvininkų ištraukimu, palyginti su kitaip plačiausiai naudojamais SAM sudarančiais junginiais, tokiais kaip 2PACz ar MeO-2PACz. Tačiau plačiau jį naudoti trukdo gana didelis suformuoto monosluoksnio hidrofobiškumas, o tai lemia prastą perovskito sluoksnio padengimą iš jo komponentų tirpalų [205]. Idealiu atveju saulės elementų gamyba turėtų būti patikima ir paprasta, tačiau dėl prasto Me-4PACz modifikuoto ITO paviršiaus vilgymo perovskito sluoksnio suformavimas tampa sudėtingesnis, o ir jo

kokybė gali nekontroliuojamai kisti. Todėl neretai tampa sunku pasiekti gerą rezultatų pasikartojamumą ne tik skirtingose, bet net ir toje pačioje laboratorijoje.



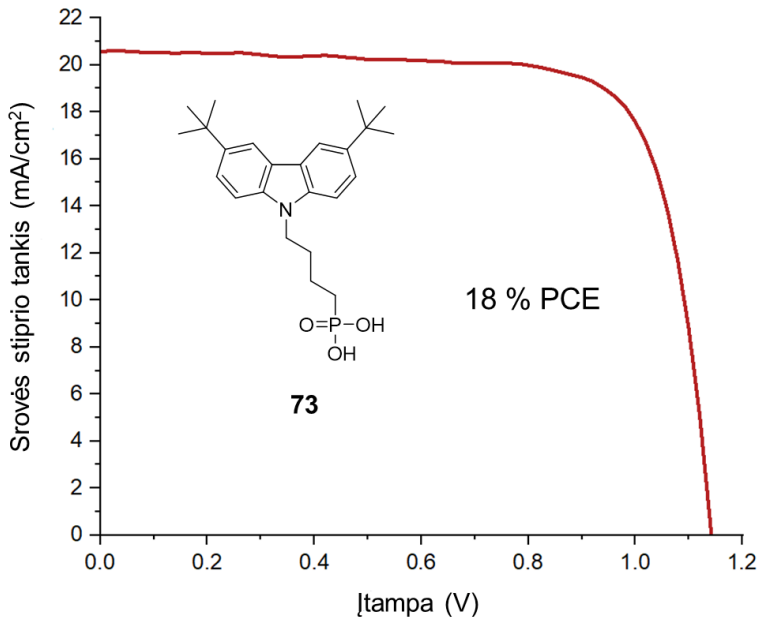
5.9 pav. Junginių, naudotų monosluoksniui formuoti, cheminės struktūros: (a) Me-4PACz ir (b) 6dPA. Reprezentacinės PSCs su (c) Me-4PACz ir (d) Me4-PACz+6dPA nuotraukos. Raudona spalva pažymėtos vietos, nepadengtos perovskitu. Mastelis = 5 mm. (e, f) Vilgymo kampo matavimų nuotraukos, lašinant trijų katijonų perovskito komponentų tirpalą ant ITO/monosluoksnio substratų.

Paprastas būdas išspręsti Me-4PACz problemas – į jo tirpalą pridėti komerciškai prieinamą junginį 1,6-heksilfosfonrūgštį (6dPA) (5.9 pav., b). Siekiant įvertinti šio priedo įtaką, buvo sukonstruoti įrenginiai, kuriuose ant Me-4PACz ir 6dPA suformuoto monosluoksnio buvo dengiamas trijų katijonų perovskitas. Atlikus *J-V* charakteristikų matavimus, buvo nustatyta, kad 67 % pirmojo substrato pikselių buvo neveikiantys (5.9 pav., c) (jų V_{oc} buvo gerokai žemesnė nei 1 V). Pridėjus 6dPA (20 mol %), įrenginio veikimas buvo smarkiai pagerintas, o neveikiančių pikselių sumažėjo iki 8 % (5.9 pav., d), kadangi monosluoksniu padengto ITO vilgymas buvo pagerintas nuo 42° iki 28° (5.9 pav., e, ir 5.9 pav., f), ir tai lėmė geresnį perovskito sluoksnio padengimą.



5.10 pav. Prietaisų PCE statistinis pasiskirstymas (neveikiantys įrenginiai nebuvu įtraukti) naudojant skirtinges perovskitus bei Me-4PACz ir Me-4PACz + 6dPA (skenavimas atgal – tamsesnė spalva, skenavimas pirmyn – šviesesnė spalva)

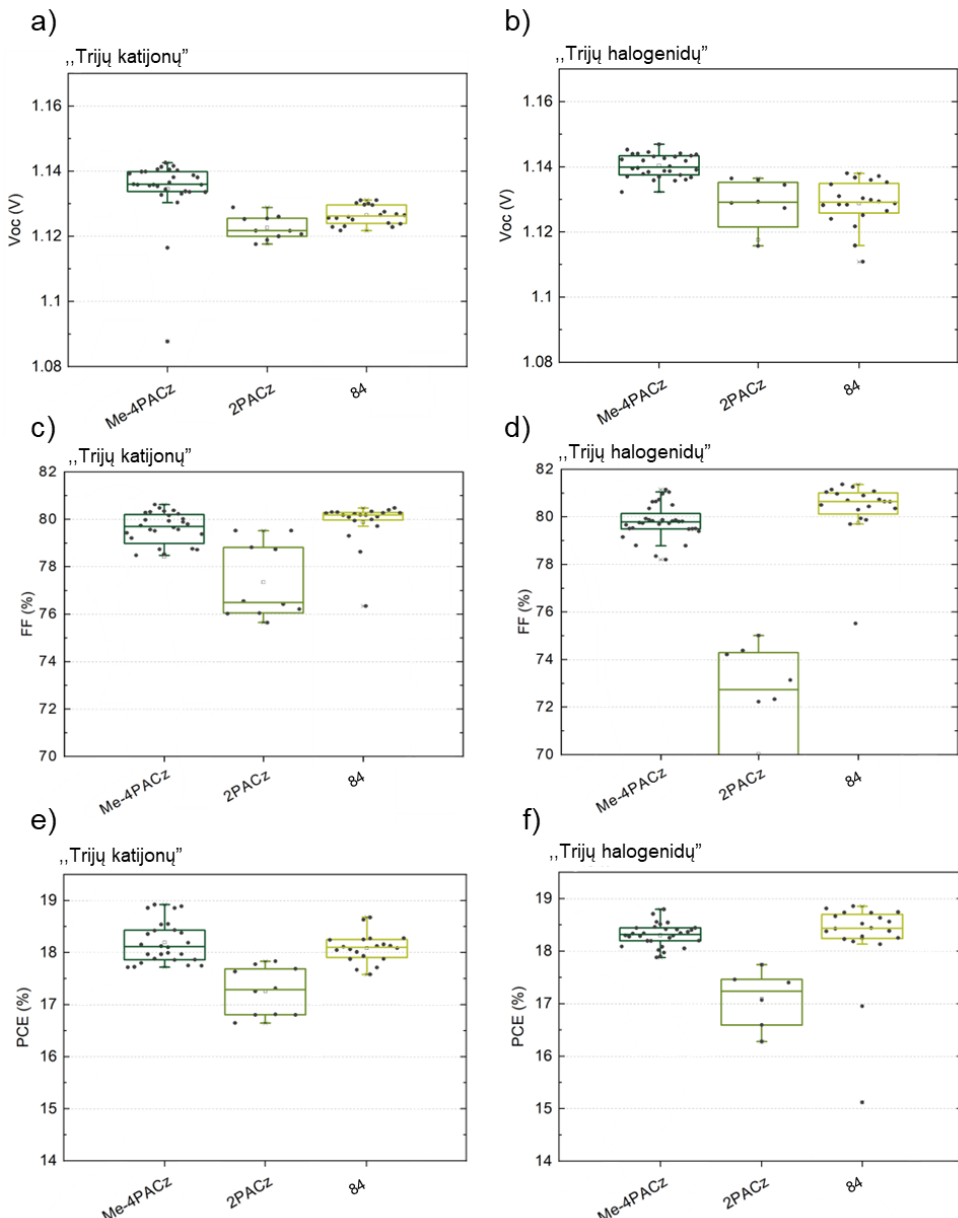
6dPA priedo įtaka saulės elementų veikimui buvo ištirta sukonstravus p-i-n architektūros ITO/SAM/Perovskito/LiF/C₆₀/BCP/Ag konstrukcijos perovskitinius saulės elementus. Tam buvo panaudotos dvi dažniausiai sutinkamos perovskito sudėtys, žinomos kaip „trijų katijonų“ ($FA_{0.79}MA_{0.16}Cs_{0.05}Pb(I_{0.83}Br_{0.17})_3$) [206] ir „trijų halogenidų“ ($FA_{0.75}Cs_{0.22}MA_{0.03}Pb(I_{0.82}Br_{0.15}Cl_{0.03})_3$) [207]. Remiantis rezultatais, 6dPA priedas neturėjo jokios neigiamos įtakos prietaiso veikimui (5.10 pav.), o tiek vidutinės, tiek geriausių pikselių vertės buvo netgi šiek tiek didesnės. Didžiausias 20,9 % efektyvumas buvo pasiektas naudojant trijų halogenidų perovskitą bei Me-4PACz + 6 dPA monosluoksnį.



5.11 pav. Geriausias efektyvumas buvo prietaiso, sukonstruoto naudojant karbazolą **73** + 6dPA, skenavimo atgal *J-V* kreivę

6dPA galimybėms įrodyti buvo sukonstruoti prietaisai naudojant susintetintą junginį **73**, turintį stambias alifatinės *tret*-butilo funkcines grupes (5.11 pav.), dėl kurių suformuotas monosluoksnis pasižymėjo ypač prastu vilgymu, ir tai trukdė sukonstruoti veikiančius PSCs. Tačiau, pridėjus ši priedą, pavyko gauti veikiančius prietaisus, kurių *PCE* siekė 18 % (5.11 pav.). Nepaisant mažesnių *FF* verčių, šis pavyzdys rodo, kad galima ir toliau plėsti skyles pernešančią medžiagą, formuojančią savitvarkį monosluoksnį, optimizavimą.

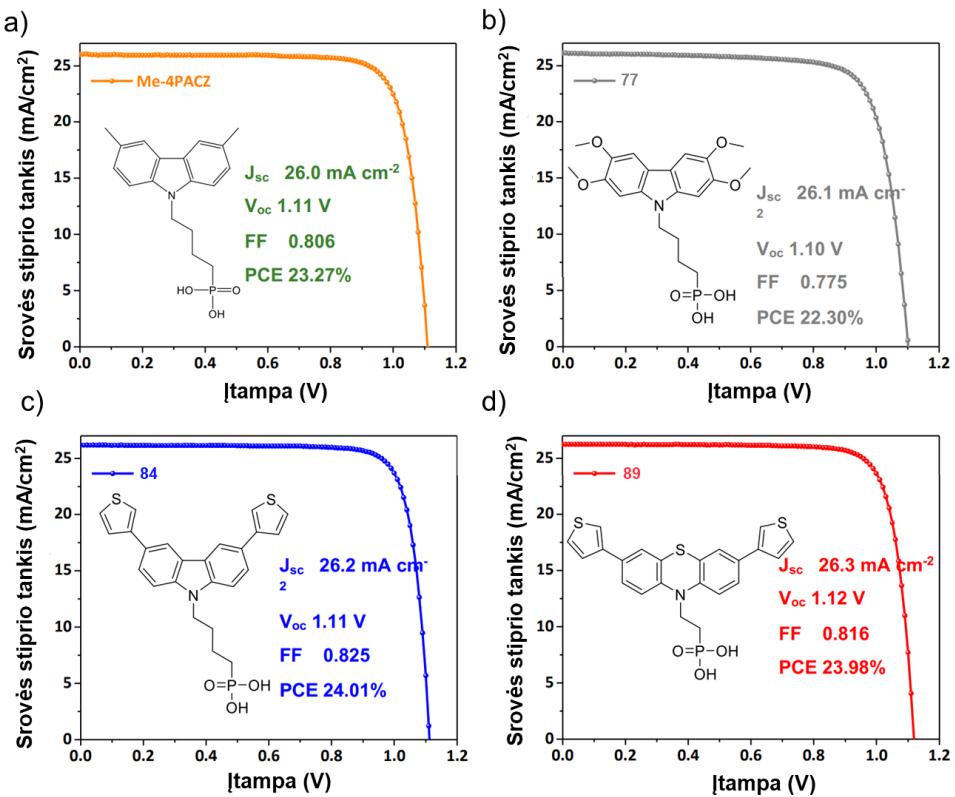
Toliau buvo tiriamas karbazolas **84**, turintis tiofeno fragmentus. Jis buvo panaudotas konstruojant „trijų katijonų“ ($\text{FA}_{0.79}\text{MA}_{0.16}\text{Cs}_{0.05}\text{Pb}(\text{I}_{0.83}\text{Br}_{0.17})_3$) ir „trijų halogenidų“ ($\text{FA}_{0.75}\text{Cs}_{0.22}\text{MA}_{0.03}\text{Pb}(\text{I}_{0.82}\text{Br}_{0.15}\text{Cl}_{0.03})_3$) kompozicijų PSCs. Naujas junginys buvo lygintas su tos pačios šeimos standartais 2PACz ir Me-4PACz, siekiant ivertinti tiofenų galimybes pasyvuoti perovskitą sluoksnį sandūroje.



5.12 pav. P-i-n architektūros perovskitinių saulės elementų fotovoltinės charakteristikos, naudojant skirtingus perovskitus ir lyginant skirtingus SAM sudarančius HTMs: (a) V_{OC} statistiniai rezultatai; (b) J_{SC} statistiniai rezultatai; (c) užpildymo faktoriaus statistiniai rezultatai; (d) efektyvumo statistiniai rezultatai

Bandymų rezultatai pateikti 5.12 paveiksle. Remiantis fotovoltinėmis charakteristikomis, 2PACz, kuris yra laikomas vienu iš geriausiai veikiančiu SAM

junginių, buvo pranoktas tiek etaloninio Me-4PACz, tiek tiofeno fragmentus turinčio karbazolo darinio **84**. Tai ypač atispindī „trijų halogenidų“ perovskito įrenginių *FF* ir *PCE* sekcijose (5.12 pav., d, ir 5.12 pav., f), kuriuose junginys **84** pasirodė geriausias ir pasiekė gerą statistinį pasiskirstymą. Geras užpildymo koeficientas atispindėjo efektyvumę, junginio **84** buvo panašus *PCE* „trijų katijonų“ elementuose (18,27 %) arba šiek tiek geresnis *PCE* „trijų halogenidų“ elementuose (18,81 %), palyginti su Me-4PACz *PCE*, siekiančius atitinkamai 18,36 % ir 18,55 % (5.12 pav., e, 5.12 pav., f, ir A3 pav.). Atsižvelgiant į ankstesniame skyriuje pastebėtą jonizacijos potencialo ir efektyvumo koreliaciją, buvo galima tikėtis, kad tarp tirtų medžiagų karbazolas **84** bus mažiausiai efektyvus dėl jo mažiausio I_p (5,44 eV). Tačiau jis pasižymėjo geresniu efektyvumu nei 2PACz, kurio I_p yra 5,6 eV, ir panašiu efektyvumu kaip Me-4PACz, kurio I_p yra 5,8 eV [208], todėl tai gali būti siejama su perovskito pasyvavimu, dėl kurio padidėja *PCE*. Taip pat verta pažymeti, kad **84** monosluoksnis buvo suformuotas įprastiniu būdu, nenaudojant 6dPA, ir jo paviršiaus vilgymas buvo pakankamas perovskito sluoksnui suformuoti.



5.13 pav. PSCs naudojant Me-4PACz and SAM sudarančius junginius **77**, **84** ir **89** $J-V$ kreivės bei fotovoltaikos charakteristikos¹⁶

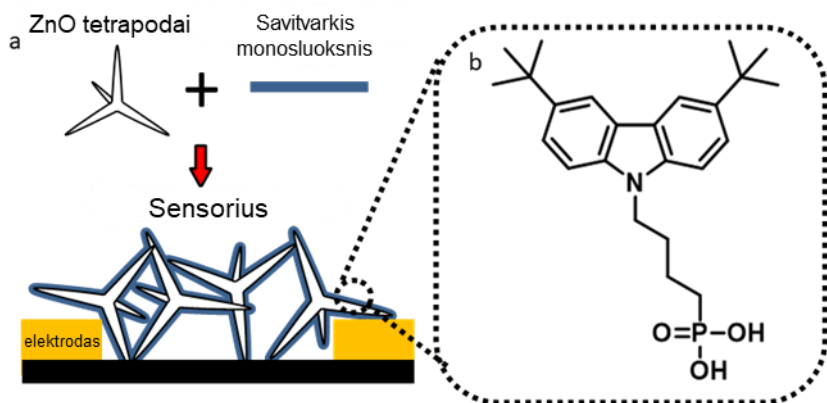
Susintetinti junginiai **77** ir **89** kartu su tiofeno fragmentus turinčiu karbazolu **84** taip pat buvo tiriami p-i-n perovskitiniuose saulės elementuose. Preliminarūs prietaisų rezultatai pateikti 5.13 paveiksle. Visų elementų efektyvumas viršijo 22 %, o tai rodo gerą PSC sluoksnį kokybę ir jų suderinamumą. Tetrametoksi pakeisto karbazolo **77 PCE** buvo mažesnis (22,30 %), palyginti su Me-4PACz (23,27 %). O tiofeno fragmentus turintys **84**, ir **89** buvo efektyvesni už naudotą standartą Me-4PACz, jų efektyvumai siekė atitinkamai 24,01 % ir 23,98 %. Šis rezultatas taip pat gali būti siejamas su tiofeno fragmentus turinčiu SAM ir perovskito tarpusavio sąveika.

5.3.4. Junginių panaudojimas ZnO tetrapodų dujų jutikliuose

Karbazolas **77** buvo pritaikytas palyginti mažai iširtoje modifikuotų metalų oksidų jutiklių srityje. Palyginti su įprastu ZnO, kuris paprastai veikia aukštesneje temperatūroje, cinko oksido tetrapodai (ZnO-T) dėl didelio paviršiaus ir tūrio santykio

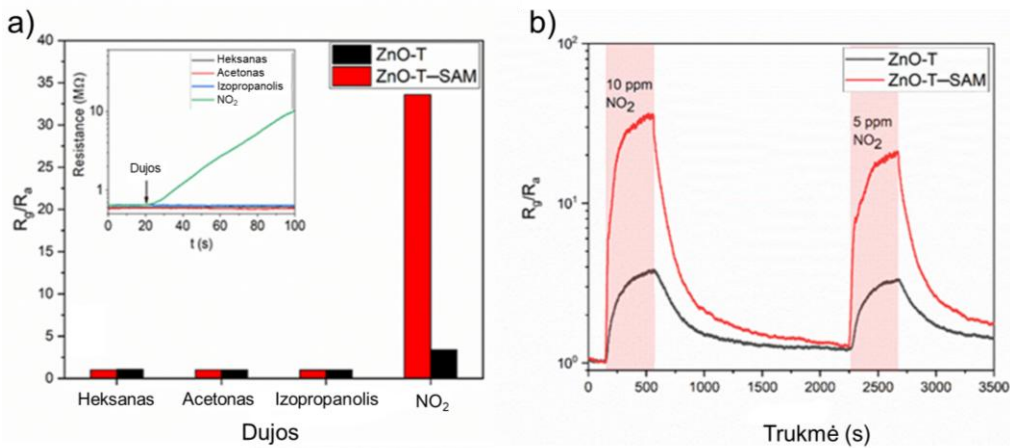
¹⁶ Įrenginiai buvo sukonstruoti ir matavimai atlikti Lozanos federalinėje politechnikos mokykloje (École polytechnique fédérale de Lausanne (EPFL)), Lausanne, Šveicarija, M. K. Nazeeruddin tyrimų grupėje.

pasižymi itin dideliu jautrumu esant žemoms temperatūroms [209]. Aukšta temperatūra nesuderinama su lankščiais polimeriniais substratais, taip pat gali kilti jutikliams naudojamu medžiagų stabilumo problemą. Toliau metalo oksidų jutiklius funkcionalizavus organinėmis medžiagomis, galima sukonstruoti dujų jutiklius, pasižyminčius dideliu jautrumu, stabilumu, selektyvumu, greitu atsaku, galinčius veikti kambario temperatūroje (RT) ir pasižyminčius mažomis medžiagų sąnaudomis [210]. Iki šiol dauguma darbų buvo orientuoti į alkilsilanų SAM [211], nes šių struktūrų junginiai ir jų padengimų metodai yra gerai žinomi. Kita vertus, jų įtaka paviršiaus energetiniams lygmenims yra ribota dėl konjuguotų, elektronakceptorinių ar elektrodonorinių sistemų nebuvinimo. Todėl puslaidininkinio junginio 77 potencialas buvo ištirtas jį panaudojant ZnO-T paviršiui modifikuoti ir dujų jutiklio įrenginiui sukonstruoti.



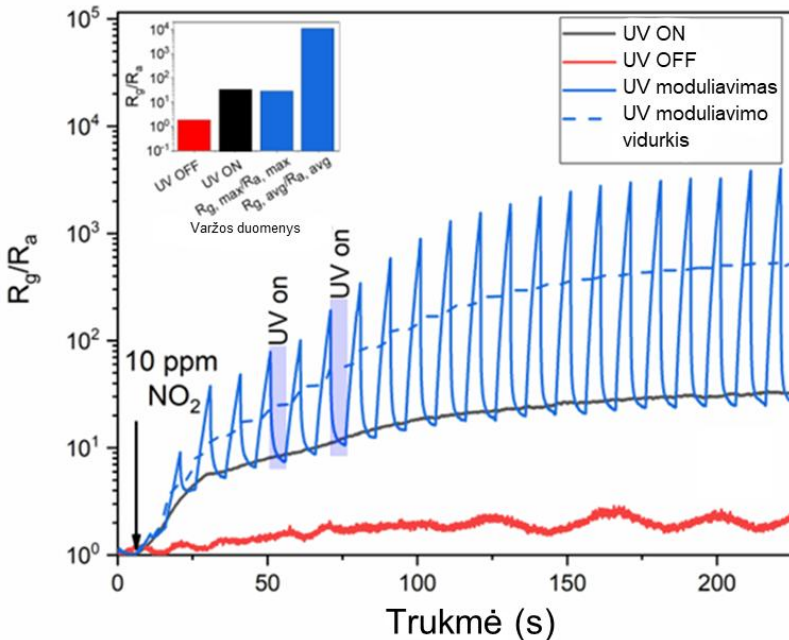
5.14 pav. Modifikuotų ZnO-Ts karbazolo 77 monosluoksniių schemas: a) jutiklio schema; b) karbazolo 77 cheminė struktūra.

Jutiklio, sukonstruoto naudojant karbazolu 77 modifikuotus ZnO tetrapodus, schema pateikta 5.14 paveiksle. Elektrodams padengti buvo naudojamas auksas, užpurkštas ant stiklo, sudarant 3x5 mm dydžio daugiakampius, kuriuos skiria 1, 3, 5, 10 ir 15 mikrometru tarpai. Šiame eksperimente naudotas 3 μm tarpas.



5.15 pav. ZnO-T ir modifikuotų ZnO-T jutiklių charakterizavimas: a) atsakas į lakiuosius junginius ir dujas, kai koncentracija yra 10 ppm; b) atsakas ir atsistatymas esant skirtingai NO₂ koncentracijai

Buvo įvertintos ZnO-T ir modifikuotų ZnO-T jutiklių charakteristikos, įvertinant jų optoelektronines savybes ir atsaką į įvairias dujas. Į analizę buvo įtraukti lakielji junginiai, tokie kaip acetonas, heksanas bei izopropilo alkoholis, taip pat NO₂ dujos. Tieki ZnO-T, tieki ZnO-T-SAM sensoriai pasižymėjo minimaliu atsaku į lakiuosius junginius. O atsakas į NO₂, padidėjo beveik 10 kartų, lyginant modifikuotus ZnO-T su nemodifikuotais (5.15 pav., a). Ši pagerėjimą galima paaiškinti karbazolo 77 SAM sąveika su NO₂ dujomis, arba tankios paviršinės dangos, galinčios atliliki molekulinių sietų funkciją, susidarymu. Nors atsakas į NO₂ buvo beveik momentinis, kaip pavaizduota 5.15 pav. b, užtrukės vos kelias sekundes, atsistatymo procesas buvo pakankamai lėtas ir užtruko keliasdešimt minučių.



5.16 pav. ZnO-T jutiklio atsakas esant kambario temperatūrai. Naudoti modifikuoti ZnO-T su 77 esant skirtingoms UV salygomis: esant UV apšvietimui (UV On), tamsoje (UV Off) ir moduliujant UV (10 s periodas)

Siekiant dar labiau pagerinti ir pagreitinti dujų jutiklio atsaką ir veikimą, buvo panaudota UV moduliacija, kai UV spinduliuotė įjungama ir išjungama vienos sekundės intervalais. Šis dinaminis procesas gali būti naudojamas dujų adsorbcijos ir desorbcijos procesams ZnO-T paviršiuje stimuliuoti. Leidžiant sistemai pasiekti naują pusiausvyrą, UV moduliacija veiksmingai pagerina jautrumą dujoms. 5.16 paveiksle pavaizduotas ZnO-Ts, funkcionalizuotų junginio 77 SAM, atsakas į 10 ppm NO₂, esant skirtingoms UV salygomis. Punktyrinė linija žymi UV moduliuoto atsako vidurkį, kuris apskaičiuojamas išvedant didžiausių verčių vidurkį esant išjungtam UV spinduliuavimui (R_{g, max}) ir mažiausiu verčių vidurkį esant įjungtam UV spinduliuavimui (R_{g, min}). Mažiausias atsakas į NO₂ buvo tamsos salygomis be UV apšvietimo, o įjungus UV per visą matavimą jis padidėjo ~17 kartų. Šis padidėjimas siejamas su UV aktyvavimu, palengvinančiu adsorbcijos-desorbcijos reakcijas ZnO-T paviršiuje.

5.3.5. Skyriaus apibendrinimas

Buvo susintetinti nauji karbazolo ir fentiazino centrinius fragmentus turintys SAM sudarantys junginiai, turintys fukcines *tret*-butilo, metoksigrupes ar tiofeno fragmentus. Furano fragmentus turinčio fosfonrūgšties darinio sintezė nebuvo sėkminga dėl furano žiedo reaktingumo hidrolizės salygomis. Buvo pademonstruotas paprastas ir lengvai pritaikomas SAM modifikuoto ITO prasto paviršiaus vilgymo

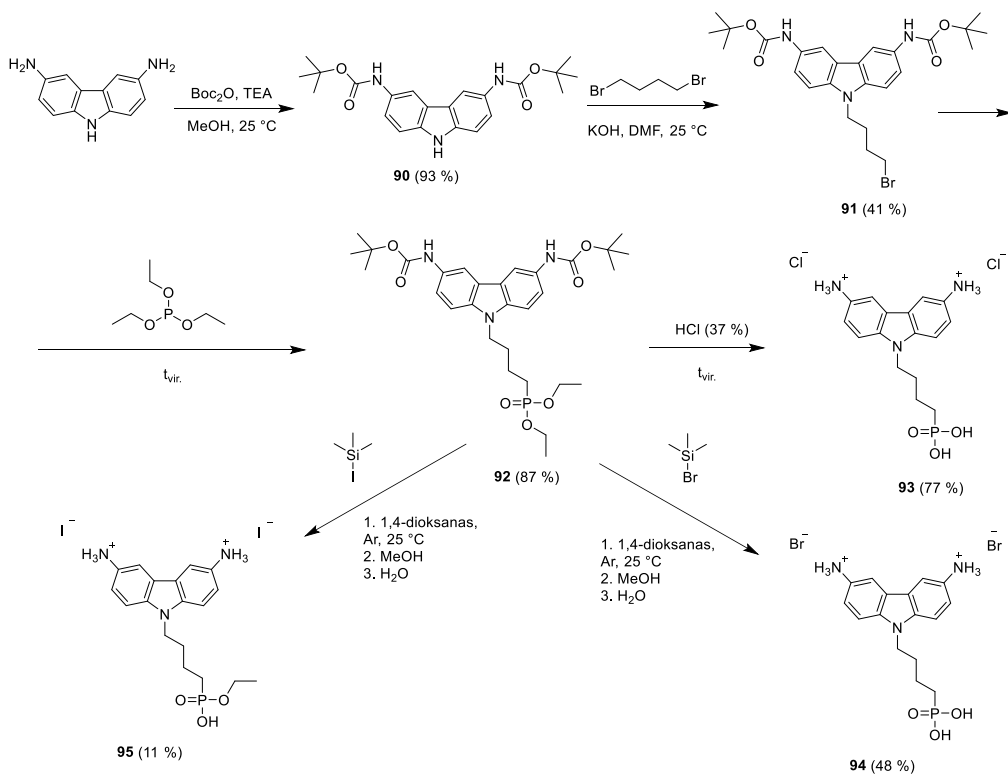
problemų, paprastai atsirandančių naudojant Me-4PACz, sprendimo būdas. I SAM junginio tirpalą pridėjus 6dPA, pagerėja substrato vilgymas perovskito komponentų tirpalui, kartu išlaikant ir net šiek tiek padidinant prietaiso efektyvumą. Taikant šią 6dPA priedo strategiją, pavyko gauti veikiančius prietaisus naudojant karbazolą 73, turintį hidrofobiškumą suteikiančias *tret*-butilo funkcinės grupes. Junginiai 84 ir 89 turėjo aukščiausio lygio efektyvumą PSC, pasiekdamai 24,01 % ir 23,98 % PCE, todėl tiofenai yra perspektyvūs fragmentai taikyti fotovoltaikoje įrenginiuose dėl jų gebėjimo pasyvuoti perovskito paviršių arba sąveikauti su OPV absorberiais. Karbazolas 73 su *tret*-butilo grupėmis buvo panaudotas ZnO tetrapodams modifikuoti, kuriant efektyvius kambario temperatūroje veikiančius dujų jutiklius. Ši strategija yra labai perspektyvi, nes ZnO funkcionalizavimas SAM pagerina selektyvumą NO₂ dujoms, kuris gali būti dar labiau padidintas naudojant UV moduliavimą.

5.4. SAM sudarantys junginiai su fosfonrūgštis bei amonio funkcinėmis grupėmis

Paskutinė šiame darbe pateikta strategija, siekiant padidinti fosfonrūgštis grupę turinčių SAM junginių funkcionalumą, buvo amonio funkcinį grupių pridėjimas. Amonio grupės yra žinomos dėl savo savybių pasyvuoti perovskito defektus [212]. Todėl molekulės su šiais fragmentais galėtų sąveikauti ir su metalo oksido substratu, ir su perovskito sluoksnio paviršiumi, o tai galėtų lemti didesnį PSC efektyvumą ir pagerinti ilgalaikį stabilumą.

5.4.1. Junginių su amonio ir fosfonrūgštis grupėmis sintezė

Karbazolo ir indolo centrinio fragmento SAM sudarantys junginiai, turintys amonio grupes, buvo sintetinami pradžioje apsaugant pradinių medžiagų aminogrupes naudojant *tret*-butilosikarbonilo grupę (Boc) ir toliau taikant 3 žingsnių procedūrą – alkalinimą, Michaelio-Arbuzovo ir hidrolizės reakcijas. Siekiant gauti produktus, turinčius skirtingus anijonus, buvo taikomos skirtingos hidrolizės reakcijos.



5.8 schema. Karbazolo darinių, turinčių fosfonrūgštis ir aromatinį amonio funkinių grupių, sintezė

Pradžioje karbazol-3,6-diaminas reagavo su di-*tret*-butildikarbonatu metanolje, dalyvaujant trietilaminui, susidarant 3,6-N-Boc apsaugotam karbazolo dariniui **90** (5.8 schema). Tolesnė alkalinimo reakcija naudojant 1,4-dibrombutaną ir KOH DMF buvo sėkminga, tačiau gauto tarpinio produkto **91** išeiga buvo vidutiniška (41 %), o tai susiję su padidėjusia šalutinių produktų susidarymo tikimybe esant aromatinėms karbamato grupėms. Bandant susintetinti fosfonatą **92**, išeiga taip pat nebuvo didelė (43 %), todėl reakcijos sąlygos buvo pakeistos sumažinant Michaelio-Arbuzovo reakcijos trukmę iki 4 valandų (vietoje vienos nakties) ir reakcijos išeiga padidėjo du kartus (87 %). Paskutinei hidrolizės reakcijai buvo naudojami trys skirtinių agentai: koncentruota druskos rūgštis, bromtrimetilsilanas ir jodtrimetilsilanas. Pastarasis negalėjo visiškai hidrolizuoti fosfonrūgštis esterio, ir gautame produkte **95** liko viena etilo grupė. Junginiai **93** ir **94** buvo susintetinti sėkmingai, juose amonio grupės gautos atitinkamai su chlorido ir bromido anjonais.

Analogiška sintezės procedūra buvo pritaikyta sintetinant alifatinius amino pakaitus turinčius karbazolo darinius **99** ir **100**, kaip pradinę medžiagą naudojant karbazol-3,6-dietanamino dihidrochloridą, bei alifatinius amino pakaitus turinčius indolo darinius **108**, **111**, **118** ir **119**. Pabrėžtina, kad 5-metoksi-indolų dariniai nėra tinkami SAM junginių sintezei, kadangi vykdant hidrolizę, ši grupė taip pat dalyvauja

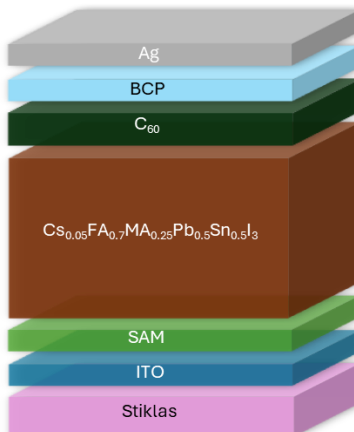
reakcijoje, susidarant nepageidaujamiems šalutiniams produktams, o ne tiksliniam produktui.

Gauti junginiai buvo naudojami tolimesniems tyrimams, formuojant savitvarkę monosluoksnį ant ITO. Monosluoksnio formavimo procedūra pateikta 3.1 skyriuje.

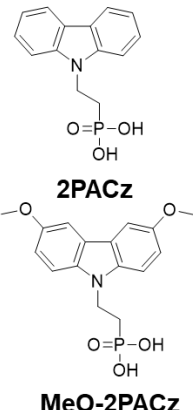
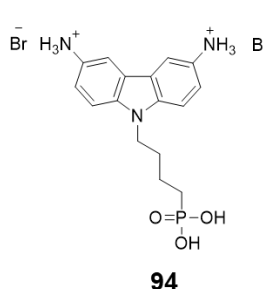
5.4.2. Junginių panaudojimas NBG perovskitiniuose saulės elementuose¹⁷

Karbazolas **94**, turintis amonio bromido funkcinės grupes, buvo išbandytas siauro juostų tarpo (NBG) perovskitiniuose saulės elementuose. Norint pasiekti 1,24 eV NBG, buvo sukonstruoti ITO/SAM/Cs_{0.05}FA_{0.70}MA_{0.25}Pb_{0.5}Sn_{0.5}I₃/C₆₀/BCP/Ag architektūros prietaisai (5.17 pav., a), kuriuose Pb buvo sumaišytas su Sn santykiiu 1:1. 2PACz ir MeO-2PACz buvo naudojami kaip etaloninės SAM medžiagos (5.17 pav., b).

a)



b)

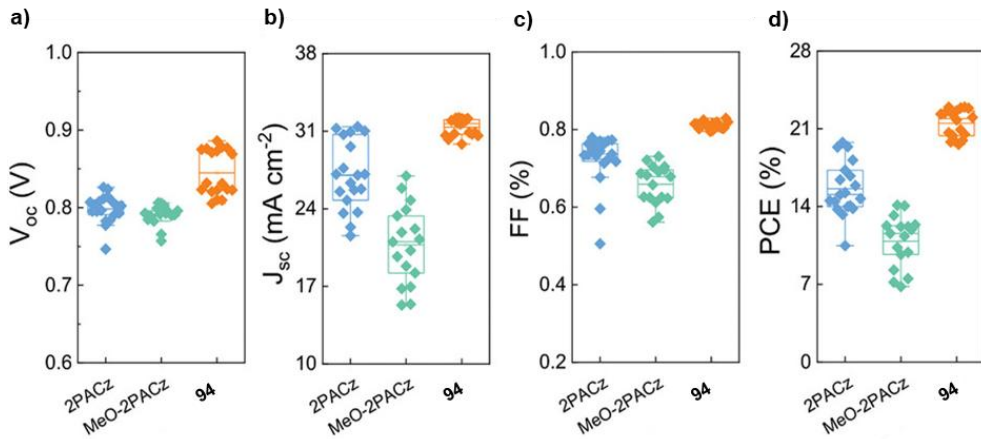


5.17 pav. (a) Sn-Pb PSC architektūra; (b) junginių, naudotų monosluoksniniu formuooti, cheminės struktūros

Sukonstruotų prietaisų statistiniai fotovoltainiai parametrai pateikti 5.18 paveiksle. Įrenginiai su karbazolu **94** turėjo gerokai didesnę V_{OC} ir FF (atitinkamai 0,88 V ir 82 %), palyginti su standartais 2PACz (atitinkamai 0,83 V ir 76 %) ir MeO-2PACz (atitinkamai 0,81 V ir 73 %). Šios charakteristikos atsišpindį ir efektyvumę – naudojant junginį **94** buvo pasiekta 23,0 % efektyvumas, kuris prilygsta geriausiais rezultatais pasižymintiems NBG Pb-Sn perovskitiniams saulės elementams. Labai geri fotovoltainiai parametrai yra tiesiogiai susiję amonio grupėmis, galinčiomis pasyvuoti perovskitą sluoksnių sandūroje. Joninės amonio bromido grupės gali lengvai disocijuoti į prie paviršiaus prisijungusį SAM amonio katijoną ($-NH_3^+$), kuris pasyvuoja perovskito A padėtyse esančius katijonų defektus, ir bromido anijoną (Br^-).

¹⁷ Įrenginiai buvo sukonstruoti ir matavimai atliki Karaliaus Abdulos mokslo ir technologijų universitete (King Abdullah University of Science and Technology (KAUST)), Saudo Arabija, prof. S. De Wolf tyrimų grupėje.

), kuris gali laisvai užpildyti jodidų defektus išiterpiant oktaedrų kampuose. Toks daugiafunkcinis pasyvacijos poveikis ir padidino prietaisų V_{OC} , nes sumažino tarpfazinių krūvininkų sulaikymo ir nespinduliuojančios rekombinacijos nuostolius.



5.18 pav. NBG p-i-n architektūros perovskitinių saulės elementų fotovoltaikos charakteristikos, lyginant skirtingus HTM, naudojamus kaip SAM: (a) V_{OC} statistiniai rezultatai; (b) J_{SC} statistiniai rezultatai; (c) užpildymo koeficiente statistiniai rezultatai; (d) efektyvumo statistiniai rezultatai

5.4.3. Skyriaus apibendrinimas

Šiame skyriuje pateikiama pažangesnių SAM sudarančių junginių koncepcija. Pridėjus papildomas amonio funkcinės grupės, tradiciniai puslaidininkiniai fosfonrūgščių dariniai galėtų vienu metu sąveikauti su dviem PSC komponentais – ITO ir perovskitu. Tuo tikslu buvo susintetinti karbazolo centrinių fragmentų turintys junginiai su fosfonrūgštis grupėmis, turintys aromatinius amonio halogenidų pakaitus **93** ir **94** bei alifatinius amonio halogenidų pakaitus **99** ir **100**. Tačiau amonio halogenidų įvairovė tiksliniuose junginiuose buvo aprūpinta chloridais ir bromidais, nes hidrolizės agentas jodtrimetilsilanas negalėjo iki galo hidrolizuoti dietilfosfonato. Tolimesnėje sintezėje buvo naudojami komerciškai prieinami skirtingas funkcinės grupės turintys indolo reagentai. Buvo pasirinkti indolai, turintys alifatinio amino pakaitus 3-ijoje indolo padėtyje, tam, kad hidrolizės metu nevyktų šalutinės reakcijos. Taip buvo susintetinti indolo dariniai **108** ir **111**, turintys ir fosfonrūgštis, ir amonio grupės, bei 5-chlor pakeisti indolo dariniai **118** ir **119**, turintys fosfonrūgštis ir amonio grupės. 5-Metoksi pakeistas indolas nėra tinkamas fosfonrūgščių sintezei, kadangi ši funkcinė grupė dalyvavo hidrolizės reakcijoje ir tiksliniai produktai nebuvvo gauti. Indolo centrinių fragmentų turintys junginiai **118** ir **119** šiuo metu yra tiriami organiniuose šviesos dioduose Thomas D. Anthopoulos tyrimų grupėje Karaliaus Abdulos mokslo ir technologijų universitete (King Abdullah University of Science and Technology) Saudo Arabijoje. Karbazolas **94** buvo išbandytas NBG Sn-Pb perovskitiniuose saulės elementuose ir efektyvumu bei kitais fotovoltainiais parametrais pranoko standartinius SAM sudarančius junginius 2PACZ ir MeO-2PACZ.

Geri rezultatai yra susiję su amonio grupių buvimu, šioms gebant pasyvuoti perovskitą sluoksnį sandūroje. Visi susintetinti junginiai pasižymi panašiais jonizacijos potencialais į MeO-2PACz, 2PACz ar Me-4PACz, todėl kartu su papildomomis perovskito pasyvacijos savybėmis šios medžiagos turėtų pasižymeti geru veikimu optoelektronikoje, kurioje yra naudojami įvairūs perovskitai.

Pagrindiniai rezultatai ir išvados:

1. Buvo susintetinti ir ištirti karbazolo centrinio fragmento skyles pernešantys junginiai turintys fosfonrūgšties funkcines grupes ir buvo nustatyta, kad:

- Halogenintų karbazolo centrinį fragmentą turinčių HTMs energetiniai lygmenys yra tinkami taikyti tūrio heterosandūros organiniuose saulės elementuose ir organiniuose šviesos dioduose.
- Halogenidų funkcinių atomų skaičius ir jų padėtis turi įtakos OPV veikimui. 3,6-Pakeisti karbazolai **5**, **8** ir **11** buvo efektyvesni nei 2,7-pakeisti dariniai **26**, **29** ir keturis halogenidų pakaitus turintis junginys **32**.
- Lyginant keturių ir dviejų anglies atomų ilgio alifatinės grandines karbazolo SAM sudarančių junginių struktūroje, trumpesnioji yra tinkamesnė efektyviems BHJ OPV konstruoti.
- Tarp tirtų halogenidų funkcinių atomų chloridai suteikia didžiausią jonizacijos potencijalo vertę (6,05 eV), kuri atispindi geriausiam OPV efektyvumė (18,5 %).
- Halogenidų funkcinių atomų dydis turi įtakos ITO paviršiaus padengimui. Didžiausi jodidų pakaitai lemia geriausią ITO padengimą, o tai lemia geriausią OLED efektyvumą.

2. Buvo susintetinti nekarbazoliniai dariniai, turintys fentiazino, fenoksazino, difenilamino, 5H-dibenzo[*b,f*]azepino ar 10,11-dihidro-5H-dibenzo[*b,f*]azepino chromoforus bei fosfonrūgšties grupes, ir jų tyrimas parodė, kad:

- Nesubstituotas indolas nėra tinkamas fosfonrūgšties grupę turinčių junginių sintezei. Esant hidrolizės sąlygomis indolo 3-H padėtis reaguoja susidarant neatsikiriamais šalutiniams produktams.
- Žemesnės junginių **58** ir **61** I_p vertės (atitinkamai 5.29 eV ir 5.44 eV) nėra palankios siekiant geriausio BHJ OPV efektyvumo, kadangi abu junginiai nusileido našumu HTM standartui PEDOT:PSS.
- Pastebėta koreliacija tarp PSC našumo ir SAM sudarančių junginių jonizacijos potencijalo. 2PACz ir susintetintų junginių **58** ir **61** efektyvumo gradientas (atitinkamai 19,5 % > 17,3 % > 16,0 %) gali būti tiesiogiai siejamas su mažėjančiomis jonizacijos potencijalo reikšmėmis (atitinkamai 5,6 eV > 5,44 eV > 5,29 eV), indikuojant geresnį suderinamumą su perovskitu esant didesnėms I_p reikšmėms.
- Palyginti su standartinėmis SAM sudarančiomis medžiagomis, difenilamino **64** pasižymėjo geriausiomis krūvininkų ištraukimo savybėmis, todėl jo našumas PSC buvo geresnis nei 2PACz. Difenilamino chromoforas gali būti

laikomas perspektyvia medžiaga tolimesniams efektyvių SAM sudarančių junginių kūrimui.

3. Buvo susintetintos skirtinges funkcines grupes turintys SAM sudarantys junginiai, o jų tyrimas parodė, kad:

- Tiofenai yra universalūs fragmentai, galintys suteikti SAM sudarančioms medžiagoms papildomų savybių, pavyzdžiu, sąveiką su skirtingais absorberiais, o tai turi teigiamos įtakos BHJ OPV ir PSC efektyvumui.
- Metoksigrupes turintys indolų dariniai negali būti naudojami fosfonatų hidrolizės reakcijoms, kadangi jų metu šie pakaitai elgiasi kaip paliekančioji grupė, sukurdami reaktingą vietą.
- Amonio grupių pridėjimas į SAM sudarančių junginių struktūrą yra perspektyvi monosluoksnio ant ITO formavimo strategija, norint kartu sluoksninių sandūroje pasyvuoti perovskitą. Karbazolas 94, turintis amonio bromido funkcines grupes, pasižymėjo geresniu efektyvumu bei rezultatu pasikartojamumu, palyginti su standartais 2PACz ir MeO-2PACz, todėl ši strategija yra ypač perspektyvi, siekiant pagerinti PSC fotovoltaicinės savybes.

4. Pasiūlytas inovatyvus sprendimas Me-4PACz monosluoksnio paviršiaus vilgymo problemoms spręsti. Paviršiaus hidrofilišumas gali būti smarkiai padidintas į SAM sudarančio junginio tirpalą pridėjus 1,6-heksilendifosfonrūgšties, todėl taip pagerinama dengiamo perovskito sluoksnio kokybė. Šis metodas yra universalus ir gali būti naudojamas su kitomis SAM sudarančiomis medžiagomis, kurios yra linkusios suformuoti prasto vilgymo monosluoksnius.

5. Pademonstruotas fosfonrūgšties universalumas modifikuojant metalų oksidus. SAM sudarantys junginiai, turintys fosfonrūgšties grupę, gali modifikuoti nanostruktūrinius ZnO tetrapodus, kurie buvo panaudoti konstruojant kambario temperatūroje veikiančius dujų jutiklius. Jų funkcionalizavimas karbazolo 73 SAM pagerino atsako į NO₂ dujas intensyvumą. Jutiklių atsaką galima dar labiau padidinti taikant UV moduliavimą.

REFERENCES

1. ZHANG, Q. et al. Recent Progress in Emerging Organic Semiconductors. *Advanced Materials* [interactive]. 2022, 34, 2108701. Access via: doi:10.1002/adma.202108701.
2. BRONSTEIN, H. et al. The role of chemical design in the performance of organic semiconductors. *Nature Reviews Chemistry* [interactive]. 2020, 4, 66–77. Access via: doi:10.1038/s41570-019-0152-9.
3. XU, X. et al. Organic and hybrid organic-inorganic flexible optoelectronics: Recent advances and perspectives. *Synthetic Metals* [interactive]. 2019, 256, 116137. Access via: doi:10.1016/j.synthmet.2019.116137.
4. MAGOMEDOV, A. et al. Self-Assembled Hole Transporting Monolayer for Highly Efficient Perovskite Solar Cells. *Advanced Energy Materials* [interactive]. 2018, 8, 1801892. Access via:doi:10.1002/aenm.201801892.
5. AL-ASHOURI, A. et al. Conformal monolayer contacts with lossless interfaces for perovskite single junction and monolithic tandem solar cells. *Energy Environ. Sci.* [interactive]. 2019, 12, 3356–3369. Access via: doi:10.1039/C9EE02268F.
6. ALMASABI, K. et al. Hole-Transporting Self-Assembled Monolayer Enables Efficient Single-Crystal Perovskite Solar Cells with Enhanced Stability. *ACS Energy Lett.* [interactive]. 2023, 8, 950–956. Access via: doi:10.1021/acsenergylett.2c02333.
7. JOŠT, M. et al. Perovskite/CIGS Tandem Solar Cells: From Certified 24.2% toward 30% and Beyond. *ACS Energy Lett.* [interactive]. 2022, 7, 1298–1307. Access via: doi:10.1021/acsenergylett.2c00274.
8. AL-ASHOURI, A. et al. Monolithic perovskite/silicon tandem solar cell with >29% efficiency by enhanced hole extraction. *Science* [interactive]. 2020, 370, 1300–1309. Access via: doi:10.1126/science.abd4016.
9. LAN, Z.-R. et al. Self-assembled monolayers as hole-transporting materials for inverted perovskite solar cells. *Mol. Syst. Des. Eng.* [interactive]. 2023, 8, 1440–1455. Access via: doi:10.1039/D3ME00144J.
10. ZHANG, H. and PARK, N.-G. Progress and issues in p-i-n type perovskite solar cells. *DeCarbon* [interactive]. 2024, 3, 100025. Access via: doi:10.1016/j.decarb.2023.100025.
11. WHITESIDES, G. M. and BONCHEVA, M. Beyond molecules: Self-assembly of mesoscopic and macroscopic components. *Perspective* [interactive]. 2002, 99, 4769–4774. Access via: doi:10.1073/pnas.082065899.
12. CASALINI, S. et al. Self-assembled monolayers in organic electronics. *Chem. Soc. Rev.* [interactive]. 2017, 46, 40–71. Access via: doi:10.1039/C6CS00509H.
13. DU, X. et al. Transparent In-Ga-Zn-O field effect glucose sensors fabricated directly on highly curved substrates. *Sensors and Actuators B: Chem.* [interactive]. 2018, 268, 123–128. Access via: doi:10.1016/j.snb.2018.04.087.

14. SMITH, R. K. et al. Patterning self-assembled monolayers. *Prog. Surf. Sci.* [interactive]. 2004, 75, 1–68. Access via: doi:10.1016/j.progsurf.2003.12.001.
15. HOTCHKISS, P. J. et al. The Modification of Indium Tin Oxide with Phosphonic Acids: Mechanism of Binding, Tuning of Surface Properties, and Potential for Use in Organic Electronic Applications. *Acc. Chem. Res.* [interactive]. 2012, 45, 337–346. Access via: doi:10.1021/ar200119g.
16. HASAN, A. and PANDEY, L. M. Self-assembled monolayers in biomaterials. *Nanobiomaterials* [interactive]. 2018, 137–178. Access via: doi:10.1016/B978-0-08-100716-7.00007-6.
17. RUDRA, J. S. et al. Self-Assembling Biomaterials. *Comprehensive Biomaterials* [interactive]. 2011, 2, 77–94. Access via: doi:10.1016/B978-0-12-803581-8.10210-3.
18. KIM, S. and YOO, H. Self-Assembled Monolayers: Versatile Uses in Electronic Devices from Gate Dielectrics, Dopants, and Biosensing Linkers. *Micromachines* [interactive]. 2021, 12, 565. Access via: doi:10.3390/mi12050565.
19. SCHREIBER, F. Structure and growth of self-assembling monolayers. *Progress in Surface Science* [interactive]. 2000, 65, 151–257. Access via: doi:10.1016/S0079-6816(00)00024-1.
20. SINGH, M. et al. The role of self-assembled monolayers in electronic devices. *J. Mater. Chem. C.* [interactive]. 2020, 8, 3938–3955. Access via: doi:10.1039/D0TC00388C.
21. ULMAN, A. Formation and Structure of Self-Assembled Monolayers. *Chem. Rev.* [interactive]. 1996, 96, 1533–1554. Access via: doi:10.1021/cr9502357.
22. PERKINS, C. L. Molecular Anchors for Self-Assembled Monolayers on ZnO: A Direct Comparison of the Thiol and Phosphonic Acid Moieties. *J. Phys. Chem. C.* [interactive]. 2009, 113, 18276–18286. Access via: doi:10.1021/jp906013r.
23. FRYXELL, G. E. et al. Design and synthesis of self-assembled monolayers on mesoporous supports (SAMMS): The importance of ligand posture in functional nanomaterials. *J. Mater. Chem.* [interactive]. 2007, 17, 2863–2874. Access via: doi:10.1039/B702422C.
24. PAJURI, S. P. et al. Covalent Surface Modification of Oxide Surfaces. *Angew. Chem. Int. Ed.* [interactive]. 2014, 53, 6322–6356. Access via: doi:10.1002/anie.201306709.
25. LESSEL, M. et al. Self-assembled silane monolayers: an efficient step-by-step recipe for high-quality, low energy surfaces. *Surface and Interface Analysis* [interactive]. 2015, 47, 557–564. Access via: doi:10.1002/sia.5729.
26. HELMY, R. et al. Reaction of Organosilicon Hydrides with Solid Surfaces: An Example of Surface-Catalyzed Self-Assembly. *J. Am. Chem. Soc.* [interactive]. 2004, 126, 7595–7600. Access via: doi:10.1021/ja0498336.
27. QUEFFLEC, C. et al. Surface modification using phosphonic acids and esters. *Chem. Rev.* [interactive]. 2012, 112, 3777–3807. Access via: doi:10.1021/cr2004212.

28. GIZA, M. et al. Adsorption Kinetics of Organo-Phosphonic Acids on Plasma-Modified Oxide-Covered Aluminum Surfaces. *Langmuir* [interactive]. 2008, 24, 8688–8694. Access via: doi:10.1021/la8000619.
29. BRODARD-SEVERAC, F. et al. High-Field ^{17}O MAS NMR Investigation of Phosphonic Acid Monolayers on Titania. *Chem. Mater.* [interactive]. 2008, 20, 5191–5196. Access via: doi:10.1021/cm8012683.
30. BREWSTER, T. P. et al. Hydroxamate Anchors for Improved Photoconversion in Dye-Sensitized Solar Cells. *Inorg. Chem.* [interactive]. 2013, 52, 6752–6764. Access via: doi:10.1021/ic4010856.
31. MARTINI, L. A. et al. Modular assembly of high-potential zinc porphyrin photosensitizers attached to TiO_2 with a series of anchoring groups *J. Phys. Chem. C.* [interactive]. 2013, 117, 14526–14533. Access via: doi:10.1021/jp4053456.
32. SILVERMAN, B. M., et al. Comparative properties of siloxane vs phosphonate monolayers on a key titanium alloy. *Langmuir* [interactive]. 2005, 21, 225–228. Access via: doi:10.1021/la0482271.
33. MCDERMOTT, J. E., et al. Organophosphonate self-assembled monolayers for gate dielectric surface modification of pentacene-based organic thin-film transistors: A comparative study. *J. Phys. Chem. A.* [interactive]. 2007, 111, 12333–12338. Access via: doi:10.1021/jp075177v.
34. SEVRAIN, C. M. et al. Phosphonic acid: preparation and applications. *Beilstein J. Org. Chem.* [interactive]. 2017, 13, 2186–2213. Access via: doi:10.3762/bjoc.13.219.
35. BARTON, D. H. R. and EMBSE, R. A. V. The invention of radical reactions. Part 39. The reaction of white phosphorus with carbon-centered radicals. An improved procedure for the synthesis of phosphonic acids and further mechanistic insights. *Tetrahedron* [interactive]. 1998, 54, 12475–12496. Access via: doi:10.1016/S0040-4020(98)00729-7.
36. ALBOUY, D. et al. Phosphorylating Power of Red Phosphorus towards Aldehydes in Basic and in Acidic Media. *Eur. J. Org. Chem.* [interactive]. 1999, 861–868. Access via: doi:10.1002/(SICI)1099-0690(199904)1999:4<861::AID-EJOC861>3.0.CO;2-J.
37. PEREZ, O. et al. Topochemical Route from Supramolecular to Hybrid Materials: Tetraphenylmethane-Based Tectons and Lanthanum Phosphonate Derivative. *Cryst. Growth Des.* [interactive]. 2016, 16, 6781–6789. Access via: doi:10.1021/acs.cgd.6b00823.
38. SÁNCHEZ-MORENO, M. J. et al. Synthesis and acid-base properties of (1H -benzimidazol-2-yl-methyl)phosphonate (Bimp^{2-}). Evidence for intramolecular hydrogen-bond formation in aqueous solution between ($\text{N-1}\text{H}$) and the phosphonate group. *Org. Biomol. Chem.* [interactive]. 2003, 1, 1819–1826. Access via: doi:10.1039/B301281F.
39. ASH, J. et al. Selective hydrolysis of phosphorus(v) compounds to form organophosphorus monoacids. *Org. Biomol. Chem.* [interactive]. 2021, 19, 6007–6014. Access via: doi:10.1039/D1OB00881A.

40. TVERDOMED, S. N. et al. Aromatization of 1,4-cyclohexadienes with tetracyanoethylene: a case of varying mechanism. *Tetrahedron* [interactive]. 2011, 67, 3887–3903. Access via: doi:10.1021/jo00249a020.
41. MICHAELIS, A. and KAEHNE, R. Ueber das Verhalten der Jodalkyle gegen die sogen. Phosphorigsäureester oder O -Phosphine. *Berichte* [interactive]. 1898, 31, 1048–1055. Access via: doi:10.1002/cber.189803101190.
42. ARBUZOV, B. A. Michaelis–Arbusow- und Perkow-Reaktionen. *Pure Appl. Chem.* [interactive]. 1964, 9, 307–353. Access via: doi:10.1351/pac196409020307.
43. DEMMER, C. S. et al. Review on Modern Advances of Chemical Methods for the Introduction of a Phosphonic Acid Group. *Chem. Rev.* [interactive]. 2011, III, 7981–8006. Access via: doi:10.1021/cr2002646.
44. CAURET, L. et al. An efficient protocol for the synthesis of 2-chloroethylphosphonic acid. *Synth. Commun.* [interactive]. 1997, 27, 647–653. Access via: doi:10.1080/00397919708003338.
45. COLLE, K. S. and LEWIS, E. S. Methoxyphosphonium ions: Intermediates in the Arbuzov reaction. *J. Org. Chem.* [interactive]. 1978, 4, 571–574. Access via: doi:10.1021/jo00398a010.
46. MANSFELD, D. et al. Arylphosphonic acid esters as bridging ligands in coordination polymers of bismuth. *Main Group Metal Chemistry* [interactive]. 2013, 36. Access via: doi:10.1515/mgmc-2013-0047.
47. CHAKHMOURADIAN, A. R. et al. Celebrating 175 Years of Perovskite Research: A Tribute to Roger H. Mitchell. *Phys. Chem. Miner.* [interactive]. 2014, 41, 387–391. Access via: doi:10.1007/s00269-014-0678-9.
48. JENA, A. K. et al. Halide Perovskite Photovoltaics: Background, Status, and Future Prospects. *Chemical Reviews* [interactive]. 2019, 119, 3036–3103.
49. GIOVANNI, D. *Optical-spin dynamics in organic-inorganic lead halide perovskites* [interactive]. Access via: doi:10.13140/RG.2.2.35356.59523.
50. BRENNER, T. M. et al. Hybrid Organic–inorganic Perovskites: Low-cost Semiconductors with Intriguing Charge-transport Properties. *Nature Reviews Materials* [interactive]. 2016, 1, 15007. Access via: doi:10.1038/natrevmat.2015.7.
51. YUAN, Y. et al. Arising Applications of Ferroelectric Materials in Photovoltaic Devices. *Journal of Materials Chemistry A* [interactive]. 2014, 2, 6027–6041. Access via: doi:10.1039/C3TA14188H.
52. GHOLIPOUR, S. et al. From Exceptional Properties to Stability Challenges of Perovskite Solar Cells. *Small* [interactive]. 2018, 14, 1802385. Access via: doi:10.1002/smll.201802385.
53. WEBER, D. $\text{CH}_3\text{NH}_3\text{PbX}_3$, ein Pb (II)-system mit kubischer perowskitstruktur/ $\text{CH}_3\text{NH}_3\text{PbX}_3$, a Pb (II)-system with cubic perovskite structure, *Z. Naturforsch* [interactive]. B. 1978, 33, 443–1445. Access via: doi:10.1515/znb-1978-1214.

54. KHORASANI, A. et al. Opportunities, Challenges, and Strategies for Scalable Deposition of Metal Halide Perovskite Solar Cells and Modules. *Advanced Energy and Sustainability Research* [interactive]. 2024, 5, 2470017. Access via: doi:10.1002/aesr.202470017.
55. CHANG, W.-C. et al. Controlled Deposition and Performance Optimization of Perovskite Solar Cells Using Ultrasonic Spray-Coating of Photoactive Layers. *ChemSusChem* [interactive]. 2017, 10, 1405–1412. Access via: doi:10.1002/cssc.201601711.
56. LUO, P. et al. simple in situ tubular chemical vapor deposition processing of large-scale efficient perovskite solar cells and the research on their novel roll-over phenomenon in J-V curves. *Journal of Materials Chemistry A* [interactive]. 2015, 3, 12443–12451. Access via: doi:10.1039/C5TA02306H.
57. WEI, Z. et al. Inkjet printing and instant chemical transformation of a $\text{CH}_3\text{NH}_3\text{PbI}_3$ /nanocarbon electrode and interface for planar perovskite solar cells. *Angewandte Chemie International Edition* [interactive]. 2014, 53, 13239–13243. Access via: doi:10.1002/anie.201408638.
58. ROß, M. et al. Co-evaporated formamidinium lead iodide based perovskites with 1000 h constant stability for fully textured monolithic perovskite/silicon tandem solar cells. *Adv. Energy Mater.* [interactive]. 2021, 11, 2101460. Access via: doi:10.1002/aenm.202101460.
59. WU, W.-Q. et al. Bilateral alkylamine for suppressing charge recombination and improving stability in blade-coated perovskite solar cells. *Sci. Adv.* [interactive]. 2019, 5. Access via: doi:10.1126/sciadv.aav8925. Access via: doi:10.1126/sciadv.aav8925.
60. SUBBIAH, A. S. et al. High-performance perovskite single-junction and textured perovskite/silicon tandem solar cells via slot-die-coating. *ACS Energy Lett.* [interactive]. 2020, 5, 3034–3040. Access via: doi:10.1021/acsenergylett.0c01297.
61. IM, J.-H. et al. Morphology-photovoltaic property correlation in perovskite solar cells: One-step versus two-step deposition of $\text{CH}_3\text{NH}_3\text{PbI}_3$. *APL Mater.* [interactive]. 2014, 2, 081510. Access via: doi:10.1063/1.4891275.
62. BAE, S.-R. et al. Recent progress of perovskite devices fabricated using thermal evaporation method: Perspective and outlook. *Mater. Today Adv.* [interactive]. 2022, 14, 100232. Access via: doi:10.1016/j.mtadv.2022.100232.
63. XU, C. et al. Self-woven monolayer polyionic mesh to achieve highly efficient and stable inverted perovskite solar cells. *Chem. Eng. J.* [interactive]. 2022, 428, 132074. Access via: doi:10.1016/j.cej.2021.132074.
64. BECKER, M. and WARK, M. Recent progress in the solution-based sequential deposition of planar perovskite solar cells. *Cryst. Growth Des.* [interactive]. 2018, 18, 4790–4806. Access via: doi:10.1021/acs.cgd.8b00686.
65. KAJAL, P. et al. Manufacturing techniques of perovskite solar cells. *Applications of Solar Energy* [interactive]. 2018, 1, 341–364. Access via: doi:10.1007/978-981-10-7206-2_16.

66. RAZZA, S. et al. Research update: Large-area deposition, coating, printing, and processing techniques for the upscaling of perovskite solar cell technology. *APL Mater.* [interactive]. 2016, 4, 091508. Access via: doi:10.1063/1.4962478.
67. SHEN, P.-S. et al. Research update: Hybrid organic-inorganic perovskite (HOIP) thin films and solar cells by vapor phase reaction. *APL Mater.* [interactive]. 2016, 4, 091509. Access via: doi:10.1063/1.4962142.
68. YIN, W.-J. et al. Unusual defect physics in $\text{CH}_3\text{NH}_3\text{PbI}_3$ perovskite solar cell absorber. *Appl. Phys. Lett.* [interactive]. 2024, 104, 063903. Access via: doi:10.1063/1.4864778.
69. STRANKS, S. D. et al. Electron-hole diffusion lengths exceeding 1 micrometer in an organometal trihalide perovskite absorber. *Science* [interactive]. 2013, 342, 341–344. Access via: doi:10.1126/science.1243982.
70. PONSECA JR, C. S., et al. Organometal halide perovskite solar cell materials rationalized: ultrafast charge generation, high and microsecond-long balanced mobilities, and slow recombination. *J. Am. Chem. Soc.* [interactive]. 2014, 136, 5189–5192. Access via: doi:10.1021/ja412583t.
71. LIU, Y. et al. Two-Inch-Sized Perovskite $\text{CH}_3\text{NH}_3\text{PbX}_3$ ($\text{X} = \text{Cl}, \text{Br}, \text{I}$) Crystals: Growth and Characterization. *Advanced Materials* [interactive]. 2015, 27, 5176–5183. Access via: doi:10.1002/adma.201502597.
72. BAIKIE, T. et al. Synthesis and crystal chemistry of the hybrid perovskite $(\text{CH}_3\text{NH}_3)\text{PbI}_3$ for solid-state sensitised solar cell applications. *Journal of Materials Chemistry A*. [interactive]. 2013, 1, 5628–5641. Access via: doi:10.1039/C3TA10518K.
73. D'INNOCENZO, V. et al. Excitons versus free charges in organo-lead trihalide perovskites. *Nature Communications* [interactive]. 2014, 5, 3586. Access via: doi:10.1038/ncomms4586.
74. POINDEXTER, J. R. et al. High Tolerance to Iron Contamination in Lead Halide Perovskite Solar Cells. *ACS Nano* [interactive]. 2017, 11, 7101–7109. Access via: doi:10.1021/acsnano.7b02734.
75. KOJIMA, A. et al. Organometal halide perovskites as visible-light sensitizers for photovoltaic cells. *J. Am. Chem. Soc.* [interactive]. 2009, 131, 6050–6051. Access via: doi:10.1021/ja809598r.
76. CHUNG, I. et al. All-solid-state dye-sensitized solar cells with high efficiency. *Nature* [interactive]. 2012, 485, 486–489. Access via: doi:10.1038/nature11067.
77. YOO, S.-M. et al. Nanoscale Perovskite-Sensitized Solar Cell Revisited: Dye-Cell or Perovskite-Cell? *ChemSusChem* [interactive]. 2020, 13, 2571–2576. Access via: doi:10.1002/cssc.202000223.
78. KIM, H.-S. et al. Lead iodide perovskite sensitized all-solid-state submicron thin film mesoscopic solar cell with efficiency exceeding 9%. *Scientific Reports* [interactive]. 2012, 2, 591. Access via: doi:10.1038/srep00591.
79. GRÄTZEL, M. The light and shade of perovskite solar cells. *Nature Materials* [interactive]. 2014, 13, 838–842. Access via: doi:10.1038/nmat4065.

80. HEO, J. H. et al. Efficient inorganic-organic hybrid heterojunction solar cells containing perovskite compound and polymeric hole conductors. *Nature Photonics* [interactive]. 2013, 7, 487–492. Access via: doi:10.1038/nphoton.2013.80.
81. GRÄTZEL, C. et al. Recent trends in mesoscopic solar cells based on molecular and nanopigment light harvesters. *Materials Today* [interactive]. 2013, 16, 11–18. Access via: doi:10.1016/j.mattod.2013.01.020.
82. LIU, M. et al. Efficient planar heterojunction perovskite solar cells by vapour deposition. *Nature* [interactive]. 2013, 501, 395–398. Access via: doi:10.1038/nature12509.
83. MALINKIEWICZ, O. et al. Perovskite solar cells employing organic planar-heterojunction hybrid solar cells. *Nature Photonics* [interactive]. 2014, 8, 128–132. Access via: doi:10.1038/nphoton.2013.341.
84. LIU, S. et al. Recent progress in the development of high-efficiency inverted perovskite solar cells. *NPG Asia Materials* [interactive]. 2023, 15, 27. Access via: doi:10.1038/s41427-023-00474-z.
85. LEE, M. M. et al. Efficient hybrid solar cells based on meso-superstructured organometal halide perovskites. *Science* [interactive]. 2012, 338, 643–647. Access via: doi:10.1126/science.1228604.
86. KIM, M. et al. Enhanced electrical properties of Li-salts doped mesoporous TiO₂ in perovskite solar cells. *Joule* [interactive]. 2021, 5, 659–672. Access via: doi:10.1016/j.joule.2021.02.007.
87. JIANG, Q. et al. Planar-Structure Perovskite Solar Cells with Efficiency beyond 21%. *Advanced Materials* [interactive]. 2017, 29, 1703852. Access via: doi:10.1002/adma.201703852.
88. JIANG, Q. et al. Enhanced electron extraction using SnO₂ for high-efficiency planar-structure HC(NH₂)₂PbI₃-based perovskite solar cells. *Nat. Energy* [interactive]. 2017, 2, 16177. Access via: doi:10.1038/nenergy.2016.177.
89. CAO, Z. et al. Metal oxide alternatives for efficient electron transport in perovskite solar cells: beyond TiO₂ and SnO₂. *J. Mater. Chem. A* [interactive]. 2020, 8, 19768–19787. Access via: doi:10.1039/D0TA07282F.
90. CHEN, Y. et al. Self-elimination of intrinsic defects improves the low-temperature performance of perovskite photovoltaics. *Joule* [interactive]. 2020, 4, 1961–1976. Access via: doi:10.1016/j.joule.2020.07.006.
91. JIANG, Q. et al. Surface passivation of perovskite film for efficient solar cells. *Nat. Photonics* [interactive]. 2019, 13, 460–466. Access via: doi:10.1038/s41566-019-0398-2.
92. BU, T. et al. Universal passivation strategy to slot-die printed SnO₂ for hysteresis-free efficient flexible perovskite solar module. *Nat. Commun* [interactive]. 2018, 9, 1–10. Access via: doi:10.1038/s41467-018-07099-9.
93. JEONG, M. et al. Large-area perovskite solar cells employing spiro-Naph hole transport material. *Nat. Photonics* [interactive]. 2022, 16, 119–125. Access via: doi:10.1038/s41566-021-00931-7.

94. REN, G. et al. Strategies of modifying spiro-OMeTAD materials for perovskite solar cells: a review. *J. Mater. Chem. A.* [interactive]. 2021, *9*, 4589–4625. Access via: doi:10.1039/D0TA11564A.
95. ROMBACH, F. M. et al. Lessons learned from spiro-OMeTAD and PTAA in perovskite solar cells. *Energy Environ. Sci.* [interactive]. 2021, *14*, 5161–5190. Access via: doi:10.1039/D1EE02095A.
96. CHEN, H. et al. Quantum-size-tuned heterostructures enable efficient and stable inverted perovskite solar cells. *Nat. Photonics.* [interactive]. 2022, *16*, 352–358. Access via: doi:10.1038/s41566-022-00985-1.
97. LI, Z. et al. Organometallic-functionalized interfaces for highly efficient inverted perovskite solar cells. *Science* [interactive]. 2022, *376*, 416–420. Access via: doi:10.1126/science.abm8566.
98. JIANG, Q. et al. Surface reaction for efficient and stable inverted perovskite solar cells. *Nature* [interactive]. 2022, *611*, 278–283. Access via: doi:10.1038/s41586-022-05268-x.
99. AZMI, R. et al. Damp heat-stable perovskite solar cells with tailored-dimensionality 2D/3D heterojunctions. *Science* [interactive]. 2022, *376*, 73–77. Access via: doi:10.1126/science.abm5784.
100. LIN, R. et al. All-perovskite tandem solar cells with improved grain surface passivation. *Nature* [interactive]. 2022, *603*, 73–78. Access via: doi:10.1038/s41586-021-04372-8.
101. DONG, H. et al. Improving Electron Extraction Ability and Device Stability of Perovskite Solar Cells Using a Compatible PCBM/AZO Electron Transporting Bilayer. *Nanomaterials* [interactive]. 2018, *8*, 720. Access via: doi:10.3390/nano8090720.
102. PANG, S. et al. Efficient Bifacial Semitransparent Perovskite Solar Cells Using Ag/V₂O₅ as Transparent Anodes. *ACS Applied Materials and Interfaces* [interactive]. 2018, *10*, 12731–12739. Access via: doi:10.1021/acsami.8b01611.
103. KAYSER, L. V. and LIPOMI, D. J. Stretchable conductive polymers and composites based on PEDOT and PEDOT:PSS. *Adv. Mater.* [interactive]. 2019, *31*, 1806133. Access via: doi:10.1002/adma.201806133.
104. JENG, J.-Y. et al. CH₃NH₃PbI₃ perovskite/fullerene planar-heterojunction hybrid solar cells. *Advanced Materials* [interactive]. 2013, *25*, 3727–3732. Access via: doi:10.1002/adma.201301327.
105. YOU, J. et al. Low-temperature solution-processed perovskite solar cells with high efficiency and flexibility. *ACS Nano* [interactive]. 2014, *8*, 1674–1680. Access via: doi:10.1021/nn406020d.
106. YANG, X. et al. Perovskite hetero-bilayer for efficient charge-transport-layer-free solar cells. *Joule* [interactive]. 2022, *6*, 1277–1289. Access via: doi:10.1016/j.joule.2022.04.012.
107. KIM, Y. et al. Sequentially fluorinated PTAA polymers for enhancing Voc of high-performance perovskite solar cells. *Adv. Energy Mater.* [interactive]. 2018, *8*, 1801668. Access via: doi:10.1002/aenm.201801668.

108. STOLTERFOHT, M. et al. Visualization and suppression of interfacial recombination for high-efficiency large-area pin perovskite solar cells. *Nat. Energy* [interactive]. 2018, 3, 847–854. Access via: doi:10.1038/s41560-018-0219-8.
109. LUO, D. et al. Enhanced photovoltage for inverted planar heterojunction perovskite solar cells. *Science* [interactive]. 2018, 360, 1442–1446. Access via: doi:10.1126/science.aap9282.
110. YANG, S. et al. Tailoring Passivation Molecular Structures for Extremely Small Open-Circuit Voltage Loss in Perovskite Solar Cells. *J. Am. Chem. Soc.* [interactive]. 2019, 141, 5781–5787. Access via: doi:10.1021/jacs.8b13091.
111. ALMASABI, K. et al. Hole-Transporting Self-Assembled Monolayer Enables Efficient Single-Crystal Perovskite Solar Cells with Enhanced Stability. *ACS Energy Lett.* [interactive]. 2023, 8, 950–956. Access via: doi:10.1021/acsenergylett.2c02333.
112. SINGH, S. et al. Impact of Buried Interface Texture on Compositional Stratification and Ion Migration in Perovskite Solar Cells. *Advanced Functional Materials* [interactive]. 2024, 34, 2402655. Access via: doi:10.1002/adfm.202402655.
113. NI, Z. et al. Evolution of defects during the degradation of metal halide perovskite solar cells under reverse bias and illumination. *Nat. Energy* [interactive]. 2022, 7, 65–73. Access via: doi:10.1038/s41560-021-00949-9.
114. NI, Z. et al. Resolving spatial and energetic distributions of trap states in metal halide perovskite solar cells. *Science* [interactive]. 2020, 367, 1352–1358. Access via: doi:10.1126/science.aba0893.
115. CHEN, H. et al. Regulating surface potential maximizes voltage in all-perovskite tandems. *Nature* [interactive]. 2023, 613, 676–681. Access via: doi:10.1038/s41586-022-05541-z.
116. METCALF, I. et al. Synergy of 3D and 2D Perovskites for Durable, Efficient Solar Cells and Beyond. *Chem. Rev.* [interactive]. 2023, 123, 9565–9652. Access via: doi:10.1021/acs.chemrev.3c00214.
117. TAN, S. et al. Stability-limiting heterointerfaces of perovskite photovoltaics. *Nature* [interactive]. 2022, 605, 268–273. Access via: doi:10.1038/s41586-022-04604-5.
118. AZMI, R. et al. Double-side 2D/3D heterojunctions for inverted perovskite solar cells. *Nature* [interactive]. 2024, 628, 93–98. Access via: doi:10.1038/s41586-024-07189-3.
119. CHIN, X. Y. et al. Interface passivation for 31.25%-efficient perovskite/silicon tandem solar cells. *Science* [interactive]. 2023, 381, 59–63. Access via: doi:10.1126/science.adg0091.
120. ULLAH, A. Versatile Hole Selective Molecules Containing a Series of Heteroatoms as Self-Assembled Monolayers for Efficient p-i-n Perovskite and Organic Solar Cells. *Advanced Functional Materials* [interactive]. 2022, 32, 2208793. Access via: doi:10.1002/adfm.202208793.

121. ZHANG, S. et al. Minimizing buried interfacial defects for efficient inverted perovskite solar cells. *Science* [interactive]. 2023, *380*, 404–409. Access via: doi:10.1126/science.adg3755.
122. GUO, R. Tailoring Multifunctional Self-Assembled Hole Transporting Molecules for Highly Efficient and Stable Inverted Perovskite Solar Cells. *Advanced Functional Materials* [interactive]. 2023, *33*, 2211955. Access via: doi:10.1002/adfm.202211955.
123. TRUONG, M. A. et al. Tripodal Triazatruxene Derivative as a Face-On Oriented Hole-Collecting Monolayer for Efficient and Stable Inverted Perovskite Solar Cells. *J. Am. Chem. Soc.* [interactive]. 2023, *145*, 7528–7539. Access via: doi:10.1021/jacs.3c00805.
124. ACKERMANN, J. et al. Growth of organic semiconductors for hybrid solar cell application. *Thin Solid Films* [interactive]. 2002, *403-404*, 157–161. Access via: doi:10.1016/S0040-6090(01)01578-4.
125. KAMEL, M. S. A. et al. Inorganic nanoparticles to overcome efficiency inhibitors of organic photovoltaics: An in-depth review. *Renewable Sustainable Energy Rev.* [interactive]. 2022, *166*, 112661. Access via: doi:10.1016/j.rser.2022.112661.
126. MAILOA, J. P. A 2-terminal perovskite/silicon multijunction solar cell enabled by a silicon tunnel junction. *Appl. Phys. Lett.* [interactive]. 2015, *106*, 121105. Access via: doi:10.1063/1.4914179.
127. HALOUI, H. et al. Modeling of a hybrid thermal photovoltaic (PVT) collector based on thin film organic solar cells. *Electr. Power Syst. Res.* [interactive]. 2022, *210*, 108131. Access via: doi:10.1016/j.epsr.2022.108131.
128. KIM, Y. K. et al. Hetero-tandem organic solar cells drive water electrolysis with a solar-to-hydrogen conversion efficiency up to 10. *Appl. Catal. B: Environmental* [interactive]. 2022, *309*, 121237. Access via: doi:10.1016/j.apcatb.2022.121237.
129. MOORTHY, V. M. and SRIVASTAVA, V. M. Device Modeling of Organic Photovoltaic Cells with Traditional and Inverted Cells Using s-SWCNT:C₆₀ as Active Layer. *Nanomaterials* [interactive]. 2022, *12*, 2844. Access via: doi:10.3390/nano12162844.
130. MARKS, R. N. et al. The photovoltaic response in poly(p-phenylene vinylene) thin-film devices. *J. Phys. Condens. Matter.* [interactive]. 1994, *6*, 1379–1394. Access via: doi:10.1088/0953-8984/6/7/009.
131. SOLAK, E. K. and IRMAK, E. Advances in organic photovoltaic cells: a comprehensive review of materials, technologies, and performance. *RSC Advances* [interactive]. 2023, *13*, 12244–12269. Access via: doi:10.1039/D3RA01454A.
132. TANG, C. W. Two-layer organic photovoltaic cell. *Appl. Phys. Lett.* [interactive]. 1986, *48*, 183–185. Access via: doi:10.1063/1.96937.
133. KNUPFER, M. Exciton binding energies in organic semiconductors. *Appl. Phys. A.* [interactive]. 2003, *77*, 623–626. Access via: doi:10.1007/s00339-003-2182-9.

134. YU, G. et al. J. Polymer photovoltaic cells: Enhanced efficiencies via a network of internal donor-acceptor heterojunctions. *Science* [interactive]. 1995, 270, 1789–1791. Access via: doi:10.1126/science.270.5243.1789.
135. LIU, Q. et al. 18% Efficiency organic solar cells. *Sci. Bull.* [interactive]. 2020, 65, 272–275. Access via: doi:10.1016/j.scib.2020.01.001.
136. LIN, Y. et al. Self-assembled monolayer enables hole transport layer-free organic solar cells with 18% efficiency and improved operational stability. *ACS Energy Lett.* [interactive]. 2020, 5, 2935–2944. Access via: doi:10.1021/acsenergylett.0c01421.
137. LIN, Y. et al. A simple n-dopant derived from diquat boosts the efficiency of organic solar cells to 18.3%. *ACS Energy Lett.* [interactive]. 2020, 5, 3663–3671. Access via: doi:10.1021/acsenergylett.0c01949.
138. LI, Y. et al. Recent Progress in Organic Solar Cells: A Review on Materials from Acceptor to Donor. *Molecules* [interactive]. 2022, 27, 1800. Access via: doi:10.3390/molecules27061800.
139. SHAHEEN, S. E. et al. 2.5% efficient organic plastic solar cells. *Appl. Phys. Lett.* [interactive]. 2001, 78, 841–843. Access via: doi:10.1063/1.1345834.
140. PADINGER, F. et al. Effects of postproduction treatment on plastic solar cells. *Adv. Funct. Mater.* [interactive]. 2003, 13, 85–88. Access via: doi:10.1002/adfm.200390011.
141. LI, G. et al. High-efficiency solution processable polymer photovoltaic cells by self-organization of polymer blends. *Nat. Mater.* [interactive]. 2005, 4, 864–868. Access via: doi:10.1038/nmat1500.
142. MA, W. et al. Thermally stable, efficient polymer solar cells with nanoscale control of the interpenetrating network morphology. *Adv. Funct. Mater.* [interactive]. 2005, 15, 1617–1622. Access via: doi:10.1002/adfm.200500211.
143. WIENK, M. M. et al. Efficient methano[70]fullerene/MDMO-PPV bulk heterojunction photovoltaic cells. *Angew. Chem. Int. Ed. Engl.* [interactive]. 2003, 42, 3371–3375. Access via: doi:10.1002/anie.200351647.
144. TROSHIN, P. A. et al. Material solubility-photovoltaic performance relationship in the design of novel fullerene derivatives for bulk heterojunction solar cells. *Adv. Funct. Mater.* [interactive]. 2009, 19, 779–788. Access via: doi:10.1002/adfm.200801189.
145. LIANG, Y. et al. For the bright future-bulk heterojunction polymer solar cells with power conversion efficiency of 7.4%. *Adv. Mater.* [interactive]. 2010, 22, E135–E138. Access via: doi:10.1002/adma.200903528.
146. LIU, Y. et al. Aggregation and morphology control enables multiple cases of high-efficiency polymer solar cells. *Nat. Commun.* [interactive]. 2014, 5, 5293. Access via: doi:10.1038/ncomms6293.
147. DEY, S. Recent progress in molecular design of fused ring electron acceptors for organic solar cells. *Small* [interactive]. 2019, 15, 1900134. Access via: doi:10.1002/smll.201900134.

148. ZHANG, G. et al. Nonfullerene acceptor molecules for bulk heterojunction organic solar cells. *Chem. Rev.* [interactive]. 2018, 118, 3447–3507. Access via: doi:10.1021/acs.chemrev.7b00535.
149. LIN, Y. et al. An electron acceptor challenging fullerenes for efficient polymer solar cells. *Adv. Mater.* [interactive]. 2015, 27, 1170–1174. Access via: doi:10.1002/adma.201404317.
150. ZHAO, W. et al. Fullerene-free polymer solar cells with over 11% efficiency and excellent thermal stability. *Adv. Mater.* [interactive]. 2016, 28, 4734–4739. Access via: doi:10.1002/adma.201600281.
151. XU, X. et al. Realizing over 13% efficiency in green-solvent-processed nonfullerene organic solar cells enabled by 1,3,4-thiadiazole-based wide-bandgap copolymers. *Adv. Mater.* [interactive]. 2018, 30, 1703973. Access via: doi:10.1002/adma.201703973.
152. TRAN, H. N. et al. 17% Non-fullerene organic solar cells with annealing-free aqueous MoO_x. *Adv. Sci.* [interactive]. 2020, 7, 2002395. Access via: doi:10.1002/advs.202002395.
153. CUI, Y. et al. Single-junction organic photovoltaic cells with approaching 18% efficiency. *Adv. Mater.* [interactive]. 2020, 32, 1908205. Access via: doi:10.1002/adma.201908205.
154. SONG, J. et al. High-efficiency organic solar cells with low voltage loss induced by solvent additive strategy. *Matter.* [interactive]. 2021, 4, 2542–2552. Access via: doi:10.1016/j.matt.2021.06.010.
155. HOU, W. et al. The applications of polymers in solar cells: A review. *Polymers* [interactive]. 2019, 11, 143. Access via: doi:10.3390/polym11010143.
156. ZHAO, G. et al. 6.5% efficiency of polymer solar cells based on poly(3-hexylthiophene) and indene-C₆₀ bisadduct by device optimization. *Adv. Mater.* [interactive]. 2010, 22, 4355–4358. Access via: doi:10.1002/adma.201001339.
157. TAN, Z. et al. High performance polymer solar cells with as-prepared zirconium acetylacetone film as cathode buffer layer. *Sci. Rep.* [interactive]. 2014, 4, 4691. Access via: doi:10.1038/srep04691.
158. YUAN, J. et al. Single-junction organic solar cell with over 15% efficiency using fused-ring acceptor with electron-deficient core. *Joule* [interactive]. 2019, 3, 1140–1151. Access via: doi:10.1016/j.joule.2019.01.004.
159. BIN, H. et al. Finetuning Hole-Extracting Monolayers for Efficient Organic Solar Cells. *ACS App. Mater. Interfaces* [interactive]. 2022, 14, 16497–16504. Access via: doi:10.1021/acsami.2c01900.
160. YAO, J. et al. Cathode Engineering with Perylene-Diimide Interlayer Enabling over 17% Efficiency Single-Junction Organic Solar Cells. *Nat. Commun.* [interactive]. 2020, 11, 2726. Access via: doi:10.1038/s41467-020-16509-w.
161. SORRENTINO, R. et al. Interlayers for Non-Fullerene Based Polymer Solar Cells: Distinctive Features and Challenges. *Energy Environ. Sci.* [interactive]. 2021, 14, 180–223. Access via: doi:10.1039/D0EE02503H.

162. KANG, Q. et al. n-Doped Inorganic Molecular Clusters as a New Type of Hole Transport Material for Efficient Organic Solar Cells. *Joule* [interactive]. 2021, 5, 646–658. Access via: doi:10.1016/j.joule.2021.01.011.
163. ALHUMMIANY, H. et al. XPS Analysis of the Improved Operational Stability of Organic Solar Cells Using a V₂O₅ and PEDOT:PSS Composite Layer: Effect of Varied Atmospheric Conditions. *J. Phys. Chem. C* [interactive]. 2017, 121, 7649–7658. Access via: doi:10.1021/acs.jpcc.6b13016.
164. SMALL, C. E. et al. High-efficiency inverted dithienogermole-thienopyrrolodione-based polymer solar cells. *Nat. Photonics* [interactive]. 2012, 6, 115–120. Access via: doi:10.1038/nphoton.2011.317.
165. TAN, W.-Y. et al. Lending Triarylphosphine Oxide to Phenanthroline: a Facile Approach to High-Performance Organic Small-Molecule Cathode Interfacial Material for Organic Photovoltaics utilizing Air-Stable Cathodes. *Adv. Funct. Mater.* [interactive]. 2014, 24, 6540–6547. Access via: doi:10.1002/adfm.201401685.
166. SEITKHAN, A. et al. Use of the Phen-NaDPO: Sn (SCN)₂ Blend as Electron Transport Layer Results to Consistent Efficiency Improvements in Organic and Hybrid Perovskite Solar Cells. *Adv. Funct. Mater.* [interactive]. 2019, 29, 1905810. Access via: doi:10.1002/adfm.201905810.
167. HUANG, F. et al. Novel electroluminescent conjugated polyelectrolytes based on polyfluorene. *Chem. Mater.* [interactive]. 2004, 16, 708–716. Access via: doi:10.1021/cm034650o.
168. ZHANG, L. et al. “N-π-N” Type Oligomeric Acceptor Achieves an OPV Efficiency of 18.19% with Low Energy Loss and Excellent Stability. *Advanced Science* [interactive]. 2022, 9, 2202513. Access via: doi:10.1002/advs.202202513.
169. ZHANG, Z.-G. et al. Perylene diimides: a thickness-insensitive cathode interlayer for high performance polymer solar cells. *Energy Environ. Sci.* [interactive]. 2014, 7, 1966–1973. Access via: doi:10.1039/C4EE00022F.
170. XU, H. et al. Hole transport layers for organic solar cells: recent progress and prospects. *Journal Mater. Chem. A* [interactive]. 2020, 8, 11478–11492. Access via: doi:10.1039/D0TA03511D.
171. TAN, J.-K. et al. Ohmic transition at contacts key to maximizing fill factor and performance of organic solar cells. *Nat. Commun.* [interactive]. 2018, 9, 3269. Access via: doi:10.1038/s41467-018-05200-w.
172. LI, G. et al. High-efficiency solution processable polymer photovoltaic cells by self-organization of polymer blends. *Nat. Mater.* [interactive]. 2005, 4, 864–868. Access via: doi:10.1038/nmat1500.
173. SHI, S. et al. Simple Solvent Treatment Enabled Improved PEDOT:PSS Performance toward Highly Efficient Binary Organic Solar Cells. *CS Omega* [interactive]. 2022, 7, 41789–41795. Access via: doi:10.1021/acsomega.2c06181.
174. WIJEYASINGHE, N. et al. Copper(I) Thiocyanate (CuSCN) Hole-Transport Layers Processed from Aqueous Precursor Solutions and Their Application in

- Thin-Film Transistors and Highly Efficient Organic and Organometal Halide Perovskite Solar Cells. *Adv. Funct. Mater.* [interactive]. 2017, 27, 1701818. Access via: doi:10.1002/adfm.201701818.
175. DE JONG, M. P. et al. Stability of the interface between indium-tin-oxide and poly(3,4-ethylenedioxythiophene)/poly(styrenesulfonate) in polymer light-emitting diodes. *Appl. Phys. Lett.* [interactive]. 2000, 77, 2255–2257. Access via: doi:10.1063/1.1315344.
176. LIU, J. et al. Enhancement of inverted polymer solar cells with solution-processed ZnO-TiOX composite as cathode buffer layer. *Appl. Phys. Lett.* [interactive]. 2012, 100, 213906. Access via: doi:10.1063/1.4722800.
177. ECKER, B. et al. Degradation Effects Related to the Hole Transport Layer in Organic Solar Cells. *Adv. Funct. Mater.* [interactive]. 2011, 21, 2705–2711. Access via: doi:10.1002/adfm.201100429.
178. KIM, J. S. et al. Control of the electrode work function and active layer morphology via surface modification of indium tin oxide for high efficiency organic photovoltaics. *Appl. Phys. Lett.* [interactive]. 2007, 91, 112111. Access via: doi:10.1063/1.2778548.
179. DAS, S. et al. Self-assembled monolayer modified ITO in P3HT:PC₆₁BM organic solar cells with improved efficiency. *Sol. Energy Mater. Sol. Cells* [interactive]. 2014, 124, 98–102. Access via: doi:10.1016/J.SOLMAT.2014.01.048.
180. LIN, Y. et al. 18.4 % Organic Solar Cells Using a High Ionization Energy Self-Assembled Monolayer as Hole-Extraction Interlayer. *ChemSusChem* [interactive]. 2021, 14, 3569–3578. Access via: doi:10.1002/cssc.202100707.
181. LIN, Y. et al. 17.1% Efficient Single-Junction Organic Solar Cells Enabled by n-Type Doping of the Bulk-Heterojunction. *Adv. Science* [interactive]. 2020, 7, 1903419. Access via: doi:10.1002/advs.201903419.
182. XU, X. et al. Highly efficient non-fullerene organic solar cells enabled by a delayed processing method using a non-halogenated solvent. *Energy Environ. Sci.* 2020, 13, 4381–4388. Access via: doi:10.1039/D0EE02034F.
183. XU, X. et al. Interface-enhanced organic solar cells with extrapolated T₈₀ lifetimes of over 20 years. *Science Bull* [interactive]. 2020, 65, 208–216. Access via: doi:10.1016/j.scib.2019.10.019.
184. CHOICKALINGAM, M. et al. Importance of the Indium Tin Oxide Substrate on the Quality of Self-Assembled Monolayers Formed from Organophosphonic Acids. *Langmuir* [interactive]. 2011, 27, 2545–2552. Access via: doi:10.1021/la104464w.
185. WU, T. et al. Self-Assembled Monolayer Hole-Selective Contact for Up-Scalable and Cost-Effective Inverted Perovskite Solar Cells. *Adv. Funct. Mater.* [interactive]. 2024, 34, 2316500. Access via: doi:10.1002/adfm.202316500.
186. UTOMO, D. S. et al. Nonfullerene Self-Assembled Monolayers As Electron-Selective Contacts for n-i-p Perovskite Solar Cells. *ACS Energy Lett.*

- [interactive]. 2024, 9, 1682–1692. Access via: doi:10.1021/acsenergylett.4c00306.
187. SALIBA, M. et al. A molecularly engineered hole-transporting material for efficient perovskite solar cells. *Nat Energy* [interactive]. 2016, 1, 15017. Access via: doi:10.1038/nenergy.2015.17.
188. RAM, V. J. et al. Chapter 5 - Five-Membered Heterocycles. *The Chemistry of Heterocycles* [interactive]. 2019, 149–478. Access via: doi:10.1016/B978-0-08-101033-4.00005-X.
189. LIU, S. et al. Sulfur-rich benzodithieno[3,2-b]thiophene-cored hole transporting materials for long-time stability of perovskite solar cells. *Dyes and Pigments* [interactive]. 2021, 193, 109506. Access via: doi:10.1016/j.dyepig.2021.109506.
190. ULLAH, A. et al. Novel Phenothiazine-Based Self-Assembled Monolayer as a Hole Selective Contact for Highly Efficient and Stable p-i-n Perovskite Solar Cells. *Adv. Energy Mater.* [interactive]. 2022, 12, 2103175. Access via: doi:10.1002/aenm.202103175.
191. DATTA, K. et al. Monolithic All-Perovskite Tandem Solar Cells with Minimized Optical and Energetic Losses. *Adv. Mater.* [interactive]. 2022, 34, 2110053. Access via: doi:10.1002/adma.202110053.
192. SALIBA, M. et al. Cesium-containing triple cation perovskite solar cells: improved stability, reproducibility and high efficiency. *Energy Environ. Sci.* [interactive]. 2016, 9, 1989–1997. Access via: doi:10.1039/C5EE03874J.
193. XU, J. et al. Triple-halide wide-band gap perovskites with suppressed phase segregation for efficient tandems. *Science* [interactive]. 2020, 367, 1097–1104. Access via: doi:10.1126/science.aa5074.
194. WANG, S. et al. Advantages and challenges of self-assembled monolayer as a hole-selective contact for perovskite solar cells. *Mater. Futures* [interactive]. 2023, 2, 012105. Access via: doi:10.1088/2752-5724/acbb5a.
195. ZHANG, J. et al. Nanostructured Materials for Room-Temperature Gas Sensors. *Adv. Mater.* [interactive]. 2016, 28, 795–831. Access via: doi:10.1002/adma.201503825.
196. JIAN, Y. et al. Gas Sensors Based on Chemi-Resistive Hybrid Functional Nanomaterials. *Nano-Micro Lett.* [interactive]. 2020, 12, 71. Access via: doi:10.1007/s40820-020-0407-5.
197. SINGH, M. et al. SAM Functionalized ZnO Nanowires for Selective Acetone Detection: Optimized Surface Specific Interaction Using APTMS and GLYMO Monolayers. *Adv. Funct. Mater.* [interactive]. 2020, 30, 2003217. Access via: doi:10.1002/adfm.202003217.
198. RAKŠTYS, K. et al. Steric hindrance driven passivating cations for stable perovskite solar cells with an efficiency over 24%. *Journal of Mater. Chem. A.* [interactive]. 2024, 12, 1422–1428. Access via: doi:10.1039/D3TA03423B.
199. BAN, J. et al. Site-Specific Synthesis of Carbazole Derivatives through Aryl Homocoupling and Amination. *Synthesis* [interactive]. 2020, 52, 917–927. Access via: doi:10.1055/s-0039-1690759.

200. PENG, W. Using Two Compatible Donor Polymers Boosts the Efficiency of Ternary Organic Solar Cells to 17.7%. *Chem. Mater.* [interactive]. 2021, 33, 7254–7262. Access via: doi:10.1021/acs.chemmater.1c01433.
201. TAMULEVIČIUS, T. et al. Antireflection Coatings Based on Randomly Oriented ZnO Nanowires. *Solar RRL* [interactive]. 2023, 7, 2201056. Access via: doi:10.1002/solr.202201056.
202. RAČKAUSKAS, S. et al. A Novel Method for Continuous Synthesis of ZnO Tetrapods. *The Journal of Physical Chemistry C*. [interactive]. 2015, 119, 16366–16373. Access via: doi:10.1021/acs.jpcc.5b03702.
203. TAMULEVIČIENĖ, A. et al. Highly-hydrophobic, transparent, and durable coatings based on ZnO tetrapods with diamond-like carbon nanocomposite. *Surf. Coat. Technol.* [interactive]. 2023, 470, 129863. Access via: doi:10.1016/j.surfcoat.2023.129863.
204. ILICKAS, M. et al. ZnO tetrapod morphology influence on UV sensing properties. *Nanotechnology* [interactive]. 2024, 35, 015502. Access via: doi:10.1088/1361-6528/acfcbf.

CURRICULUM VITAE

Mantas Marčinskas

Mantas.marcinskas@ktu.lt, mantas.marcinskas@gmail.com

Education:

- 2006 – 2014 Jeronimas Ralys Gymnasium, Jonava, Lithuania
2014 – 2018 Kaunas University of Technology (Bachelor of Chemistry)
2018 – 2020 Kaunas University of Technology (Master of Chemistry)
2020 – 2024 Kaunas University of Technology (Chemistry PhD studies)

Professional experience:

- May 2020 – August 2020 Project engineer
August 2020 – currently Project junior researcher
April 2022 – June 2022 University lecturer
April 2024 – June 2024 University lecturer
July 2024 – August 2024 Project supervisor

Areas of research interest:

Synthesis of organic semiconductors which could be used in optoelectronics.

Scientific papers related to the topic of dissertation:

1. Lin, Yuanbao; Zhang, Yadong; Zhang, Junxiang; **Marcinskas, Mantas**; Malinauskas, Tadas; Magomedov, Artiom; Nugraha, Mohamad Insan; Kaltsas, Dimitris; Naphade, Dipti R.; Harrison, George T.; ElLabban, Abdulrahman; Barlow, Stephen; De Wolf, Stefaan; Wang, Ergang; McCulloch, Iain; Tsetseris, Leonidas; Getautis, Vytautas; Marder, Seth R.; Anthopoulos, Thomas D. 18.9% efficient organic solar cells based on n-doped bulk-heterojunction and halogen-substituted self-assembled monolayers as hole extracting interlayers. *Advanced Energy Materials*. 2022, Vol. 12, iss. 45, art. No. 2202503. (IF = 27.8, Q1).
2. Al-Ashouri, Amran; **Marčinskas, Mantas**; Kasparavičius, Ernestas; Malinauskas, Tadas; Palmstrom, Axel; Getautis, Vytautas; Albrecht, Steve; McGehee, Michael D.; Magomedov, Artiom. Wettability improvement of a carbazole-based hole-selective monolayer for reproducible perovskite solar cells. *ACS Energy Letters*. 2023, Vol. 8, p. 898–900. (IF = 22.0, Q1).
3. Geka, Despoina; Hamilton, Iain; Stavridis, Thalis; Liu, Zhongzhe; Faber, Hendrik; Naphade, Dipti; **Marčinskas, Mantas**; Malinauskas, Tadas; Harrison, George; Adilbekova, Begimai; Maksudov, Temur; Yuan, Yue; Kaltsas, Dimitrios; Tsetseris, Leonidas; Getautis, Vytautas; Lanza, Mario; Patsallas, Panos; Fatayer, Shadi; Anthopoulos, Thomas D. Tuning Hole-Injection in Organic-Light Emitting Diodes with Self-Assembled Monolayers. *ACS Applied Materials & Interfaces*. 2024, Vol. 16, iss. 30, p. 39728–39736. (IF = 8.3, Q1).

4. Zhumagali, Shynggys; Li, Chongwen; **Marčinskas, Mantas**; Dally, Pia; Liu, Yuan; Ugur, Esma; Petoukhoff, Christopher E; Ghadiyali, Mohammed; Prasetio, Adi; Marengo, Marco; Pininti, Anil R; Azmi, Randi; Schwingenschlögl, Udo; Laquai, Frédéric; Getautis, Vytautas; Malinauskas, Tadas; Aydin, Erkan; Sargent, Edward H; De Wolf, Stefan. Efficient Narrow Bandgap Pb-Sn Perovskite Solar Cells Through Self-Assembled Hole Transport Layer with Ionic Head. *Advanced Energy Materials*. 2025, art. No. 2404617 (Early View). (IF = 27.8, Q1).

Scientific conferences related to the topic of dissertation:

1. Marcinskas, Mantas; Pocobut, Elzbieta; Malinauskas, Tadas. Organic semiconductors with reactive functional groups for application in optoelectronics // *Balticum organicum syntheticum* [BOS] 2022: in memory of prof. Victor Sniečkus: July 3–6, 2022, Vilnius, Lithuania. 2022, P075. ISBN 9786099603940. eISBN 9786099603933. p. 119.
2. Marcinskas, Mantas; Malinauskas, Tadas. Organic semiconductors with phosphonic acid functional groups for application in photovoltaics // *CRF-ChemCYS* 2022: October 12–14, 2022, Blankenberge, Belgium. 2022, FM-B03, p. 266.
3. Marcinskas, M.; Magomedov, A.; Malinauskas, T.; Getautis, V. Synthesis and investigation of carbazole-based halogenated SAM materials // *FEMS EUROMAT 2023*: 17th European congress and exhibition on advanced materials and processes: book of abstracts / editor: E. Zschech. Sankt Augustin: DGM - Deutsche Gesellschaft für Materialkunde, 2023. ISBN 9783883554341. p. 1368.
4. Marcinskas, M.; Magomedov, A.; Malinauskas, T.; Getautis, V. Carbazole-Based Halogenated SAMs as High Performing Hole Transporting Materials for Organic Photovoltaics // *Asia-Pacific International Conference on Perovskite, Organic Photovoltaics and Optoelectronics* (IPEROP24). 2024, January 21–23, Tokyo, Japan.

Patent application:

1. EP24200646.8. Musiienko Artem, Frasca Chiara, Stacchini Valerio, Abate Antonio, Rastgoo Madineh, **Mantas Marčinskas**, Vytautas Getautis, Tadas Malinauskas, Skirmantas Musteikis. Compounds forming hole-transporting selfassembled monolayer / Applicants: Helmholtz-Zentrum Berlin für Materialien und Energie GmbH; Kaunas University of Technology. September 16, 2024.

ACKNOWLEDGEMENTS

I would like to acknowledge my supervisor and advisor Prof. Dr. Tadas Malinauskas, who has been guiding me since Bachelor studies and who has immensivly helped me to become who I am today. Thanks to him, I was able to grow not only as a chemist and a scientist, but as a future supervisor too. Also, I would like to thank Prof. Dr. Vytautas Getautis and all of our research group members for continuous and comprehensive support. Our partners are also worthy of praise – without them these results demonstrated in the thesis would not have been possible. Even my own students had an impact – all of them contributed to the development of my skills and personality.

ANNEXES

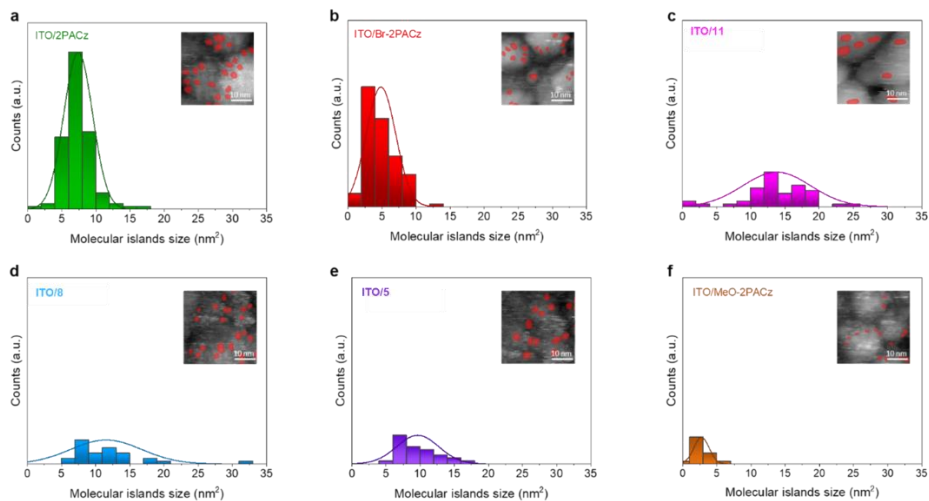


Figure A1. Statistical STM analysis of various SAM-modified ITO samples where SAM forming ‘islands’ are highlighted in red (inset STM images)

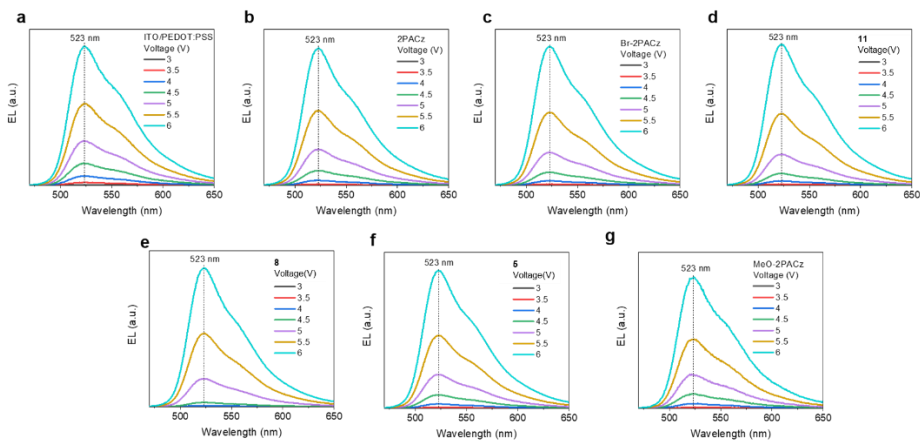


Figure A2. Comparison of voltage-dependent electroluminescence (EL) spectra of OLEDs based on different hole-injection layers. All devices show stable green EL emission

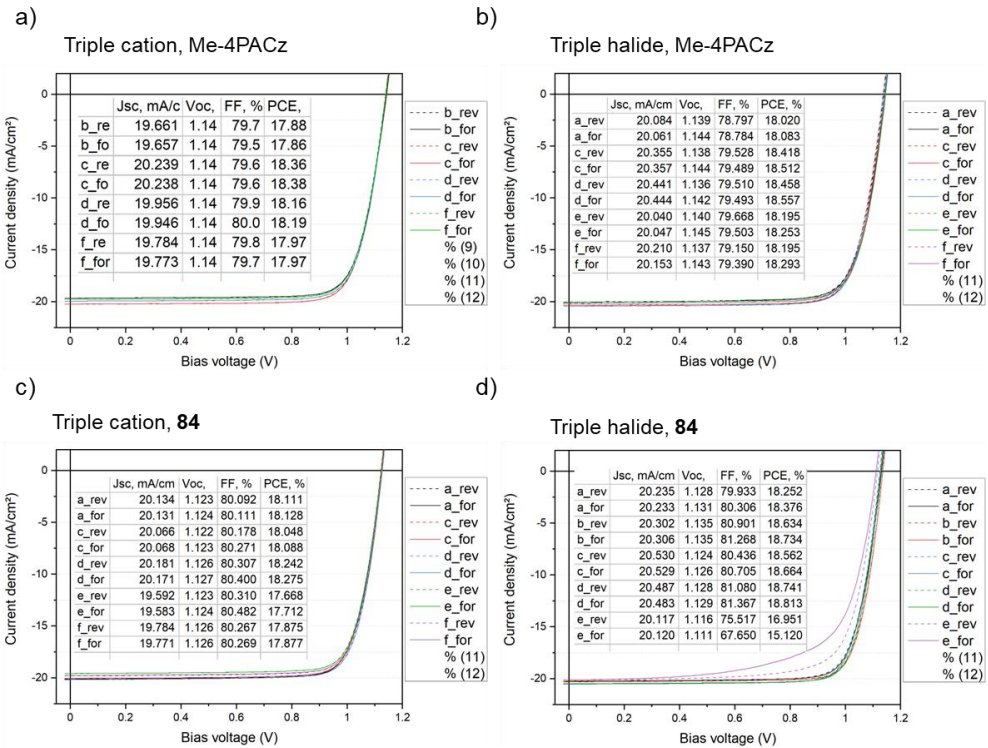


Figure A3. Statistical photovoltaic characteristics and J-V curves of ‘triple cation’ and ‘triple halide’ perovskite solar cells, based on Me-4PACz or compound **84**

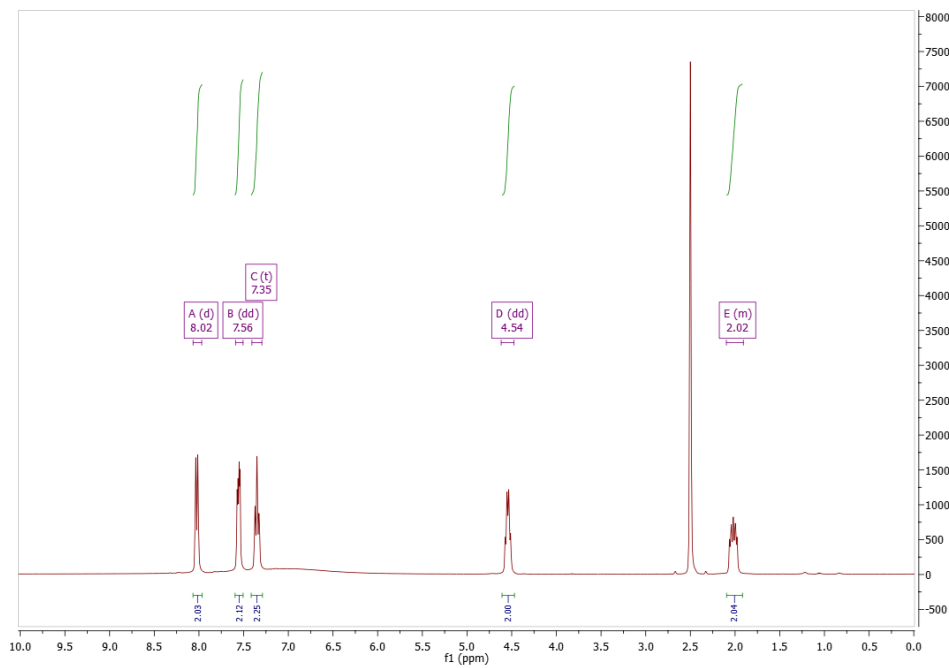


Figure A4. ^1H NMR spectrum of compound **5** in DMSO-d_6

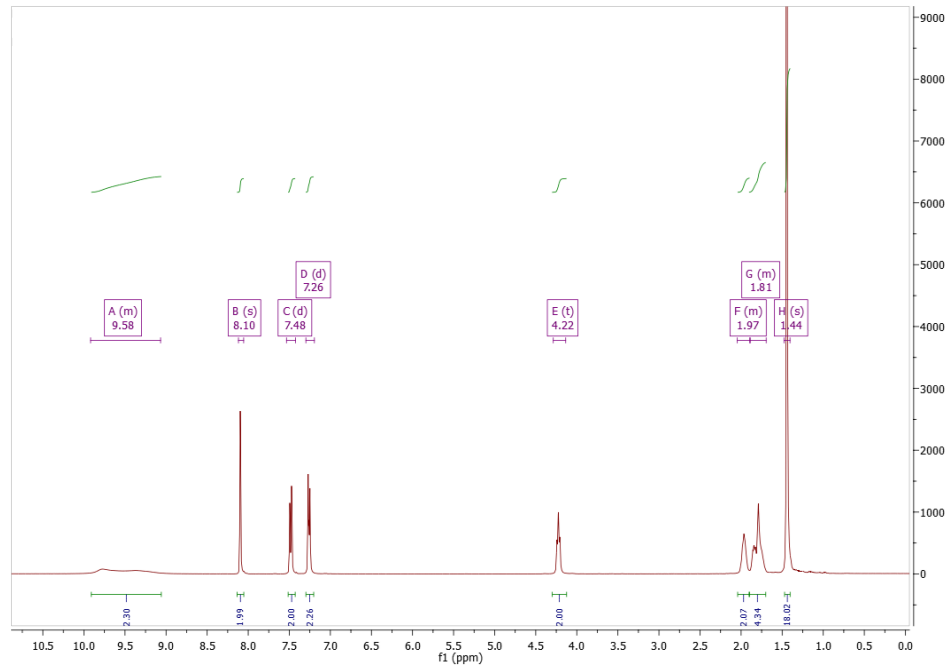


Figure A5. ^1H NMR spectrum of compound **77** in CDCl_3

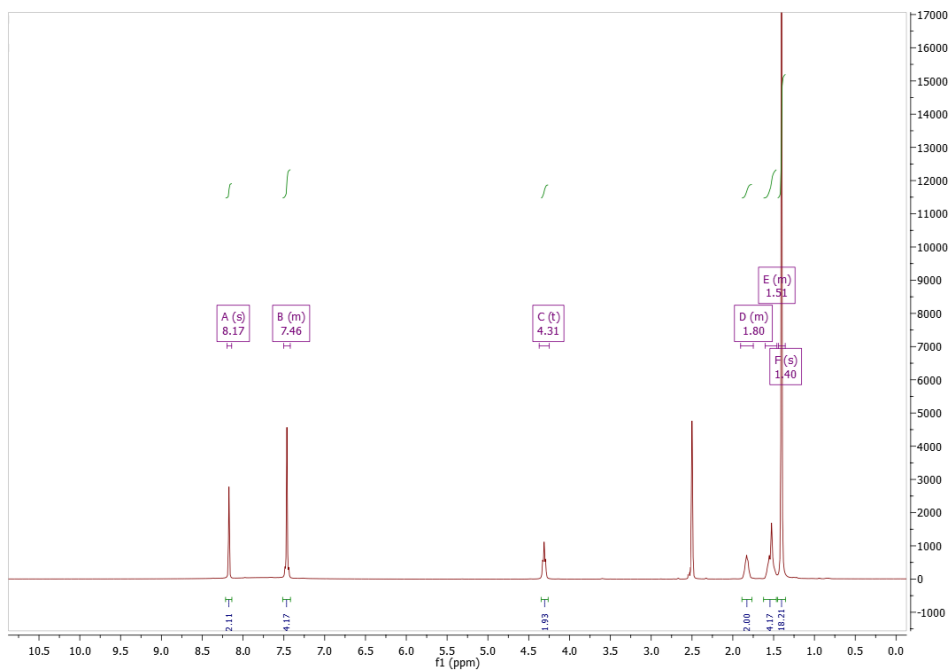


Figure A6. ^1H NMR spectrum of compound 77 in DMSO-d_6

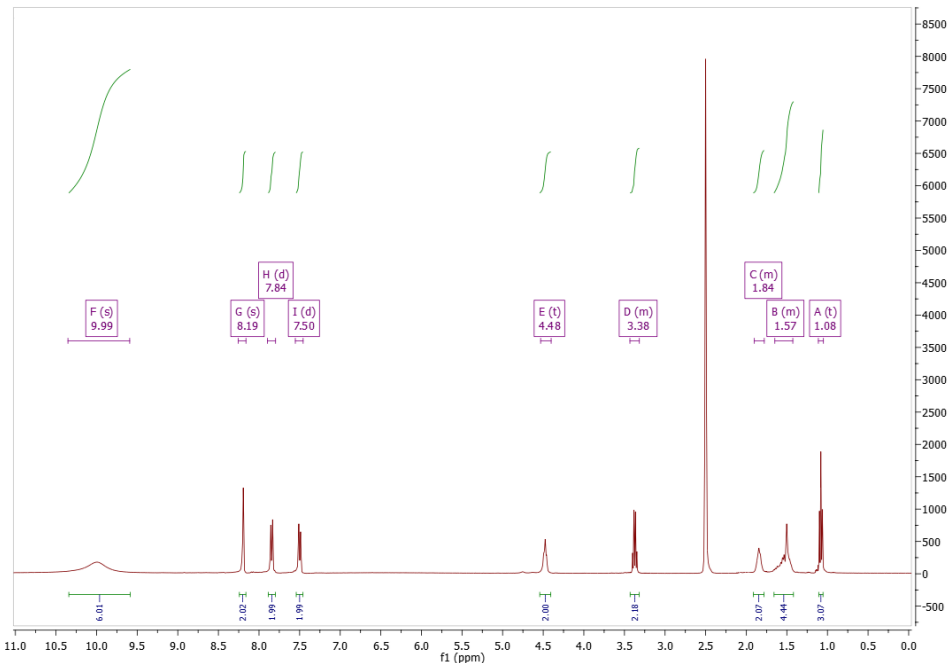


Figure A7. ^1H NMR spectrum of compound 95 in DMSO-d_6

UDK 547.7+621.383.51+621.315.59](043.3)

SL344. 2025-01-09, 27,25 leidyb. apsk. 1. Tiražas 14 egz. Užsakymas 219.
Išleido Kauno technologijos universitetas, K. Donelaičio g. 73, 44249 Kaunas
Spausdino leidyklos „Technologija“ spaustuvė, Studentų g. 54, 51424 Kaunas